Transactions of the ASME

The Journal of Engineering for Gas Turbines and Power (ISSN 0022-0825) is published quarterly for $100 per year by The American Society of Mechanical Engineers, 345 East 47th Street, New York, NY 10017. Second class postage paid at New York, NY and additional mailing offices. POSTMASTER: Send address change to The Journal of Engineering for Gas Turbines and Power, c/o The AMERICAN SOCIETY OF MECHANICAL ENGINEERS, 22 Law Drive, Box 2300, Fairfield, NJ 07007-2300.

CHANGES OF ADDRESS must be received at Society headquarters seven weeks before they are to be effective. Please send old label and new address.

PRICES: To members, $24.00, annually; to nonmembers, $100.00. Add $6.00 for postage to countries outside the United States and Canada.

INDEXED by Engineering Information

Journal of Engineering for Gas Turbines and Power

Published Quarterly by The American Society of Mechanical Engineers

VOLUME 108 • NUMBER 3 • JULY 1986

TECHNICAL PAPERS

432 The Great Plains Coal Gasification Project Status (85-WA/Fu-A)
B. J. Bodnaruk

440 Influence of Coal Properties on Forward Combustion in Laminar Flow (84-WA/Fu-B)
W. R. Lockwood, R. C. Corlett, H. R. Mortazavi, and A. F. Emery

446 Variations of the Lean Blowout Limits of a Homogeneous Methane-Air Stream in the Presence of a Metallic Wire Mesh (85-WA/Fu-E)
G. A. Karim and M. G. Kibrya

450 Bench Scale Process Evaluation of Reburning for In-Furnace NO_x Reduction (84-JPGC-APC-9)
S. B. Greene, S. L. Chen, D. W. Pershing, M. P. Heap, and W. R. Seeker

455 Combustion Gas Properties: Part II – Prediction of Partial Pressures of CO_2 and H_2O in Combustion Gases of Aviation and Diesel Fuels (86-GT-163)
Ö. L. Gülder

460 Fuel Deposit Characteristics at Low Velocity (85-IGT-130)
E. J. Szetela, A. J. Giovanetti, and S. Cohen

465 Internal Flow Effects in Prefilming Airblast Atomizers: Mechanisms of Atomization and Droplet Spectra (86-GT-150)
T. Sattelmayer and S. Wittig

473 Experimental and Analytical Investigation on the Variation of Spray Characteristics Along Radial Distance Downstream of a Pressure Swirl Atomizer (86-GT-51)
Y. H. Zhao, W. M. Li, and J. S. Chin

479 Measurements of Entrainment by Acoustically Pulsed Axisymmetric Air Jets (86-GT-86)
P. J. Vermeulen, V. Ramesh, and Wai Keung Yu

485 Study on Two-Phase Fuel Distributions in High-Speed Hot Transverse Air Stream (85-IGT-118)
Yang Mao-lin, Gu Shan-jian, and Li Xiang-yi

491 An Improved Method for Accurate Prediction of Mass Flows Through Combustor Liner Holes (86-GT-149)
R. C. Adkins and D. Gueroui

498 Velocity and Turbulence Fields in Pipe Entrance Regions in the Presence of Cross Flows (86-GT-119)
S. Lloyd and A. Brown

504 Thermal Mechanical Fatigue Life Prediction for Advanced Anisotropic Turbine Alloys (86-GT-124)
P. N. Pejsa and B. A. Cowles

507 Comparison of Methods for Lifetime Calculations of Highly Loaded Aero-Engine Discs (86-GT-102)
R. Hefele, G. Kappler, and D. Rist

515 A Simplified Thermal Mechanical Fatigue (TMF) Test Method (86-GT-120)
J. R. Warren and B. A. Cowles

521 Improvement of a Cycle *J* Integral for CT Specimens (85-IGT-66)
Liu Shao-Lun and Xie Ji-Zhou

525 A Nonlinear Theory of Dynamic Systems With Dry Friction Forces (86-GT-8)
A. V. Srinivasan and B. N. Cassenti

531 Reliability Evaluation of Ceramic Rotor for Passenger-Car Turbochargers (86-GT-10)
Y. Hamano, N. Sagawa, and H. Miyata

536 Fabrication of Near-Net-Shape Silicon Nitride Parts for Engine Application (86-GT-11)
G. Bandyopadhyay and K. W. French

540 SCARE: A Postprocessor Program to MSC/NASTRAN for Reliability Analysis of Structural Ceramic Components (86-GT-34)
J. P. Gyekenyesi

547 Friction Losses and Flow Distribution for Rotating Disks With Shielded and Protruding Bolts (86-GT-158)
H. Zimmermann, A. Firsching, G. H. Dibelius, and M. Ziemann

553 Effects of Honeycomb-Shaped Walls on the Flow Regime Between a Rotating Disk and a Stationary Wall (86-GT-161)
T. Uzkan and N. J. Lipstein

562 Lip Separate Flow Blowing and Analysis of Coherence of Inlet (85-IGT-68)
Z. W. He and S. Y. Zhang

(Continued on p. 439)

(Contents Continued)

ANNOUNCEMENTS

431 Editorial

565 *Change of address form for subscribers*

566 Reference citation format

Inside back cover Information for authors

Journal of Engineering for Gas Turbines and Power

Editorial

Concurrently with this issue of the JOURNAL OF ENGINEERING FOR GAS TURBINES AND POWER, a new ASME journal has come into existence called the *Journal of Turbomachinery*. The *Journal of Turbomachinery* is a spinoff from the JOURNAL OF ENGINEERING FOR GAS TURBINES AND POWER. It was created to provide the increased publishing capacity necessary to accommodate the increasing number of papers appearing in the field of power generation. This journal will concentrate on compressor and turbine component technology. Judging from the present backlog, the heaviest concentration of papers will be in the area of compressor and turbine aerodynamics, followed by turbine cooling and heat transfer.

The JOURNAL OF ENGINEERING FOR GAS TURBINES AND POWER will continue to publish all papers dealing with research, development, and operating experience with complete systems including gas turbines, fossil fuel and nuclear-fired steam power plants, and internal combustion engines. It will also retain all papers on combustion, on system dynamics, most papers on structures and materials topics, and those on control systems and all types of auxiliaries such as fuel systems, pollution control systems, inlet and exhaust systems, etc.

Papers dealing with the fluid mechanics of hydraulic turbines and pumps will continue to appear in the *Journal of Fluids Engineering*.

ARTHUR J. WENNERSTROM
Technical Editor

The Great Plains Coal Gasification Project Status

B. J. Bodnaruk
Technical Monitor,
U.S. Department of Energy,
Chicago Operations Office,
Argonne, IL 60439

The Great Plains Gasification Project is the first commercial-sized plant to produce substitute natural gas from coal in the United States. The plant is designed to convert 14,000 tons/D of North Dakota lignite into 137.5 million standard cubic feet of gas per day. The plant construction has been successfully completed per original design, on schedule and on budget. The plant has also been successfully turned over from construction to operations, as per the original plan. With the completion of the capital projects being implemented at the plant, plans are to achieve 70 percent stream factor in the first year of production (1985). The DOE-Chicago Operations Office has been assigned the responsibility for monitoring the project's performance against baselines of cost, schedule, and technical criteria. During the startup phase of the project, significant technological advancements have been made and considerable knowledge has been gained, both by the operators and DOE (considering this to be a first of a kind plant built in the U.S.).

Introduction and General Overview

The Great Plains Gasification Associates Coal Gasification Project (Fig. 1) is the first commercial-sized plant designed to produce 137.5 MMSCFD of pipeline quality synthetic natural gas from lignite utilizing Lurgi high-Btu technology. Further, this is the leading commercial-sized synthetic fuel project in the United States today. This plant was designed and constructed to demonstrate the technical, economic, and environmental feasibility of this type of facility.

This project is sponsored by the owners: American Natural Resources Company; MidCon Corp.; Tenneco, Inc.; Pacific Lighting Corp.; and Transco Energy Company, with the Great Plains Gasification Associates (GPGA) being the overall day-to-day project operators.

This project has come a long, long way from its original inception (Fig. 2) approximately 13 years ago to where it is today. As we all are probably aware, the project was plagued with past problems relating to obtaining FERC regulatory approvals and the arranging of major project financing. However, this is all behind us now!

With the final approval of the Department of Energy loan guarantee for $2.1 billion and all permits in hand, the project's major construction got underway in August of 1981. The cost breakdown of the major facilities consists of a $1.6 billion coal gasification plant, Great Plains' $160 million share of a coal mine which is jointly developed with Basin Electric Power Cooperative, a local company, and $18 million for a gas pipeline plus various contingencies.

The FERC settlement provided that the Great Plains Coal Gasification Plant in North Dakota will operate on an unregulated basis, not subject to the jurisdiction of the agency.

The integration of the Lurgi process design into the overall plant was the major responsibility of U.S. engineering contractors: The Lummus Company and Kaiser Engineers, Inc. These firms had the primary responsibilities for the engineering, procurement, and construction for the overall plant. The South African Coal, Oil, and Gas Corporation (SASOL) was engaged as the major consultant to the project.

In 1974, 12,000 tons of North Dakota lignite was shipped to South Africa for a commercial-scale test in a single Lurgi gasifier at the SASOL I plant. After an extremely successful test, optimism ran high with schedules projecting a plant producing 250 MMSCFD of SNG to be constructed and operating by 1979. While this schedule was completely realistic from an engineering and construction viewpoint, the regulatory and financing nightmares that followed could never have been anticipated.

It should be mentioned here that the services of SASOL on this project have been invaluable. These services have included testing of North Dakota lignite byproducts and wastewater; review of all process and proprietary equipment designs; and advice on operating and maintenance procedures.

SASOL is well on its way to making South Africa energy independent. Their original coal gasification plant (SASOL I), which has been in operation for over 25 years, now contains 17 operating Lurgi gasifiers. SASOL II has 36 Lurgi gasifiers installed and started production in 1980. Recently they installed 36 additional Lurgi gasifiers at SASOL III and completed a 100 percent expansion of SASOL II; they are currently designing SASOL IV facilities. When these facilities are complete, the major portion of South Africa's hydrocarbon products will be produced from coal.

The DOE-Chicago Operations Office has been assigned the responsibility for monitoring the project's performance against baselines of cost, schedule, and technical criteria.

Process Description

Figure 3 is a simplified block flow diagram illustrating the

Contributed by the Fuels and Combustion Technologies Division and presented at the Energy Sources Technology Conference, New Orleans, LA, February 23, 1986. Manuscript received by the Fuels and Combustion Technologies Division June 27, 1985. Paper No. 85-WA/Fu-A.

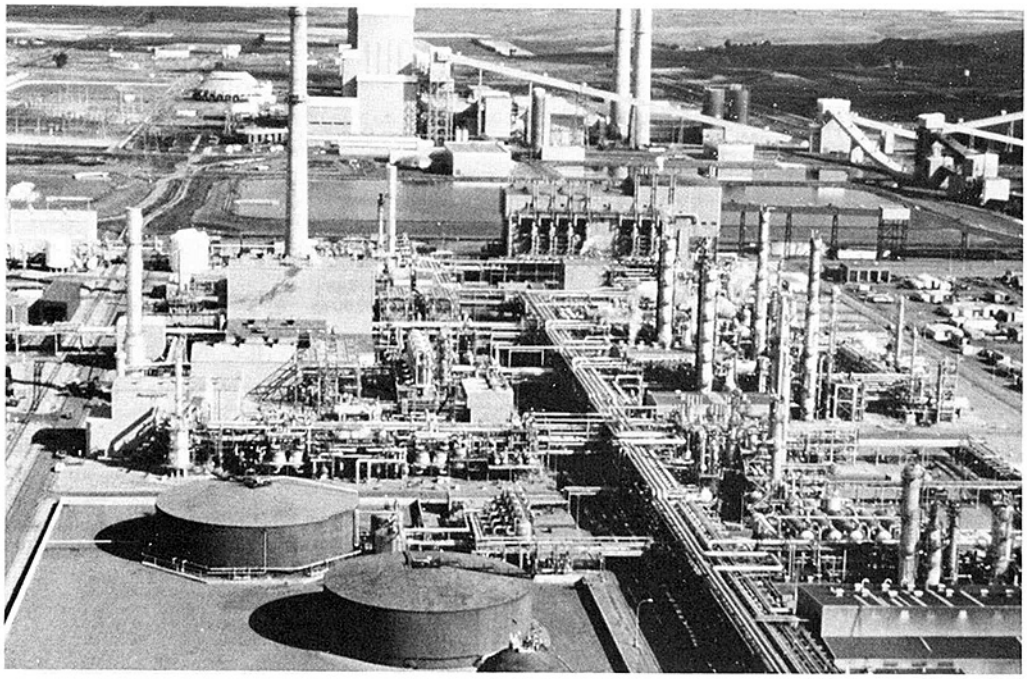

Fig. 1

GREAT PLAINS GASIFICATION ASSOCIATES

Abbreviated Highlights
1972-1982

March, 1977	• Peoples Energy joined with ANR to jointly construct plant
May, 1978	• GP formed - ANR/Peoples/Tenneco/Transco/ Columbia Gas (Columbia Gas later withdraws)
August, 1978 to August, 1981	• Innumerable negotiations, & hearings relative to Government authorization, financing methods, sales contracts
July, 1980	• President Carter approved a conditional letter of commitment - $240 million loan guarantee
August, 1981	• President Reagan authorized DOE to issue conditional loan guarantee - $2.02 billion
August, 1981	• Full scale construction commenced
January, 1982	• Loan Agreement executed

Fig. 2

gasification process. Approximately 22,000 tons per day of lignite are crushed to 8-in.-pieces in the primary crushers. It is then crushed to less than 2 in. in the secondary crushers and fed onto a seven-day live storage pile. The coal is reclaimed from storage with rotary plow feeders and screened with high probability sizers. Approximately 14,000 tons per day of 2 in. × 1/4 in. coal is fed to the gasifiers and 8000 tons per day of 1/4 in. coal is fed to Basin Electric (a nonaffiliated electric generating facility adjacent to the gasification plant) to fuel its boilers.

The heart of the gasification plant is the gasifier building containing 14 Lurgi Mark IV dry bottom gasifiers. During normal operations, 12 gasifiers are in operation with two serving as spares. The coal is charged through the top by means of lock hoppers. The ash is likewise discharged by means of lock hoppers at the bottom. Steam and oxygen are mixed and distributed through the grate upward through the coal bed. The gasifiers operate at about 430 psig.

The raw gas produced is quenched and cooled from approximately 370°F to 95°F, to condense the tar, oil, phenols, am-

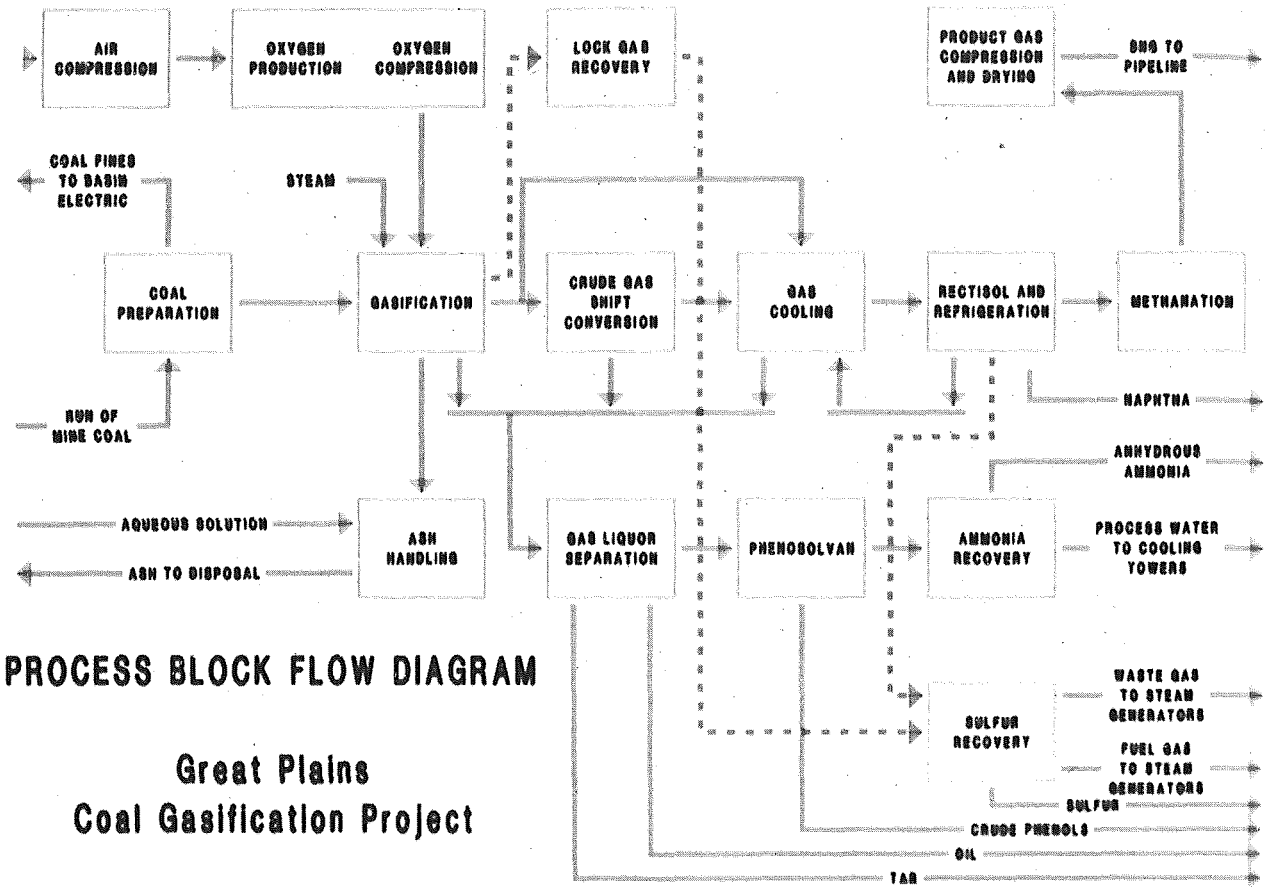

Fig. 3

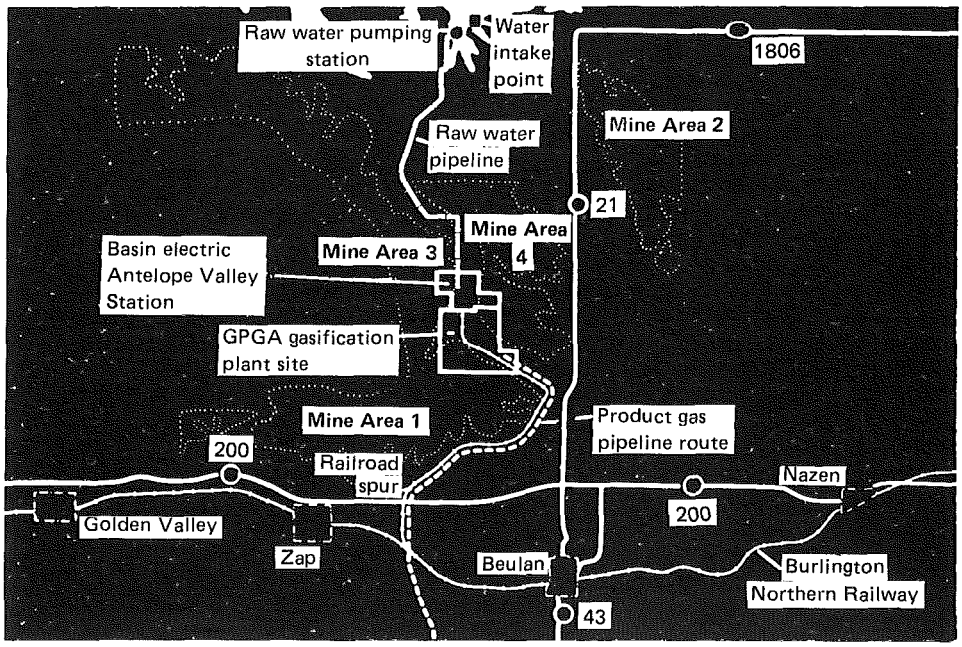

Fig. 4

monia, and water from the gas stream. These components comprise the gas liquor stream which is treated separately.

About 30 percent of the gas stream is "shifted" in catalytic reactors to produce the correct ratio of hydrogen to carbon monoxide for methanation slightly more than 3 to 1. Carbon monoxide reacts with steam over a cobalt molybdenum catalyst to produce the additional hydrogen required

$$CO + H_2O \xrightarrow{Co\text{–}Mo} CO_2 + H_2 \qquad (1)$$

The gas is further purified by a low-temperature methanol wash in the Rectisol Unit. In this unit, all naphtha, essentially all sulfur, and 97 percent of the CO_2 are removed to prepare the gas for methanation. An ammonia refrigeration system supplies the cooling for Rectisol. The Rectisol off-gases are

scrubbed in a Stretford Unit producing elemental sulfur for sale

$$H_2S + 1/2\,O_2 \rightarrow 1/8\,S_8 + H_2O \text{ (overall reaction)} \quad (2)$$

while the Stretford off-gases are incinerated in the boilers to avoid emitting residual hydrocarbons and undesirable sulfur compounds.

The clean synthesis gas is then diluted with recycled methanated gas and passed through parallel beds of reactors containing a reduced nickel catalyst. Carbon oxides react with hydrogen to form methane

$$CO + 3H_2 \overset{Ni}{\rightleftharpoons} CH_4 + H_2O \quad (3)$$

A final cleanup reactor removes remaining traces of carbon monoxide and ensures a high-Btu product gas. The gas is cooled, dried, and compressed to a minimum of 900 psig and enters the pipeline with a higher heating value of 977 Btu per cubic foot.

After removal from the raw gas, the gas liquor stream passes through three stages of gravity separation to remove the tar and oil. The phenols are then removed by extraction with di-isopropyl ether (IPE). Phenols are separated from IPE by distillation.

The dephenolized water is stripped in a Phosam still to remove ammonia and acid gases and is then used as makeup water in the cooling tower. Anhydrous ammonia is produced for sale and the tar, oil, phenols, and naphtha are used to fuel the plant boilers and superheaters.

Socio-Economic Impact

The Great Plains Project is located near Beulah, Mercer County, in West Central North Dakota, about 85 miles from Bismarck, the state capital (Fig. 4). North Dakota is a sparsely populated state of approximately 600,000 people with agriculture being its principal economic activity. As such, early project planning efforts had to be directed at assuring the people and political leaders that the project could be implemented with full protection for the farming interests and with proper environmental safeguards.

The peak construction work force numbered around 4600 (July/Aug. 1983) which required extensive planning, including a construction worker camp for up to 1500 workers; development of project support infrastructure, including schools, health care facility assessments, operating employee housing, mortgage pool funding to finance housing, city development, planning and zoning; and many other impact mitigating considerations that result from superimposing a "super project" on a rural community. Prepayment of taxes and other fiscal related considerations had to be planned, studied, and handled through new state legislation.

Since the coal for the project is to be surface mined, land use and reclamation were an absolute necessity.

When fully operational, the plant will employ 920 operational and maintenance personnel. The local skill levels could not support this need so extensive recruiting and training were essential.

GPGA worked with the state of North Dakota to establish entry level job training programs to maximize the employment of North Dakota citizens and minimize out-of-state recruiting. Nevertheless, a substantial portion of the operating staff is attracted from chemical, refining, and other process industries located in other regions of the country.

To facilitate the labor availability required to construct the project, GPGA negotiated a labor agreement with the presidents of 17 international unions representing all the crafts required to perform on-site construction. The labor agreement gave the contractors certain rights for recruiting skilled labor and it established favorable work rules, work practices, and apprentice/journeyman crew size ratios. Lastly, the agreement contained an innovative labor wage rate formula that used a 19 city rolling average wage rate to determine annual wage rates. This procedure eliminated annual contract negotiations as local contracts expired. The labor agreement, coupled with the slowdown in other construction activities, has provided the project with an uninterrupted supply of labor in sufficient quantities.

Great Plains Construction Expenditures
(millions of dollars)

		Plant	Mine	Total
Through	1981	$ 236	$ 20	$ 256
	1982	621	32	653
	1983	636	52	688
	1984	465	51	516
		$ 1,958	$ 155	$ 2,113

Fig. 5

Project Cost

The current estimate of the cost of the project at completion, in as-spent dollars, is $2.113 billion, including a coal mine that will produce 4.1 million tons of lignite annually (Fig. 5). The cost estimate is continually reviewed and updated. By any standard of comparison, the GPGA project is enormous in size. To illustrate, consider just some of the principal elements of cost included within the $2.1 billion:

1 Gasification plant $1.6B
(engineering, materials, field labor, indirect, taxes, insurance, etc.)

2 Mine $155M

3 Interest during construction $350M

The latest estimate at completion shows the project to be on budget. The largest contribution to this has been the soft economic conditions experienced to date. These conditions have benefited the project by allowing for very favorable price breaks and the achievement of lump-sum contracting with material and equipment suppliers. In addition, interest rates have been lower than forecast resulting in substantial cost benefit. All of this was offset by increasing construction costs resulting from workaround plans developed to maintain the original schedule.

The key schedule events were:

1 Startup testing commenced in September 1983 and was completed in December 1984 after a 63-week time frame.

2 The first cubic foot of SNG was pumped into the pipeline July 28, 1984.

3 Full gas production at design rates began July 1985.

Project Economics

Under the FERC-approved settlement, all of the synthetic gas produced by the plant would be sold to pipeline affiliates of the sponsors of Great Plains. The price of syngas would be adjusted from a base price of $6.75 per million Btu by indexing to No. 2 fuel oil and wholesale price indices, but with increases limited primarily by No. 2 fuel oil prices in the earlier years of operation and by unregulated domestic gas prices in the later years.

The basic formula provides for a base price of $6.75 per MMBtu as of Jan. 1, 1981, escalated quarterly based equally on increases in the Producer Price Index and the price of No. 2 fuel oil. In addition, the basic formula is subject to various "caps," namely, the price of No. 2 fuel oil; the average of Canadian and Mexican international import border prices for natural gas during the second five years of operation; and the

average of a band of high-priced domestic natural gas prices after ten years of operation.

Therefore, the economic viability of this project is very much dependent upon the world price of oil. A "long-term" lowering of oil prices has a direct negative impact upon return of investment (ROI). However, this demonstration project was not built for 1985, 1986, or 1987, but rather for the 25-year period of 1984 to 2009. This is what we mean by "long term" and over that period it is expected that energy prices will increase substantially, making the project a financial success.

A key factor in profitability will be assumptions regarding the operating ratio for the plant. The plant is designed to operate at a 91 percent operating ratio. Translated into production volume, the plant is expected to produce 137.5 MMSCF/D 91 percent of the time or an average of 125 MMSCF/D on an annual basis. For economic evaluation purposes, operating ratios have been assumed of 70 percent in 1985, 77 percent in 1986, 84 percent in 1987, and 91 percent thereafter. This is based upon the fact that it will take a few years to gain operating skills, remove process unit bottlenecks, work out the startup kinks, and achieve a high level of training. This is obviously a critical assumption that has tremendous impact upon profitability, and to the extent these ratios can be accelerated, the plant's profitability could show earlier benefits.

The marketing of the SNG is assured through gas purchase contracts with affiliates of the partners of Great Plains. These contracts have been approved by the regulatory authorities and the gas must be purchased under these contracts. The amount of gas produced by the plant is relatively small in terms of the total requirements of the pipeline companies buying the gas. It is less than 2 percent of their present needs and, when rolled in with other lower cost gas, it will not distort their present resale prices.

Project Status

Plant Construction. The construction of the plant was completed in December 1984, as per the original schedule. The gasification plant has been fully turned over to operations as per the original plan.

Mine. In February 1982 ANG directed the Coteau Properties Co. to initiate mine development, engineering, procurement, and construction activities for a 9.9 million tons/year mine, providing the annual lignite requirements of 4.7 million tons to the GPGA plant and 5.2 million tons to Basin Electric Antelope Valley Station (adjacent to the gasification plant).

Initial coal delivery to Basin Electric began in August 1983 and initial coal delivery to the GPGA plant began in March 1984. The 1985 lignite production through June was 3.4 million tons.

SNG Pipeline. The SNG pipeline is a 36-mi pipeline consisting primarily of 24-in. o.d. line pipe with a 1440 psig design pressure which terminates at the 42-in. Northern Border Pipeline in the southwest corner of Mercer County. Pipeline meter stations are located at each end of the pipeline. Construction at a cost of $18 million was completed in August 1983 and the pipeline was ready to receive the startup gas required by the plant in September 1983.

Startup. Startup activities began with the handing over of the plant from construction to operations begining with the water treating plant in August 1983. GPGA received the mechanically completed systems from American Natural Gas (ANG), the project administrator. Next, the plant was thoroughly checked from an operating and safety point of view.

As it turned out, relatively few startup modifications were required to ensure a "clean" startup and safe operation of the process units. This is good evidence of the excellent cooperation between all parties involved – and indeed, there were quite a few:

ANG, as project administrators
GPGA, as owners/operators of the plant
Parsons, as licensors
Lurgi, as licensors/engineers and startup advisors
Lummus, as engineers
Kaiser, as engineers/constructors
SASOL, teamed up with Lurgi as startup advisors
Lotepro/Linde, turnkey contractors
Riley, turnkey contractors

The startup of the SNG process units was GPGA's responsibility. A team made of Lurgi and SASOL engineers was on site to work as consultants to GPGA during the startup.

Under GPGA's overall responsibility, the startup of the SNG process units went along very smoothly, and in adherence to a rather tightly planned schedule. Based on the plant's two-train concept, one train could be started while the other was still being mechanically completed – a major factor in GPGA's ability to stick to a rather tight schedule. The utilities took about ten months to be commissioned and made reliable.

Approximately seven weeks were required to bring the first train of seven gasifiers on line. After these seven weeks, there were few interruptions of gas production due to gasifier or instrument failures – a good demonstration of the Lurgi Mark IV gasifiers' rather high availability.

Another quite interesting feature was that for the startup of the first train (including the gasifier train) approximately three and a half months were required. On the other hand, the second train (including the gasifier train) took only two and a half months to start, indicating both good progress on the learning curve and proof of the wisdom of adopting the two-train concept.

The entire startup period has proven that the processes installed in the SNG production route can be started up and operated safely. At present, all of the startup consultants are gone and the plant is operated by approximately 920 permanent GPGA employees.

Initial Plant Operation

Obviously one cannot expect that so huge an industrial complex comprising a large number of both utility and process units will operate from the onset without problems. As is the case with each similarly sized plant, this one had its share.

Control system, mechanical equipment, trip system failures, etc., may cut out part or all of the SNG process units. However, in order to minimize production losses, it is highly important that failures be both detected and fixed in less than 30 min, lest gasifiers have to come down. Within 30 min, the gasifiers can be restarted immediately, whereas after half an hour they have to be depressurized first and then restarted, which is, of course, more time consuming.

In case of a trip of a unit downstream of gasification, the gasifiers can stay in operation at minimal load and can be brought back to high load in a relatively short time. Thus, trips occurring upstream of gasification (such as in the steam supply) would usually cause longer downtimes of the SNG production than would downstream trips.

However, GPGA managed within the first couple of weeks of the initial operating period to lower the duration of production interruptions due to equipment and other failures from days to hours. Likewise, the number of outages was reduced significantly to what is now a reasonable level for this stage of operation in a plant with 3000 pieces of major equipment and 10,000 instrument loops.

Considerable experience has been gained and many lessons were learned during the startup and initial plant operation.

Among others, the following areas will be of general interest for discussion:

Overdesign
Underdesign
Corrosion/materials handling
New technology
Odor

Overdesign. The boilers and superheaters were designed to take a variety of fuels, including fuel oils, natural gas, SNG, coal dust, dusty tar, naphtha, oils. This required complex instrumentation and considerable changes had to be made in the boilerhouse and superheater.

Underdesign. The wet lignite created many problems in the coal handling areas, such as plugging screens, excess of fines, etc. Ash handling had its share of problems including plugging, agglomeration, underdesigned pumps, etc.

Corrosion/Materials Handling. Handling corrosive materials such as phosphoric acid, ammonia, etc., caused severe corrosion problems. Metallurgy had to be redesigned in heat exchangers and in the Rectisol Unit (due to tremendous temperature variations).

New Technology. With the appearance of mercaptans in the Rectisol Unit, odor problems and poisoning of Ni catalyst occurred. The original Stretford Unit design could not meet the permitting levels of H_2S. Solution rates have to be changed and many modifications are planned in order to meet the 100 ppm H_2S level.

Due to the harsh climatic conditions (from $-80°F$ in winter to $+100°F$ in summer) many structural steel modifications have to be made.

Table 1 Crude gas composition

	Design	Actual
H_2/CO	2.47	2.5
$CO_2 + H_2S$	33.0	32.0
CO	15.9	15.8
H_2	39.3	39.6
CH_4	11.0	11.8
C_NH_M	0.8	0.8
	100.0	100.0

Odor. This was a sensitive issue and GPGA instituted quite an extensive program to solve the problem of odors emanating from the plant.

On the outside, GPGA is conducting an excellent educational and training program for the surrounding population in the immediate area. Inside the plant, GPGA is implementing 20 projects at a cost of $10 million to solve the odor problem.

Capital Projects

The purpose of the capital projects is to solve existing plant problems and increase plant capacity and reliability.

There are a total of 69 capital projects budgeted at $81 million for 1985/1986. Presently these projects are being implemented at the site. Even with the $81 million expenditure, the GPGP will be within the original budget.

With the progression of the capital projects, the plant should increase its reliability and achieve 70 percent on stream factor in 1985, as specified in the original agreement.

SNG Production

The average crude SNG composition is shown in Table 1. After the startup of the first methanation train (end of July 1984), SNG was produced at rates of approximately 50 MMSCFD until the end of October 1984. During this period, the SNG process units did trip several times, mainly caused by utility failures.

After the second SNG process train had been started up, the period began in which production rates were more or less pushed up continuously. As of July 1, 1985 (when this paper was written), the year-to-date total of net SNG pumped into the pipeline was approximately 25,000 MMSCF, with a June daily average of 120 MMSCFD or 87.3 percent of the design rate. During the same time period the following byproducts were recovered and marketed:

16,700,000 lb NH_4
12,500,000 lb S

Agreement has been made between DOE and GPGA on the plant "in-service date." The plant would be considered technically in service if it met the two criteria below:

1 Each train would run for 72 hr at the design rate, i.e., at 68.75 MMSCFD.

2 The plant would run for 90 consecutive days at an average rate of 70 percent design, i.e., at 96.25 MMSCFD.

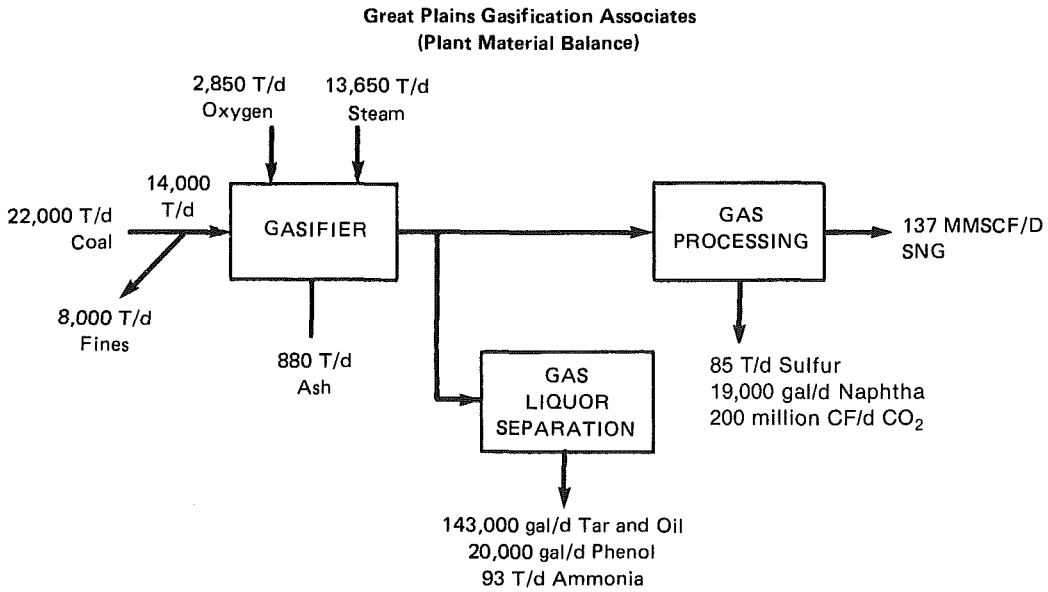

Fig. 6

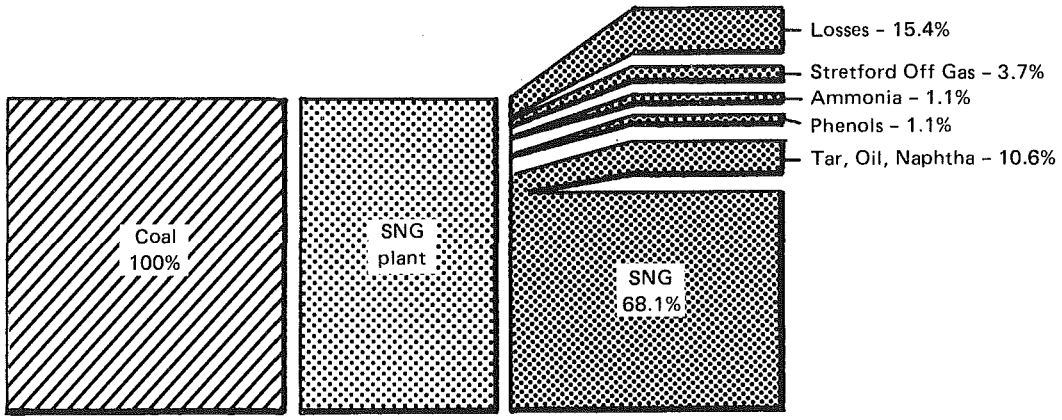

Fig. 7

The first criterion was met on April 1985 and the second criterion was met on June 14, 1985. At this time the plant is considered technically to be in service. The plant design material balance is shown in Fig. 6 and the design energy balance is given in Fig. 7.

Government Involvement

The major question continually asked is "What's in it for the Federal government (and the U.S. taxpayers)?" The statutory purpose of the Non-Nuclear Act is to foster a demonstration program to produce alternate fuels from domestic resources and to gather information, to be made available to the public, which will aid in the development of a synfuels industry. The specific objectives of the project are to enhance the U.S. engineering and construction management "know how" for high-Btu gasification technology; reduce financial and technical risks associated with the technology for future projects; ascertain the environmental acceptability of this technology in the U.S.; provide an accurate basis for determining investment and operations costs for commercial-sized application of this technology in the U.S.; provide performance/failure data for components and equipment; and demonstrate the marketability of synthetic natural gas (SNG).

The loan guarantee is managed by the DOE through the Assistant Secretary for Fossil Energy. The Chicago Operations Office has been delegated responsibility for administration and monitoring of the loan guarantee agreement (LGA). The GPGP Project Office has been formed which consists of the equivalent of ten full-time personnel, including technical, cost/schedule monitors, and financial/economics monitors. Support is also provided by the DOE Grand Forks (ND) Office for process monitoring, Argonne National Laboratory for environmental and economic analysis, and by a technical support contractor (Fluor Engineers, Inc.).

Key objectives of DOE–CH monitoring efforts are to ensure that the plant is built within established cost and schedule and will perform as designed, and that there is continued assurance of repayment of the loan. Elaborate project control systems have been developed to oversee cost, schedule, and technical performance. Extensive reporting is required of GPGA so that the DOE is continuously advised of construction performance and economic viability.

DOE monitoring involves the routine receipt and assessment of a variety of project information combined with a periodic process to ensure the integrity of the data being submitted. Initially, detailed project plans were developed which resulted in cost/schedule/technical baselines against which the project is managed. During the various phases of the project, monthly and quarterly status of the actual progress is taken and compared to those baselines. Analysis and evaluation of events and trends resulting from this input enables the DOE–Chicago Project Office to evaluate performance and initiate any required corrective actions. Construction monitoring was performed utilizing standard construction systems and techniques developed for projects of this size and complexity. The data are used to maintain continued visibility of project status (progress) and thereby assess the benefits and/or alternatives to DOE in the continuation of the LGA.

Environmental Aspects

A major purpose of the loan guarantee program established under the authority of the Non-Nuclear Act is "the opportunity to gather information about the technological, economic, environmental, and social costs, benefits, and impacts of such facilities." The Non-Nuclear Act then places the responsibility on the DOE to collect such data and to evaluate such aspects of this "new" synfuels industry. DOE expects to receive substantial amounts of data useful in the replication of synfuels facilities. To assure that the information is meaningful and based on sound methodology, DOE must provide direction and guidance in the collection and analysis of the data.

It was determined that any studies undertaken to gather this information base should meet certain criteria including the following:

1 They should evaluate *significant* environmental/health issues.

2 They should represent studies/research that will not likely be addressed elsewhere (uniqueness), i.e., a study that can just as easily be performed at a coal-fired power plant probably wouldn't warrant investigation at a coal gasification facility.

3 They should not be redundant.

4 They should maximize the applicability to other coal gasification and/or other synfuels technologies.

Basically then what we expect to gain is a data base of *real* information/data compiled from the construction and operation of an actual commercial-scale synthetic fuels facility that will allow DOE to make important determinations relative to environmental impact and worker health issues.

There are two types of environmental monitoring required of this project's sponsors. First, there is that monitoring which must be undertaken to comply with permits, licenses, and other approvals from state, Federal, and local agencies. In many cases, the monitoring protocol is clearly established by the permitting agency. Because the DOE is a partner of this project, through the loan guarantee process, there is a second monitoring requirement, specifically, the monitoring which goes beyond that required by permit, but which must be performed as required under the authority of the Non-Nuclear

Act. This *supplemental research*, perhaps described as over-and-above or beyond compliance, might be considered the cost of doing business with the Government.

Basically, DOE is seeking answers to very important questions regarding this new industry's impact on worker health and environmental impact in order to keep a clear perspective on the issues and to help in keeping the lid on the possibility of overregulation.

DOE considers the health and environmental issues "high priority" and is making every attempt to address the issues and maintain a realistic perspective, and thereby assist the synthetic fuels industry in making a smooth transition to commercial energy production.

Conclusion

The plant construction has been completed on schedule and on original budget. The turnover has been completed as per the original plan. After the implementation of the capital projects, the GPGP should achieve 70 percent of stream factor, as specified in the loan guarantee agreement. During the startup and initial operation phases, significant technological advancements were achieved and many lessons have been learned.

The Government considers the role of synthetic fuels facilities as being a major contributor, in the not-so-distant future, toward this nation's goal of "energy independence." Coal is an abundant energy resource and coal gasification offers a possibility of converting this "dirty" solid fuel into a clean-burning synthetic natural gas which is easily transported to the user through the existing extensive network of pipelines through this country.

Because coal gasification is a "contained" process, the pollutants/hazards can more easily be contained, controlled, and removed. In addition, the product offers the most flexibility and is very "clean" fuel.

While no projects the size of Great Plains are risk free, there is confidence that the project will demonstrate SNG production from coal in an economically, technically, and environmentally acceptable fashion. It is the first such project to be built in the United States and, therefore, has received great attention and enthusiasm. It will, by all projects to date, acquit itself well as the initiation project in the free world's quest for a reliably available source of energy.

References

1 Great Plains Gasification Associates, *The Great Plains Story: Synthetic Fuel for America*, Bismarck, ND, Oct. 1984.

2 Great Plains Gasification Associates, *Great Plains Coal Gasification Project: Pioneering Alternative Fuels for America*, Bismarck, ND, Oct. 1984.

3 Mujadin, M. J., *GPGA's SNG From Coal Plant – Start-Up and Operation*, presented at the Coal Gasification and Synthetic Fuels for Power Generation Conference, San Francisco, CA, Apr. 14, 1985.

4 Bodnaruk, B. J., *The Great Plains Coal Gasification Project Status*, speech given to the Chicago Section of the American Institute of Chemical Engineers Meeting, Chicago, IL, Oct. 9, 1985.

W. R. Lockwood
Predoctoral Research Associate.

R. C. Corlett
Professor.
Mem. ASME

H. R. Mortazavi
Predoctoral Research Associate.

A. F. Emery
Professor.
Fellow ASME

Department of Mechanical Engineering,
University of Washington,
Seattle, WA 98195

Influence of Coal Properties on Forward Combustion in Laminar Flow

Numerical results are presented for forward combustion in coal channels wherein the flow is laminar. The work is motivated by the need to describe deviations from ideal permeative flow characteristics in theoretical models of underground rubble gasification. For simplicity, the geometry is idealized to a straight circular channel of initially uniform diameter. Coal and inlet gas properties, as well as gas flow rate and initial channel diameter, are arbitrary. A baseline case, in which O_2–steam is injected into a channel in virgin coal, is chosen to match laboratory work reported by other investigators. The results of independent variation of six major parameters are also shown. Finally, representative results are presented for injection of a hot mixture of steam and gasification products into hot char.

Introduction

Underground coal conversion (UCC) denotes a sequence of processes by which oxygen and steam or water are injected into a growing cavity in a coal seam, and react with coal or char then under generally oxygen-deficient conditions to yield a gaseous product containing a large fraction of the chemical energy of the coal. From the standpoint of capital requirements, UCC offers one of the more attractive routes to commercial coal gasification. However, because UCC cannot be directly controlled and, indeed, a UCC coal seam region chosen for reaction will be inherently less well characterized than an aboveground reactor with its prepared fuel, commercial development of UCC is especially dependent on flexible mathematical understanding of the UCC production process. Over the past five years, a number of research groups have been addressing the mathematical modeling problems which must be solved to meet this need. This paper describes a portion of that effort.

It is generally accepted that forward combustion is an essential feature of production gasification phases of UCC. In forward combustion, an oxidant gas flows through a combustible solid fuel in such a manner that the reaction front propagates relative to the solid in the direction of gas flow. This paper presents numerical results for forward combustion along channels in coal wherein the flow of gases is laminar.

How does the work presented here fit into the totality of forward combustion of interest for UCC? Conceptually, UCC operations are regarded as either open channel or permeative flows. Actually, permeative flow in this context is a limiting case of networked channel flow in which the flow network is sufficiently fine that variations of composition across flow channels may be neglected and the length scale of significant temperature variations is much larger than the transverse length scale of the channel network. The permeative limit of forward combustion in coal has been analyzed by Gunn and Whitman [1] and Corlett and Brandenburg [2], and applied specifically to production gasification along porous pathways created, presumably, by reverse combustion linkage in the absence of an initial borehole. Packed bed models for surface gasification, e.g., Stillman [3], also incorporate the permeative limit of forward combustion.

In open-channel forward combustion, the difference between local bulk and wall compositions of the gas is not generally negligible, and significant transverse temperature variations may occur in either gas or solid. Accounting for such factors by inclusion of transverse heat and mass transfer is necessary for meaningful treatment of production gasification along a bored channel which, under conditions anticipated for full-scale UCC operations, would entail highly turbulent flow. Calculations by Dinsmoor et al. [4] and McMurtry et al. [5] are applicable to such cases.

Between the ideal permeative limit and turbulent open channel flow lie two forward combustion cases of UCC interest with laminar open-channel flow. One is laboratory modeling of UCC with an initially bored channel wherein some commonly investigated parameter combinations entail laminar flow, e.g., as reported by Thorsness and Hill [6] and Harloff and Corlett [7]. The other is rubble bed gasification. Most investigators agree with the proposition that any truly commercial-scale UCC operation, regardless of linkage method or seam orientation, eventually results in formation of a rubble bed whose gasification is accomplished by throughflow of steam-bearing gases with a sufficient combination of initial temperature and oxygen to provide energy for gasification.

In many respects, rubble gasification would constitute merely a variant of the packed bed systems proposed for surface gasification. Presently we understand very little of the rubbling process. However, it must be presumed that, for relatively "new" rubble at least, the gas flow channels

Contributed by the Fuels Division for publication in the JOURNAL OF ENGINEERING FOR GAS TURBINES AND POWER. Manuscript received by the Fuels Division July 28, 1984. Paper No. 84-WA/Fu-B.

through the rubble must be too coarse for the permeative limit to be effectively reached. Moreover, a UCC rubble bed would be of irregular geometry which evolves with time as fresh rubble is supplied. Accordingly spatial nonuniformity may play a role in UCC which is much more fundamental than in surface gasifiers, which by design are approximately one dimensional. Calculation of instabilities and other transients in rubble gasification may thus be expected to require characterization of individual channel phenomena as functions of flow rate and local mean channel diameter, the coal type and degree of volatilization of the rubble, and the composition and temperature of the entering gases.

As a step toward obtaining such information, a computer code has been developed to treat forward gasification coal along straight, initially uniform, channels of circular cross section. With the important exceptions of streamwise variations of channel diameter and coal state, the most important rubble gasification variables can be investigated with a modified version of the same code. Results from its use are first compared with the laminar flow phases of data [6] for laboratory runs with a bored channel in Hanna-2 coal. Results exhibiting the effects of independent variation of coal volatiles and water fractions, coal thermal conductivity, thickness of the channel wall ash layer, channel diameter, and gas mass flow rate are then presented.

In rubble bed gasification, it is expected that formation water may be added at points in general not coincident with O_2 injection. Moreover, as the rubble bed evolves the heat addition and steam-carbon gasification steps may not be linked in the manner of gasification in a bored channel. To illustrate this, we conclude our results with an example in which a hot mixture of gasification products and steam is flowed into a hot char channel. The effects of perturbations of gas supply temperature and steam fraction are shown.

Computational Methods

The computer code is a refined version of that described previously by McMurtry et al., who presented preliminary results for turbulent channel flow. In the form used for the results presented in this paper, the code is documented in detail in report form [8].

The operation of the code may be outlined as follows. The gas flow is treated quasi-one-dimensionally with bulk values of velocity, temperature, and species concentrations computed at axial increments. For thermodynamic calculations, pressure is taken as constant. Radial transport of energy and species is accounted for by conventional engineering methods in terms of unit transport coefficients and wall values of temperature and species, e.g., a unit heat convective conductance is used for heat transfer. Transient temperature variation in the solid is computed by a fully implicit finite difference method. For purposes of release of water vapor and volatiles, pressure variations in the solid are ignored; water is assumed fully released when the local solid temperature reaches saturation corresponding to channel pressure; volatiles are assumed released to an extent determined by local temperature alone. Axial transport of water vapor and volatiles within the solid is ignored. Radial transport to the channel surface subsequent to release is assumed instantaneous. Wall conservation conditions, including finite rate chemistry for surface reactions, make the complete set of variables determinate. The kinetic rates thus determined determine wall regression, with channel radius as a function of axial distance computed at regular time intervals. Accumulation of an ash layer introduces an additional heat and mass transfer resistance. This resistance is determined mainly by the ash layer thickness which, in the code, is treated as an input.

Two substantive modifications to the earlier code have been made. First, the heat and mass transfer coefficients as a function of Reynolds number have been extended to the laminar regime. Second, the chemistry has been modified such that local equilibrium among O_2, steam, CO, and CO_2 is established just inside the channel from the wall.

For turbulent flow, development lengths are sufficiently short that engineering transport correlations based on full development appear adequate. For laminar flow, development lengths may be much longer. Moreover, as the channel diameter grows due to material consumption, continuous flow redevelopment effects become important. An entry length enhancement of transport coefficients for full development is computed for the smaller of the actual entry length or a virtual entry length taken as the distance upstream for a critical diameter change; a value of 0.05 was used for this work. It is recognized that more rigorous methods of computing flow redevelopment effects for this problem need to be developed.

In the gas stream, the only chemical reaction considered is oxidation of volatiles, which is considered instantaneous to the extent that O_2 is present. At the surface the following two reactions are considered with kinetic rates [9] as indicated below, with E in kcal/gmole-K and k in cm/s

$$C + 1/2\ O_2 \rightarrow CO \qquad E = 55, \quad k = 2.55 \times 10^{15},$$

$$C + H_2O \rightarrow CO + H_2, \quad E = 70, \quad k = 2.03 \times 10^{13}.$$

In general, the gas stream sufficiently far downstream may contain a fraction of volatiles added to the gas steam downstream of the point of oxygen exhaustion, which, therefore, should contribute to the heating value of the pro-

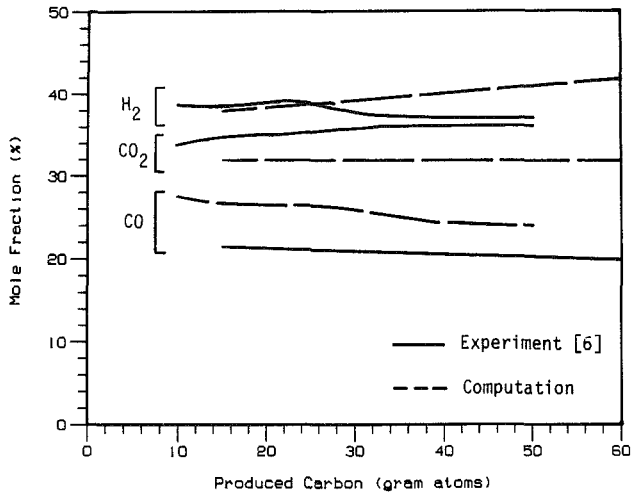

Fig. 1 Baseline product gas concentrations

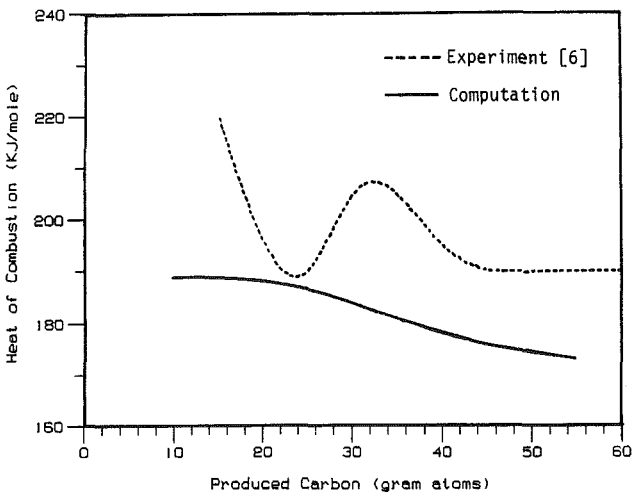

Fig. 2 Baseline dry product gas heat of combustion

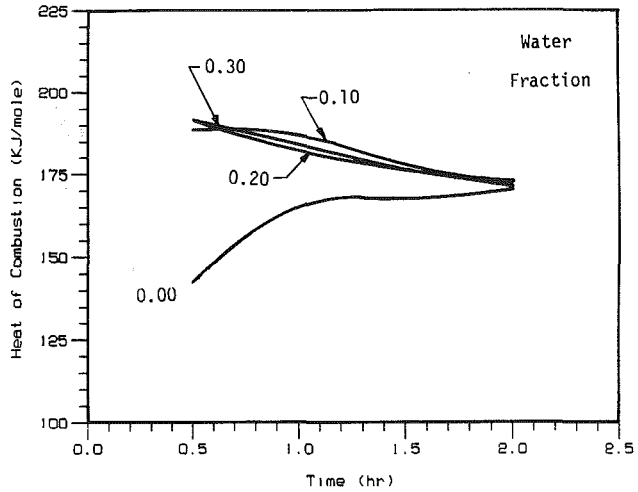

Fig. 3 Effect of initial coal water fraction on heat of combustion

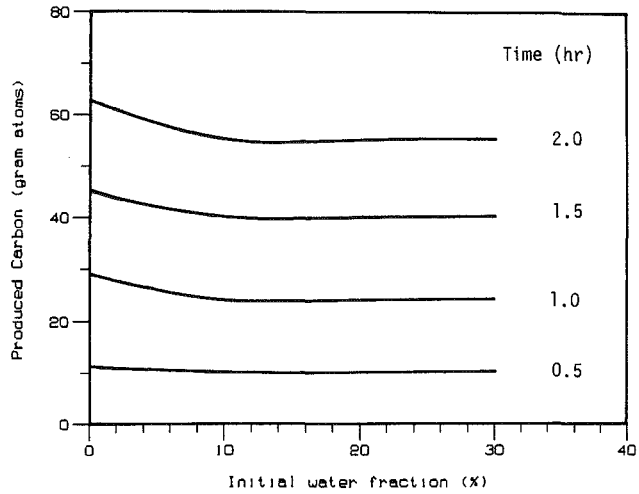

Fig. 4 Effect of initial coal water fraction on carbon production

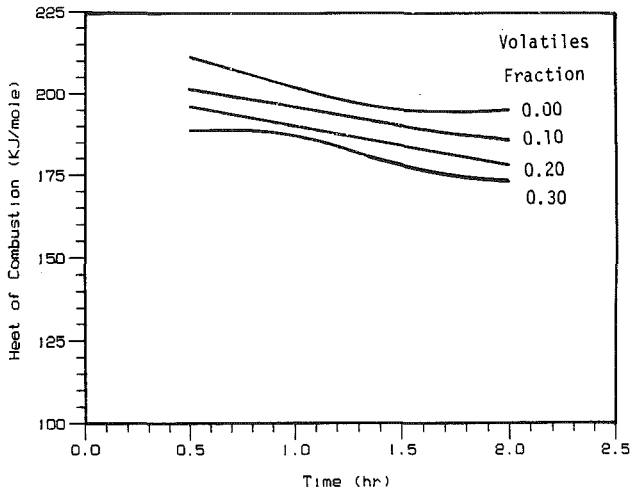

Fig. 5 Effect of initial volatile fraction on product gas heat of combustion

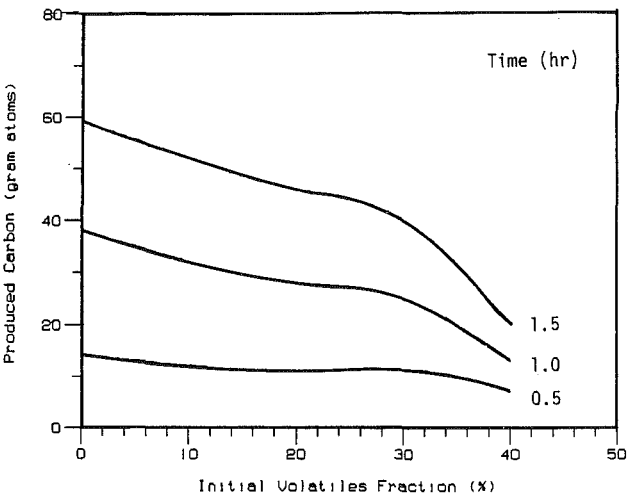

Fig. 6 Effect of initial volatile fraction on carbon production

duced gas. Under the conditions of interest for this paper, oxygen persists throughout most and, usually, all of the length of the gasification channel. Therefore contribution of volatiles to product heat of combustion is ignored.

Baseline Example

We begin by comparing calculated results with the most relevant experimental data available, namely, the early stages of the Hanna-2 portion of a series of 300 kg block experiments [6]. The initial channel diameter and flow rate for this example are sufficiently representative of rubble gasification flow parameters of interest that we also use this case as a baseline for parametric variation runs reported in the next section.

In our computations, we disregard the 15 min ignition period of the comparison experiment, and assume the following conditions. The inlet stream has O_2 mole fraction 0.33 with balance steam. The flow rate is set initially at 0.226 gm/s until 12.0 carbon gram atoms have been produced, then increased linearly to 0.343 gm/s at 15.0 carbon gram atoms, and held constant thereafter. The coal has initial mass fractions of water, volatiles, and ash fraction equal to 0.1, 0.325, and 0.2, respectively. The channel is 60 cm long with initial 1.2 cm diameter. In the comparison experiment, the flow rate was further increased into the turbulent regime after 65 carbon gram atoms. The plotted results are terminated, for convenience, at the approximately 2 hr point (55 carbon gram atoms). For these computations, 1.0 cm axial and radial grid spacings and 10 s time steps were used.

Figures 1 and 2 compare the results of the cited experiments with corresponding computed data. In Fig. 1, both the CO and CO_2 fractions are overpredicted by 2–5 percent. The hydrogen fraction is underpredicted at the end of the experiment by approximately 4 percent. In Fig. 2, the heat of combustion is underpredicted by some 20 KJ/gmole, presumably because chemistry yielding CH_4 is not included in this computational model.

In viewing the above comparison, it must be borne in mind that the experimental irreproducibility is of the same general magnitude as the differences indicated in Figs. 1 and 2. Hence, no modification of the computer code to yield better agreement with experiment would be meaningful without accounting for the sources of irreproducibility.

It is recognized that a more severe test of our numerical model would be a comparison of its results for carbon production and for channel diameter versus axial distance, as functions of time. Unfortunately, usable experimental data are unavailable at this time. Reference [7] does contain some applicable information, but not of a quantity and consistency required for meaningful comparison.

Parameter Variation

Figures 3–14 show the results of independent variation of six parameters: initial water fraction in the coal, initial volatile fraction in the coal, coal thermal conductivity, limiting ash

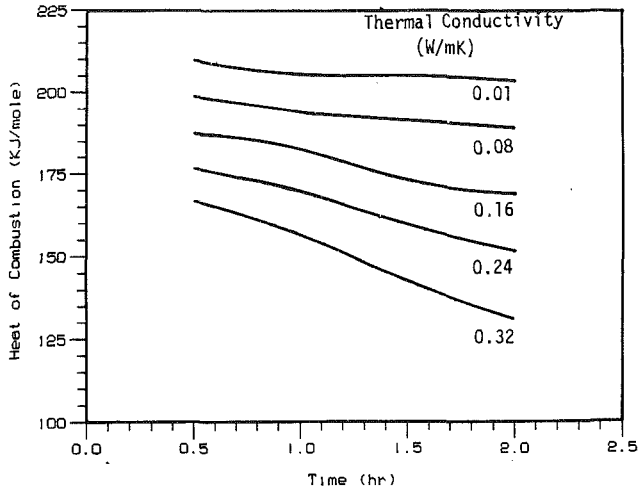

Fig. 7 Effect of thermal conductivity on product gas heat of combustion

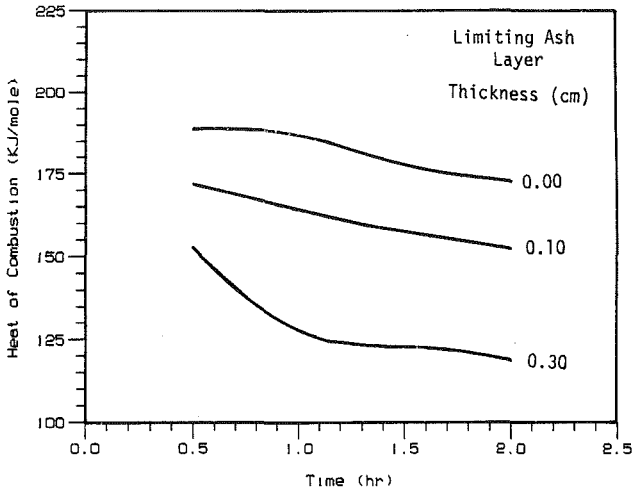

Fig. 9 Effect of ash layer thickness on product gas heat of combustion

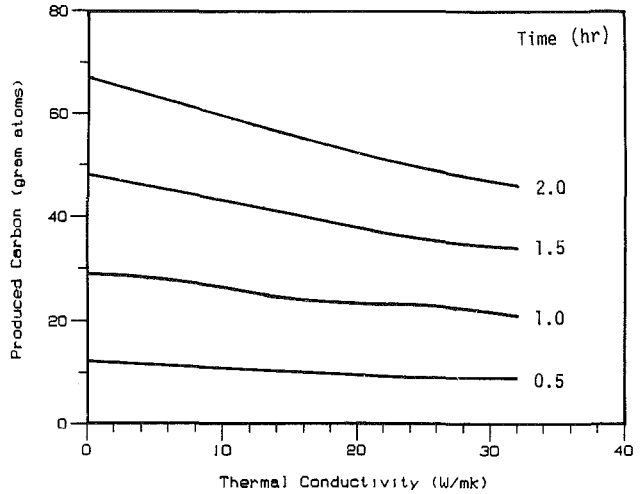

Fig. 8 Effect of thermal conductivity on carbon production

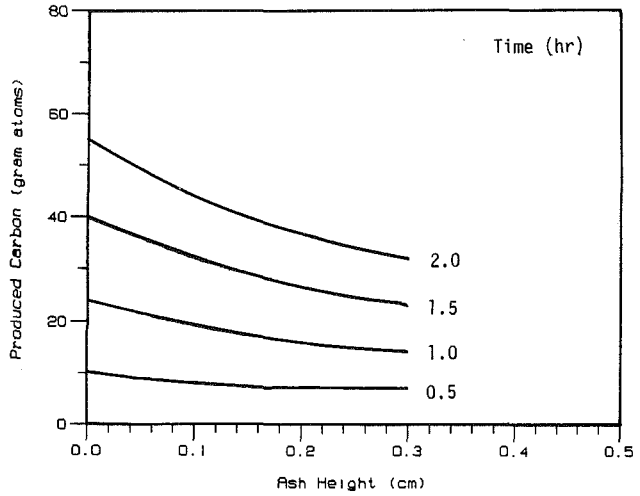

Fig. 10 Effect of ash layer thickness on carbon production

layer thickness, initial channel diameter, and inlet mass flow. Respecting inlet mass flow, only the plateau mass flow (0.343 gm/s in the baseline) is varied; there are no variations of mass flow during the first 12.0 gram atoms of carbon production or of the number of gram atoms carbon produced during the ramp to the plateau flow rate. The figures are presented in pairs showing, first, the effect on produced gas heat of combustion and, second, on the amount of produced carbon; following [6], the term "produced carbon" refers to all of the carbon transferred to the gas stream, including that oxidized to CO_2.

Of course, channel radius must grow with increasing carbon consumption. Of interest is how the axial distribution of such growth varies with coal properties and flow parameters. Figure 15 illustrates variation of the shape of the channel radius versus axial distance, in this instance due to variation of coal thermal conductivity.

Rubble Gasification Example

For the investigation of rubble gasification we select hot char at 800°C. A channel 120 cm long and 0.6 cm in diameter is assumed. The inlet gas is assumed to be a mixture of 20 mole percent steam, balance combustion products at 1300°C. Mass flux into the channel is a constant 0.3 gm/s at 1 atm.

Figures 16 and 17 present the char consumed as a function of downstream distance for the baseline and cases with perturbed inlet gas temperature and inlet gas steam fractions.

Discussion

Figure 3 shows that initial water fraction influences product gas heat of combustion only if the coal is very nearly dry, and to an extent which decreased with time. Figure 4 shows that the influence of initial water fraction on produced carbon is generally modest and restricted to nearly dry coal. These observations are readily interpreted physically. When no water is present in the coal, heat is efficiently conducted away from the reacting channel and thus lost, during the early stages of channel gasification. When water is present, the energy is consumed by the evaporating water and relatively promptly returned to the channel in the form of steam. By approximately the 2 hr point, the dry coal has heated itself thoroughly enough to preclude significant conduction loss. The product gas heat of combustion then is approximately the same for dry coal as wet.

Figures 5 and 6 show that increasing the initial volatile fraction in the coal has the effect of modestly lowering both the heat of combustion and the rate of carbon production. At present, there are no experimental data to test this computed result. The physical basis of the effect, in the present computer model, is that volatiles react in the bulk gas stream with O_2 which otherwise would react with carbon at the channel wall. For the baseline and associated perturbed parameter cases the channel wall temperature is substantially higher than that of the bulk flow. Increased release of volatiles lower this difference and, in particular, lowers the channel wall temperature

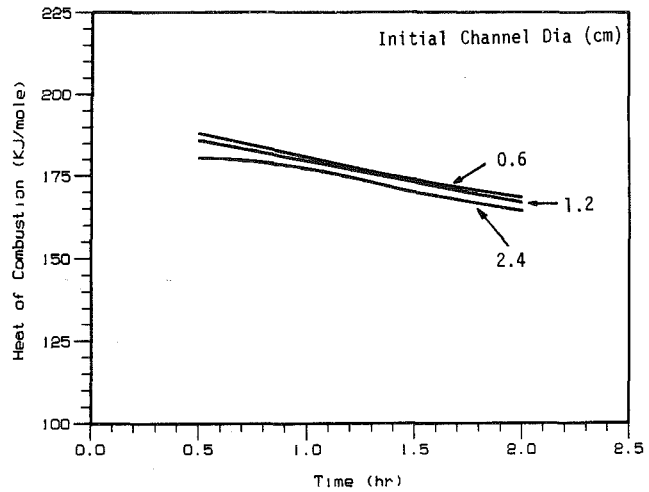

Fig. 11 Efect of initial channel diameter on product gas heat of combustion

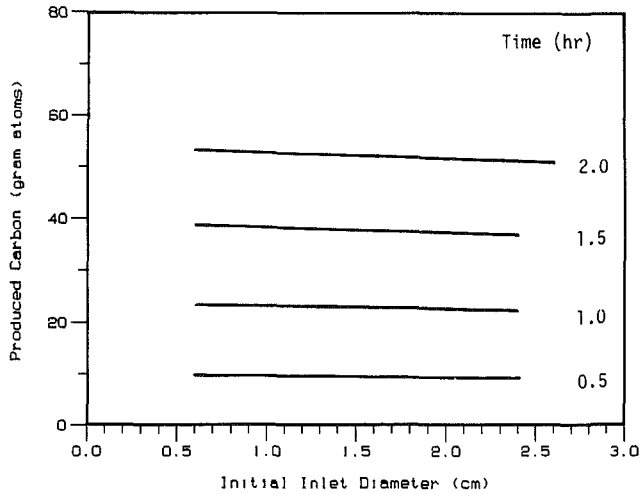

Fig. 12 Effect of initial channel diameter on carbon production

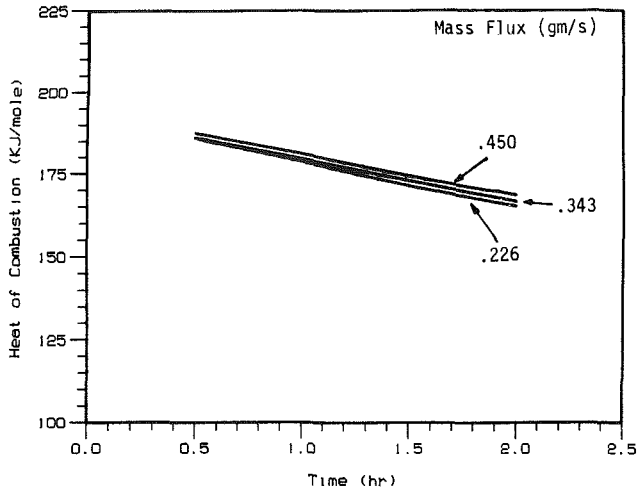

Fig. 13 Effect of mass flow rate on product gas heat of combustion

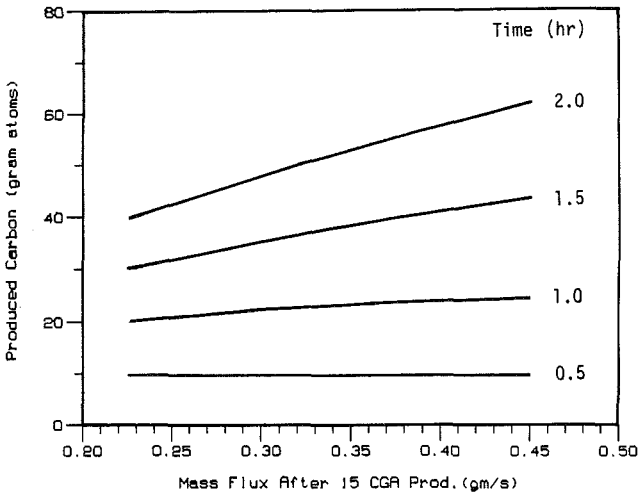

Fig. 14 Effect of mass flow rate on carbon production

thus reducing the extent of gasification there accomplished. Of course, the bulk stream temperature would increase correspondingly but not to the extent needed to support gasification downstream of the region where gasification is directly supported by surface oxidation.

Increasing thermal conductivity increases the heat loss from the reacting surface and consequently slows the rate of carbon production and lowers the heating value of the product gas. As shown in Figs. 7 and 8, this effect is more pronounced as time goes on. The reason for this is that, at relatively small times, the rapid growth of the channel radius tends to overwhelm development of a conduction-heated layer whereas, at larger times, a conduction layer can develop and then exhibit enhanced losses as thermal conductivity is increased.

The addition of an ash layer has the effect of spreading the reaction zone over a larger area by reducing the amount of reacting species which can reach the surface. The surface temperatures of the channel are therefore lower leading to a significant drop in the rate of the gasification reaction. As illustrated in Figs. 9 and 10, the addition of an ash layer even 0.3 cm thick to the surface of the channel can slow the rate of carbon production by 25 percent and reduce the heat of combustion of the product gas by 30 percent. These effects are much less dramatic than in turbulent channel flow conditions. The reason is that ash resistance acts in series with convective resistance to regulate transport of species and energy between the reacting carbon surface and the bulk stream. Since convective resistance may be very much larger in the turbulent

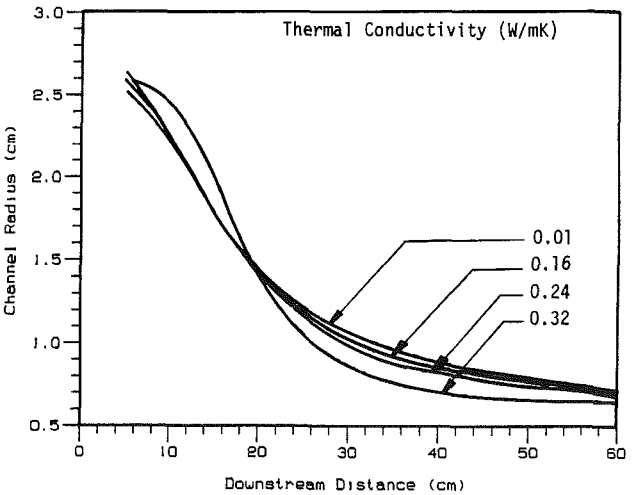

Fig. 15 Effect of thermal conductivity on channel profile (30 carbon gram atoms produced)

regime, a modest ash layer would then exert more complete control of transport rates.

In Figs. 11 and 12, initial channel diameter is shown to almost a negligible effect on either the rate of carbon consumption or on the heating value of the product gas. Similarity considerations for laminar flow dictate that, in the absence

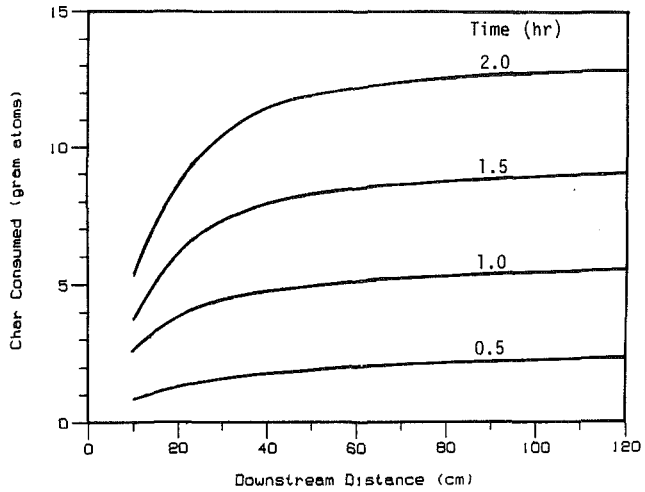

Fig. 16 Char consumption profiles (nominal case)

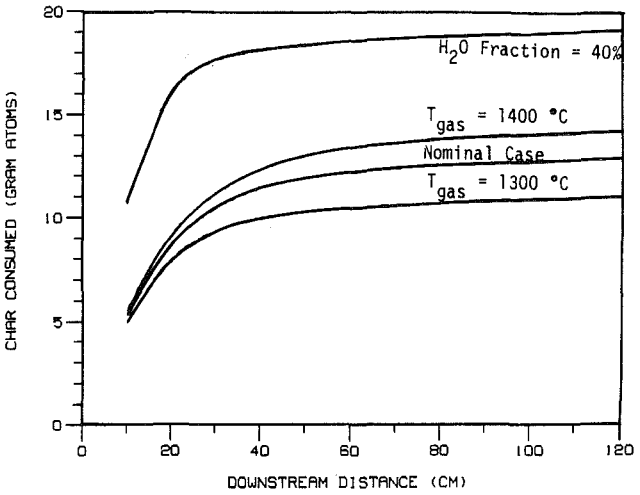

Fig. 17 Char consumption at 2 hr (perturbed cases)

of heat conduction into the coal, there would be no effect at all.

Figure 13 indicates that composition is essentially independent of plateau mass flow. The mass flow ramp begins in each case at approximately 0.5 hr. Figure 14 indicates that, subsequent to that time, produced carbon per unit gas mass flow declines but only slightly.

As an example of channel radius profile variation independent of the amount of produced carbon, Fig. 15 shows the influence of coal thermal conductivity on such profiles. In general, profiles steepen with decreasing conductivity, especially toward the lowest values. The physical reason for this is that energy efficiency near the inlet is enhanced due to reduced conduction losses. As discussed above, analogous energy efficiency enhancement is achieved by increasing the coal water fraction, which also steepens channel radius profiles.

Figure 16 shows a nearly steady rate of char consumption for the temperatures and steam fraction chosen. The corresponding 2 hr char consumption versus axial distance profile in Fig. 17 also shows, as expected, that the system energy level, as exemplified in this example by inlet gas temperature, is an important determinant of gasification rate and that gasification rate is approximately proportional to inlet steam fraction.

Acknowledgments

The work reported in this paper was supported in part by U.S. Department of Energy/University of Washington contract No. DE-AS20-821C10884.

References

1 Gunn, R. D., and Whitman, D. L., "An In-Situ Coal Gasification Model (Forward mode) for Feasibility Studies and Design," LERC/RI-76/2, US ERDA Laramie Energy Research Center, Laramie, WY, Feb. 1976.

2 Corlett, R. C., and Brandenburg, C. F., "Combustion Processes in In-Situ Coal Gasification: Phenomena, Conceptual Models and Research Status. Part 1—Overview and Continuum Wave Descriptions," 1977 Spring Meeting of Western States Section of the Combustion Institute, WSS/CI 77-3, 1977.

3 Stillman, R., "Simulation of a Moving Bed Gasifier for a Western Coal," *IBM J. Res. Develop.*, Vol. 23, No. 2, May 1979, pp. 240-252.

4 Dinsmoor, B., Galland, J. M., and Edgar, T. F., "The Modeling of Cavity Formation During Underground Coal Gasification," *J. Pet. Tech.*, May 1978.

5 McMurtry, P. A., et al., "Comprehensive Numerical Model of Forward Combustion Along a Channel," *Proc. Ninth Underground Coal Conversion Symposium*, Conf. No. 830827, 1983.

6 Thorsness, C. B., and Hill, R. W., "Coal Block Gasification Experiments: Laboratory Results and Field Plans," *Proc. Seventh Underground Coal Conversion Symposium*, Conf. No. 810923, 1981.

7 Harloff, G. J., and Corlett, R. C., "Analysis of Results of Laboratory Simulation of Underground Coal Gasification," *Proc. ASME-JSME Thermal Engineering Joint Conf.*, Vol. 2, Honolulu, HI, 1983.

8 McMurtry, P. A., "CFFC-1: A Computer Code for Forward Combustion in a Coal or Char Channel," US DOE/University of Washington report, Contract No. DE-AS20-82LC10884.

9 Walker, P. L., Rusinko, F. R., Jr., and Austin, L. G., "Gas Reactions of Carbon," *Advances in Catalysis*, Vol. 11, 1959.

Variations of the Lean Blowout Limits of a Homogeneous Methane-Air Stream in the Presence of a Metallic Wire Mesh

G. A. Karim

M. G. Kibrya

The University of Calgary,
Department of Mechanical Engineering,
Calgary, Alberta, Canada

The combustion of a homogeneous lean methane-air stream was investigated in a vertical, cylindrical combustor of 150 mm diameter in the presence of a metallic wire mesh. Eight metallic materials were deposited in turn onto a stainless steel wire mesh by electroplating. The potential improvement in the lean blowout limit due to catalytic effects was established separately from those due to the thermal and aerodynamic contributions of the wire mesh and its holder ring. The effectiveness of the various metallic surfaces tested in the lean combustion of methane was in the following descending order: Pt→Cu→Ag→brass→Cr→Cd→Ni→stainless steel. Moreover, it was confirmed that hydrogen was more sensitive to catalytic effects extending to relatively lower temperatures than methane.

Introduction

The use of a catalytic surface to enhance chemical reaction rates is a well-established and common practice. However, its use in combustion devices for enhancing combustion reactions is somewhat less common and more recent. Catalytic combustors, because of their inherent ability to operate at very lean fuel/air mixtures, can maintain a relatively low combustion temperature and hence reduce the formation of NO_x significantly. While much of the emphasis was based on the use of catalytic combustion for automobiles and gas turbine applications, its potential use in stationary power sources and household appliances [1-4] has recently received increased attention from researchers.

In these combustion applications, no attempt appears to have been made to distinguish the extent of catalytic effects, if any, from other important effects, such as thermal and aerodynamic. In the present study attempts have been made to separate the catalytic effect from other related major effects present in the system. An additional important consideration is the evaluation of the relative suitability of different materials as combustion catalysts. Accordingly, a comparative study of the activity of a selection of different common materials was undertaken, which included platinum, nickel, copper, brass, silver, cadmium, chromium, and stainless steel. The main fuel considered was methane and the effect of adding nitrogen and hydrogen to the main fuel was also considered mainly for comparative purposes. Moreover, the effects of various parameters such as the stream velocity and temperature were considered.

Approach

In order to ensure that the thermal and aerodynamic characteristics of the system remain essentially unchanged when testing one surface material relative to another, single stainless steel (type AISI No. 304) wire meshes (16 × 16 mesh with an open area of 50.7 percent and effective width of opening of 0.0445 in.) were employed throughout within a homogeneous steady flow combustor. The various materials involved in the comparative study were then deposited by electroplating of the mesh to a declared thickness of 0.005 in. (0.127 mm). This approach ensured that the mesh geometry (e.g., wire size, effective flow area, etc.) together with the thermal properties of the mesh and its support remained essentially unchanged for all the surfaces tested. Since it is known that the catalytic activity depends on the concentration of the material at the surface [5], care was taken to ensure that the metallic coating was of uniform thickness over the entire mesh area. An identical wire mesh was coated with a thin layer of silicon by flame deposition [6], and was considered to be effectively noncatalytic, while having similar thermal and aerodynamic characteristics. The results obtained with this noncatalytic mesh were then compared with those involving other materials under identical conditions.

Experimental Setup

A schematic diagram of the experimental setup employed is shown in Fig. 1. It is made up of a vertical, cylindrical combustor with a working section of 150 mm diameter and 290 mm height. A uniform-velocity, homogeneous mixture of fuel and air, which was introduced from the bottom of the combustor, was ignited initially by a pilot jet laminar diffusion flame located centrally at the base of the combustor. A pair of quartz detachable windows was provided within the test section to permit visualizing the flame and igniting the pilot flame initially. A single wire mesh was employed throughout and held horizontally within the combustion zone and normal to

Contributed by the Fuels Division and presented at the ASME Winter Annual Meeting, New Orleans, Louisiana, December 9-13, 1984. Manuscript received by the Fuels Division May 20, 1984. Paper No. 84-WA/Fu-E.

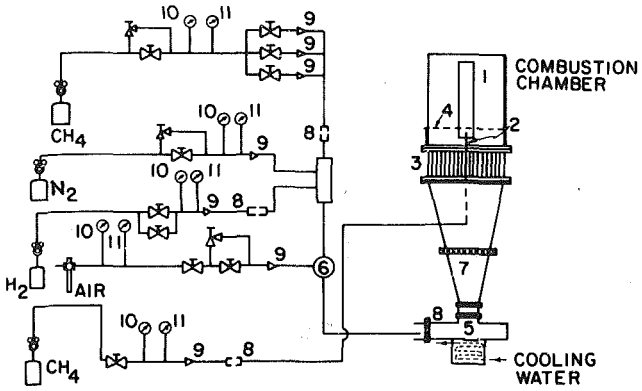

Fig. 1 Schematic diagram of the experimental setup: (1) chamber view window; (2) fuel jet; (3) flow straightener; (4) metallic mesh; (5) bursting diaphragm; (6) mixing section; (7) flow straightening mesh; (8) flame trap; (9) choked nozzle meter; (10) pressure gauge; (11) thermometer

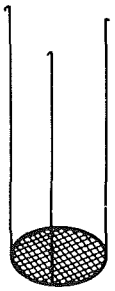

Fig. 2 A schematic representation of the mesh holder (16 mesh stainless steel—AISI No. 304)

the flow. The periphery of the mesh was sandwiched within a pair of narrow, flat, thin circular mild steel rings. The temperature of the mesh holder ring was measured directly with thermocouples welded onto the ring. Three vertical thin wires supporting this ring rested vertically on the edge of the combustor walls permitting different axial location of the mesh within the combustor, as shown schematically in Fig. 2.

The pilot flame was first established and the flow rate of air was set at the desired value. The gaseous fuel, methane, was then introduced into the streaming air gradually, until the concentration of the homogeneous mixture reached a value high enough to form a combustible charge and establish a stable flame on top of the mesh over the entire flow area. The pilot flame was then shut off and the concentration of the surrounding stream was reduced gradually and slowly, as shown schematically in Fig. 3, until the flame just blew off. The concentration of the fuel then was referred to as the "blowout limit."

Results and Discussion

The blowout limit, defined as the minimum fuel concentration to which the streaming homogeneous mixture could be leaned without blowing the flame off the mesh supports, was used as the criterion for a comparative evaluation of the catalytic activity of the coating materials employed. The blowout limit in this case was dependent, obviously, on a number of factors, including the initial temperature of the mixture supplied, as well as that of the mesh and its ring support. Therefore, for a meaningful comparison of the activity of the various materials, the blowout limits were established for the same temperature regimes. It may be suggested that the temperature of the wire mesh would be representative of this catalytic activity. The flame on leaning, however, became detached from the mesh and was attached directly to the circumferential narrow steel rings holding the mesh. Hence, the

Fig. 3 A schematic representation of the successive stages of the flame as the mixtures leaned to blowout conditions

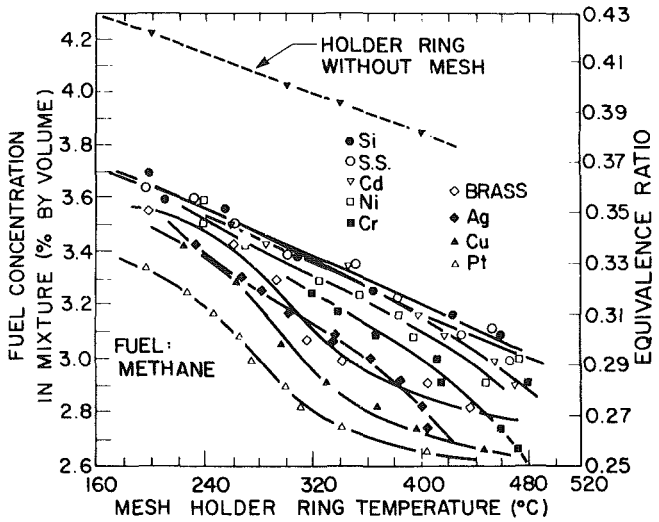

Fig. 4 Comparative study of the catalytic activity of various materials (flow velocity = 0.62 m/s; P_{atm} = 88.32 kPa; T_{atm} = 21.5°C)

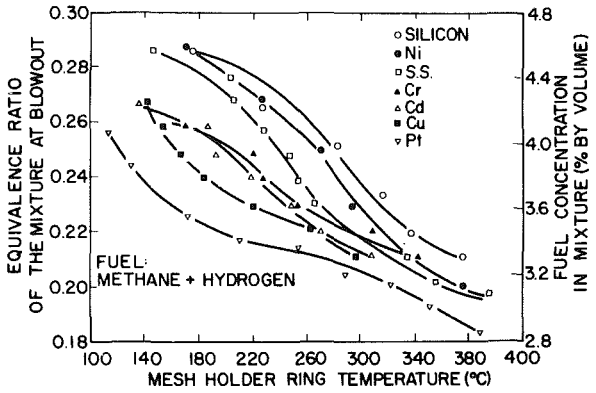

Fig. 5 Comparative study of the catalytic activity of various materials in the combustion of methane + hydrogen (flow velocity = 0.77 m/s; P_{atm} = 88.56 kPa; T_{atm} = 21.6°C)

blowout limits could be determined precisely as a function of the temperature of this mild steel mesh holder ring for the same mixture supply temperature. The ring was heated by the flame first, and then when a certain temperature level was reached the mixture was leaned until flame blowout was encountered. As shown in Fig. 4, for any material employed, the blowout limit varied with the ring temperature, permitting the performance of various materials to be compared under otherwise identical conditions.

It can be seen that the presence of a mesh, whatever its material, improves significantly the flame stabilization over the whole range of ring temperature considered. Expectedly the platinum-coated mesh was the best among the eight materials considered. It can be seen that a concentration of methane as low as 2.7 percent by volume could yield a stable flame when a platinum-coated wire mesh was employed at a ring temperature of about 400°C. Copper was next in this performance rating. On the other hand, the blowout limit was not much affected by the nickel-coated mesh in comparison to that coated with silicon. Thus, the apparent activities of the

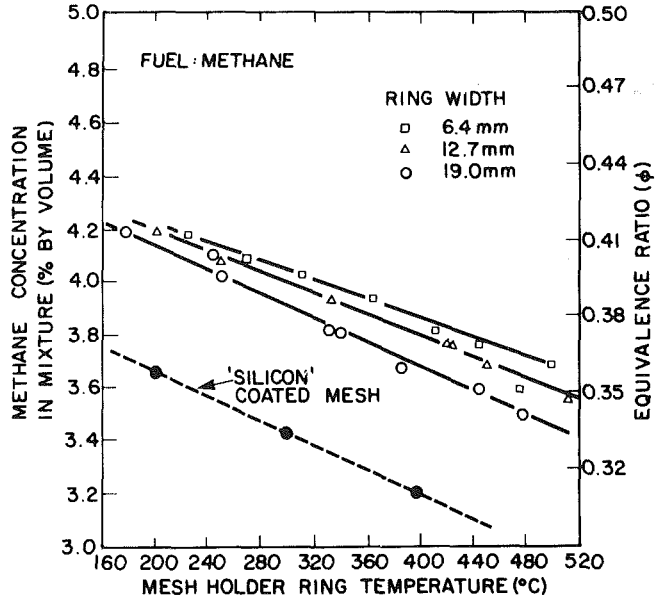

Fig. 6 Effect of the width of mesh holder ring (without a mesh) on the blowout limit; the silicon-coated mesh was 6.4 mm wide

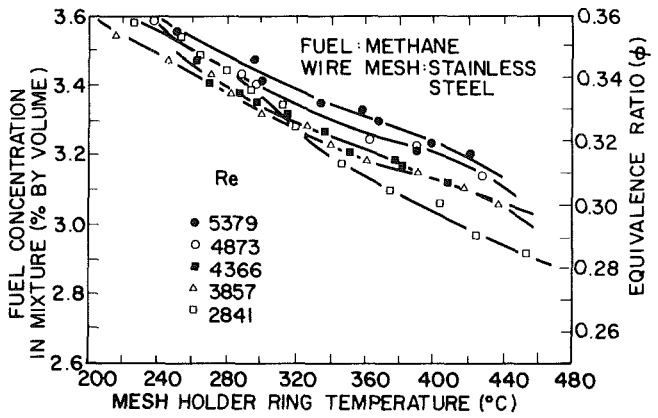

Fig. 7 Effect of Reynolds number in the presence of stainless steel mesh (P_{atm} = 87.90 kPa; T_{atm} = 21.0°C)

various coating materials tested were in the following descending order: platinum→copper→brass→chromium→nickel→cadmium→stainless steel, for the experimental conditions employed.

Figure 5 shows similar results obtained with a fuel mixture of methane and hydrogen in air, with a hydrogen to methane volumetric ratio of 0.3. Again, it was confirmed that the maximum improvement in the blowout limit was with the platinum-coated mesh. The general sequence of these materials in terms of the respective improvement of the lean blowout limit then was the following: Pt→Cu→Cd→Cr→S.S.→Ni. It can be seen that the improvement in the blowout limit, for both cases shown, was somewhat greater over part of the temperature range considered and differed with the catalytic material employed. When some hydrogen was present in the fuel mixture, this temperature zone tended to shift toward lower values, a reflection of the reactivity of hydrogen relative to methane in air, and the sensitivity of hydrogen to catalytic activity at relatively lower temperatures [7].

The presence of the coated mesh enabled the burning of fuel-air mixtures significantly leaner than normal. This improvement, aside from any catalytic effects that may be present, was aided by other factors. For example, when the flame

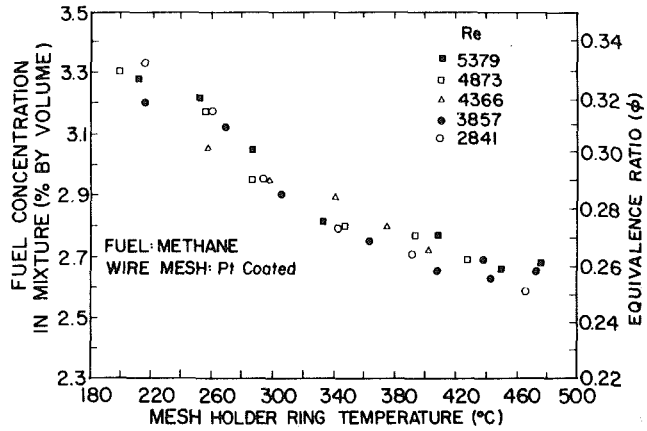

Fig. 8 Effect of Reynolds number in the presence of a catalyst (Pt) (P_{atm} = 87.90 kPa; T_{atm} = 21.0°C)

was stabilized above the mesh, the holder ring temperature became quite high and the recirculation induced by the ring improved the flame stabilization resulting in a leaner blowout limit. The hot wire mesh itself, whether catalytic or not, aided the combustion. The extent of improvement of the blowout limit due to the combined aerodynamic and thermal effects of the holder ring and the mesh itself is shown in Fig. 6, for a range of ring temperatures. Accordingly, the same ring geometry was used throughout whenever different meshes were being compared. It can be seen that although some of this improvement in the flame blowout limit can be attributed to the ring stabilization and the aerodynamic and heating effects as evidenced in the silicon-coated mesh, the contribution of the catalytic activity of the meshes coated with the test materials is evident.

The effect of the bulk flow Reynolds number based on the approach mixture velocity and combustor diameter on the blowout limit is shown in Fig. 7 for a stainless steel mesh. It is evident that an increase in the flow velocity, and hence the Reynolds number, tended to reduce the improvement in the blowout limits. Therefore, despite the increased turbulence with the increase in flow velocity, an element of the mixture passing through the mesh would have had less time for heat transfer and catalytic reactions at the surface. However, as shown in Fig. 8, when a platinum-coated mesh was employed, the variation in the blowout limit, for the range of Reynolds number considered, was generally less significant. It is probable that the greater activity of the platinum surface enhanced the rates of energy and active species released at the mesh surface. An increase in the flow velocity improved both the heat and radical transfer rates from the surface by inducing turbulence which could have compensated in part for the shorter residence time. It is evident that, in applications where the residence time is short, improved performance can be achieved not only by designing the system in such a way that better mixing and heat transfer are provided through induced recirculation and turbulence but also by using a catalytic surface in the combustion zone.

It would be very desirable to be able, with the aid of any catalytic enhancement of the combustion rates, to burn gaseous fuels containing significant concentrations of a diluent such as nitrogen. Accordingly, similar tests were conducted when nitrogen was added to the methane in constant proportions and the flame blowout limits were established similarly as a function of temperature for a range of nitrogen-to-methane ratios, as shown in Fig. 9. The presence of the coated mesh allowed a greater tolerance for the presence of nitrogen before flame blowout was encountered.

Figure 10 shows the blowout limits of methane containing a fixed percentage of hydrogen as a function of the ring

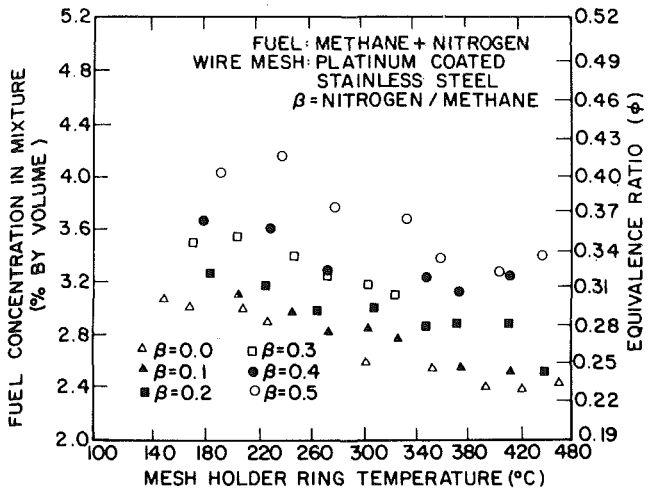

Fig. 9 The blowout limit of mixtures of methane and nitrogen for various nitrogen-to-methane ratios (flow velocity = 0.77 m/s; P_{atm} = 88.2 kPa; T_{atm} = 21.1°C

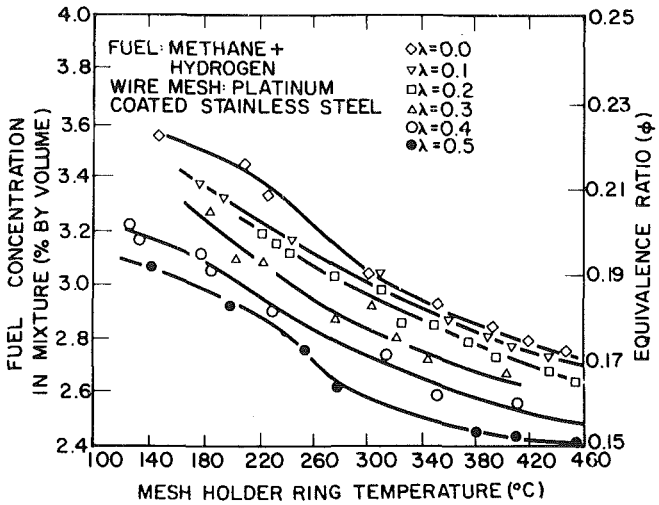

Fig. 10 The blowout limit of mixtures of methane and hydrogen as a function of the holder temperature for various hydrogen-to-methane ratios (flow velocity = 0.77 m/s; P_{atm} = 88.2 kPa; T_{atm} = 21°C)

temperature for various hydrogen-to-methane volumetric ratios. As expected, the blowout limits improved significantly with an increase in the percentage of hydrogen in the fuel, particularly for lower temperatures. The improvement in the blowout limit can be compared very favorably to the declared corresponding flammability limit of the mixture at the ring temperature. It is evident that greater relative improvement in the blowout limit could be obtained by adding increasing amounts of hydrogen to the methane. Moreover, the rate of this relative improvement in the blowout limit tended to increase with a reduction in the temperature, again a reflection of the activity of the platinum-coated mesh with hydrogen at relatively lower temperatures.

The life of the catalyst was not investigated.

Conclusions

Based on the results of the present investigation involving the combustion of steady homogeneous mixtures in the presence of a single mesh located normal to the flow and coated with different materials, the following conclusions can be made:

1 The lean blowout limit of a homogeneous stream of methane–air mixture was improved by the thermal and aerodynamic effects of the wire mesh and its steel holder.

2 A comparative assessment of the catalytic activity of the eight materials tested confirmed that platinum was the most active in the combustion of lean mixtures of methane in air. The effectiveness of the various materials in improving the blowout limits was in the following descending order: Pt→Cu→Ag→brass→Cr→Ni→Cd→S.S. Essentially, the same order of effectiveness was also observed when methane–hydrogen and methane–nitrogen mixtures were burned in air.

3 As expected, the extent of improvement in the blowout limit with various materials varied with the temperature employed. There was a tendency for the activity of the materials tested to shift toward lower temperatures as hydrogen was added to the methane.

4 The blowout limit deteriorated with an increase in the flow velocity. However, the deterioration tended to be of lower significance when a catalytic mesh was employed as the stabilizer in the combustion zone.

5 The introduction of a catalytic mesh into the combustion chamber reduced significantly the deterioration in the blowout limit due to the addition of nitrogen to the methane. Moreover, a significant improvement in the blowout limit was evident when hydrogen was added to the methane in the presence of a catalytic mesh.

Acknowledgments

The financial assistance of the Natural Sciences and Engineering Research Council of Canada (NSERC) and Alberta Energy and Natural Resources (ERRF) is gratefully acknowledged.

References

1 Blazowski, W. S., and Walsh, D. E., "Catalytic Combustion: An Important Consideration for Future Applications," *Comb. Sc. and Technol.*, Vol. 10, 1975, pp. 233–244.

2 Kesselring, J. P., Krill, W. V., Chu, E. K., and Kendall, R. M., "Development of Catalytic Combustion Systems," Symposium paper on New Fuels and Advances in Combustion Technologies, sponsored by IGT, New Orleans, LA, Mar. 26–30, 1979.

3 Johnson, D. G., Jasionowski, W. J., Pangborn, J. B., and Scott, M. I., "Development of Ventless Appliances and Catalytic Ignition System," Symposium paper on New Fuels and Advances in Combustion Technologies, sponsored by IGT, New Orleans, LA, Mar. 26–30, 1979.

4 Krill, W. V., Kesselring, J. P., and Anderson, S. J., "Prototype Catalytic Systems," 4th Workshop on Catalytic Combustion, Cincinnati, OH, May 14–15, 1980.

5 Pfefferle, W. C., "The Catalytic Combustor: An Approach to Thermal Combustion," *J. of Energy*, Vol. 2, 1978, pp. 142–146.

6 Fristrom, R. M., and Westenberg, A. A., *Flame Structure*, McGraw-Hill Series in Advanced Chemistry, 1965.

7 Schefer, R. W., Robben, F., and Cheng, R. K., "Catalyzed Combustion of Hydrogen/Air Mixture in a Flat Plate Boundary Layer: Experimental Results," *Combustion and Flame*, 1980, pp. 51–63.

S. B. Greene

S. L. Chen

D. W. Pershing

M. P. Heap

W. R. Seeker

Energy and Environmental Research Corporation,
Irvine, CA 92714

Bench Scale Process Evaluation of Reburning for In-Furnace NO_x Reduction

Reburning involves the injection of a secondary fuel above the main firing zone of pulverized coal-fired utility boilers to produce a reducing zone which acts to reduce NO_x to molecular nitrogen. Overfire air is added above the reburn reducing zone to complete the combustion. Bench scale evaluations of the process carried out in a plug flow furnace at 23 KW have indicated that NO_x reductions of up to 70 percent can be achieved depending on a number of process variables. The dominant variables include the initial NO_x level that is to be reduced, the reburning fuel type (pulverized coal type or natural gas), and the residence time and temperature in the reducing zone. The reburning process has been combined with the injection of calcium-based sorbents (limestone) to investigate the potential for combined NO_x and SO_x reduction.

Introduction

This paper addresses the reburning technology which removes NO from combustion products using fuel as the reducing agent. It has been found to involve kinetic processes similar to those involved in combustion modification by staged combustion. This technology is variously referred to as:

- In-furnace NO_x reduction
- Reburning
- Staged fuel injection

Reburning can be considered as the process which allows in-furnace NO_x reduction to take place.

The concept of NO reduction by flames has been known for over a decade. A flue gas NO_x incinerator was developed by the John Zinc Company [1] and Wendt, Sternling, and Matovich [2] found that NO could be reduced in laboratory flat flames by injecting methane to the combustion products. Recently, Japanese investigators have reported the application of reburning to large test furnaces [3]. The MACT (Mitsubishi Advanced Combustion Technology) in-furnace NO_x removal process applies the concept of reburning to a boiler. Part of the fuel bypasses the main heat release zone and is injected above the main burners to provide the fuel for reburning. It is claimed that the NO_x produced by the main firing system can be reduced "to half at any level of concentration" [3]. Hitachi Shipbuilding and Engineering has a U.S. patent on multistage fuel injection for NO_x control [4]. EER under contract to the U.S. Environmental Protection Agency has been investigating the reburning process as it might be applied to U.S. designed pulverized coal utility boilers for the last few years. The initial activity has involved lab scale and bench scale testing of the impact of process variables on the NO_x removal efficiency. The studies have been performed in tower furnaces that allow control of the time, temperature, and compositional history over the range of interest in utility boiler furnaces. The reburning process can be divided into three zones as shown in Fig. 1:

- *Primary zone*: This main heat release zone accounts for approximately 80 percent of the total heat input to the system. The zone is operated under overall fuel lean conditions, although the burners might be low NO_x distributed mixing burners. The level of NO_x exiting from this zone is the level to be reduced in the reburning process.
- *Reburning zone*: The reburning fuel (normally about 20 percent of the total fuel requirement) is injected downstream of the primary zone to create a fuel-rich reduction zone. The

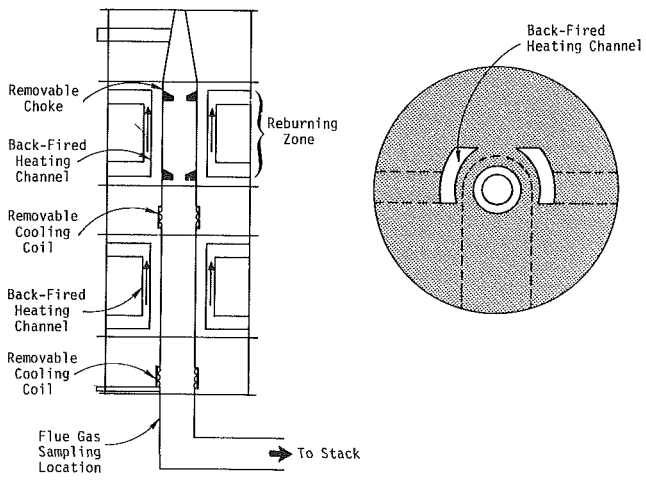

Fig. 1 Cross-sectional views of the control temperature tower

Contributed by the Air Pollution Control Division and presented at the Joint Power Generation Conference, Toronto, Ontario, Canada, September 30-October 4, 1984. Manuscript received by the Air Pollution Control Division October 11, 1984. Paper No. 84-JPGC-APC-9.

Table 1 Continuous gas analysis instruments

Gas measured	Detection principle	Manufacturer	Model No.	Range
NO, NO_2	Chemiluminescent	Thermo Electron Corp. (TECO)	10 AR	0–1000 ppm
CO	Nondispersive infrared (NDIR)	Anarad, Inc.	AR500R	0–500 ppm
CO_2	Nondispersive infrared (NDIR)	Anarad, Inc.	AR500R	0–25 percent
O_2	Paramagnetic	Taylor Servomex	QA-272	0–10 percent
SO_2	Nondispersive ultraviolet (NDUV)	DuPont	400	0–5000 ppm
H_xC_y	Flame ionization (heated)	Beckman Instruments, Inc.	402	500 ppm (C_3H_8)

reactive nitrogen entering this zone comes from two sources: the primary NO level and the fuel nitrogen in the reburning fuel. These fuel nitrogen species apparently react with the hydrocarbon fragments from the reburning fuel to produce intermediate species such as NH_3 and HCN while some is converted to N_2 and some is retained as NO. The products of this reduction zone are the reactive nitrogen species such as: NO, char nitrogen, NH_3, and HCN, which will be referred to as total fixed nitrogen (TFN). In order to optimize the NO reduction by reburning, it is necessary to minimize the total reactive nitrogen exiting the reburning zone.

- *Burnout zone*: In the burnout zone, air is added to produce overall lean conditions which oxidizes all the remaining fuel and converts the total fixed nitrogen either to NO or N_2.

The processes that take place in each of these zones have recently been evaluated in terms of the reduction of total reactive nitrogen [5]. This paper will attempt to summarize the major findings of that study. Based on these results, a process model is currently under development which will allow an assessment to be made of the effectiveness of applying reburning technology for different fuel types and applications.

Experimental

The process studies were carried out in the refractory lined Control Temperature Tower (CTT) which is shown schematically in Fig. 1. The CTT has a total firing rate of between 18 and 24 kW (60,000–80,000 Btu/h) in the main combustion chamber. The main combustion chamber is 20.3 cm in diameter and includes a long quarl entry to promote flame stabilization and to provide for one-dimensional plug flow. The time-temperature profile along the furnace could be manipulated by using back-fired heating sections located within the insulating refractory. The back-fired sections consisted of natural gas burners fired into refractory channels in the direction opposite to the main chamber. The high-temperature gases pass through the channels surrounding the main chamber (see the radial cross-sectional view in Fig. 1) and minimize the temperature decay along the furnace. A more rapid temperature decline can be achieved by leaving the back-fired channels off or by inserting cooling coils around the main chambers. The tower is equipped with numerous ports located along the axis of the reactor that allow the installation of zone separation chokes, fuel and air injectors, cooling coils, and sampling probes.

The CTT was configured into three zones: (1) The primary zone was formed using a premixed burner fired on pulverized coal or propane doped with various levels of H_2S and NO, under lean conditions (typically 10 percent excess air); (2) the reburning zone formed by injecting the reburning fuel (either coal or doped gas) at various flow rates to control the reburning zone stoichiometry; and (3) the burnout zone in which air was injected to bring the overall stoichiometry to typically 25 percent excess air. The parameters in each of these zones were examined separately in terms of how they influenced the exhaust level of NO_x. The test series were performed by establishing the level of NO_x from the primary and then to increase the amount of reburning fuel addition and burnout air correspondingly to decrease the reburning zone stoichiometry and maintain the overall burnout zone stoichiometry. In this manner, the residence time and temperature in the reburning zone were maintained relatively constant while the reburning zone stoichiometry was varied.

Both flue gas and in combustor measurements were made of NO_x, O_2, CO/CO_2, SO_2, HCN, and NH_3 by techniques presented in Table 1. In addition, the gas temperature was measured throughout the reactor by using a suction pyrometer (Type B thermocouple). Details of sampling and analysis procedures and test conditions are available elsewhere [5].

The bench scale testing has provided fundamental insight into the chemical processes that control NO_x reduction and the impact of the key process variables. The full range of parameters in each zone was investigated:

- Primary zone
  - -stoichiometry
  - -fuel type
  - -NO level
  - -SO_x level
- Reburning zone
  - -stoichiometry
  - -mixing rate of reburning fuel
  - -reburning fuel type (propane, hydrogen, CO, and coals)
  - -nitrogen content of reburning fuel
  - -temperature
  - -residence time
  - -transport media for reburning fuel (air or inert)
- Burnout zone
  - -temperature
  - -excess air
  - -air mixing rate

Nomenclature

SR_1 = stoichiometry of primary zone
$(NO_x)_p$ = NO_x measured at exit of primary zone, ppm (dry, 0 percent O_2)
SR_2 = stoichiometry of reburning zone
T_2 = inlet temperature of reburning zone, K
τ_2 = residence time of reburning zone, ms
SR_3 = stoichiometry of burnout zone
T_3 = inlet temperature of burnout zone, K
$(NO_x)_{EX}$ = NO_x measured in the exhaust, ppm (dry, 0 percent O_2)
NH_i = NH, NH_2, or NH_3

Results

Although most of the parameters investigated had some effect on the reduction level achieved by the reburning process, the dominant parameters were found to be those associated with the reburning zone condition and the primary zone NO level. In Fig. 2 is shown the effect of three parameters: reburning fuel type (propane or Utah bituminous coal), primary zone NO_x level, and reburning zone stoichiometry. These data were taken at the baseline conditions as shown in Table 2 and are expected to be typical of the times and temperatures that would exist for applications to p.c. fired boilers. The optimum NO_x reduction occurs when the reburning zone was fuel rich at an overall stoichiometry of 0.9. For high levels of primary NO_x, 630 ppm, the exhaust level of NO was reduced to 200 and 250 ppm for propane and coal as reburning fuels, respectively. For low levels of primary NO the reduction levels were not as significant, dropping from 190 ppm to 100 ppm for propane reburning and only to 180 ppm for coal. The effectiveness of propane over pulverized coal as a reburning fuel can be attributed to the fuel nitrogen difference. As propane was doped with ammonia to the same nitrogen content as the coal, similar NO_x levels were produced.

A wide variety of reburning fuels was investigated including hydrocarbon and nonhydrocarbon gaseous fuels and coals of varying rank and nitrogen content. The properties of these fuels are supplied in Table 3. A comparison of the effectiveness of different reburning fuels can be drawn from Fig. 3, and indicates that most fuels are similar. The nonhydrocarbon fuels are generally less effective than those

Table 2 Baseline operating conditions

Primary zone
- Propane fired at 17.6 kW (60×10^3 Btu/h)
- $SR_1 = 1.10$
- $(NO_x)_p = 190$ ppm (dry, 0 percent O_2)

Reburning zone
- $\tau_2 = 400$ ms
  $T_2 = 1700$ K (inlet temperature); lower auxiliary burners off

Burnout zone
- $SR_3 = 1.25$
- $T_3 \approx 1505$ K (inlet temperature); lower auxiliary burners off

Refractory chokes were placed at the reburning fuel and burnout air injection locations (see Fig. 1). The chokes separated the zones by preventing any back-mixing between the zones. The primary fuel (propane) was doped with NO to the desired concentrations.

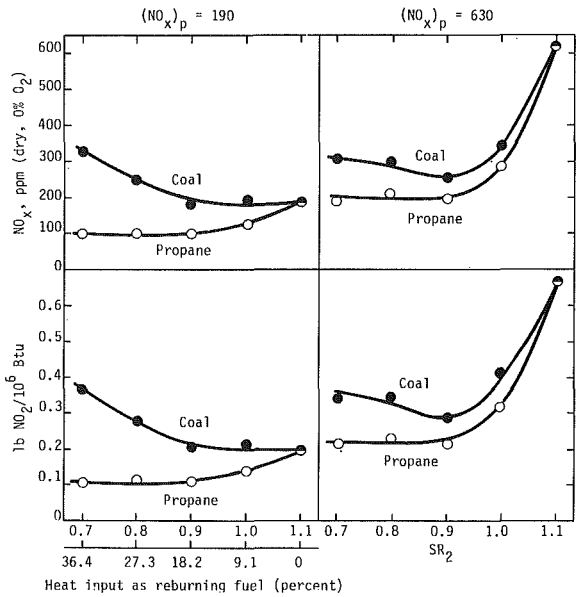

Fig. 2 Influence of process parameters on reburning effectiveness

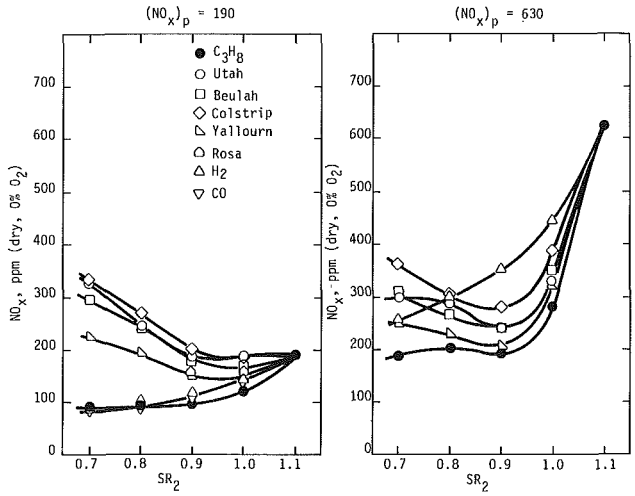

Fig. 3 Comparison of different fuels

Table 3 Fuel analysis

Property \ Fuel	Yallourn, Australia	Beulah, ND	Colstrip, MT	Indiana	Pennsylvania	Rosa AL	Utah
Rank	Brown	Lig A	Sub B	HVB	Anthracite	MV	HVB
Proximate analysis (percent, as received)							
Moisture	13.97	33.10	21.27	4 54	5.13	8.02	6.39
Ash	1.26	7.12	9.58	8.96	5.74	6.79	7.40
Volatile matter	45.20	28.65	30.82	37.73	4.39	21.81	38.89
Fixed carbon	39.57	31.13	38.33	48.77	84.74	63.38	47.32
Calorific value (Btu/h)	9,424	7,245	9,169	12,213	13,124	13,394	12,340
Sulfur	0.20	0.76	0.50	1.87	0.44	0.96	0.64
Ultimate analysis (percent, dry)							
C	66.03	65.29	67.52	71.17	88.45	81.23	73.17
H	4.55	3.96	4.36	4.75	2.14	4.73	5.55
N	0.55	0.99	1.38	1.44	0.79	1.74	1.54
S	0.23	1.14	0.63	1.96	0.47	1.04	0.66
Ash	1.46	10.64	12.17	9.39	6.05	7.38	7.90
O	27.18	17.98	13.94	11.29	2.10	3.88	11.18

Table 4 Influence of process variables on reburning effectiveness

Parameter	Impact
Primary zone	
Stoichiometry	• No effect except will reqiure more reburning fuel for burner operation
Fuel type	• No direct effect; can influence through temperature and NO_x level entering reburning zone
NO level	• Strong effect; more difficult to reduce lower levels of primary NO_x
Reburning zone	
Stoichiometry	• Optimum at overall stoichiometry of 0.9
Mixing rate of reburning fuel	• Faster mixing preferred
Fuel type	• Hydrocarbon fuels more effective; fuel nitrogen content detrimental at lower primary NO level
Temperature	• Reduction increases with increasing temperature (1590–1890 K)
Residence time	• Strong impact, increasing with time (100–750 ms)
Transport media	• Inert transport (oxygen free) desirable since less reburning fuel is required to attain optimum stoichiometry
Burnout zone	
Excess air	• Not important except for burnout
Air mixing rate	• Not important
Temperature	• Not important unless temperature is dropped to 1200 K where selective NH_i–NO reactions can take place to enhance reduction

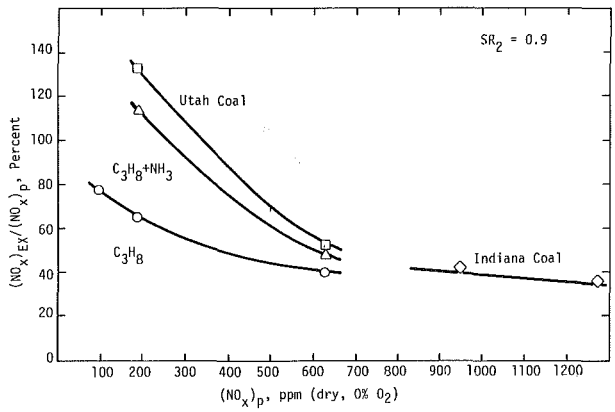

Fig. 4 Impact of primary NO_x on effectiveness of reburning

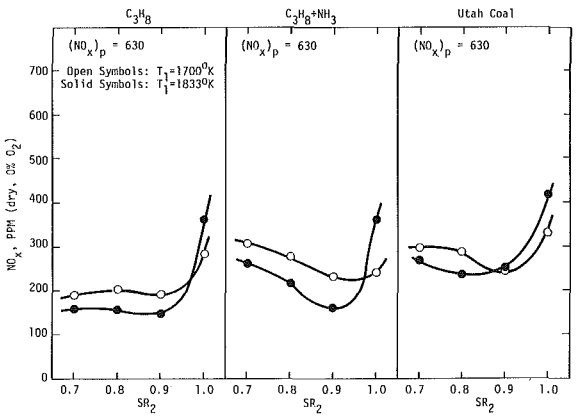

Fig. 6 Influence of reburning zone temperature

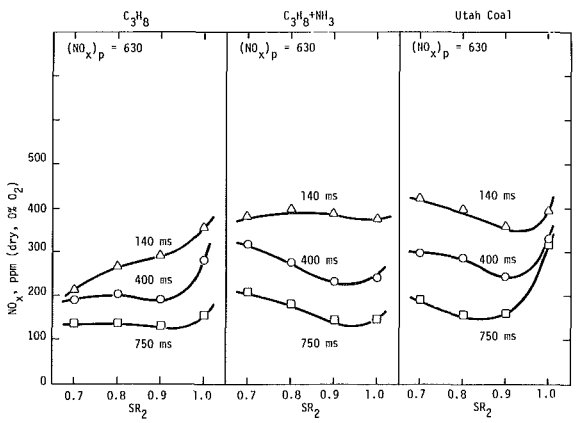

Fig. 5 Influence of residence time

containing hydrocarbons (particularly at longer reburning zone residence times). The Yallourn brown coal was the most effective reburning coal chiefly due to its low fuel nitrogen content and high volatility and there was a general decrease in effectiveness with fuel nitrogen. Some problems were encountered under these conditions to complete the burnout of lower volatile coals such as anthracite and the low volatility Rosa coal; however, similar reduction levels were achieved under conditions where burnout was achieved.

The predominant effect of fuel type was found to be the nitrogen content of the reburning fuel. The detrimental effect of the nitrogen becomes more apparent at lower levels of primary NO. As shown in Fig. 4 at high primary NO levels, the level of reduction achievable by all reburning fuels tested was similar at the optimum stoichiometry and was in the range of 70 percent reduction. It is more difficult to achieve the same reduction at lower levels of NO_x for any fuel type; however, fuels containing fuel nitrogen exacerbate the limitation. Below an initial level of 200 ppm of NO, gaseous fuels containing no fuel nitrogen are required to achieve an overall reduction by reburning.

These studies have indicated that NO_x reduction by reburning is a kinetically controlled process with features similar to the staged combustion processes that have been extensively investigated. In the rich reburning zone the temperature, reaction time, and reactant concentration all influence the ultimate reduction of NO that can be achieved. the data presented above were at the baseline reburning conditions of T_i (at the entrance of the reburning zone) of 2600°F and a total reburning zone residence time of 400 ms. The effectiveness of the process is increased at longer residence times as shown in Fig. 5 in the range of 140 to 750 ms in the rich zones for all hydrocarbon fuels; nonhydrocarbon fuels (H_2 and CO) had no residence time effects. Detailed species analysis within the reburning zone has indicated that the mechanisms suggested by Glass and Wendt [6] for the rich postflame decay of nitrogenous species are consistent with these results. Although the effectiveness of all coals tested increased with residence time, the magnitude of changes was coal dependent. The bituminous coals demonstrated the largest effect of time similar to gaseous hydrocarbon while the lower-ranked lignite and brown coals were less influenced by residence time.

The influence of the reburning zone temperature was also dependent on the reburning fuel type (Fig. 6). As the entrance temperature to the reburning zone was increased from 1700 K to 1833 K (2600°F to 2840°F) the exhaust NO_x levels decreased for all reburning fuels. The largest effect occurred for gaseous fuels while the impact with pulverized coal was less dramatic. These data suggest placing the reburning jets as

close to the main burner zone as is feasible to increase the temperature and having as large a reburning zone by separating the air injectors away from the reburning fuel jets.

Summary and Conclusions

The process chemistry of the reburning technology has been investigated in some detail and found to be similar to staged combustion processes. The influence of individual parameters for each zone of the process has been determined. Table 4 presents a summary of the effects of these parameters on the effectiveness of reburning. It is concluded that in order to minimize NO_x emissions the reburning zone should be as large and as hot as possible and that the optimum stoichiometry for the reburning zone is 0.9. These studies have also shown that it is more difficult to reduce NO_x by reburning with fuels which contain nitrogen if the NO_x from the main burner zone is low (less than 200 ppm). However, reburning with a nitrogen-free fuel, such as propane, has proved to be effective at low NO_x levels.

These studies have concentrated on the chemistry of the reburning process under ideal conditions, i.e., rapid mixing and distinct zones. Activity is now underway to investigate the impact of scale and finite rate mixing. These tests are being carried out at firing rate of 3 MW (10 MM Btu/h).

Acknowledgments

The authors wish to express their appreciation to the U.S. Environmental Protection Agency which supported this work under Contract 68-02-3925. In particular, the project officers, R. E. Hall and D. B. Henschel, along with the Reburning Program advisory panel, contributed significantly to the program direction. We would also like to thank our colleague Brian Jacobs for his technical assistance.

References

1 Reed, R. D., "Process for the Disposal of Nitrogen Oxide," John Zinc Company, U. S. Patent No. 1274637, 1969.

2 Wendt, J. O. L., Sternling, C. V., and Matovich, M. A., *Fourteenth Symposium (International) on Combustion*, The Combustion Institute, 1973, p. 897.

3 Takahashi, Y., et al., "Development of Mitsubishi 'MACT'J In-Furnace NO_x Removal Process," presented at U. S.-Japan NO_x Information Exchange, Tokyo, Japan, May 25-30, 1981.

4 Okigami, N., et al., "Multistage Combustion Method for Inhibiting Formation of Nitrogen Oxides," U. S. Patent No. 4,395,223, 1983.

5 Greene, S. B., Chen, S. L., Clark, W. D., Heap, M. P., Pershing, D. W., and Seeker, W. R., "Bench Scale Process Evaluation of In-Furnace NO_x/SO_x Reduction," EPA-600/7-85-012, Mar. 1984.

6 Glass, J. W., and Wendt, J. O. L., "Mechanisms Governing the Destruction of Nitrogenous Species During the Fuel Rich Combustion of Pulverized Coal," *Nineteenth Symposium (International) on Combustion*, The Combustion Institute, 1982, p. 1243.

Combustion Gas Properties: Part II—Prediction of Partial Pressures of CO_2 and H_2O in Combustion Gases of Aviation and Diesel Fuels

Ö. L. Gülder
National Research Council of Canada,
Division of Mechanical Engineering,
Ottawa, Ontario K1A OR6, Canada

Empirical formulae are presented by means of which the partial pressures of CO_2 and H_2O in the combustion gases of aviation fuel–air and diesel fuel–air systems can be calculated as functions of pressure, temperature, equivalence ratio, and hydrogen-to-carbon atomic ratio of the fuel. The formulae have been developed by fitting the data from a detailed chemical equilibrium code to a functional expression. Comparisons of the results from the proposed formulae with the results obtained from a chemical equilibrium code have shown that the mean absolute error in predicted partial pressures is around 0.8 percent. These formulae provide a very fast and easy means of predicting partial pressures of CO_2 and H_2O as compared to equilibrium calculations, and they are also applicable to gasolines, residual fuels, and pure alkanes and aromatics as well as aviation and diesel fuels.

Introduction

In gas turbine combustion chambers, a large proportion of the total heat flux to the liner wall is by radiation from the flame. In diesel engines, heat transfer by radiation can account for as high as 30–40 percent of the total heat flux to the combustion chamber surfaces. An important part of the total radiation heat flux occurs due to nonluminous radiation, its relative amount being dependent on the pressure, temperature, equivalence ratio, and fuel characteristics.

The main factors that govern the nonluminous radiation of combustion gases are beam length, pressure, temperature, and composition [1]. Gases radiate over discrete wavelengths called banded spectra. In nonluminous flames the banded spectra from CO_2 and H_2O are the dominant ones below 3000 K. The contribution from other gas constituents can be neglected in evaluating radiative heat flux. In order to evaluate nonluminous radiative flux, partial pressures (or mole fractions) of CO_2 and H_2O should be known.

The composition of the combustion gases is a function of fuel type (characterized by enthalpy of formation or hydrogen-to-carbon ratio), fuel-air equivalence ratio ϕ, temperatures of the fuel T_f and air T_a, and pressure P. The partial pressures of CO_2 and H_2O can be calculated by assuming chemical equilibrium of the species. Then for a given fuel, temperature, and pressure, the mass action equations can be solved directly for species concentrations, from which other thermodynamic properties can be derived. An alternative approach is to calculate the species concentrations which minimize the Gibbs free energy of the system. Unfortunately, either approach involves long iteration procedures resulting in time-consuming and expensive calculations.

Approximate but much simpler methods of estimating the partial pressures of CO_2 and H_2O can provide appreciable advantages in routine calculations and simulation studies. Ranges of application of available approximate expressions are very limited. The empirical formula proposed by Lefebvre and Herbert [2] is valid only for a fuel with H/C atomic ratio of 2, and a mixture with an equivalence ratio leaner than $\phi = 0.8$. More general formulae by Kunitomo and Kodama [3] include the effect of fuel type in terms of liquid fuel density, which is not sufficient to account for the change in the fuel's H/C ratio, but neglect the effects of pressure and temperature on the partial pressures of CO_2 and H_2O.

In this paper, simple formulae which predict the partial pressures of CO_2 and H_2O as a function of atomic hydrogen-to-carbon ratio of the fuel, equivalence ratio, reactant temperature and pressure, will be presented and their accuracies will be evaluated. The equations have been developed by curve fitting of data obtained from a detailed chemical equilibrium code. The proposed equations are applicable in the following ranges: $0.3 \leq \phi \leq 1.6$, 0.1 MPa $\leq P \leq$ 7.5 MPa, 275 K $\leq T_u \leq$ 950 K, and $0.8 \leq$ H/C ≤ 2.5. These ranges cover the conditions of interest in gas turbines and diesel engines, and the properties of conventional and future liquid aviation and diesel fuels. This work constitutes the second part of the previously reported approximate expression developed to predict adiabatic flame temperature of aviation and diesel fuels [4].

Background

For typical kerosene fuels of the form C_nH_{2n}, the partial

Contributed by the Gas Turbine Division of THE AMERICAN SOCIETY OF MECHANICAL ENGINEERS and presented at the 31st International Gas Turbine Conference and Exhibit, Düsseldorf, Federal Republic of Germany, June 8–12, 1986. Manuscript received at ASME Headquarters February 7, 1986. Paper No. 86-GT-163.

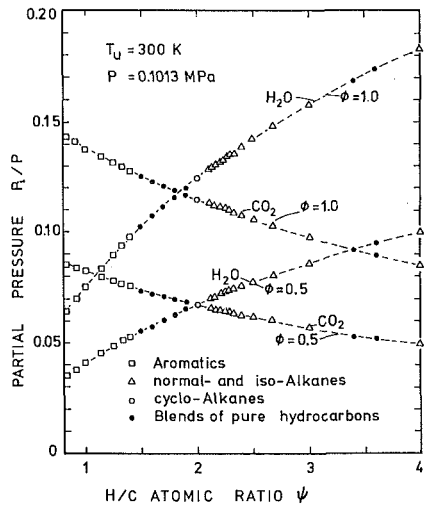

Fig. 1 Variation of the partial pressures of CO_2 and H_2O in the combustion gases of pure hydrocarbons and pure hydrocarbon blends with H/C atomic ratio

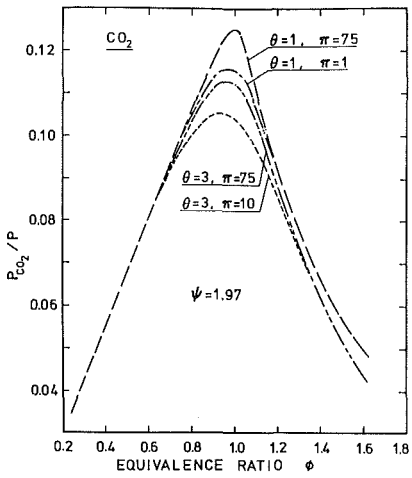

Fig. 2 Variation of the partial pressure of CO_2 with the fuel-air equivalence ratio at different initial temperatures and pressures

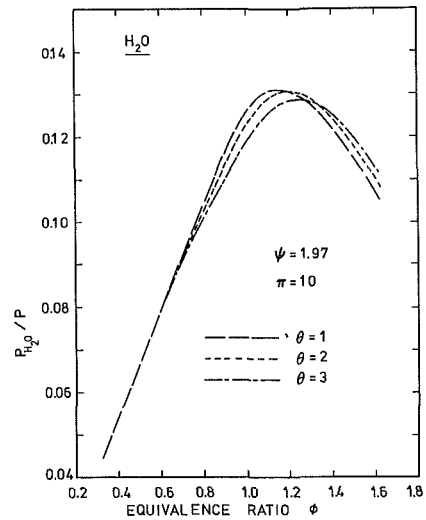

Fig. 3 Dependence of the partial pressure of H_2O on the fuel-air equivalence ratio at various temperatures

pressures of CO_2 and H_2O can be approximated by the following equation for lean mixtures [2]

$$\frac{P_{CO_2}}{P}=\frac{P_{H_2O}}{P}=\frac{2.1(F/A)}{1+1.05(F/A)} \tag{1}$$

More general formulae for estimating partial pressures of CO_2 and H_2O as a function of fuel density as well as equivalence ratio have been proposed by Kunitomo and Kodama [3] as:

For $\phi < 1.1$

$$P_{CO_2}/P=0.175-0.075/\phi+0.033\ \rho_f \tag{2}$$

For $\phi \geq 1.1$

$$P_{CO_2}/P=0.092+0.038\ \rho_f-2.619(1.01-\rho_f)(1.05-1/\phi)^2 \tag{3}$$

For $\phi \leq 1.05$

$$P_{H_2O}/P=0.259-0.068/\phi-0.0783\ \rho_f \tag{4}$$

For $\phi > 1.05$

$$P_{H_2O}/P=0.126-0.72[1/\phi+0.887\ \rho_f-1.724 -1.42(\rho_f-0.805)^2]^2 \tag{5}$$

In Fig. 1, equilibrium partial pressures of CO_2 and H_2O in the combustion gases of 50 pure hydrocarbons and 8 of their different blends are plotted as a function of H/C atomic ratio for two different equivalence ratios. It is obvious that fuel effects on the partial pressures of CO_2 and H_2O (more generally, on the composition of combustion gases) can be accurately predicted by considering only H/C atomic ratio for nonolefinic fuels (olefins less than 10 percent by volume) (Fig.

Nomenclature

A = constant, equation (6)
A/F = air-to-fuel mass ratio
a_j = constants, equations (7)–(9)
B = constant, equation (19)
b_j = constants, equations (7)–(9)
C_p = specific heat at constant pressure, kJ/kgK
$\bar{C}_p$ = mean specific heat, kJ/kgK
c_j = constants, equations (7)–(9)
F/A = fuel-to-air mass ratio
ΔH = enthalpy of evaporation, kJ/kg
N = refractive index at 20°C
P = pressure, MPa
P_i/P = dimensionless partial pressure
P_0 = reference pressure, 0.1013 MPa (= 1 atm)
T = temperature, K
T_b = distillation temperature, °C
T_0 = reference temperature, 300 K
x = pressure exponent, equation (7)
y = temperature exponent, equation (8)
z = exponent for ψ, equation (9)
α = constant, equation (6)
β = constant, equation (6)
θ = T_u/T_0 = dimensionless temperature
λ = constant, equation (6)
π = P/P_0 = dimensionless pressure
ρ_f = relative density of liquid fuel at 293 K
ρ_{f0} = density of liquid fuel at 288.6 K, kg/L
ϕ = fuel-air equivalence ratio; actual (A/F)/stoichiometric (A/F)
ψ = H/C atomic ratio
Ω_i = P_i/P = dimensionless partial pressure

Subscripts

a = air
f = fuel
i = for CO_2 i = 1, for H_2O i = 2
r = reference condition (arbitrary)
m = averaged midboiling point
u = initial mixture

Table 1 Constants of equation (6)

	H_2O	CO_2	
Constants	$0.3 \leq \phi \leq 1.6$	$0.3 \leq \phi \leq 1.0$	$1.0 < \phi \leq 1.6$
A	0.079773	0.144553	0.012252
α	0.145635	-0.314334	1.375204
β	-1.209735	-2.182043	1.364468
λ	-1.177786	-1.094678	-2.033584
a_1	-0.016521	0.015232	0.059804
b_1	0.046686	-0.070608	-0.144740
c_1	-0.022225	0.080495	0.086826
a_2	0.095917	-0.095054	-0.295175
b_2	-0.292738	0.406301	0.796634
c_2	0.166642	-0.429745	-0.657352
a_3	0.693161	-0.265207	-0.010408
b_3	0.031355	-0.141315	-1.260926
c_3	-0.046328	0.108863	1.048413

1). Similar relationships have been obtained for other equivalence ratios and initial mixture temperatures.

The variation of P_{CO_2}/P with equivalence ratio ϕ at different initial temperatures and pressures is illustrated in Fig. 2. For a given H/C atomic ratio, P_{CO_2}/P does not vary with pressure and temperature for $\phi < 0.7$, increasing pressure increases partial pressure of CO_2, and increasing initial mixture temperature decreases CO_2 due to the increasing extent of dissociation. For mixtures richer than $\phi = 1.3$, pressure does not influence the partial pressure of CO_2.

The variation of P_{H_2O}/P with equivalence ratio ϕ at different initial temperatures is shown in Fig. 3 for an H/C ratio of 1.97. Peak partial pressure of H_2O occurs on the rich side at $\phi \simeq 1.1$ for $\theta = 1$. With increasing temperature the location of the peak moves toward richer mixtures, and the absolute value of the peak decreases slightly. For mixtures leaner than $\phi = 0.65$, pressure and temperature have no effect on P_{H_2O}/P.

The results presented in Figs. 2 and 3 are for model fuels consisting of different proportions of pure hydrocarbons. The partial pressures of CO_2 and H_2O were computed by using a chemical equilibrium code which considers 14 species in the products, namely H_2, H, O_2, N_2, N, OH, H_2O, O, NO, NO_2, N_2O, CO, CO_2, and Ar. Thermochemical data were taken from standard tables [5, 6]. The solution procedure of the code is similar to that described by Benson et al. [7]. The accuracy of the program was checked against a NASA-Lewis program [8], and other published codes [9, 10] for various fuels and conditions, and good agreement has been obtained.

Empirical Formulae

A functional expression of the following form has been adapted to predict the partial pressures of both CO_2 and H_2O in the combustion gases of aviation and diesel fuels

$$\Omega_i = A\ \sigma^{\alpha} \cdot \exp[\beta(\sigma+\lambda)^2] \cdot \pi^x \theta^y \psi^z \tag{6}$$

where

$$x = a_1 + b_1\sigma + c_1\sigma^2 \tag{7}$$

$$y = a_2 + b_2\sigma + c_2\sigma^2 \tag{8}$$

$$z = a_3 + b_3\sigma + c_3\sigma^2 \tag{9}$$

and

$$\Omega_1 = P_{CO_2}/P \tag{10}$$

$$\Omega_2 = P_{H_2O}/P \tag{11}$$

π is the dimensionless pressure P/P_0 where $P_0 = 101.3$ kPa, θ the dimensionless initial mixture temperature T_u/T_0 where $T_0 = 300$ K, ψ the H/C atomic ratio of the fuel.

For P_{CO_2}/P

$$\sigma = \phi \qquad \text{if } \phi \leq 1.0 \tag{12}$$

$$\sigma = \phi - 0.7 \qquad \text{if } \phi > 1.0 \tag{13}$$

For P_{H_2O}/P

$$\sigma = \phi \qquad \text{for all } \phi \tag{14}$$

A, α, β, λ, a_j, b_j, and c_j are constants, and their values are listed in Table 1. Equation (6) has the same functional form as the adiabatic flame temperature prediction equation reported previously [4].

It should be noted that equation (6) assumes that the fuel is in vapor form and is at the same temperature as the air, i.e.,

$$T_u = T_a = T_f \tag{15}$$

However, for the cases where the fuel is in liquid form, a correction should be applied to θ so that the enthalpy of evaporation of the fuel and the temperature difference between air and fuel can be accounted for. The enthalpy of evaporation of middle distillates can be estimated from the following equation [11], in terms of fuel density and temperature

$$\Delta H = \frac{360 - 0.39\ T_f}{\rho_f} \text{ (kJ/kg)} \tag{16}$$

where ρ_f is the relative density of the liquid fuel. For more accurate estimation methods of enthalpies of evaporation, the techniques proposed in [6, 12] can be used.

For the liquid fuel temperature T_f and the air temperature T_a, the equivalent T_u can be computed as follows

$$T_u = \frac{\bar{C}_{pf}(T_f - T_r) + (A/F)\bar{C}_{pa}(T_a - T_r) - \Delta H}{\bar{C}_{pf} + (A/F)\bar{C}_{pa}} \tag{17}$$

where $\bar{C}_{pf}$ and $\bar{C}_{pa}$ are the mean specific heats of the fuel vapor and air, from T_r to T_f, and T_r to T_a, respectively, T_r is a suitable reference temperature, and (A/F) is the air-to-fuel mass ratio. C_{pf} can be calculated as a function of temperature as follows [13]

$$C_{pf} = (0.363 + 0.000467\ T)(5 - 0.001\ \rho_{f0}) \text{ (kJ/kg K)} \tag{18}$$

where ρ_{f0} is the density of the fuel (kg/L) at 288.6 K. C_{pa} can be obtained from standard tables.

The H/C atomic ratio ψ for the aviation and diesel fuels can be determined experimentally [14] with a high accuracy. It is also possible to estimate the hydrogen content using the density, averaged midboiling point, and aromatic content of the fuel [15]. Since the determination of aromatic content of middle distillates (especially of some alternative fuels) is a controversial subject [16], for accurate prediction of ψ, the following correlation, in terms of averaged midboiling point, relative density, and refractive index of the fuel, has been developed

$$\psi = B\ T_m^n\ \rho_f^S\ N^w \tag{19}$$

where

$$T_m = \frac{10 \text{ percent } T_b + 50 \text{ percent } T_b + 90 \text{ percent } T_b}{300} \tag{20}$$

10 percent T_b, 50 percent T_b, and 90 percent T_b are 10, 50,

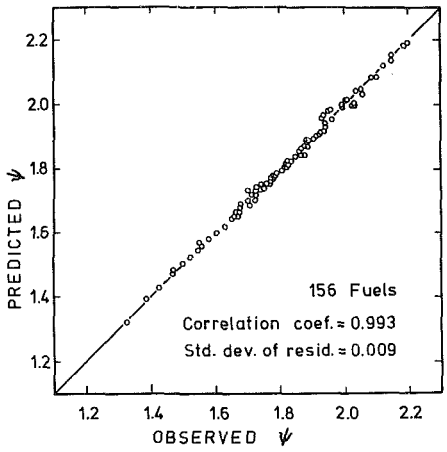

Fig. 4 Correlation between H/C atomic ratio and the function in terms of averaged midboiling point, relative density, and refractive index of the fuel

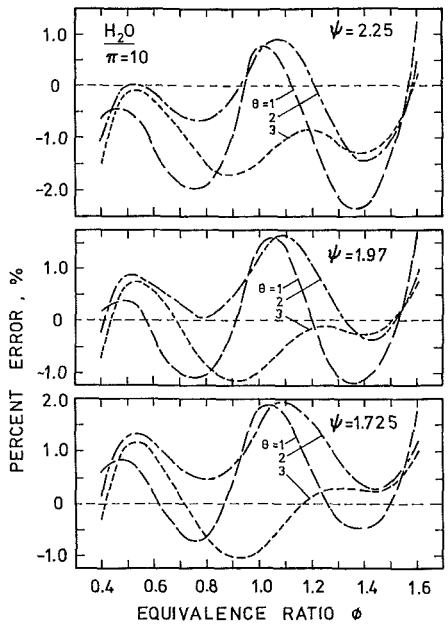

Fig. 5 Error in the predicted partial pressure of H_2O versus equivalence ratio for various fuels and temperatures at π = 10

and 90 percent distillation temperatures in °C, respectively. ρ_f is the relative density of fuel at 20°C, and N is the refractive index measured at 20°C. The values of the constants B, n, S, and w are

$$B = 12.7777$$

$$n = 0.2056$$

$$S = -0.3097$$

$$w = -5.7089$$

Equation (19) has been developed using the data for 156 aviation and diesel fuels. Hydrogen contents have been determined by low-resolution NMR [14]. Predicted H/C values are plotted against measured values in Fig. 4. The accuracy of the correlation is very good with a standard deviation of residuals of 0.009. When only density and boiling point data of the fuel are available, correlation proposed in [4] can be used to estimate H/C atomic ratio.

Accuracy of Empirical Formulae

To evaluate the accuracy of the empirical formulae for partial pressures of CO_2 and H_2O, a set of comparisons of results

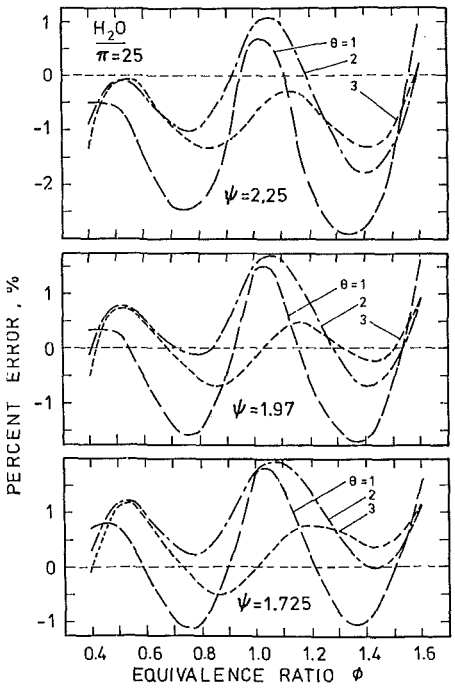

Fig. 6 Error in the predicted partial pressure of H_2O versus equivalence ratio for various fuels and temperatures at π = 25

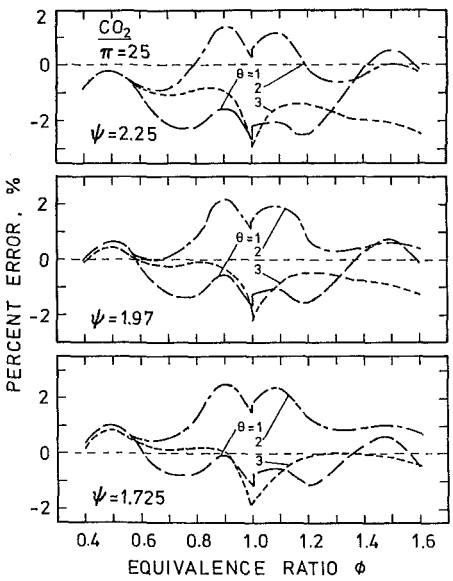

Fig. 7 Error in the predicted partial pressure of CO_2 versus equivalence ratio for various fuels and temperatures at π = 25

obtained from equation (6) and those obtained from a detailed chemical equilibrium code, which is briefly described in Background section, has been made. Results are compared for all possible combinations of the following values of H/C atomic ratio, pressure, temperature, and equivalence ratio

$\psi = 2.25, 1.97, 1.725, 1.508, 1.316, 1.143$

$\theta = 1.0, 1.133, 1.67, 2.0, 2.33, 2.67, 3.0$

$\pi = 1, 10, 25, 50, 75$

$\phi = 0.3$ to 1.6 with 0.1 increments

Comparisons made at π = 10 and π = 25 for H_2O are shown in Figs. 5 and 6, respectively. Percentage error is defined as $(P_{CO_2} - P'_{CO_2})/P_{CO_2}$, where P'_{CO_2} is the predicted partial pressure. Percentage errors similar to those of Figs. 5 and 6 have been observed at other conditions considered. For

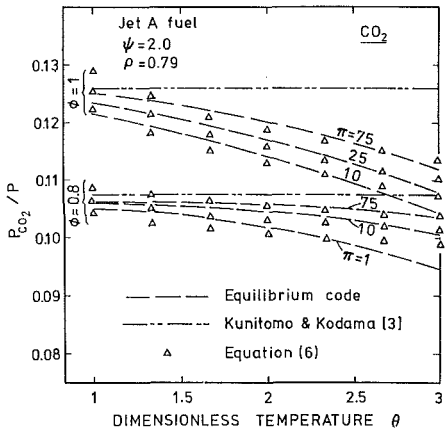

Fig. 8 Comparison of predictions of partial pressure of CO_2 by equation (6), and by equation (2) [3] to equilibrium code results

the whole range considered, the mean absolute error is 0.75 percent.

Comparisons made at $\pi = 25$ for CO_2 are shown in Fig. 7. For the whole range of conditions considered, the mean absolute error is 0.8 percent.

Partial pressures of CO_2 in the combustion gases of ASTM Jet A fuel with $\psi = 2.0$ and $\rho_f = 0.79$ are shown in Fig. 8, as obtained by a detailed equilibrium code, equation (2), and equation (6). The empirical formula of Kunitomo and Kodama [3] seems to be accurate only at very low initial temperatures, and it neglects the effects of pressure and temperature change. Errors in the predictions from equation (2) are larger for off-specification fuels (i.e., high aromatic content, low ψ) indicating that density alone is not sufficient to characterize a fuel's H/C ratio.

It should be noted here that the proposed empirical formulae are valid for the following ranges:

$$0.3 \le \phi \le 1.6$$

$$0.8 \le \psi \le 2.5$$

$$0.92 \le \theta \le 3.2$$

$$1.0 \le \pi \le 75$$

However, equivalence ratio range can be extended to $0.1 \le \phi \le 2.0$, and temperature range to $0.75 \le \theta \le 4$, with a slight increase in mean absolute error. The applicability of the formulae is not limited to only aviation and diesel fuels; they are also valid for nonolefinic (less than 10 percent olefins) gasolines and heavy residuals as well as pure alkanes and aromatics within the specified limits.

Concluding Remarks

Functional expressions are presented by means of which the partial pressures of CO_2 and H_2O in the combustion gases of aviation fuel-air and diesel fuel-air systems can be calculated as functions of pressure, temperature, equivalence ratio, and H/C atomic ratio of the fuel. These equations provide a very fast means of predicting partial pressures as compared to thermodynamic equilibrium calculations. Results of the predictions using the proposed equations are compared with the results obtained from a detailed chemical equilibrium code incorporating 14 species in the combustion products, and it is shown that the accuracy of the approximate equations is very good over the conditions of interest for a very wide range of fuel characteristics. These formulae are more general and accurate than the previous expressions reported [2, 3].

A correlation is presented for accurate predictions of the H/C atomic ratio of fuels (or mass hydrogen percentage) using the averaged midboiling point, refractive index, and relative density of the fuel. This correlation is applicable for aviation and diesel fuels.

The developed formulae are expected to reduce the computation time in gas turbine thermal calculations, and to be helpful in nonluminous radiation heat transfer analysis of diesel engine combustion chambers. Especially for the development of simulation models and heat transfer calculations requiring multiple determinations of flame temperature and partial pressures of CO_2 and H_2O as a function of time and space coordinates for varying equivalence ratios, the proposed formulae, with the flame temperature prediction equation reported previously [4], provide distinct advantages over the chemical equilibrium codes. Another advantage of the proposed formulae is that for cases where exact gas composition is required equation (6) can be used to advantage as a generator of good initial guesses (usually within 1 percent of the exact solution), to speed convergence of iterative calculations of chemical equilibrium codes.

References

1 Lefebvre, A. H., "Flame Radiation in Gas Turbine Combustion Chambers," *International Journal of Heat and Mass Transfer*, Vol. 27, No. 9, 1984, pp. 1493-1510.

2 Lefebvre, A. H., and Herbert, M. V., "Heat-Transfer Processes in Gas-Turbine Combustion Chambers," *Proceedings of Institution of Mechanical Engineers*, Vol. 174, 1960, pp. 463-473.

3 Kunitomo, T., and Kodama, K., "Radiation From Luminous Flame at High Pressures (Spray Combustion of Liquid Fuel)," *Bulletin of the Japan Society of Mechanical Engineers*, Vol. 17, No. 113, Nov. 1974, pp. 1486-1493.

4 Gülder, Ö. L., "Flame Temperature Estimation of Conventional and Future Jet Fuels," ASME JOURNAL OF ENGINEERING FOR GAS TURBINES AND POWER, Vol. 108, Apr. 1986, pp. 376-380.

5 Stull, D. R., and Prophet, H., eds., *JANAF Thermochemical Tables*, U.S. National Bureau of Standards Publications, NSRDS-NBS 37 and supplement, 1971.

6 Reid, R. C., Prausnitz, J. M., and Sherwood, T. K., *The Properties of Gases and Liquids*, 3rd ed., McGraw-Hill, New York, 1977.

7 Benson, R. S., Annand, W. J. D., and Baruah, P. C., "A Simulation Model Including Intake and Exhaust Systems for a Single Cylinder Four-Stroke Cycle Spark Ignition Engine," *International Journal of Mechanical Engineering Science*, Vol. 17, 1975, pp. 97-124.

8 Gordon, S., and McBride, B. J., "Complex Chemical Equilibrium Calculation," NASA SP-273, 1971.

9 Olikara, C., and Borman, S. L., "A Computer Program for Calculating Properties of Equilibrium Combustion Products With Some Application to I. C. Engines," SAE Paper No. 750463, 1975.

10 Agrawal, D. D., and Gupta, C. P., "Computer Program for Constant Pressure or Constant Volume Combustion Calculations in Hydrocarbon-Air Systems," ASME JOURNAL OF ENGINEERING FOR POWER, Vol. 99, 1977, pp. 246-254.

11 Lefebvre, A. H., *Gas Turbine Combustion*, McGraw-Hill, New York, Ch. 9, 1983.

12 *Technical Data Book—Petroleum Refining*, 4th ed., Vols. 1 and 2, American Petroleum Institute, PA, 1983.

13 Chin, J. S., and Lefebvre, A. H., "Steady-State Evaporation Characteristics of Hydrocarbon Fuel Drops," *AIAA Journal*, Vol. 21, No. 10, Oct. 1983, pp. 1437-1443.

14 "Hydrogen Content of Aviation Turbine Fuels by Low Resolution Nuclear Magnetic Resonance Spectrometry," Institute of Petroleum, IP 338/78, 1978.

15 ASTM, "Standard Method for Estimation of Hydrogen Content of Aviation Fuels," ASTM D 3343-74 (reapproved 1979), 1979.

16 Glavincevski, B., and Gardner, L., "An Overview of the Methods for Structural Analysis: Proton NMR and GC-MS of Middle Distillate Aromatic Fractions," SAE Fuels and Lubricants Meeting, SAE Paper No. 852079, Tulsa, OK, Oct. 1985.

Fuel Deposit Characteristics at Low Velocity

E. J. Szetela

A. J. Giovanetti

United Technologies Research Center,
East Hartford, CT

S. Cohen

NASA Lewis Research Center,
Cleveland, OH

An experimental program has been carried out to characterize the relationship between deposit mass, operating time, and temperature in studies of the thermal stability of aviation gas turbine fuel. This information is required by fuel system designers to prevent deposit buildup in fuel system components, thus allowing for more efficient designs. The program has included the design, fabrication, and operation of a novel thermal stability test apparatus for the determination of deposition rates over a range of temperatures and test durations up to several hundred hours. Experiments were run to determine the rate of deposit formation as a function of temperature in heated stainless steel tubes at low velocity using Jet A fuel. The test tube had an inside diameter of 0.22 cm, a length of 0.91 m, and a flow rate of 0.73 kg/h. Deposits obtained were often characterized as thick, porous, and nonuniform in nature. Deposit density based on carbon content was 0.08 g/cm^3. Deposit rates of 0.1 to 100 μg C/h-cm^2 were observed at surface temperatures between 400 and 600 K.

Introduction

Hydrocarbon gas turbine fuels in contact with heated surfaces form insoluble, carbonaceous deposits which often clog fuel passages in heat exchangers, fuel manifolds, and injectors. The chemical changes resulting in deposit formation are not understood, but it is believed that oxidation processes leading to the formation of free-radical species are involved [1]. The deposit process is slow yet observable at temperatures in the range 450 to 600 K. Above 600 K, the process becomes substantially more rapid [2].

A reliable correlation of the growth of deposits with operating conditions such as temperature, run time, etc. has not been available although a number of investigators have studied deposit formation in previous programs. One of the techniques used was to measure the rise in surface temperature with time and deduce the thermal resistance [3, 4]. Deposit mass has been characterized by combusting the deposit and measuring CO and CO_2 concentrations in a number of investigations which involved tests of 10 min to 100 h duration [5–10]. Visual observations have been reported after cyclic tests in a fuel system simulator which was operated for 250 h [11]. A beta-ray technique was used to analyze heated tube specimens run at temperatures between 900 and 1000 K for periods up to 100 h [12].

The purpose of the present investigation was to determine the relationship of deposit growth rate, run time, and temperature using Jet A fuel. The experimental program was divided into two groups of tests. In one group which was run at temperatures up to 500 K, test times varied from 50 to 730 h. The other group was run at temperatures up to 600 K and test times varied from 3.7 to 20 h.

Contributed by the Gas Turbine Division and presented at the 1985 Beijing International Gas Turbine Symposium and Exposition, Beijing, People's Republic of China, September 1-7, 1985. Manuscript received at ASME Headquarters June 14, 1985. Paper No. 85-IGT-130.

Experimental Apparatus and Procedure

Approach. The objectives of the tests were to measure the mass of deposit collected in a heated tube using Jet A fuel over periods of time ranging from several hours to several hundred hours and to characterize the relationship of mass, run time, and temperature. Wall-to-bulk temperature difference was to vary from 0 to 100 K and the deposits present in the bulk fuel as well as on the tube surface were to be evaluated. Fuel velocity was to be relevant to engine fuel system operation; a review of fuel velocities present in portions of an advanced gas turbine fuel system at key operating conditions indicated that velocities as low as 0.07 m/s are applicable. Because of the considerable effort required to run long-duration tests, including extensive elapsed time, data output during test runs was to be maximized.

An apparatus was designed that consists of multiple, resistance-heated tubes which are connected in series with unheated, constant-temperature (isothermal) tubes. Multiple tubes permit tests of different durations to be run concurrently. In addition, metal wafer specimens of the same material as the tubes are immersed in the fuel stream, and water-cooled, sintered metal filters are used to capture deposit material carried by the fuel. The heated tube experiments provide information on the deposit formation that occurs when the temperature differential between the surface and fuel is large, whereas the isothermal tubes and metal wafer specimens yield data for the condition where the surface and fuel temperatures are equal. The water-cooled deposit filters enable determination of residual deposit in the bulk flow without the presence of a heated metal surface.

Apparatus. The experimental apparatus, shown schematically in Fig. 1, consists of: (1) a fuel supply tank and sparging element to saturate the fuel with air prior to test; (2) a zeolite-type molecular sieve used to remove water and gum

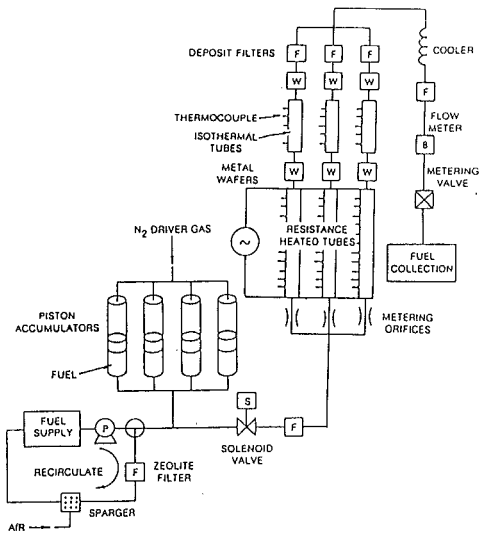

Fig. 1 Fuel deposit test apparatus

deposits from the fuel; (3) a fuel delivery system comprising four piston-type accumulators which are used to drive fuel through the test section; (4) a flow-metering orifice at the inlet of each heated tube to maintain identical flow rates in each tube; (5) a test section comprising three resistance-heated tubes connected in parallel to an a-c power supply, followed by three isothermal tubes; (6) stainless steel wafer specimens immersed in the fuel stream at locations immediately upstream and downstream of each isothermal tube; (7) a water-cooled, nominal 15-μm sintered, stainless steel deposit filter at the outlet of each isothermal tube; (8) a fuel cooler; (9) an electrically driven metering valve and tubine flow meter to control and monitor the total fuel flow rate through the test section; and (10) a fuel collection tank.

Each of the three test tube assemblies shown in Fig. 1 is fabricated from 0.22 cm i.d. $\times$ 0.32 cm o.d., 316 stainless steel tubing. The 0.91-m-long resistance-heated tube subassembly is brazed to copper electrodes which attach to the power supply, and the connecting 0.30-m-long isothermal tube subassembly is enclosed in a concentric, cylindrical ceramic oven to compensate for heat losses to the environment. Eleven chromel-alumel thermocouples are spot welded to the outer wall of the heated tube at equal spacings of 7.6 cm. The thermocouple junctions are coated with Sauereisen cement to insure good thermal contact and to minimize heat conduction losses. In the same manner, five thermocouples, spaced at 5.1-cm intervals, are attached to each isothermal tube. The use of an a-c power supply to heat the tubes assures that temperature measurement errors resulting from a voltage drop across the thermocouple bead are minimized. The test tube assemblies are electrically isolated and mounted vertically. The vertical orientation causes the buoyancy forces acting on the fuel (due to the induced axial temperature gradient) to be in the same direction as the flow, thereby suppressing any secondary flow motion that could occur at the low Reynolds number test condition.

Data Acquisition. All data are recorded with a calculating data-logger microprocessor and are subsequently reduced on a high-speed digital computer. The pertinent data parameters monitored and recorded during each test for each tube assembly are: the outer wall temperature of the tube at 16 different axial locations; the inlet and outlet fuel temperature of the heated and isothermal tubes with duplicate measurements at every station, the inlet fuel pressure and fuel pressure differential across each tube and deposit filter; the individual tube flow rates (metering orifices) and the total flow rate (turbine meter); and the applied voltage and current. Since piercing the test tubes to measure fuel temperature is not considered to be good practice (because of possible fuel leakage, insertion of preferential sites for deposition, and electrical discontinuities), only inlet and outlet fuel temperature measurements are made. Assuming the heat flux distribution along the resistance-heated tube is uniform (i.e., fuel enthalpy increases linearly with tube position), the fuel temperatures at intermediate tube positions are determined by interpolating between the inlet and outlet temperatures in an enthalpy versus temperature table. The low fuel velocity used in the experiments resulted in the use of a low heat flux from the tube wall to the fuel. As a result, radial temperature gradients across the tube wall were negligible and except for very thick deposits the radial temperature gradients in the deposits were small.

Test Procedure. During most of the test runs of the three tubes, the fuel flow rate and inlet and outlet fuel temperatures (hence, input electrical power) are identical for all tubes. A proportional temperature controller and solid state relay maintain a constant input a-c electrical power to the tubes for the test time, and the electrically driven fuel metering valve responds to the output of the turbine flow meter to hold the flow rate within prescribed setpoints. In some test runs, the electrical power to one of the three tubes was reduced allowing data to be obtained simultaneously for three tubes at identical flowrates while the heat flux to one tube was different from the others. Complete control of the input variables permitted the experimental apparatus to operate unattended for the long-duration tests. If any critical operating parameter (i.e., fuel pressure or tube temperature) varied outside its specified range, automatic shutdown would be initiated.

After testing, each test tube was cut into sections which were then vacuum dried at 390 K to remove residual fuel, and the quantity of carbon on each of these sections was determined by burning off the deposit in oxygen, collecting the effluent gases in evacuated flasks, and measuring the concentrations of CO_2 and CO in the gases using nondispersive infrared analyzers. The carbon deposition rate was defined as the mass of carbon deduced from the burnoff analysis divided by the product of the inside lateral surface area of the tube and the test time; it is expressed in the units μg C/cm^2-h. Equally spaced sections, each approximately 6.4 cm long, were cut from the heated and isothermal tubes and used in the burnoff analysis; other sections of the tubes were sliced into longitudinal sections which were examined microscopically. The burnoff procedure was used to determine the mass of carbon particulate trapped in the deposit filters. The amounts of deposit formed on the stainless steel wafer specimens (0.64 cm long $\times$ 0.32 cm wide $\times$ 0.005 cm thick) were determined by weighing them prior and subsequent to testing.

Deposit mass measurement accuracy was established by processing clean tubes and wafers through the burnoff and weighing procedures. By this means, a minimum carbon mass was determined which was used as the lowest value of reliable measurement. The heated tube and wafer deposit data were found to be inaccurate and scattered when this minimum was approached. The lowest deposit mass accepted for analysis and correlation on the tube specimens was 200 μg and on the wafers, 10 μg.

Fuel Properties

The fuel used in the program was a single batch of Jet A drawn from a large supply that is maintained for gas turbine development testing. The fuel was placed into new steel drums and the total quantity was large enough for the entire ex-

Table 1 Properties of Jet A

	SPL	NASA
API gravity @ 289 K	41.8	41.7
Viscosity, CS	1.51@311 K	1.98(est.)@297 K
Paraffins, vol. percent	76.8	78.0
Olefins, vol. percent	1.9	0.5
Aromatics, vol. percent	21.2	21.5
Hydrogen, wt. percent	13.4	13.7
Sulfur, wt. percent	0.05	0.02
Nitrogen, ppm	12.4	8.0
Distillation temperature, K		
10 percent	461	456
50 percent	486	485
90 percent	518	518
Thermal stability*		

*Breakpoint temperature as measured in two tests at Southwest Research Institute was found to be between 525 and 533 K.

Table 2 Test conditions

Test No.	Test duration, h	Exit fuel temperature, K
1	730	420
2	406	420
3	233	420
4	157	450
5	157	450
6	103	450
7	53	450
8	50	450
9	20	560
10	20	560
11	20	560
12	10	505
13	6.7	560
14	3.7	560

Table 3 Deposit rate in μg C/cm^2-hr

Distance from entrance, cm	46	53	61
Tube No. 1	133	123	123
Tube No. 2	135	115	113
Tube No. 3	135	105	98
Total variation, percent	1.5	16	22

perimental program. Indoor storage of the drums at ambient temperature was provided over the eight month test period. Properties of the fuel were measured at two independent laboratories, namely, Southern Petroleum Laboratories (SPL) and NASA Lewis Research Center (NASA). The properties of the fuel are contained in Table 1.

Experimental Conditions

All tests were conducted at the nominal flow rate of 0.73 kg/h which corresponded to a fuel velocity of 0.07 m/s and a Reynolds number of 60 at the tube inlet. The fuel pressure throughout the tube was maintained at 34 atm which was well above the critical pressure (22 atm), but maximum tube temperatures did not exceed the critical temperature (670 K); therefore, the fuel was in a compressed liquid state.

The test conditions included long-duration tests with times ranging from 50 to 730 h and with exit fuel temperatures of 420 and 450 K. Also included were short-duration tests with times ranging from 3.7 to 20 h and with exit fuel temperatures of 505 and 560 K. The entire test matrix is shown in Table 2. Data at a number of distinct wall temperatures were derived from each test.

In some cases, test precision was high, as in the test of test series 9 to 11 in Table 2. To investigate precision, the exit fuel temperature from one of the tubes was held at 560 K, while the supply voltage to all three tubes was identical. These conditions were held for 20 h. Following the test, three tube sections at each of three positions were analyzed in the burnoff apparatus to measure deposit formation rate.

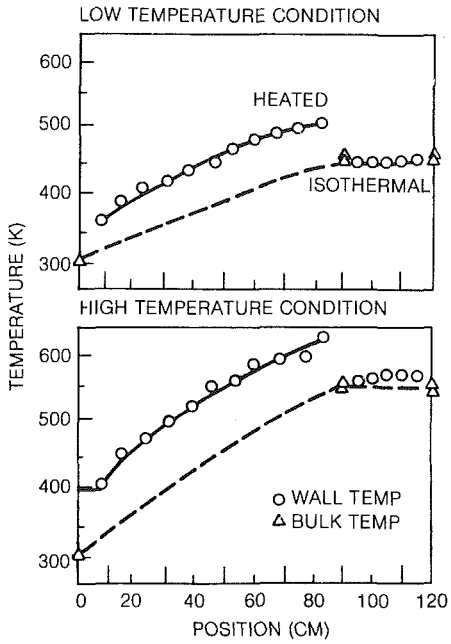

Fig. 2 Wall temperature distribution

Precision in this test series which yielded the most repeatable results in the program is shown in the data contained in Table 3.

Experimental Results and Discussion

Tube wall temperatures and fuel bulk temperature measurements made during the tests were found to be repeatable and relatively free of scatter. Typical temperatures obtained at the low-temperature and high-temperature conditions are shown in Fig. 2. Wall temperature increases in the higher temperature cases (higher heat flux) were sometimes noted during the tests when deposits became thick; the highest recorded increase was 70 K.

Deposit mass measurements obtained from tubes run at the low-temperature condition resulted in monotonic curves while measurements made at the high temperatures resulted in nonmonotonic curves when deposit rate was plotted against initial wall temperature. Typical results are shown in Fig. 3. Also shown is the reproducibility of the results because duplicate tests were run at the 20-h and at the 157-h conditions. The trends in the curves in Fig. 3 would be the same if the deposit rate were plotted against tube length because tube wall temperature increases with length as shown in Fig. 2.

The nonmonotonic data have been observed previously [6–9, 13] in experiments with heated tubes. The reasons for the shape of the curve have not been established with certainty, but it has been surmised that along the tube, depletion of active species such as dissolved oxygen and hydroperoxides exerts a strong influence on local deposit rate. Concentration measurements of oxygenated compounds showing hydroperoxide depletion were reported in [13].

Thin deposits were found on the surfaces of the immersed specimens and the isothermal tubes. In many cases, the collected mass correlated with the deposit measurements obtained from heated tubes as shown in Fig. 3. Exceptions to this behavior usually occurred when the curves were nonmonotonic and depletion of active species affected the deposit rate in the downstream portion of the tube. Deposits were also found in the fuel filters where the mass collected was up to 10 percent of the combined mass found on the other surfaces.

The deposit was found to be cellular with a structure that could be described as filamentous. The carbonaceous mass

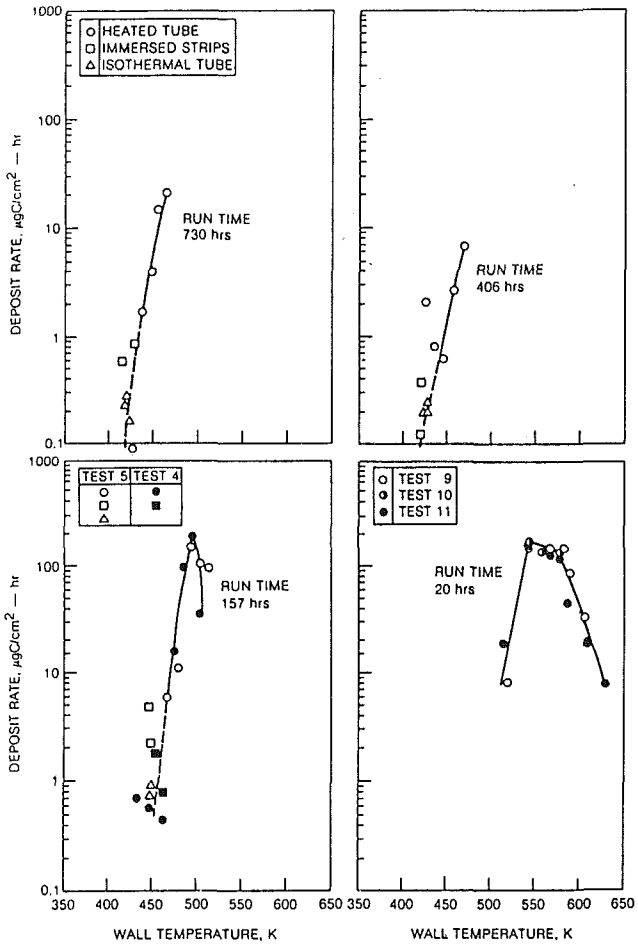

Fig. 3 Deposit rate measurements

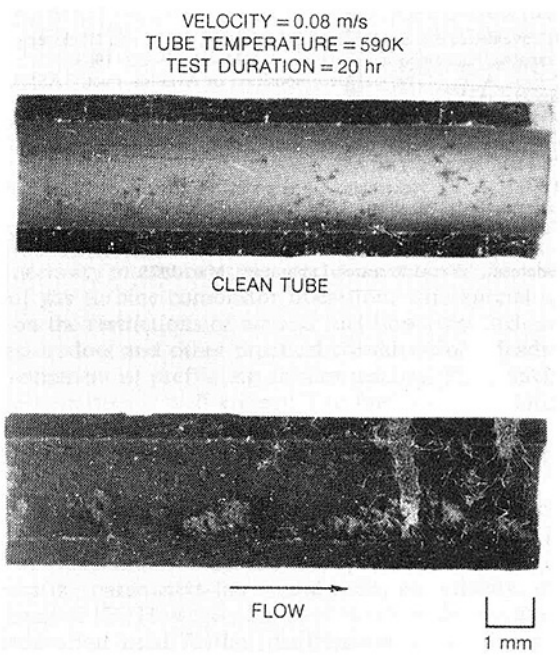

Fig. 4 Jet A fuel deposits at low velocity

was irregular, often appearing in lumps having the shapes shown in Fig. 4. Average deposit thickness was measured in several tube specimens using high-magnification photographs. From the average thickness and the measured carbon mass, the density was found to be approximately 0.08 g/cc.

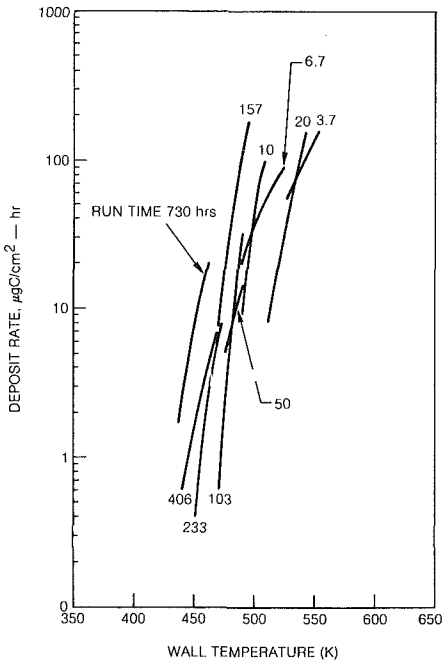

Fig. 5 Composite plot of deposit data

Deposit rate data were plotted for all runs in a manner shown in Fig. 3. A composite plot of the smoothed data is shown in Fig. 5. Where the data were nonmonotonic, only the region where deposit rate increases with temperature are shown. These data (Fig. 5) can be considered to have a more general application than the data in regions where deposit rate decreases with temperature as in Fig. 3. The latter data are too closely related to residence time of the fuel in the tube to be of general value.

It can be seen in Fig. 5 that run time has an effect on deposit rate. This effect was explored by crossplotting the data in Fig. 5, transforming the deposit rate to a deposit loading, and replotting this parameter against run time in Fig. 6. The effect of run time is very strong; the average slope of the lines of constant wall temperature is 3. One possible explanation for this nonlinear behavior is that the surfaces produced by the deposit may become active and result in a rapid increase in deposited mass. A similar set of lines produced by plotting deposit thickness against run time, assuming constant specific gravity of 0.08, is shown in Fig. 7. It can be seen that deposit thickness reached values in excess of 0.1 cm which resulted in plugging of the tube.

Data Interpretation

The data presented here indicate that deposits grew with approximately the third power of time. Average deposit thickness reached a value greater than 0.1 cm in tests of 157 h to 730 h duration. The mass deposit rate observed at the low velocities run in this program during short-duration tests was similar, at a given temperature, to the short-duration, high-velocity data reported in [9]. However, the density of the deposits reported in [9] was more than ten times the density observed in this program.

It is important to consider whether the deposit buildup observed in this program could be observed in gas turbine engine fuel systems during normal operation. The tests reported herein were run at steady conditions. Shutdowns, which were infrequent, were confined primarily to tube changeovers. In gas turbines, steady conditions are reached only during extended cruise periods. Between these periods, flow rate varies from idle to sea-level takeoff conditions. The thermal environment also varies because of changes in fuel

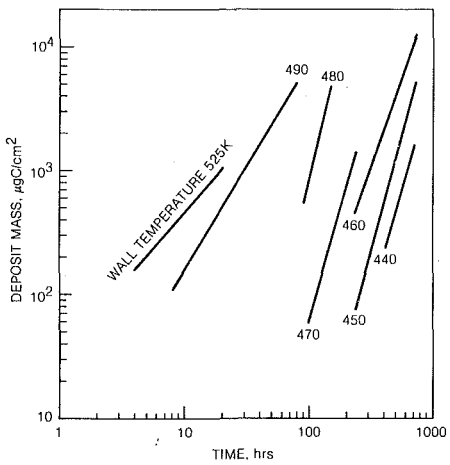

Fig. 6 Increase of mass with time

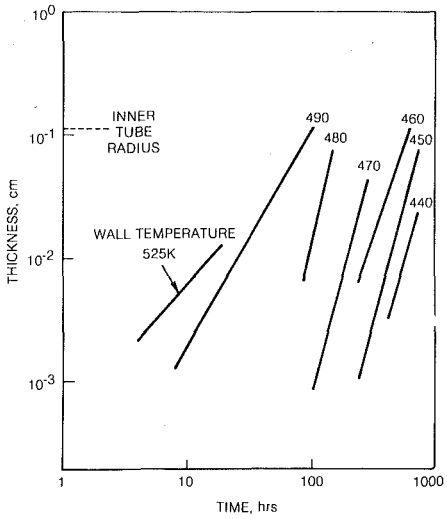

Fig. 7 Increase of thickness with time

flow, air flow, fuel temperature, and air temperature. As a result, there is a resultant variation in shear conditions at the deposit–fuel stream interface and a changing gradient in temperature between the metal surfaces and the deposit. Consequently, it is possible that deposit buildup occurs at a different rate in engine systems than in steady-flow, long-duration rig tests, particularly in the case of low-density deposits.

Conclusions

Long-duration and short-duration tests can be correlated into a useful group of data except in regions where residence time is sufficient for depletion of active oxygen compounds. Wall temperature has a profound effect on deposit buildup. Run time in tests at steady conditions can have a substantial influence on deposit growth. However, the interpretation and application of long-duration test data at steady conditions to gas turbine operation must be made with great care. Repeated changes in shear and thermal gradients resulting from frequent changes in power setting during normal engine operation may have unique influences on deposit buildup.

Acknowledgments

This work was performed with the support of the NASA Lewis Research Center under Contract NAS3-24091. The Project Manager was S. Cohen.

References

1 "CRC Literature Survey on the Thermal Oxidation Stability of Jet Fuel," CRC Report No. 590, Coordinating Research Council, Inc., Atlanta, GA, Apr. 1979.

2 Szetela, E. J., "Deposits from Heated Gas Turbine Fuels," ASME Paper No. 76-GT-9.

3 Hatcher, J. B., "High-Flux Heat Transfer and Coke Deposition of JP3 Fuel Mixture," JPL CIT Progress Report No. 20-157, Feb. 1952.

4 Mills, J. S., and Edwards, F. R., "The Thermal Stability of Aviation Fuel," ASME Paper No. 84-GT-69.

5 Watt, J. J., Evans, A., and Hibbard, R. R., "Fouling Characteristics of ASTM Jet-A Fuel When Heated to 700 F in a Simulated Heat Exchanger Tube," NASA TN D-4958. Dec. 1968.

6 Taylor, W. F., "Development of High Stability Fuel," Exxon Report GRUS, 11GAHF.73, July 1973.

7 Szetela, E. J., and TeVelde, J. A., "Experimental Study of External Fuel Vaporization," *Combustion Science and Technology*, Vol. 35, 1983.

8 Roback, R., Szetela, E. J., and Spadaccini, L. J., "Deposit Formation in Hydrocarbon Fuels," ASME JOURNAL OF ENGINEERING FOR POWER, Vol. 105, 1983.

9 TeVelde, J. A., Spadaccini, L. J., Szetela, E. J., and Glickstein, M. K., "Alternative Fuel Deposit Formation," AGARD CP-353, 1983.

10 Peat, A. E., "Thermal Decomposition of Aviation Fuel," ASME Paper No. 82-GT-27.

11 Bradley, R., Bankhead, R., and Bucher, W., "High Temperature Hydrocarbon Fuels Research in an Advanced Aircraft Fuel System Simulator," AFFB-14-70, AFAPL-TR-73-95, Apr. 1974.

12 Faith, L. E., Ackerman, G. H., and Henderson, H. T., "Heat Sink Capability of Jet A Fuel: Heat Transfer and Coking Studies," NASA CR-72951, July 1971.

13 Hazlett, R. N., "Progress Report on Advanced Hydrocarbon Fuel Development," Naval Research Laboratory, Mar. 1975.

Internal Flow Effects in Prefilming Airblast Atomizers: Mechanisms of Atomization and Droplet Spectra

T. Sattelmayer

S. Wittig

Lehrstuhl und Institut für
Thermische Strömungsmaschinen,
Universität Karlsruhe,
D-7500 Karlsruhe, West Germany

Fuel atomization with prefilming airblast nozzles has been investigated. The present analysis is directed toward a detailed investigation of the atomization processes and the clarification of the fundamental phenomena. Two-dimensional models were utilized. High-speed films, showing the deterioration of the liquid film close to the atomizing edge, reveal the dynamics of the liquid's deterioration and show the motion of the film during the drop formation. The liquid separation is shown to be a periodic process with the drop formation caused by momentum transfer. The frequency spectrum of the liquid separation is determined by means of an optical technique. It is seen that the main frequencies depend only on the air velocity. They are always lower than the corresponding wave frequencies. The droplet size measurements obtained by a light scattering technique emphasize the dominant role of the air velocity at the atomizing edge. A decrease in the surface tension provides an improvement in atomization quality. Other parameters such as liquid flow rate, liquid viscosity, gap height, and length of the prefilming surface within the nozzle were found not to affect directly the droplet size distribution produced, if the air velocity in each of the two ducts of the nozzle is kept constant. The pressure drop of the air, however, rises. It is shown that the droplet size distribution can be easily determined, if the arithmetic mean value of the air velocity in both ducts is known, e.g., from a calculation of the internal flow. Due to the high liquid mass flow rates of airblast nozzles, the wavy film is partly atomized within the nozzle before the liquid separates at the atomizing edge. The measurements show that the portion of the liquid mass flow atomized remains relatively small and that the droplet sizes are equivalent to those produced at the atomizing edge.

Introduction

The necessity to ensure proper performance over the whole range of gas turbine combustor operation, with special emphasis on the restrictions of air and fuel flow rates including the pressure loss and other practical considerations, leads to the development of prefilming airblast nozzles. The principle of these atomizers is well known: The fuel is driven along a surface within the nozzle as a wavy film by the air flow. Arriving at the atomizing edge, the liquid film separates and droplet formation takes place (Fig. 1).

A large number of investigations have been conducted utilizing particular, empirically optimized nozzles [1]. Primarily correlations of the mean drop size as a function of the operating parameters (air–liquid ratio, air velocity, etc.) were obtained [2]. However, the basic mechanisms leading to the atomization need further clarification as a number of determining parameters, which influence the droplet size distribution, have not in general been investigated separately. In particular, the behavior of the internal two-phase flow, the influence of the liquid film properties on the droplet spectra, and the mechanisms of film separation and drop formation as of yet are not fully understood.

In the larger context of a major research program at our in-

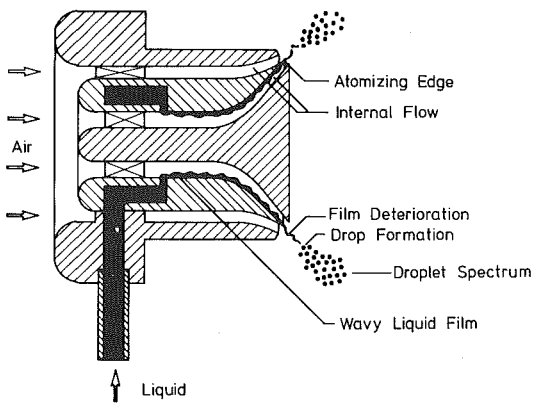

Fig. 1 Prefilming airblast nozzle

Contributed by the Gas Turbine Division of THE AMERICAN SOCIETY OF MECHANICAL ENGINEERS and presented at the 31st International Gas Turbine Conference and Exhibit, Düsseldorf, Federal Republic of Germany, June 8–12, 1986. *Manuscript received at ASME Headquarters January 30, 1986. Paper No. 86-GT-150.*

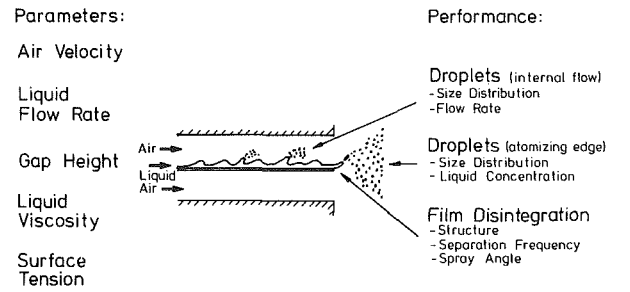

Fig. 2 Model of the simplified flow through prefilming airblast nozzles

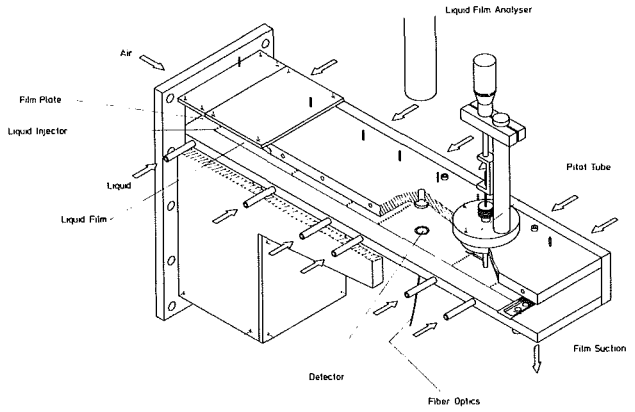

Fig. 3 Test section (internal flow)

stitute [3, 4] the internal flow of airblast nozzles, the concepts for the calculation of the two-phase flow (air–liquid film) as well as the film disintegration, and finally the drop formation are studied in detail. The main aspect of the present paper is the analysis of the internal flow effects on film disintegration and drop size distributions.

In the present study, the flow through airblast nozzles is simplified to obtain more detailed information about the substantial effects and to reduce the number of parameters. Figure 2 illustrates the two-dimensional model under consideration.

The internal flow affects the flow conditions at the atomizing edge (Fig. 2), which in turn influence the liquid film disintegration and the resulting drop size distribution. In the case of high liquid flow rates, an additional atomization process above the wavy liquid film occurs, which can influence the atomization quality.

To assure well-defined initial conditions for the atomization process, the test facility was designed to create a fully developed flow near the atomizing edge within the nozzle. Both ducts are approximately parallel.

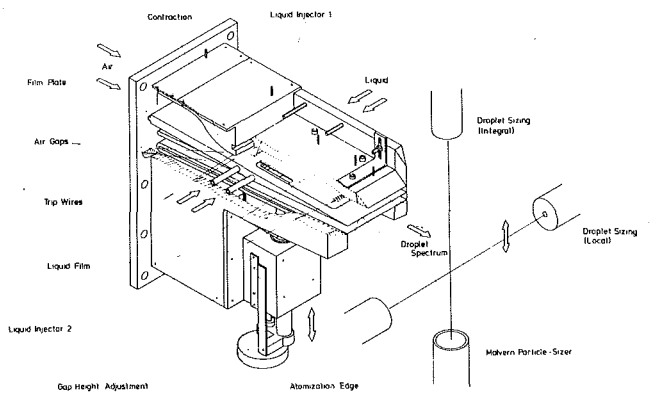

Fig.4 Test section (liquid film disintegration and drop formation)

Experimental Setup

For the experimental study of the internal flow as well as the liquid film separation and the drop size measurements, a setup employing two different test sections was utilized: A special test section (Fig. 3) was designed for the investgation of droplet formation within the nozzle as well as the liquid film/air-flow interaction. Only one of two available air gaps was used for the droplet formation study above the film and the liquid film was sucked from the plate's surface at the end of the test section. Six liquid injectors are spaced in streamwise direction for the variation of the film length. Each injector of the 450-mm-long and 80-mm-wide stainless steel plate consists of a row of small holes of 0.5 mm. On the symmetry line the detector of a newly designed liquid film analyzer [5] is mounted flush with the plate's surface, in order to determine the characteristics of the liquid film and particularly the spectrum of the wave frequencies. By special design of the upper wall, gap heights from 30 mm to 1.1 mm can be achieved.

An alternate test section (Fig. 4) was developed mainly for the photography and the size distribution measurements of the droplets formed after the film's disintegration. The atomizing edge is located at the same streamwise coordinate as the liquid film analyzer (Fig. 3).

Both walls of the lower gap have profiled leading edges. The gap height can be finely adjusted. The length of the air gaps of both test sections is sufficient to ensure fully developed flow conditions near the atomizing edge and the liquid film analyzer, respectively, if the gap height does not exceed 8 mm.

Figure 5 illustrates the whole experimental setup including the test section. The atomizing air supplied by a compressor is divided into two branches and fed to a double-chamber settling tank. A nozzle of high contraction ratio leads to the test section. The flow rate in both gaps of the test section is in-

Nomenclature

b = liquid film width, m
D = droplet diameter, m
$D_{15.9}$, D_{50}, $D_{84.1}$ = characteristic diameters; indices indicating volume percent which have smaller diameter than D, m
D_s = Sauter mean diameter = $\Sigma D^3/\Sigma D^2$, m
f = frequency, Hz
h = height, m
l = film length within nozzle, m
SC = liquid concentration
u = velocity (x direction), m/s
$\dot{V}$ = volumetric flow rate, m^3/s
x_z = distance between atomizing edge and probe volume (Fig. 4), m
y_z = distance between symmetry plane and probe volume (Fig. 4), m
α = spray angle, deg
μ = viscosity, Ns/m^2
σ = surface tension, N/m

Subscripts

dr = droplet
G = gap
int = integral averaged value
L = liquid
l = lower, without liquid film
u = upper, with liquid film

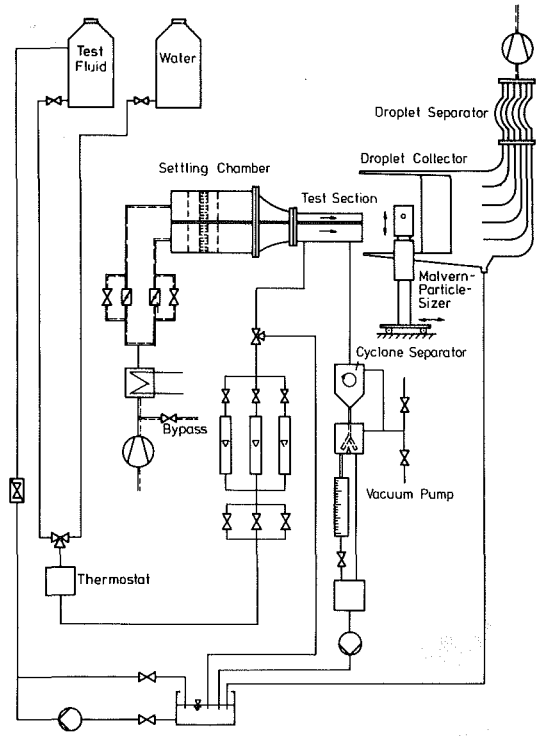

Fig. 5 Experimental setup

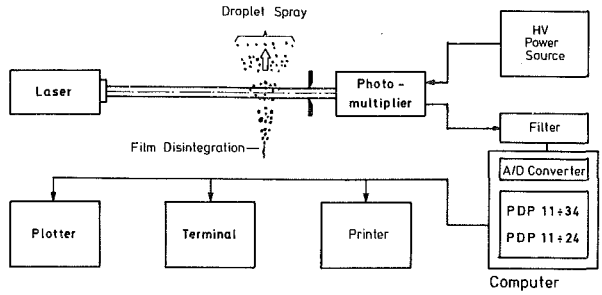

Fig. 6 Technique for measuring the periodicity of the liquid separation

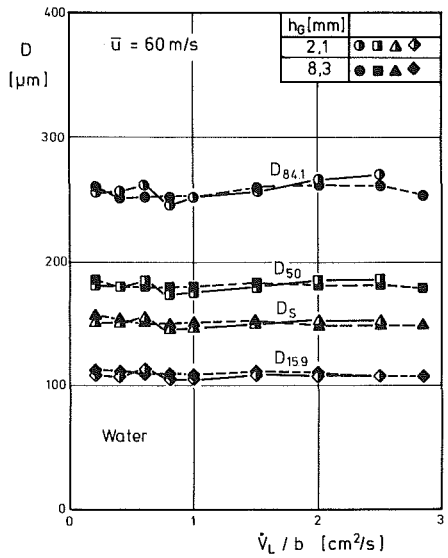

Fig. 7 Effect of gap height and liquid flow rate on droplet size distribution

dividually controlled. After åtomization, the droplets are collected and separated from the atomizing air.

The liquid from the feeding tank passes through a thermostat, a valve, and a flow meter before injection onto the film plate. After sampling of the separated droplets at the bottom of the collector, the liquid is pumped back to the feeding tank to close the loop. If the film suction at the end of the test section (Fig. 3) is employed, the liquid flow rate is determined by means of a buret.

Optical Diagnostics

Droplet Size Distribution. The droplet size distributions were obtained with the well-known Malvern particle sizer, a nonintrusive, light-scattering technique [6]. In using $D_{15,9}$, D_{50}, and $D_{84,1}$ besides the Sauter mean diameter, as previously proposed [7], the drop size distribution is characterized. The major goal of the drop size measurements presented is the characterization of the nozzle performance as a function of the parameters (see Fig. 2) by means of one size distribution. Measurements with the probe volume (laser beam) normal to the film plate (Fig. 4) accomplish this task. This technique, subsequently called "integral measurement," detects all droplets irrespective of the individual angle between film plate and droplet trajectory. Additional measurements with the probe volume parallel to the film plate ("local measurements") show the local drop size distribution and liquid concentration if the flow field behind the nozzle is assumed to be two dimensional.

Photographic Diagnostics. The motion of the liquid during the film disintegration and the structure of the film ligaments were recorded by means of a short-duration photographic technique and a high-speed camera (8000 frames per second, 12.5 ms exposure time).

Periodicity of the Film Disintegration. The high-speed films reveal the film disintegration as a periodic process. In order to determine the main frequencies of the liquid separation, an optical measurement technique was developed (Fig. 6). The light of a laser beam passes through the spray normal to the film plate. After suppression of the scattered light by means of an aperture, the light intensity of the central beam is recorded by a photomultiplier. Liquid concentration fluctuations result in periodic light intensity fluctuations, which can be analyzed by Fourier transformation after band-pass filtering.

Film Disintegration and Droplet Formation at the Atomizing Edge

In contrast to earlier investigations using empirically optimized nozzles, the number of relevant parameters for the plane nozzle model is relatively small. This is of importance as the coupled effects of these parameters on the nozzle performance will be clearer. We were able to separate the effects of the flow within the nozzle from the processes taking place during the film disintegration. Consequently, it is possible to clearly sumarize the measurements and to illustrate the dominant effects.

Figure 7 shows two series of measurements at different gap heights. In order to compensate for effects of the liquid film on the air flow, the upstream pressure of the air was adjusted such that in each air gap the individual average volumetric air velocities based on the gap height without film are kept constant. The characteristic diameters of the droplet size distribution, therefore, are independent of the liquid flow rate. Moreover, it is shown in Fig. 7 that the droplet sizes are almost constant for gap heights of 2.1 mm and 8.3 mm, respectively. The same result was also obtained for test cases with other gap heights (4.3 mm and 1.1 mm). A change in the air velocity would result in a change of the characteristic diameters. The droplet size distribution, however, remains independent of both the gap height and the liquid flow rate, and a simple rela-

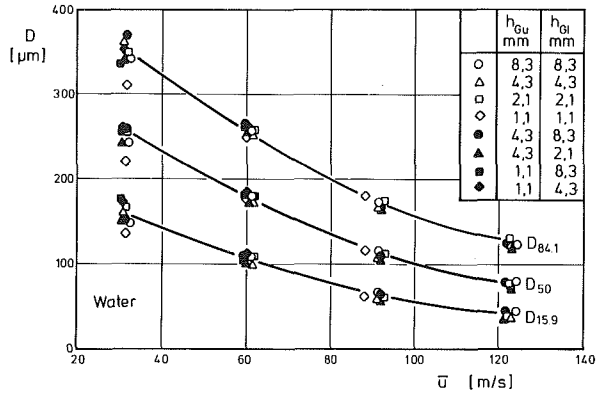

Fig. 8 Influence of gap height and air velocity on drop size distribution

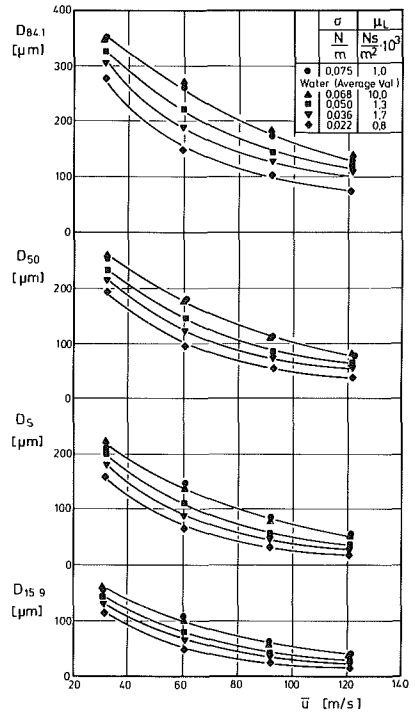

Fig. 9 Effect of liquid viscosity and surface tension on the droplet size distribution

tion between the air velocity and the characteristic droplet diameters for water films as shown in Fig. 8 is obtained.

Each point in Fig. 8 represents the average of five to eight measurements at different liquid flow rates. All characteristic diameters of the droplet size distribution decrease with an increase of the air velocity. As expected, the results obtained with different gap heights for the top and the bottom gap coincide with those of equal heights.

The viscosity of the liquid and the surface tension are well-known parameters affecting the film disintegration. In order to assess their effect on the droplet formation, integral measurements were conducted with different viscosities and surface tensions. If the effect of the liquid film on the internal flow is compensated as previously described, it is found that the droplet formation again is independent of both the liquid flow rate and the gap height. In this case, the results can be represented in a simple relationship as shown in Fig. 9.

Here, each point represents the average of several measurements with different gap heights and liquid flow rates. For comparison, a summary of the results for water films is also plotted in Fig. 9. The water–glycerine mixture used here has approximately the same surface tension as water but its

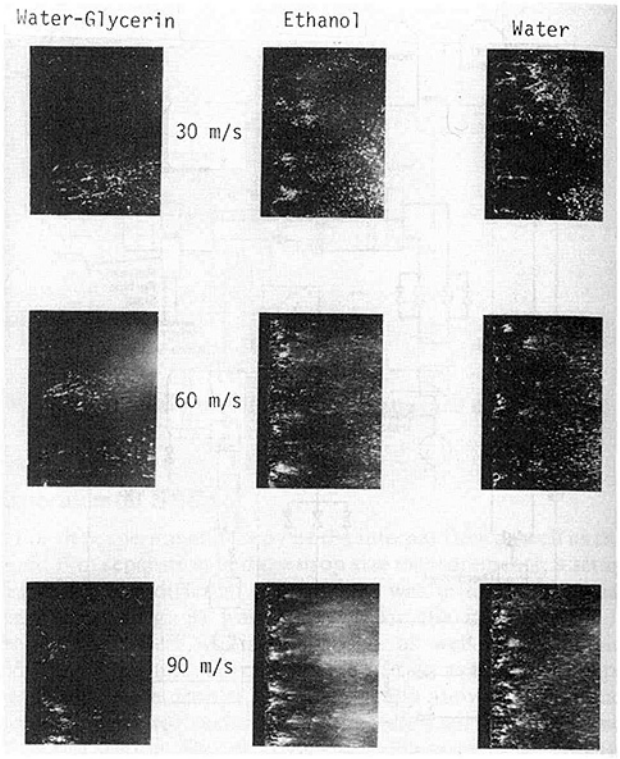

Fig 10 Effect of liquid viscosity and surface tension on film disintegration

viscosity is one order of magnitude higher. Despite the high viscosity, the measured droplet size distributions are found to be close to those obtained for water. On the other hand, the atomization characteristics were drastically improved if a water–ethanol mixture was used, which possesses a surface tension comparable to that of normal fuels. At low air velocities the mass median diameter D_{50} for pure ethanol is about 25 percent and at high air velocities it can be even 50 percent less than that of water. The ratio $D_{15.9}/D_{50}$ ranges between 0.5 and 0.6, whereas the ratio $D_{84.1}/D_{50}$ fluctuates between 1.4 and 1.8. In contrast to frequently cited results [2], a significant influence of the liquid viscosity on the droplet size distribution was mainly observed as an indirect effect: Obviously, as will be shown later, the viscosity determines the drag within the film-carrying gap, thus inducing under certain conditions an inequality of the velocities in the two gaps. Furthermore, the total flow rate of the atomizing air may be insufficient for atomizing the viscous liquid.

In conclusion, it is observed that the parameters affecting the droplet size distribution are the air velocity in each of the air gaps and the surface tension. If these parameters are kept constant, there is no effect of the gap height, the liquid flow rate, and the liquid viscosity on the results, if the whole spray is considered (integral measurement technique). The resulting droplet size distribution is obtained from Fig. 9.

In an attempt to understand the rather simple relationships, a thorough analysis of the process of film disintegration is a necessity. In comparing short-duration photographs, Fig. 10 illustrates the effects of the viscosity and the surface tension on the disintegration processes of the film. Principally, three cases are shown. The disintegration of a water film (high surface tension, low viscosity) is compared with that of an ethanol film (low surface tension, low viscosity) and of a water–glycerine film (high surface tension, high viscosity). The photographs show a part of the atomization edge of 30 mm length. It is clear that the liquid film separates neither continuously nor uniformly, but rather it leaves the nozzle at particular locations varying with time. The separation process

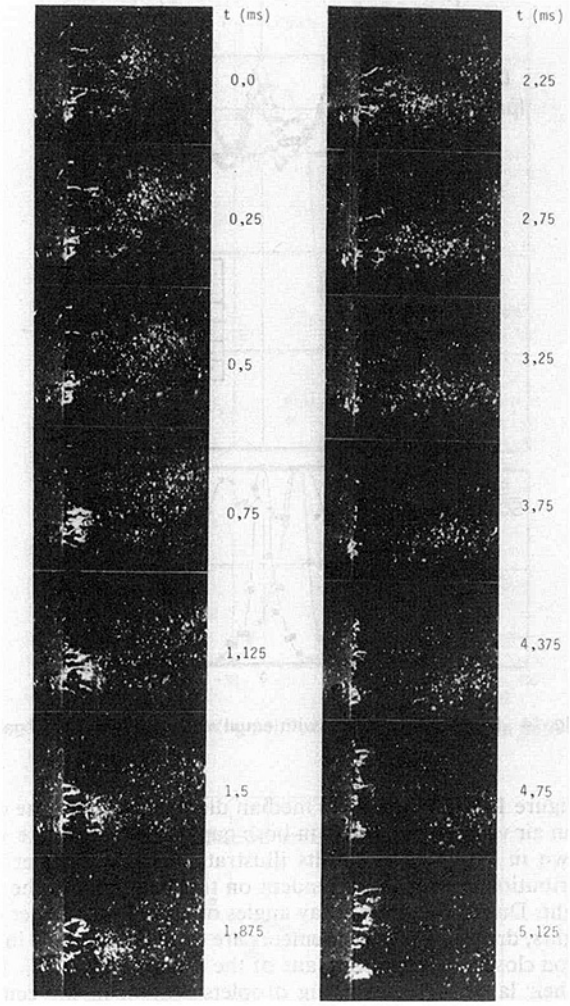

Fig. 11 Film disintegration, top view (Fig. 4), water, u = 30 m/s

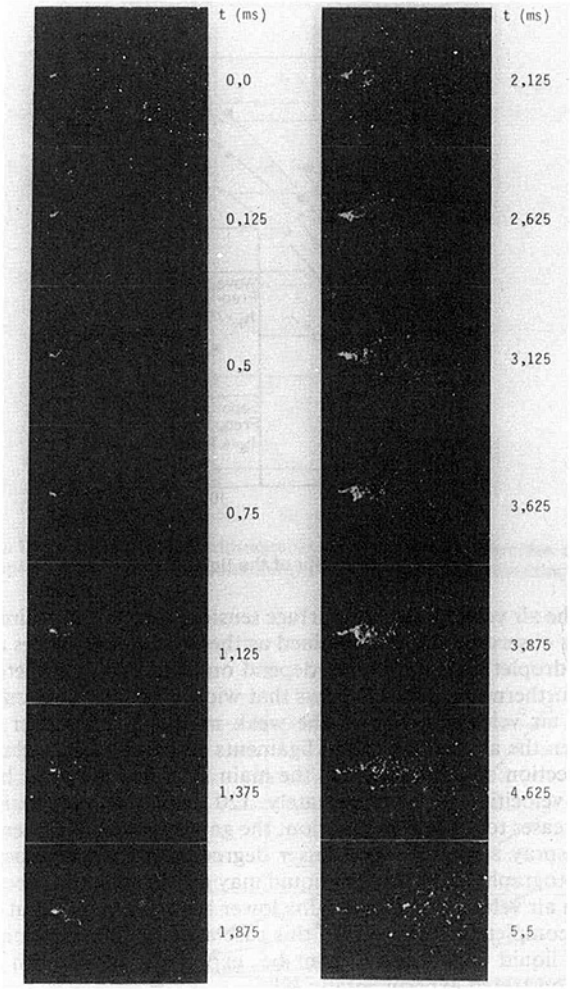

Fig. 12 Film disintegration, side view (Fig. 4), water, u = 30 m/s

becomes more uniform with increasing air velocity or with reduced viscosity and surface tension. The disintegration of the liquid film takes place always close to the atomizing edge, regardless of the liquid's properties. Small liquid ligaments are formed in the main flow direction while string-like structures are observed only at very high viscosities and low air velocities. The droplet formation process follows without any characteristic intermediate stage. As an example, the disintegration of a water film at an air velocity of 60 m/s is almost similar to that of ethanol at 30 m/s. As a consequence, nearly the same droplet size distribution is obtained. Furthermore, an increase in the viscosity affects the disintegration process but has little influence on the resulting droplet size distribution.

The photographs reveal a time-dependent droplet concentration downstream of the nozzle. In order to investigage these intermittent processes, high-speed films were recorded. Thus, a good impression of the dynamics of the film disintegration was obtained. Figure 11 shows a typical example of a film disintegration through a series of photographs taken over a period of approximately 5 msec.

The photographs show clearly that the disintegration possesses a periodic component at all air velocities investigated. However, the frequency of separation increases sharply with air velocity. Generally, several film waves move toward the atomizing edge before the liquid is separated at a certain location and carried away by the air. Directly before arriving at the edge, liquid accumulates periodically. This observation leads to the important conclusion that the original film thickness is not to be considered a relevant parameter for the atomization process. Immediately following the "collection" process the separation of the liquid begins over a large portion of the atomization edge and a zone of high droplet concentration moving downstream is formed. At high liquid viscosity, the air is unable to atomize the liquid immediately after separation due to the high damping capacity. Ligaments, therefore, are formed which can be observed.

High-speed films showing a side view of the atomization process give important information about the liquid motion during the film disintegration. Figure 12 shows a typical example at low air velocities. Immediately after separating from the atomizing edge, the liquid is forced to move with a strong component normal to the main flow direction of the air. Subsequently, the liquid is deflected in the opposite direction by the aerodynamic forces. The atomization of the liquid begins simultaneously. During a second deflection, the liquid is completely atomized. No preferred direction of the first motion normal to the main air flow was detected. The disintegration process of the ligament is observed as a vortexlike motion. Its direction of rotation is reversed periodically in streamwise direction by interaction with the air flow. At high air velocities the atomization mechanism seems to be similar to that at low velocities, but the liquid disintegration takes place in a very small zone near the atomizing edge.

The questions concerning the governing mechanisms are complex. However, the observation that the atomization mainly takes place during the deflection indicates a major importance of the momentum transfer, which reaches its maximum at that instant. With this assumption, the dominant role

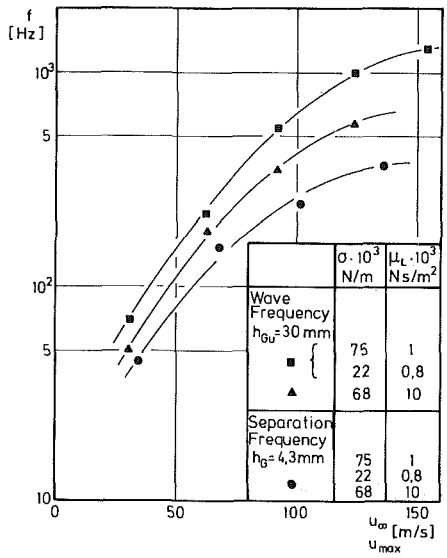

Fig. 13 Periodicity of the liquid separation

of the air velocity and the surface tension, which is experimentally observed, can be explained as the momentum forces and the droplet stability mainly depend on these two parameters.

Furthermore, Fig. 12 shows that wide spray angles occur at low air velocities, due to the weak momentum transfer between the air and the liquid ligaments which causes a delayed deflection of the liquid into the main flow direction. At high air velocities of approximately 120 m/s the spray angle decreases to 15 deg. In addition, the gap height also influences the spray angle, but to a lesser degree than the air velocity. Photographs show that the liquid may get through the sheet of high air velocitiy at gap heights lower than 1 mm without being completely atomized. In this case a rapid deterioration of the liquid atomization can be expected, which can be demonstrated experimentally [8].

In addition, the optical measuring technique applied to determine the periodicity of the film disintegration shows the air velocity to be the only main parameter affecting the liquid separation process (Fig. 13). An effect of other parameters such as the flow rate, the liquid viscosity, the gap height, and the surface tension on the separation frequency was hardly detected. At low air velocities the liquid film analysis [5] showed that the preferred frequency is somewhat lower than the main wave frequency. The latter is additionally affected by the liquid viscosity. At high air velocities, however, a large difference between the two frequencies was observed. This should be expected if it is realized that more than one wave (up to three) transport the liquid to the atomization edge before the separation occurs. This is shown in the high-speed films.

In conclusion it should be noted that the atomization process with prefilming airblast nozzle is completely different from that with other atomizers [9, 10]. The results of the previously mentioned integral measurements show that in the case of equal air velocities in both gaps the viscosity of the liquid, its flow rate, and the gap height do not substantially affect the resulting droplet size spectra. On the other hand, photographs reveal clearly that the spray angle is dependent on the air gap height. In other words, there is some additional effects which need further attention and which cannot be detected by the integral measurement technique.

More detailed information on the resulting droplet spectra were obtained from the optical droplet sizing with the probe volume adjusted parallel to the atomizing edge. During the traverse of the laser beam (Fig. 4) through the spray with the probe volume at a fixed distance of 100 mm from the exit of the test section, the operating conditions of the nozzle were kept constant.

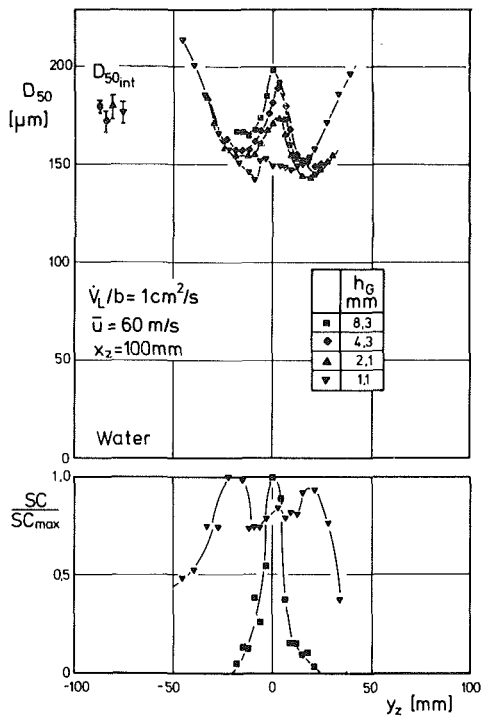

Fig. 14 Local droplet sizing with equal air velocities in both gaps

Figure 14 shows the mass median diameter D_{50} for the case of an air velocity of 60 m/s in both gaps. The coordinate y_z is shown in Fig. 4. The results illustrate that the droplet size distribution is strongly dependent on the location and the gap height. Due to the small spray angles observed with larger gap heights, droplet size measurements are of relevance only in the region close to the central plane of the atomizer ($y_z = 0$). Due to their large inertia, the big droplets remain in the central region of the spray. At the same time, the smaller droplets are laterally diffused as a consequence of the air/liquid interaction. Another mechanism dominates at small gap heights. In this case, the spray angle is enlarged and the droplets diffuse over a wider range from the atomization edge as previously shown (Fig. 12). Consequently, the droplet concentration assumes large values over a wide range so that in some cases even two maxima are observed off the axis, as the lower part of Fig. 14 shows. If the gap height is small enough, the strong lateral motion observed during the film disintegration is responsible for liquid ligaments leaving the region of high air velocity during the atomization process. Large droplets, therefore, will exit at larger values of y_z. For this reason the largest droplets were detected in the outer region of the spray in the case of the minimum gap height investigated (1.1 mm). These effects become less significant with increasing air velocity, as the droplets move only within a small range near the central plane.

To illustrate the effect of the inequality of the air velocities in both gaps on the local droplet size distribution, two series of measurements were conducted as shown in Fig 15. First, the air velocity in the film-containing gap was held higher than that in the other. Subsequently, the condition was reversed. The fact that different values for the droplet sizes were obtained with the integral measuring technique ($D_{50_{int}}$) initially may be surprising. As the local measurements also show, the atomization quality is generally better with lower air velocity in the film-containing gap. These results can be understood, if the ratio of the shear stress at the upper surface of the film in the film-containing gap and that at the lower film surface in the other gap directly after film separation is considered. A fact generally observed with wavy liquid film flows is an in-

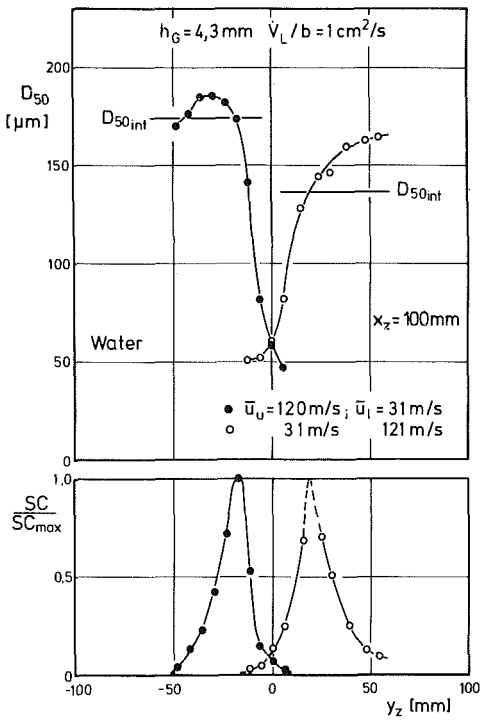

Fig. 15 Local droplet sizing with unequal air velocities in both gaps

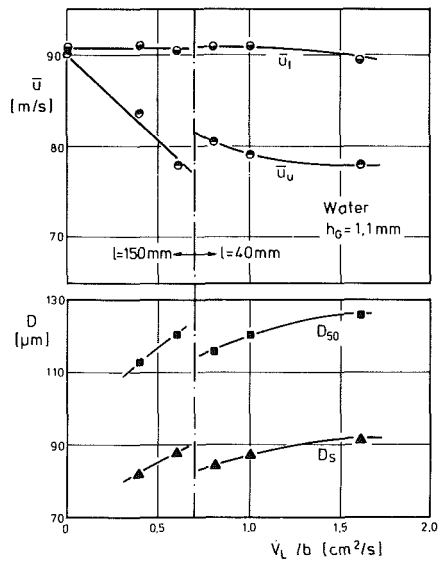

Fig. 16 Influence of liquid flow rate and liquid film length on the droplet size distribution (constant pressure drop of the air)

crease of the average shear stress at the film surface due to roughness effects of the wavy liquid-film interface [11]. In a first case with the higher air velocity in the film-containing gap both shear stresses are extremely unequal. On the other hand, the roughness effect of the film partly compensates the inequality if the higher velocity is in the gap without film. For this reason the deteriorating liquid shows a stronger deflection toward the side of the lower velocity in the first case as photographs clearly indicate. Consequently, a smaller portion of liquid is atomizied by the high-velocity air and a coarser spray is obtained.

Up to now, the air velocities in both gaps were held at a predetermined value during the measurements despite varying other parameters (Fig. 2). However, in most applications of prefilming airblast nozzles such as the fuel atomization in gas

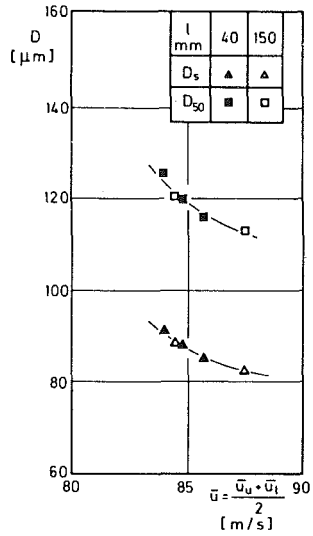

Fig. 17 Influence of the arithmetic mean of the two air velocities on the droplet size distribution (constant pressure drop of the atomizing air)

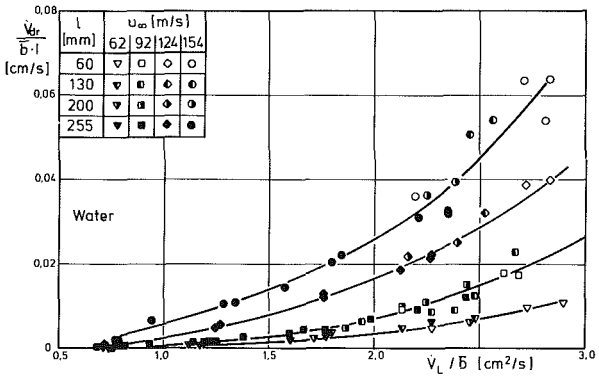

Fig. 18 Flow rate of the droplets formed within the nozzle

turbine combustors, the pressure drop of the atomizing air is dependent on the operating conditions. The air flow rate and particularly the air velocity at the atomizing edge, therefore, depend on the nozzle geometry and the air–liquid interaction within the atomizer.

Figure 16 shows a series of measurements with the pressure drop of the atomizing air kept constant as usual. The volumetric mean velocity in the film containing gap remarkably decreases if the liquid flow rate is increased. Consequently, the atomization quality deteriorates. This effect is directly caused by the liquid film since displacement and roughness effects become more relevant with increasing liquid flow rate. For this reason, the increase of the droplet size also depends on the film length within the nozzle, as depicted in Fig. 16 for two film lengths of 40 mm and 150 mm, respectively. If the resulting droplet sizes shown in Fig. 16 are plotted versus the arithmetic mean value of the volumetric averaged air velocities, a simple relationship again is obtained (Fig. 17). Parameters such as the liquid flow rate, the gap height, or the liquid film length only affect the droplet size distribution in changing the flow conditions at the atomizing edge. Besides the surface tension, the arithmetic mean value of both air velocities was found to be the only parameter acting on the drop formation directly. A comparison of Fig. 17 with Fig. 8 or Fig. 9 points out that the resulting droplet size distribution is similar to that at equal velocities in both gaps if the air velocity in Fig. 8 and Fig. 9 is substituted by the arithemtic mean value. With this assumption, the simple relationships for equal velocities previously described remain valid in the more realistic case of an equal pressure drop along the two air gaps.

Here, the air velocities at the atomizing edge are calculated considering the effects of air-gap geometry, the liquid-film length, and its flow rate as well as the viscosity. A special procedure has been developed and tested which also accounts for the liquid-film motion and the air/liquid-film interaction [4].

Atomization and Drop Formation Within the Nozzle

As reported earlier [11] an upper limitation for the stable regime of the wavy film flow has been observed, which depends on the mean shear stress along the film's surface. An increase of the liquid flow rate beyond its critical value results in the formation of "roll" waves with high propagation velocities. At the same time, portions of liquid are atomized after separation from the film surface. Consequently, a second atomizing mechanism may occur in prefilming airblast nozzles besides the film separation at the atomizing edge.

For the determination of the fraction of liquid which is atomized before the film reaches the end of the nozzle, the test section depicted in Fig. 3 was utilized. In order to prevent the droplets from depositing on the opposite wall the largest gap height of 30 mm was applied. The difference between the injected liquid flow rate and that sucked from the film plate at the end of the test section (Fig. 3) was determined. Consequently, an integral value of droplet formation along the whole film length was obtained. During the measurements the film length has been changed in using liquid film injectors located at various streamwise coordinates.

The measurements indicate (Fig. 18) that the droplet production within the nozzle is strongly amplified with increasing both the air velocity and the injected liquid flow rate. Additionally the volume fraction was found to be proportional to the actual liquid film length. For this reason, all results can be summarized in dividing the droplet flow rate by the liquid film length as shown in Fig. 18. In the case of a short distance between the liquid film injector and the atomizing edge as found for airblast nozzles, the fraction of water atomized before the film reaches the exit of the nozzle does not exceed approximately 5 percent under all operating conditions. Consequently, as an important result of the investigations it might be asserted that the droplet spectrum mainly depends on the liquid film deterioration at the atomizing edge even in the case of very high liquid flow rates and unstable liquid film flow. Furthermore, it was shown that the size distributions obtained generally agree with those of the droplets formed after the film disintegration at the atomizing edge.

Acknowledgments

Thanks are due to the working group of the "Forschungsvereinigung Verbrennungskraftmaschinen" (FVV) for their discussions and financial support. Continuing assistance is obtained from the German Science Foundation (DFG) through the "Sonderforschungsbereich 167."

References

1 Lefebvre, A. H., and Miller, D., "The Development of an Air Blast Atomizer for Gas Turbine Application," College of Aeronautics, Cranfield, Report Aero No. 193, 1966.

2 Lefebvre, A. H., "Air Blast Atomization," *Prog. Energy Combust. Sci.*, Vol. 6, 1980, pp. 233–261.

3 Wittig, S., Leuckel, W., Sakbani, K., Aigner, M., Horvay, M., and Sattelmayer, Th., "Experimentelle und theoretische Untersuchung der Strömung und Tropfenbildungsmechanismen in Zerstäubungsdüsen für Gasturbinenbrenn-kammern," *Forschungsvereinigung Verbrennungskraftmaschinen, Abschlussbericht*, Paper No. 347, 1984.

4 Sattelmayer, Th., "Zum Einfluss der ausgebildeten, turbulenten Luft-Flüssigkeitsfilm-Strömung auf den Filmzerfall und die Tropfenbildung am Austritt von Spalten geringer Höhe," Dissertation, Universität Karlsruhe, 1985.

5 Sill, K. H., "Experimentelle Bestimmung der Grenzflächenstuktur und der mittleren Filmdicke von strömenden Flüssigkeitsfilmen mit Hilfe einer Lichtabsorptionsmethode," *Forschung in der Kraftwerkstechnik*, Sammelband der VGB-Tagung, Essen, 1980, pp. 232–238.

6 Swithenbank, J., Beer, J. M., Taylor, D. S., Abbot, D., and McGreath, C. G., "A Laser Diagnostic Technique for the Measurement of Particle Size Distribution," *AIAA Prog. in Astron. and Aeron.*, Vol. 5, 1977.

7 Wittig, S., Aigner, M., Sakbani, K., and Sattelmayer, Th., "Optical Measurements of Droplet Size Distribution. Spacial Considerations in the Parameter Definition for Fuel Atomizers," AGARD, *62nd PEP-Symposium on Combustion Problems in Turbine Engines*, Turkey, Conference Proceedings No. 353, 1983.

8 Aigner, M., and Wittig, S., "Performance and Optimization of an Airblast Nozzle: Drop Size Distribution and Volumetric Air Flow," *Proceedings of the International Conference on Liquid Atomization and Spray Systems*, London, 1985.

9 Elkotb, M. M., "Fuel Atomization for Spray Modelling," *Prog. Energy Combust. Sci.*, Vol. 8, 1982, pp. 61–91.

10 Fritzsche, A., "Über den Zusammenhang von Strahlzerfall und turbulentem Stoffaustausch, untersucht am Beispeil des runden Strahles," *Forschungsberichte*, VDI-Z, Vol. 7, No. 2, 1965.

11 Wurz, D., "Experimentelle Untersuchung des Strömungsverhaltens dünner Wasserfilme und deren Rüchwirkung auf einen gleichgerichteten Luftstrom mässiger bis hoher Unterschallgeschwindigkeit," Dissertation, Universität Karlsruhe, 1971.

Y. H. Zhao

W. M. Li

J. S. Chin
Mem. ASME

Beijing Institute of Aeronautics
and Astronautics,
Beijing, People's Republic of China

Experimental and Analytical Investigation on the Variation of Spray Characteristics Along Radial Distance Downstream of a Pressure Swirl Atomizer

The variation of spray characteristics (Sauter Mean Diameter and Rosin-Rammler drop-size distribution parameter) downstream of a pressure swirl atomizer along radial distance has been measured by laser light scattering technology. An analytical model has been developed that is capable of predicting the variation of spray characteristics along radial distance. A comparison between the prediction and experimental data shows excellent agreement. It shows that the spray model proposed, although relatively simple, is correct and can be used with some expansion and modification to predict more complicated spray systems.

Introduction

Owing to the fast development of combustion technology, the spray characteristics produced by an atomizer in a liquid-fueled combustion device are extremely important for the performance, stability, and pollutant formation of the combustor. The spray characteristics should be measured accurately. It is also desirable to construct models to predict the variation of spray characteristics, droplet trajectory, spray dispersion, evaporation history, etc., in order to further understand the influence of various factors on the measurement of spray characteristics. The comparison between the spray characteristic measurements and the predictions will provide useful insight into spray combustion. Such research has significance to engineering applications, and on the fundamental understanding of spray combustion.

The authors analyzed the variation of spray characteristics along axial distance downstream of a pressure swirl atomizer. The effect of spray evaporation on the variation of spray characteristics was shown in [1, 2]. The influence of downstream distance on the spray characteristics of pressure swirl atomizers caused by the effect of spray dispersion and the effect of drop acceleration or deceleration has been analyzed in [3]. These analyses have been partially proven by some experimental data. Up to now there are few experimental data of the spray characteristic variation along radial distance downstram of a pressure-swirl atomizer. Dodge and Moses published the measurement results shown in Fig. 1 [4]. They show that both SMD and drop-size distribution parameter in-

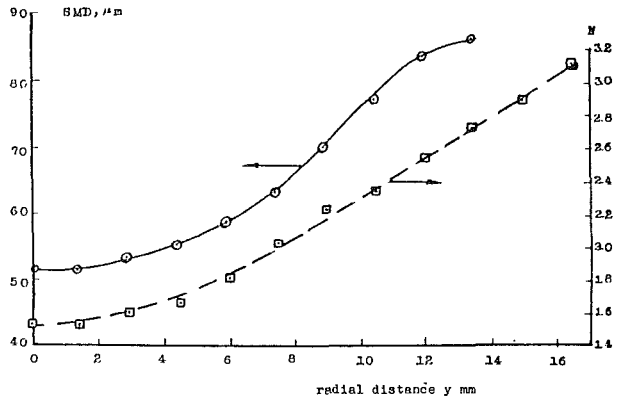

Fig. 1(*a*) Dodge's measurement results: $x = 25.4$ mm [4]; atomizer pressure drop $\Delta p = 100$ lb/in.^{2}

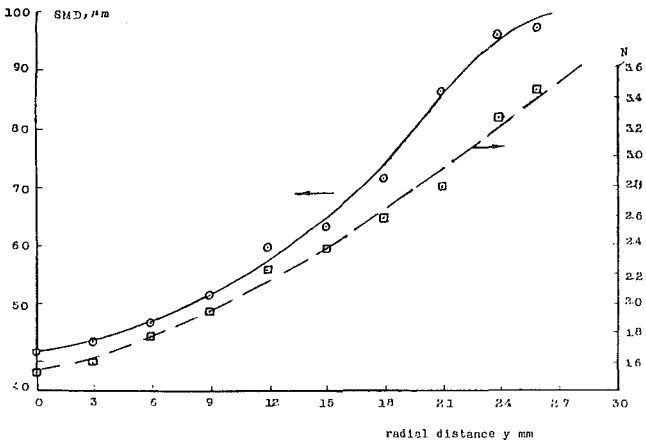

Fig. 1(*b*) Dodge's measurement results: $x = 50.8$ mm [4]; atomizer pressure drop $\Delta p = 100$ lb/in.^{2}

Contributed by the Gas Turbine Division of THE AMERICAN SOCIETY OF MECHANICAL ENGINEERS and presented at the 31st International Gas Turbine Conference and Exhibit, Dusseldorf, Federal Republic of Germany, June 8–12, 1986. Manuscript received at ASME Headquarters January 10, 1986. Paper No. 86-GT-51.

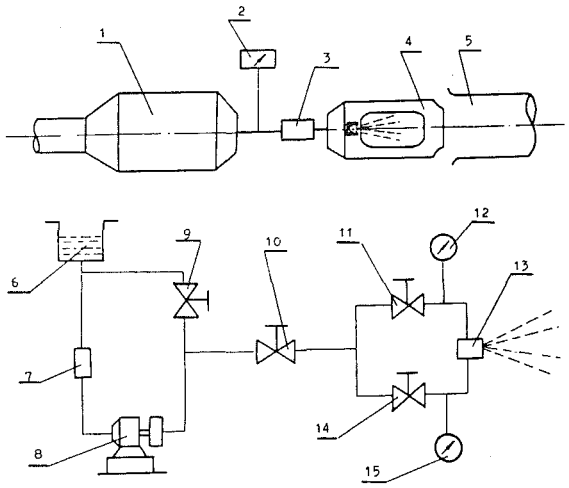

Fig. 2 Experimental system: (1) plenum chamber; (2) air temperature; (3) air flow meter; (4) test section; (5) exhaust pipe; (6) fuel tank; (7) filter; (8) pump; (9) return valve; (10) valve; (11) pilot fuel flow valve; (12) pressure gage; (13) atomizer; (14) main fuel flow valve; (15) pressure gage

crease with radial distance. There is, however, no analysis on this aspect available now. It is an interesting research topic to carefully measure the spray characteristic variation along radial distance in a well-defined experimental condition and to develop an analytical model to predict the variation and to make a comparison between the experimental data and prediction. These comparisons will promote our understanding of spray dispersion and of the factors influencing drop-size measurement. After we have been able to predict the simple spray system, we will be able to expand and modify the proposed spray model to extend its ability for more complicated sprays.

The authors proposed a flat fan spray model for the fuel distribution downstream of a plain orifice injector under cross air flow [5]. The model was validated by fuel distribution measured by gas analysis and by drop-size measurement. It is obvious that for the validation of a given spray model, the spray characteristic measurement is reliable, accurate, and much simpler than the fuel distribution measurement. In this paper it is also the authors' intention to validate a spray model by the spray characteristic measurement along radial distance. The same spray model has also been validated by the spray characteristic measurement along different angles θ (as shown in Fig. 5), which will be reported in another paper.

Test Apparatus, Atomizer, and Particle Sizer

The test section is a rectangular chamber with transparent windows for optical drop-size measurement. The test apparatus includes an air system and a fuel system, as shown in Fig. 2.

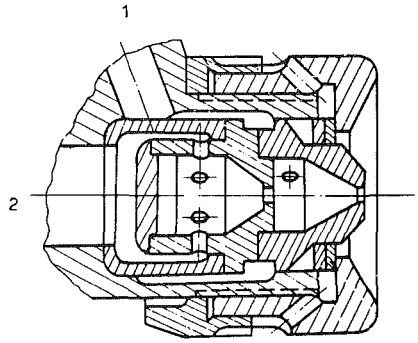

Fig. 3 Atomizer: (1) pilot fuel flow; (2) main fuel flow

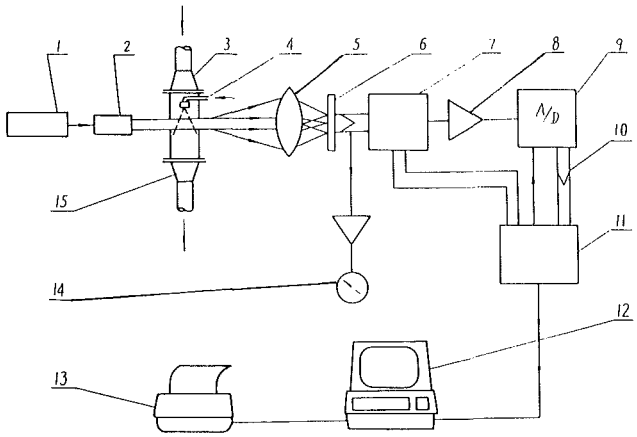

Fig. 4 Laser drop particle sizer: (1) laser; (2) beam expander; (3) test section; (4) fuel nozzle; (5) lens; (6) photo detector; (7) solid valve; (8) amplifier; (9) A/D converter; (10) data transfer; (11) interface; (12) computer; (13) printer; (14) micro tune

The atomizer tested is shown in Fig. 3, which is a pressure swirl atomizer taken from an existing aero gas turbine engine. The atomizer has a pilot fuel flow and a main fuel. In this test we used the pilot fuel passage. Since with pilot fuel flow the flow rate is relatively lower, the obscuration is in the right range.

The Malvern drop-size analyzer model 2200 is used. This Malvern instrument is based on light-scattering technology. The instrument was calibrated against a reticule designed by Prof. Hirleman of ASU. It was also calibrated by a standard particle model prepared by our own lab. The calibration showed that the measurement of Malvern is reliable. The schematic diagram of the particle sizer is shown in Fig. 4. The instrument was set on Rosin–Rammler distribution mode. The direct results from the instrument are the characteristic diameter $\bar{D}$ and drop-size distribution parameter N in the R–R distribution which is expressed by

Nomenclature

C_D = droplet drag coefficient
D = diameter of droplet
$\bar{D}$ = characteristic droplet, at which $Q = 0.632$
D_{max} = maximum diameter of the whole spray
D_{min} = minimum diameter which laser light beam will meet
dj = diameter of laser light beam
N = Rosin–Rammler drop-size distribution parameter
Δp_1 = pressure drop across the nozzle
Q = fraction of total volume contained in drops of diameter less than D
R = radius
Re = Reynolds number
SMD = Sauter Mean Diameter
t = time
V = velocity
w = relative velocity between droplet and air flow
x, y = coordinates
μ = viscosity, flow coefficient
ρ = density
φ = angle shown in Fig. 5

Subscripts

a = air
l = liquid
0 = initial
R = radial
X = axial

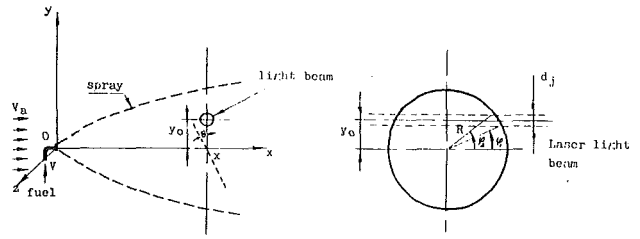

Fig. 5 Physical model

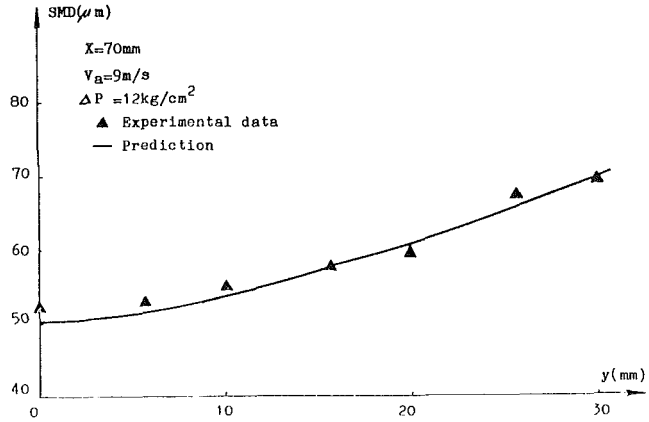

Fig. 6 Variation of SMD along radial distance: experimental data and prediction

$$Q = 1 - \exp\left[-\left(\frac{D}{\bar{D}}\right)^N\right] \tag{1}$$

where Q is the fraction of total volume contained in drops of diameter less than D.

The Sauter Mean Diameter SMD can be obtained as

$$\text{SMD} = \bar{D} \cdot \left[\Gamma\left(1 - \frac{1}{N}\right)\right]^{-1} \tag{2}$$

where Γ is the gamma function.

Experimental Results

During drop-size measurement tests, the laser light beam was first adjusted to pass perpendicularly through the central axis of the atomizer at a given distance downstream from its face. At this position the spray characteristics were measured. This was defined as $y = 0$ position (Fig. 5). Then the Malvern particle sizer was put on some blocks of known dimension, and thus the height of the laser beam was changed, so the radial distance where the particle sizer measured the drop size was changed. The summation of the size blocks was defined as the radial distance y. The dimensions of size blocks chosen are 2.5 mm, 3.0 mm, and 10 mm. Thus the following radial distance y value can be obtained by different combinations of the size blocks: $y = 0$, 5.5, 10.0, 15.5, 20.0, 25.5, and 30.0 mm. The experimental results are shown in Figs. 6–13. From these figures it is clear that the Sauter Mean Diameter and drop-size distribution parameter increase with radial distance until the edge of the spray has been reached. The experimental results obtained by present authors are qualitatively in good agreement with the results of Dodge and Moses. The explanation of the measured results shown in Figs. 6–13 is obvious: that with increasing radial distance the possibility for the laser light beam to meet large drops is higher than that with smaller radial distance. This shows that when we measure the drop size, it is necessary to take a good sample which is representative of the spray formed.

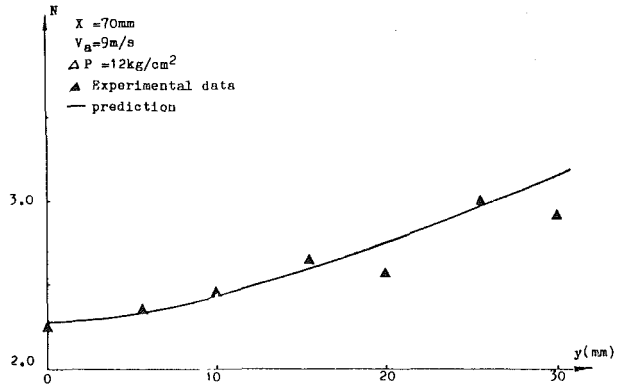

Fig. 7 Variation of N along radial distance: experimental data and prediction

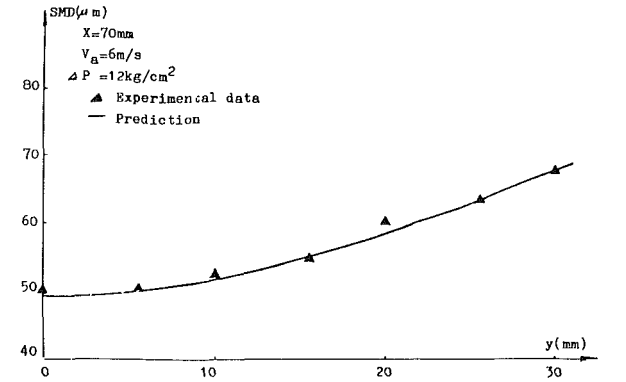

Fig. 8 Variation of SMD along radial distance: experimental data and prediction

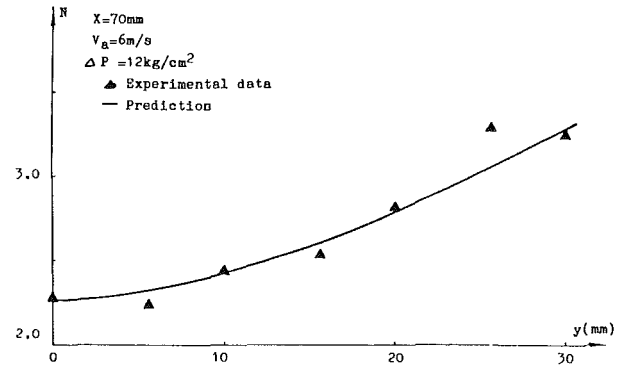

Fig. 9 Variation of N along radial distance: experimental data and prediction

From the comparison of Fig. 6 with Fig. 8 and Fig. 7 with Fig. 9, it can be seen that at higher air flow velocity, the change of spray characteristics along radial distance is weaker. From the comparison of Figs. 8 and 10 with Fig. 12, and Figs. 9 and 11 with Fig. 13, it is shown that with lower pressure drop across the nozzle, the change of spray characteristics along radial distance is weaker. These results tell us that when the spray is expanded less radially, the change of spray characteristics is also flatter. The converse is also true. The experimental data obtained in this way are used to check the proposed spray model.

Physical Model

The spray formed by a pressure-swirl atomizer is shown in Fig. 5. The physical model is proposed with the following assumptions:

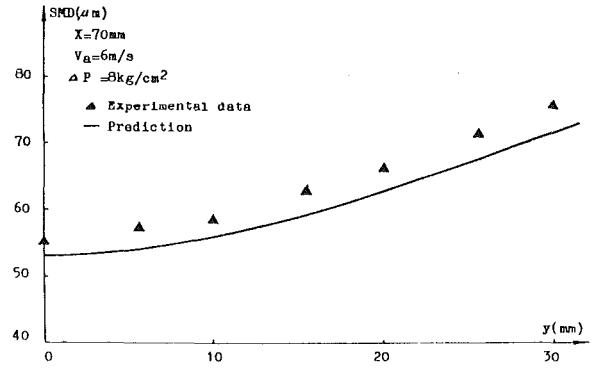

Fig. 10 Variation of SMD along radial distance: experimental data and prediction

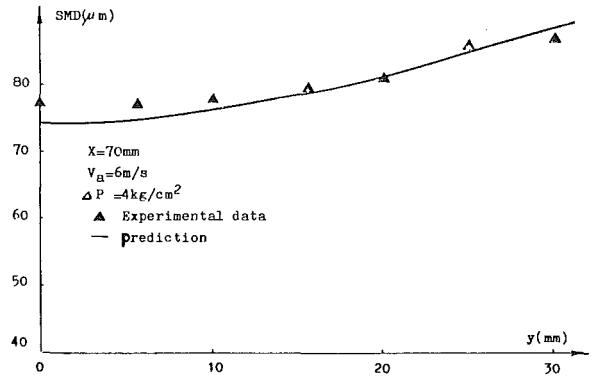

Fig. 12 Variation of SMD along radial distance: experimental data and prediction

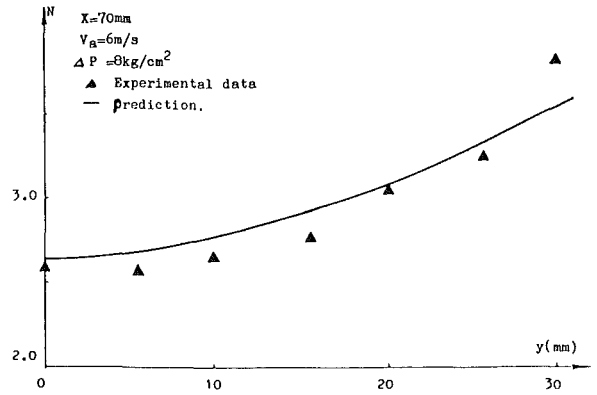

Fig. 11 Variation of N along radial distance: experimental data and prediction

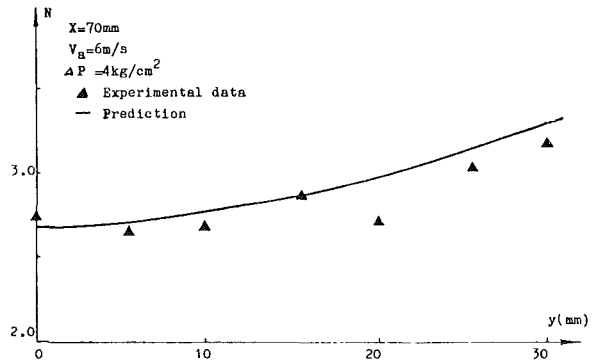

Fig. 13 Variation of N along radial distance: experimental data and prediction

1 The atomization process is finished at the exit of the atomizer nozzle, which means droplets of different sizes start their movement at the origin. The droplets of different sizes are assumed to have the same initial velocity. Because it is suitable to use a cylindrical coordinate system to describe droplet motion, the tangential velocity and the radial velocity component can be combined and treated as one velocity component.

2 The air flow is uniform.

3 The air is of ambient temperature, so the droplet evaporation can be neglected.

4 The influence of different droplet velocities on drop-size measurement by the Malvern particle sizer is neglected.

From equation (1) the drop-size distribution at $(x, y) = (0, 0)$ can be expressed as a function of $\bar{D}_0$ (SMD_0), N_0, with the expression $(dQ/dD)_0$

$$\left(\frac{dQ}{dD}\right)_0 = \frac{N_0}{\bar{D}_0}\left(\frac{D}{\bar{D}_0}\right)^{N_0-1} \cdot \exp\left[-\left(\frac{D}{\bar{D}_0}\right)^{N_0}\right] \tag{3}$$

Since all the droplets are assumed to depart from the source into a uniform stream with the same velocity, their subsequent trajectory will be determined only by drag forces, and therefore will be a function only of the droplet diameter.

At a downstream distance x, all droplets of diameter D (of which the initial volume fraction was $(dQ/dD)_0$) are now distributed on a circumference of radius $R(D)$. The laser light beam of diameter dj will only meet part of these droplets

$$\left(\frac{dQ}{dD}\right)_0 \cdot \frac{2(\varphi_2 - \varphi_1)}{2\pi} \tag{4}$$

where

$$\varphi_1 = \arcsin \frac{y_0 - \frac{1}{2}dj}{R(D)} \tag{5}$$

$$\varphi_2 = \arcsin \frac{y_0 + \frac{1}{2}dj}{R(D)} \tag{6}$$

The definition of φ_2, φ_1 is shown in Fig. 5.

When $y_0 - 1/2dj \le R(D) \le y_0 + 1/2dj$, $\varphi_2 = \pi/2$, where y_0 is the radial distance, d_j is the diameter of the light beam.

The summation of the liquid fraction of droplets of various diameters passing through the laser light beam is

$$\int_{D_{\min}}^{D_{\max}} \left(\frac{dQ}{dD}\right)_0 \frac{\varphi_2 - \varphi_1}{\pi}\, dD \tag{7}$$

Here the minimum diameter $D_{\min}$ which laser light beam can see is determined by

$$R(D_{\min}) = y_0 - 1/2dj$$

That is, at downstream distance x, if $R(D) \le y_0 - 1/2dj$, this droplet will not pass through the laser light beam. The relationship $R = R(D)$ can be determined by an equation for droplet trajectory derived in the next section and by taking $D_{\max} = 3.5 \cdot SMD$.

The liquid volume fraction of droplets of diameter D measured by the laser beam in an off-axis position ($y_0 > 0$) is then:

$$\frac{dQ'}{dD}=\frac{\left(\frac{dQ}{dD}\right)_0\frac{\varphi_2-\varphi_1}{\pi}}{\int_{D_{\min}}^{D_{\max}}\left(\frac{dQ}{dD}\right)_0\frac{\varphi_2-\varphi_1}{\pi}\,dD} \tag{8}$$

Thus Q' may be obtained as a function of D. If we assume that the Rosin–Rammler distribution can be used for data fitting of the off-axis sample, we now obtain SMD′, N' for the sample. These values SMD′, N' are changing with the distance y_0. If we delete the prime, what we obtain is the functional relationship SMD $=f(y)$, $N=f(y)$.

Droplet Trajectory Equation

The equation $R(D)$ is derived in this section. If we use a coordinate system which is moving with the air flow, then the droplet motion equation is

$$\frac{\pi}{6}\cdot\rho_l\cdot D^3\cdot\frac{dw}{dt}=-C_D\cdot\frac{\rho_a w^2}{2}\cdot\frac{\pi}{4}D^2 \tag{9}$$

where ρ_l = liquid density; w = droplet relative velocity; C_D = droplet drag coefficient = $15/\sqrt{\mathrm{Re}}$; Re = $\rho_a\cdot D\cdot W/\mu_a$; ρ_a, μ_a are the density and viscosity of air.

Equation (9) can be rewritten as

$$\frac{d(w/w_0)}{dt}=-\frac{45}{4}\frac{(\rho_a\cdot\mu_a\cdot w_0)^{1/2}}{\rho_l}\cdot D^{-\frac{3}{2}}\left(\frac{w}{w_0}\right)^{\frac{3}{2}} \tag{10}$$

where W_0 is the droplet initial relative velocity.

By integration of equation (10), we obtain

$$\frac{w}{w_0}=(Bt+1)^{-2} \tag{11}$$

where

$$B=\frac{45}{8}\cdot\frac{(\rho_a\mu_a\cdot w_0)^{1/2}}{\rho_l}\cdot D^{-\frac{3}{2}} \tag{12}$$

We know at downstream distance x, droplet velocity, air velocity, and their relative velocity have the relationship

$$V_x=V_a+(V_{x0}-V_a)\frac{w}{w_0} \tag{13}$$

$$V_R=V_{R0}\cdot\frac{w}{w_0}$$

where V_x, V_R are the axial and radial velocity components of the droplet; V_{x0}, V_{R0} are their initial values.

Thus we obtain the droplet trajectory equation

$$x=V_a\cdot t+(V_{x0}-V_a)\int_0^t\frac{w}{w_0}\,dt \tag{14}$$

$$R=V_{R0}\int_0^t\frac{w}{w_0}\,dt$$

From equation (11), we have

$$\int_0^t\frac{w}{w_0}\,dt=\frac{t}{B_t+1} \tag{15}$$

From equations (14) and (15), we have the radial position (droplet size D) at downstream distance x

$$R(D)=V_{R0}\cdot\frac{1}{B+\frac{1}{t}} \tag{16}$$

The time t can be determined by

$$t=\frac{X\cdot B-V_{x0}+[(X\cdot B-V_{x0})^2+4V_a\cdot BX]^{1/2}}{2V_a\cdot B} \tag{17}$$

where B is determined by equation (12).

From equations (14) and (15), substituting x, $R_{\min}=R(D_{\min})=y_0-1/2dj$, we have

$$D_{\min}=\left[\frac{45}{8}\frac{(\rho_a\cdot\mu_a w_0)^{1/2}}{\rho_l}\cdot\frac{\frac{V_{x0}-V_a}{V_{R0}}\cdot R_{\min}^2-X\cdot R_{\min}}{V_{x0}\cdot R_{\min}-x\cdot V_{R0}}\right]^{2/3} \tag{18}$$

Calculation Method and Results

In order to calculate the variation of spray characteristics along radial distance the following parameters must be known:

1 axial distance x
2 pressure drop across the nozzle Δp_l
3 fuel properties and the physical properties of air
4 atomizer spray cone angle
5 initial spray characteristics $(\mathrm{SMD})_0$ and N_0.

The calculation method used in the present paper may be summarized as follows:

1 We use the measured SMD and N values at $y=0$ and downstream distance x as approximations of $(\mathrm{SMD})_0$, N_0. We know that there is some difference between $(\mathrm{SMD})_0$ and $\mathrm{SMD}_{y=0}$, N_0 and $N_{y=0}$ [3], but so far these are the most reasonable approximate values to be used.

2 Calculate the initial droplet velocity $V_l=\mu\cdot(2\Delta p_l/\rho_l)^{1/2}$ where μ is the flow coefficient for the pressure drop. For the atomizer used in present research, the spray angle is close to 90 deg

$$V_{x0}=0.566\cdot\left(\frac{2\Delta p_l}{\rho_l}\right)^{1/2}$$

$$V_{R0}=0.566\cdot\left(\frac{2\Delta p_l}{\rho_l}\right)^{1/2} \tag{20}$$

3 Determine D_{min} for different y_0 values from equation (18). Here we assume $D_{\max}=3.5$ (SMD).

4 Use the Simpson method to solve equation (8), while $R(D)$ value may be calculated from equations (16) and (17).

5 Determine the integration $Q'=\int_{D_{\min}}^{D}(dQ'/dD)dD$. Thus we are able to obtain a set of data of Q' and D.

6 We assume that Q' can be fitted by the R–R distribution

$$Q'=1-\exp\left[-\left(\frac{D}{\bar{D}'}\right)^{N'}\right]$$

by using the least-squares method, $\bar{D}'$ and N' can be obtained, then SMD′ and N' can be calculated. These SMD′ and N' values are plotted against y in Figs. 6–13.

The calculation results for different air flow velocities and nozzle pressure drop are shown in Figs. 6–13, and compared with the corresponding experimental data. It is obvious that the predictions are in excellent agreement with the experimental results.

Discussion

1 In the present study the droplet evaporation has been neglected; as is shown in [2], taking into consideration the effect of droplet evaporation is not a difficult job.

2 After this model has been validated, it is relatively simple to predict the fuel distribution downstream of a pressure swirl atomizer [7].

3 From the experiments and the analysis, one interesting point has been noticed: that the larger droplets are always at the spray edge; the ignition spark plug is always positioned close to the spray edge; in this case, the spark meets larger droplets, which will do harm to the ignition.

Conclusion

1 The variation of spray characteristics along radial distance has been measured by laser light scattering technology.

2 The prediction based on the spray model proposed is in excellent agreement with experimental data.

References

1 Chin, J. S., Durrent, R., and Lefebvre, A. H., "The Interdependence of Spray Characteristics and Evaporation History of Fuel Sprays," ASME JOURNAL OF ENGINEERING FOR GAS TURBINES AND POWER, Vol. 106, July 1984.

2 Chin, J. S., and Zhu, J. Y., "The Interdependence of Spray Characteristics and Evaporation History of Fuel Sprays in High Temperature Air Flows," to be published.

3 Chin, J. S., Nickolaus, D., and Lefebvre, A. H., "Influence of Downstream Distance on the Spray Characteristics of Pressure-Swirl Atomizers," ASME JOURNAL OF ENGINEERING FOR GAS TURBINES AND POWER, Vol. 108, Jan. 1986.

4 Dodge, L. G., and Moses, C. A., "Mechanisms of Smoke Reduction in the High Pressure Combustion of Emulsified Fuels; Vol. 1. Construction of Apparatus and Preliminary Experiments," Yearly Progress Report No. 1, Sept. 29, 1980 to Sept. 29, 1981.

5 Cao, M. H., Chin, J. S., et al., "Semi-empirical Analysis of Liquid Fuel Distribution Downstream of a Plain Orifice Injector Under Cross-stream Air Flow," ASME JOURNAL OF ENGINEERING FOR POWER, Oct. 1982.

6 Chin, J. S., Wang, X. F., and Li, W. M., "Experimental and Analytical Investigation of the Spray Characteristics Downstream of Pressure-Swirl Atomizer," to be published in *Combustion Science and Technology* (in Chinese).

7 Chin, J. S., and Lefebvre, A. H., "Prediction of Liquid Fuel Distribution Downstream of a Swirl Atomizer in Flowing Air," Spring Technical Meeting, Central States Section of the Combustion Institute, Paper No. CSS/CI 83-20, 1983.

P. J. Vermeulen
Associate Professor.

V. Ramesh
Research Associate.

Wai Keung Yu
Graduate Student.

Department of Mechanical Engineering,
The University of Calgary,
Calgary, Alberta, Canada

Measurements of Entrainment by Acoustically Pulsed Axisymmetric Air Jets

Direct measurements of entrainment by acoustically pulsed axisymmetric air jets flowing into surrounding air have been made for a range of orifice sizes, Strouhal numbers, and excitation powers. The entrainment was considerably increased, by up to 5.8 times at distances greater than 15 diameters axially downstream of the orifice exit plane. The entrainment of the excited jet varied linearly with downstream distance. The jet response varied nonlinearly with excitation strength, indicating that there may be a practical upper limit to the acoustic augmentation of entrainment. The response depends on Strouhal number and appears to be optimum at about 0.25.

Introduction

Ricou and Spalding [1] made the first direct measurements of the entrainment by steady fully developed turbulent axisymmetric free gaseous jets. Hill [2], later on, extended this work by the "measurement of local entrainment rate in the initial region of axisymmetric turbulent air jets." Indirect evidence from acoustic control of dilution-air mixing in a gas turbine combustor [3] also suggested that the jet entrainment rate was increased by acoustic modulation. Furthermore, Crow and Champagne [4], by integrating velocity profiles, showed that the entrained volume flow was increased 32 percent for a low level of periodic excitation of the jet. Also by indirect means, and using external excitation, Binder and Favre-Marinet [5] established that the entrainment rate was increased by 90 percent for stronger pulsation than in [4]. Self-excited jet flows have been studied by Anderson [6] and more recently by Hill and Greene [7] who by integration of velocity profiles showed that the entrainment rate was increased. Vermeulen and Yu [8] carried out "an experimental study of the mixing by an acoustically pulsed axisymmetrical air-jet" for external excitation strengths much greater than those used by previous workers, and showed indirectly for an excitation strength half of the maximum used that the entrainment mass flow rate was approximately doubled. This study also summarizes relevant work on excited jet flows. Thus it appears that direct measurements of the entrainment rate of pulsating jets have not been made before, and despite the evidence from indirect measurements, that the entrainment rate is significantly increased, the potential for improvement in entrainment rate by pulsing jet flows has not been thoroughly explored.

Jet entrainment is responsible for the mixing produced by a jet; acoustic control over jet flow mixing may therefore promote closer achievement of the design objectives in processes dependent on jet mixing, such as those associated with a gas turbine combustor. It is therefore of important technical interest to make direct measurements of the entrainment rate of pulsating jets and to determine the significant control variables.

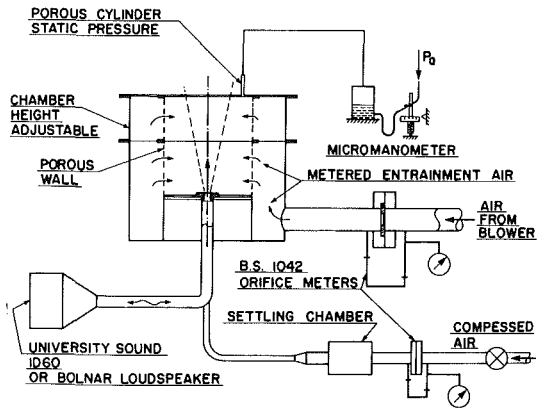

Fig. 1 Cross section through entrainment chamber

Experimental

Entrainment Measurement Apparatus. The apparatus used follows that developed by Ricou and Spalding [1], and consists of a porous walled chamber surrounding a 19.1-mm-dia bore tube, terminated by a smooth profile nozzle, mounted in the base plate of the porous cylinder (Fig. 1). The base of the cylinder is completely closed except for the nozzle orifice. The nozzle can be exchanged with others of different-sized bore for a range of sizes of 6.35, 9.53, 12.70, and 15.88 mm diameter. The porous wall of 300 mm diameter forms an annulus with the 550-mm-dia outer wall of the chamber. Air from the nozzle creates a jet on the chamber axis entraining air which was supplied through the porous wall from air metered to the annulus by a 76-mm-dia bore pipe. A centrifugal blower

Contributed by the Gas Turbine Division of THE AMERICAN SOCIETY OF MECHANICAL ENGINEERS and presented at the 31st International Gas Turbine Conference and Exhibit, Düsseldorf, Federal Republic of Germany, June 8–12, 1986. Manuscript received at ASME Headquarters January 17, 1986. Paper No. 86-GT-86.

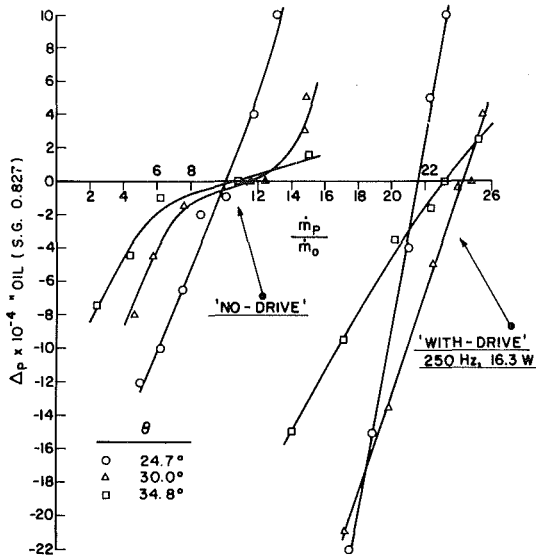

Fig. 2 Variation of pressure drop across aperture plate with mass flow rate through porous wall for various aperature included angles θ; orifice 9.53 mm diameter, x/d_o = 38.8

delivers the entrainment air metered by a standard sharp-edged orifice meter. Compressed air was admitted to the nozzle tube via a needle valve, a standard sharp-edged orifice meter, and a settling chamber positioned to protect the flow meter from acoustic pulsations in the flow. The temperature and pressure upstream of the needle valve were kept constant, with the upstream pressure sufficiently large to ensure choked flow at the valve, ensuring constant mass flow rate. The nozzle tube bends at right angles, at the junction with the air supply tube, to couple to the acoustic excitation source of about 60 W rating.

The porous-walled annulus consists of several bolted sections, so that the chamber height is adjustable, thereby allowing the entrainment flow rate to be found for a range of jet flow lengths. The range of dimensionless axial distances (x/d_o) over which measurements could be made was from 7.0 to 68.5. The top of the chamber was partially closed by a series of aperture plates, with carefully chosen aperture diameters that would not interfere with the jet flow. A pressure tap in the aperture plates allowed the porous cylinder static pressure to be measured with the aid of an oil-filled micromanometer gauge.

A rigid framework of 3.18-mm-dia aluminum rods and flanges supported the porous wall of three layers of fine-weave cotton cloth. Three layers of cloth were necessary in order to provide sufficient pressure drop to ensure a uniform, radially inward flow of air, passed through the porous wall. This was checked by traversing a smoke source closely all over the inside porous surface.

For safe operation of the acoustic source, power to the loudspeaker was measured by an a-c voltmeter and ammeter, a small correction for power factor having been established by calibration against an audio frequency wattmeter. The response of the system can be divided into that of the mechanical system of tube plus loudspeaker and that of the jet flow. The mechanical system response determines the frequencies at which the strongest excitation of the jet takes place. A previous investigation [8], of essentially the same mechanical system, established these frequencies to be about 250 Hz using the Bolnar loudspeaker, and about 410 Hz with the University Sound ID60 driver. The jet flow response depends on the Strouhal number, and [8] showed this to be optimum at about 0.25 for a free jet.

Upon acoustic excitation the jet velocity at the nozzle orifice pulses, which in turn excites the jet flow into wave motion growing into a train of toroidal vortices [8]. The amplitude, on the center line at the orifice exit plane, of this pulsation velocity (pulsation strength) was measured by a hot-film anemometer in a manner similar to that described in the previous work [8].

The main variables affecting the entrainment rate, and to be investigated, are the nozzle or orifice diameter d_o, the jet axial length x measured from the orifice exit plane, the average steady (unexcited) jet velocity in the nozzle exit plane U_o, the pulsation strength U_e, the driving frequency f, and the associated dimensionless parameters, Reynolds number Re and Strouhal number St.

Measurement Method. When the jet is flowing "free," that is when the surrounding reservoir (room) is large, it is essentially at uniform pressure (atmospheric), and the entrained air flows radially inward toward the jet axis. Now consider the jet to be partially surrounded, as in the apparatus described above, then with no air from the blower, entrainment by the jet reduces the porous cylinder pressure below atmospheric. If air from the blower is now adjusted such that the pressure in the porous cylinder is atmospheric, and the flow through the porous wall is radially inward, then free-jet flow conditions are re-established and the air mass flow rate delivered by the blower becomes equal to the entrainment mass flow rate of the jet. The method of measurement for a particular jet flow

Nomenclature

d_o = jet orifice diameter
f = frequency
F, F_1, F_2, F_3 = functions
K, K_1 = constants
$\dot{m}_e$ = entrained mass flow rate
$\dot{m}_{eN}$ = entrained mass flow rate for "no-drive" conditions
$\dot{m}_{eW}$ = entrained mass flow rate for "with-drive" conditions
$\dot{m}_o$ = constant average mass flow rate through the jet orifice
$\dot{m}_p$ = mass flow rate through the porous wall
$\dot{m}_T$ = jet total mass flow rate crossing a plane normal to jet axis
$\dot{m}_{TN}$ = jet total mass flow rate for "no-drive" conditions
$\dot{m}_{TW}$ = jet total mass flow rate for "with-drive" conditions
Re = orifice Reynolds number = $\rho_o d_o U_o/\mu_o$
St = orifice Strouhal number = fd_o/U_o
U_e = center-line jet velocity excitation pulsation amplitude, or pulsation strength, at the orifice exit plane (unsteady flow)
U_o = average steady (unexcited) jet velocity at orifice exit plane
$\dot{W}$ = power at acoustic driver
x = jet axial length from orifice exit plane
μ_o = jet viscosity at the orifice
ρ_o = jet density at the orifice
ρ_s = density of the fluid surrounding the jet

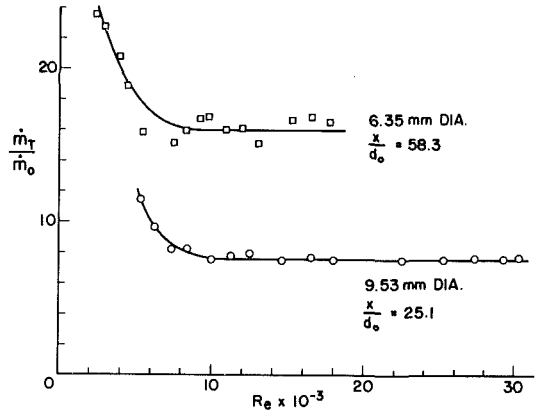

Fig. 3 Variation of total mass flow rate ratio with Reynolds number for "no-drive" conditions

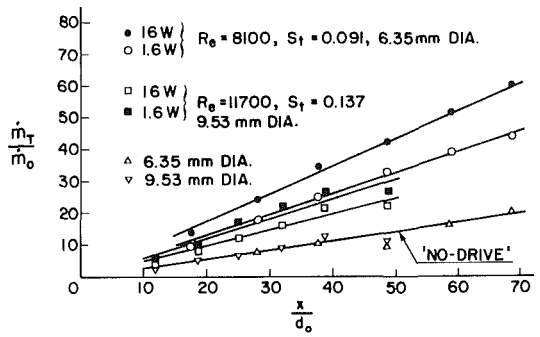

Fig. 4 Variation of entrainment rate with axial distance for isothermal conditions, temperature 26°C, atmospheric pressure 88.8 kPa, U_o = 17.4 m/s, 250 Hz

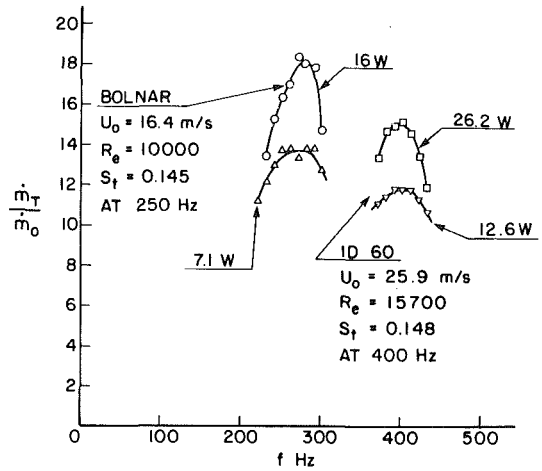

Fig. 5 Total mass flow rate ratio versus frequency for the system with either the Bolnar driver or ID60 driver; orifice diameter 9.53 mm, x/d_o = 25.1

length, for conditions with or without acoustic drive, is therefore simply to adjust the air flow rate through the porous wall until the micromanometer can detect no pressure difference between the porous cylinder static pressure and the atmosphere. For truly radially inward entrainment flow for this condition there must be no axial pressure gradient in the porous cylinder; measurement at two static pressure taps in the base plate of the porous cylinder confirmed that this was true.

The aperture diameter influences the pressure drop measured across the aperture plate; a minimum-sized hole was desirable in order to produce a pressure drop sensitive to changes in the flow rate through the porous wall, particularly as free-jet conditions were being approached. If the hole was too small the plate interfered with the jet axial flow, producing a reduced value for the measured entrainment flow rate. Thus if the pressure drop is plotted against the ratio of the porous wall mass flow rate $\dot{m}_p$ to $\dot{m}_o$, the constant mass flow rate through the jet orifice of fixed diameter d_o, as in Fig. 2, then as the aperture size varies so does the curve crossing point for zero pressure drop. As can be seen a hole size can be chosen such that the crossing point value is little affected, and the curve slope is steep enough that an accurate value can be obtained, which is taken to be the required ratio of $\dot{m}_e$, the entrained mass flow rate to the mass flow rate through the jet orifice $\dot{m}_o$ ($\dot{m}_e/\dot{m}_o$), corresponding to free-jet conditions. Furthermore, for acoustic drive conditions, the aperature size which subtends an included angle of 30 deg at the orifice gives the maximum value for the measured entrainment flow rate, which is assumed to be the free-jet value. It is possible that a slightly different aperture size would give an improved value; however, the change is likely to be small, and a 30 deg aperture angle is also the best size for "no-drive" conditions (in agreement with [1]), a great convenience. An aperture angle of 30 deg was therefore chosen for all entrainment measurements.

Initial Tests to Establish the Experimental Method. Before embarking on the main measurements it was possible to check the soundness of design of the apparatus, and to develop a good experimental technique, by duplicating some of the experimental results of Ricou and Spalding. The influence of Reynolds number, for no acoustic drive, was therefore investigated by varying the nozzle flow rate, since density and viscosity were essentially constant. Figure 3 presents data for the 6.35-mm and 9.53-mm-dia nozzles, in terms of the ratio of the total mass flow rate $\dot{m}_T$ of the jet crossing a plane distance x from the orifice to the orifice mass flow rate $\dot{m}_0$ ($\dot{m}_T/\dot{m}_o$) versus the Reynolds number at the orifice. The distance x is identical to the entrainment chamber length, and $\dot{m}_T$ is for free-jet conditions and related to $\dot{m}_e$ by

$$\dot{m}_T = \dot{m}_e + \dot{m}_o \tag{1}$$

or

$$\frac{\dot{m}_T}{\dot{m}_o} = \frac{\dot{m}_e}{\dot{m}_o} + 1 \tag{2}$$

As can be seen $\dot{m}_T/\dot{m}_o$ is constant for Reynolds numbers exceeding about 10,000. Ricou and Spalding established a critical Reynolds number of about 25,000; it is presumed that the difference is caused by higher turbulence levels in the nozzle flows of the apparatus for this investigation.

The next aspect which could be checked was the dependency of entrainment rate on jet length x for "no-drive" conditions; however, since varying the chamber height was a tedious operation it was also convenient to make simultaneous measurements for "with-drive" conditions at each value of x investigated. Thus Fig. 4 shows data for the "no-drive" condition at two orifice sizes, with an initial jet velocity of 17.4 m/s, chosen because of good driving possibilities and for possible comparison with other data [8]. A linear relationship is indicated, represented by

$$\frac{\dot{m}_T}{\dot{m}_o} = 0.29\,\frac{x}{d_o} \tag{3}$$

The slope of this line is somewhat lower than the 0.32 obtained by Ricou and Spalding, which was later confirmed by Hill [2]. The degree of agreement, however, was considered to be sufficiently close to assume that the apparatus and technique were giving results as reliable as possible with the instrumentation available.

The frequencies for best mechanical system response were then verified by measuring $\dot{m}_T/\dot{m}_o$ versus frequency, for the two acoustic drivers, at orifice jet velocities giving approximately the same orifice Strouhal number. Evidently as shown

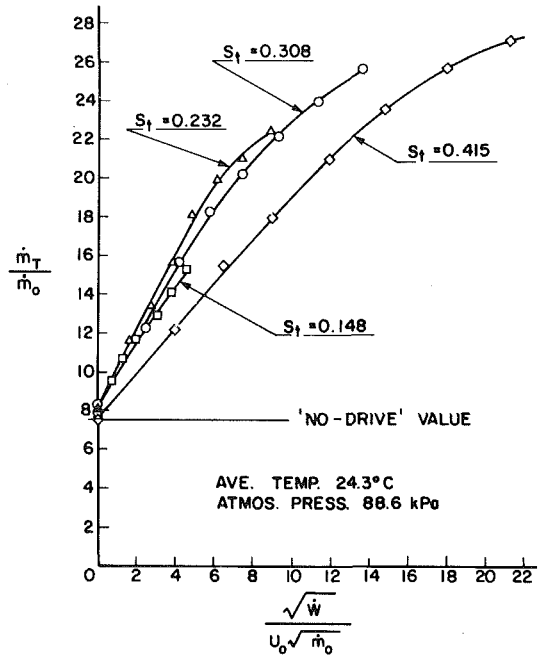

Fig. 6 Variation of entrainment rate with pulsation strength parameter for 9.53-mm-dia orifice, x/d_o = 25.1, 400 Hz, data corrected for Re effects

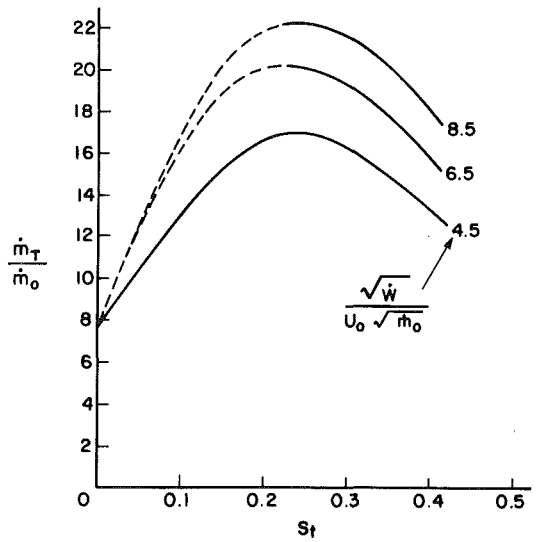

Fig. 7 Variation of entrainment rate with Strouhal number for various values of pulsation strength parameter; 9.53-mm-dia orifice, x/d_o = 25.1, 400 Hz, data corrected for Re effects

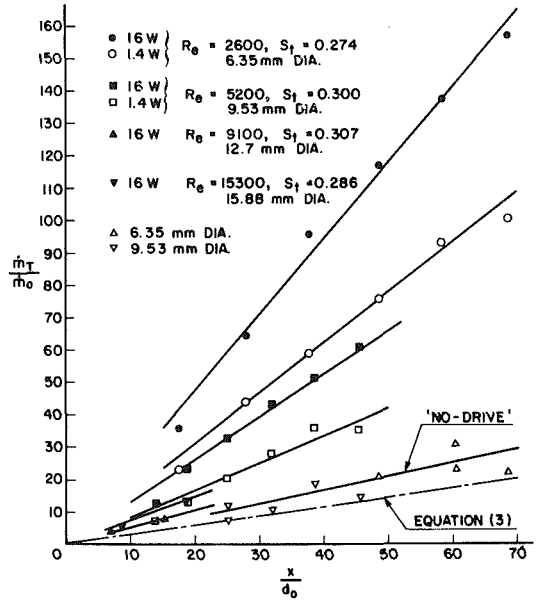

Fig. 8 Variation of entrainment rate with axial distance for isothermal conditions, temperature 26°C, atmospheric pressure 88.8 kPa, 250 Hz

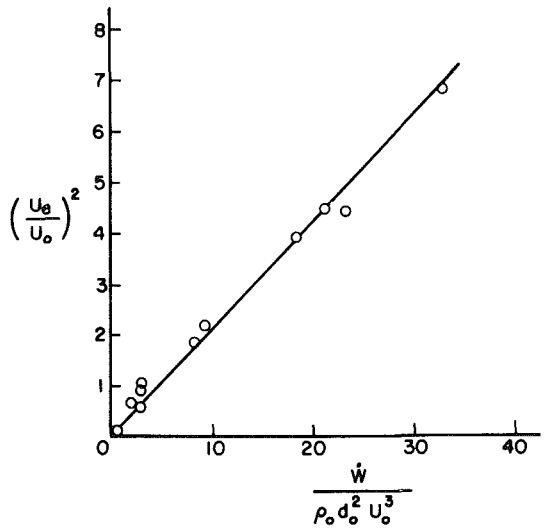

Fig. 9 Correlation between pulsation strength and dimensionless power, 9.53-mm-dia orifice, 250 Hz

by Fig. 5 good response was obtained at frequencies of 250 Hz and 400 Hz. A frequency of 250 Hz is not quite optimum, but since a considerable number of data at this frequency for other measurements had been obtained [8] it was selected to facilitate possible comparisons.

Experimental Results With Acoustic Drive. The test results for U_o = 17.4 m/s, shown in Fig. 4, indicate the typical effects of acoustic drive, and in general the entrainment mass flow rate was increased, relative to the no-drive condition, as shown by the increase in $\dot{m}_T/\dot{m}_o$ for a particular value of x/d_o. It is noteworthy that over the power (or U_e/U_o) range tested a linear relationship still exists between $\dot{m}_T/\dot{m}_o$ and x/d_o. Because of the several orifice sizes tested the data have been obtained over a Reynolds number range of 8100 to 11,700, and a Strouhal number range of 0.091 to 0.137. The Reynolds numbers are high enough to obviate the need for corrections, but the effect of Strouhal number may be significant and was investigated further. It is apparent that the effect of power, or pulsation strength U_e/U_o, causes a nonlinear response in $\dot{m}_T/\dot{m}_o$, which was therefore studied in more detail.

The effect of Strouhal number, and nonlinear response with pulsation strength, were further investigated using the University Sound driver in order to examine as wide a Strouhal number range as possible. The Strouhal number was varied by changing the jet velocity, which resulted in a Reynolds number range of 5600 to 15,700. This necessitated that corrections be made to the data for Reynolds numbers less than 12,000, based on the results from Fig. 3, by assuming that the "with-drive" results are affected by viscosity in a similar manner to the "no-drive" results. It was not possible to operate at higher Reynolds numbers, thereby avoiding corrections, because of frequency limitation by the mechanical system response (Fig. 5), and because a larger diameter orifice could not be driven strongly enough by the driver power available. It will be shown later that

$$\frac{U_e}{U_o} = \frac{K_1\sqrt{\dot{W}}}{U_o\sqrt{\dot{m}_o}} \tag{7}$$

at a particular frequency, where $\dot{W}$ is the driver power, and K_1 is a constant; hence the corrected experimental results for the 9.53-mm-dia orifice, at $x/d_o = 25.1$, for a range of driver powers, have been presented in Fig. 6 in terms of the parameter $\sqrt{\dot{W}}/U_o\sqrt{\dot{m}_o}$. The nonlinear response of $\dot{m}_T/\dot{m}_o$ with pulsation strength is immediately apparent indicating that there may be a practical upper limit to the acoustic augmentation of entrainment mass flow rate. It will also be observed that the data for the lower Strouhal numbers have been curtailed because of the restriction on driver power (<30 W) to avoid destruction of the "voice coil." By cross-plotting the data at $\sqrt{\dot{W}}/U_o\sqrt{\dot{m}_o} = 4.5$ (U_e/U_o constant) the response with Strouhal number can be shown, as in Fig. 7, and is seen to peak at a Strouhal number of approximately 0.25.

The variation of $\dot{m}_T/\dot{m}_o$ with x/d_o, near optimum Strouhal number conditions, is given in Fig. 8 for several orifice sizes. Equation (3) has also been shown for comparative purposes, which immediately indicates that the experimental points for "no-drive" conditions have been affected by viscosity; presumably the "with-drive" data are similarly affected. This is the result of having to obtain a Strouhal number of 0.3 by lowering the jet velocity, resulting in low Reynolds numbers. The "no-drive" data also unfortunately suffer from undue experimental scatter caused by the difficulty in the measurement of $\dot{m}_o$ at such low jet velocities; the lower limit of the instrumentation available was being reached. Despite this criticism the data clearly show the increased entrainment produced by acoustic drive, and that a linear relationship exists between $\dot{m}_T/\dot{m}_o$ and x/d_o for the power (or U_e/U_o) range used. Clearly the data are similar to those of Fig. 4 for lower Strouhal numbers.

Discussion

Dimensional Analysis. The discussion is facilitated by considering the dimensional analysis of the problem, which may be conveniently divided into two parts: (*a*) examination of the relationship between pulsation strength and power, and (*b*) the relationship between pulsation strength and jet mass flow rate.

(*a*) Consider the nozzle flow to be incompressible and that geometric similarity applies, then since pulsation strength has been shown to depend on the power, jet velocity, and orifice diameter [8], it may be assumed that

$$U_e = F(\dot{W}, \rho_o, d_o, U_o, \mu_o) \tag{4}$$

where ρ_o is the density and μ_o is the viscosity. Then by selecting ρ_o, d_o, and U_o as common factors it follows that

$$\frac{U_e}{U_o} = F_1\left(\frac{\dot{W}}{\rho_o d_o^2 U_o^3}, \quad \frac{\rho_o d_o U_o}{\mu_o}\right) \tag{5}$$

where $\rho_o d_o U_o/\mu_o$ is the orifice Reynolds number. By plotting U_e/U_o versus $\dot{W}/\rho_o d_o^2 U_o^3$ it quickly becomes apparent that

$$\left(\frac{U_e}{U_o}\right)^2 = \frac{K\dot{W}}{\rho_o d_o^2 U_o^3} \tag{6}$$

(where K is a constant), as shown in Fig. 9 for data obtained at 250 Hz, for the 9.53-mm-dia orifice. Hence

$$\frac{U_e}{U_o} = \frac{K_1\sqrt{\dot{W}}}{U_o\sqrt{\dot{m}_o}} \tag{7}$$

These data were obtained for a Strouhal number (fd_o/U_o) range of 0.033 to 0.131. There was no discernable dependence on the Strouhal number, which justifies the omission of the frequency f as an independent parameter in equation (4). Furthermore, the Reynolds number range of the data was from 6000 to 38,000 with no noticeable effect, implying that viscous effects may be neglected. Thus equation (7) is the performance

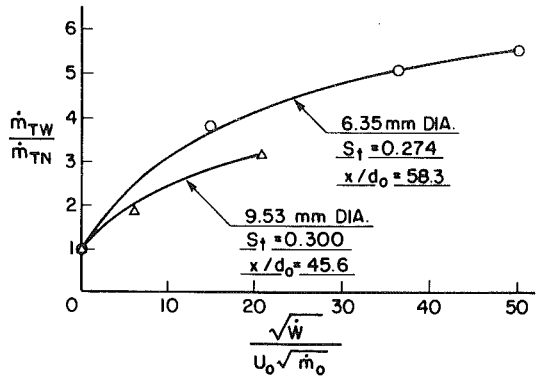

Fig. 10 Variation of mass flow rate ratio with pulsation strength parameter, frequency 250 Hz

law at 250 Hz. At other frequencies the constant K_1 is expected to change because of mechanical system response, and changing the orifice size may introduce a geometry parameter since geometric similarity will not be preserved.

(*b*) Consider the air jet flow to be incompressible, to have the same density as the entrained air, and conditions are geometrically similar. Then since the experimental results show that the total mass flow rate through a given plane depends on the distance from the orifice, the jet velocity, the orifice diameter, the pulsation strength, the Reynolds number, and Strouhal number, a functional relationship may be assumed as follows

$$\dot{m}_T = F_2(U_e, \rho_o, d_o, U_o, \mu_o, f, x) \tag{8}$$

Again, selecting ρ_o, d_o, and U_o as common factors it may be shown that

$$\frac{\dot{m}_T}{\dot{m}_o} = F_3\left(\frac{U_e}{U_o}, \quad \frac{\rho_o d_o U_o}{\mu_o}, \quad \frac{f d_o}{U_o}, \quad \frac{x}{d_o}\right) \tag{9}$$

In principle it would be possible to establish the effect of Reynolds number on $\dot{m}_T/\dot{m}_o$ at a particular drive condition. However, this would involve keeping U_e/U_o, S_t, and x/d_o constant while the Reynolds number was varied, a very difficult experimental task, which has so far not been attempted. The assumption has therefore been made that Reynolds number effects at "with-drive" conditions are similar to those at the "no-drive" conditions.

When the Reynolds number is high viscous effects can be neglected, and for fully developed flow, that is when $x > 15d_o$ [2], $\dot{m}_T$ is a linear function of x for "no-drive" conditions [1]. Thus the Reynolds number can be dropped from equation (9) and there may be a simple dependence on x/d_o for "with-drive" conditions.

Furthermore, when the density of the injected fluid ρ_o is different from that of the surroundings ρ_s, being entrained, Ricou and Spalding [1], from their data, showed that the data could be normalized to those for no density difference by multiplying the mass flow rate ratio by $\sqrt{\rho_o/\rho_s}$, i.e.,

$$\frac{\dot{m}_T}{\dot{m}_o}\sqrt{\frac{\rho_o}{\rho_s}}$$

All the data presented here have been corrected in this manner, even though small, because of small differences in temperature of the jet flow air and the entrained air (299 K and 306 K typically).

Entrainment Results. Figures 4 and 8 present the entrainment mass flow rate results without corrections for Reynolds number effects. This is not important since it is the ratio of $\dot{m}_T/\dot{m}_o$ "with-drive" to $\dot{m}_T/\dot{m}_o$ "no-drive" which is of interest. Thus any Reynolds number factors cancel, provided viscous effects are similar. Also since $\dot{m}_o$ was kept constant,

during a particular test, the above ratio reduces to $\dot{m}_{TW}$ "with-drive" divided by $\dot{m}_{TN}$ "no drive." Clearly the "with-drive" behavior is linear with x/d_o over a wide range of pulsation strength and Strouhal number, and the ratio $\dot{m}_{TW}/\dot{m}_{TN}$ increases substantially with the driving power. Thus the entrained mass flow rate has been considerably increased by pulsating the jet flow. Some data are shown for 12.70-mm and 15.88-mm-dia orifices, but because of driver power limitations entrainment changes are small.

The variation of $\dot{m}_T/\dot{m}_o$ with pulsation strength is clearly shown in Fig. 6, for 400 Hz, and a maximum value of 3.6 for $\dot{m}_{TW}/\dot{m}_{TN}$ was measured. All curves in Fig. 6 should pass through $\dot{m}_T/\dot{m}_o = 7.56$; the small discrepancies shown are the result of experimental error. A wider range of data variation was covered by the results of Fig. 8, which have been replotted in Fig. 10 (together with an extra experimental point) as $\dot{m}_{TW}/\dot{m}_{TN}$ versus $\sqrt{\dot{W}}/U_o\sqrt{\dot{m}_o}$. Data from Fig. 6 have not been included because their abscissa scale is different, i.e., the constant K_1 is known only for the 9.53-mm-dia orifice at 250 Hz driving frequency. This is because measuring the pulsation strength U_e is difficult with the instrumentation available, and would be more so in engineering situations. The measurement of driving power $\dot{W}$ is more convenient and gives a better idea of the power requirements required to increase the entrainment rate. A maximum value of $\dot{m}_{TW}/\dot{m}_{TN}$ of 5.59 (corresponding to $\dot{m}_{eW}/\dot{m}_{eN} = 5.82$) at St = 0.274 (250 Hz), was recorded for a driver power of 16 W. This is considerably greater than a ratio of 2, the maximum previously reported [8]. The pronounced separation of the curves at St values of 0.274 and 0.300 seems rather large in light of Fig. 7 and may be the result of geometric similarity not being preserved.

The driving power required for, e.g., doubling $\dot{m}_{TW}/\dot{m}_{TN}$ may be compared with the jet power, $\dot{m}_o U_o^2/2$, using the data from Fig. 10. Thus for the 6.35-mm-dia orifice the power required is 32 times the jet power, and for the 9.53-mm-dia orifice it is 72 times the jet power. This is indeed large, and considered in isolation of the process being affected by acoustic control it may be misleading. For instance Vermeulen et al. [9] showed that the power required to acoustically control the dilution-air mixing of a combustor, under scaled "full-load" operating conditions, was less than 1/2 percent of the combustor energy conversion rate. Hence the power required to produce a pulsating flow may still be small when compared with the overall power of the process.

In constructing the "best-fit" lines to the data of Fig. 8 the lines have been drawn through the origin of axes, as was done by Ricou and Spalding [1]. But, $\dot{m}_T/\dot{m}_o$ may have the value unity at $x/d_o = 0$, and certainly has for no-drive conditions. However, the accuracy of the data does not warrant this discrimination, and it has been ignored. For the unexcited jet Hill [2], for the initial region $x/d_o < 15$, showed that the slope of the entrainment law decreased from 0.32 to 0.12 at one nozzle diameter from the orifice. The present experiments were incapable of obtaining similar data for the excited jet, and measurements in the initial zone were not made. However, Vermeulen and Yu [8], by means of velocity and temperature profile measurements, showed, for the modulated jet, that increased entrainment took place over the first five diameters downstream of the jet orifice where the toroidal vortices are formed and are strongest. Hence, it is expected that future measurements in the initial zone will show that the local entrainment rate is substantially increased by acoustically exciting the jet.

Figures 6 and 10 indicate that the increase in entrainment mass flow rate begins to saturate with pulsation strength at the higher driver powers. This is in agreement with the findings of [8], and may be due to the excitation of the toroidal vibration mode of the toroidal vortices. The data are of the form $y = ax^b + 1$ for a particular Strouhal number. This allows an overall performance law to be found for say optimum Strouhal number conditions. The following equation was obtained for the data of Fig. 10 at St = 0.274 (6.35-mm-dia orifice, 250 Hz)

$$\frac{\dot{m}_{TW}}{\dot{m}_o} = 0.13\,\frac{x}{d_o}\left(\frac{\sqrt{\dot{W}}}{U_o\sqrt{\dot{m}_o}}\right)^{0.62} + 0.29\,\frac{x}{d_o} \qquad (10)$$

This equation is valid for $x/d_o > 15$, for the given system, and reduces to equation (3) for zero driving power.

An optimum Strouhal number of 0.25 was established by the results of Fig. 7. This is in agreement with the findings of [8] from velocity measurements, and is consistent with the findings of Crow and Champagne [4] who found that the turbulence intensity was optimal for St $\simeq$ 0.3. Both findings were for conditions essentially independent of Reynolds number effects. The incomplete curves in Fig. 7 suggest that the optimum value may depend on the pulsation strength U_e/U_o, but more data at lower Strouhal numbers are required before a definite conclusion can be drawn.

Conclusions

The experimental results show that jet entrainment was considerably increased by pulsing the jet flow. Specifically for $x/d_o > 15$ the jet total mass flow rate was increased by up to a factor of 5.6 (corresponding mass flow rate entrained by up to a factor of 5.8) for a Strouhal number of 0.274 and a driver power of 16 W. The entrainment of the excited jet varies linearly with distance downstream from the jet orifice, as for the unexcited jet.

The jet response varies nonlinearly with the excitation pulsation strength, indicating that there may be a practical upper limit to the acoustic augmentation of entrainment mass flow rate. The response depends on Strouhal number and appears to be optimum at about 0.25.

Acknowledgments

The authors are indebted to Mr. W. A. Anson, Chief Technical Supervisor; Mr. R. Bechtold, Machine Shop Supervisor; and Mr. P. Halkett, Technician, for their careful work in the building of the test rig. The work was supported financially by the Natural Sciences and Engineering Research Council of Canada, under Grant No. A7801.

References

1 Ricou, F. P., and Spalding, D. B., "Measurements of Entrainment by Axisymmetrical Turbulent Jets," *Journal of Fluid Mechanics*, Vol. 11, 1961, pp. 21–32.

2 Hill, B. J., "Measurement of Local Entrainment Rate in the Initial Region of Axisymmetric Turbulent Air Jets," *Journal of Fluid Mechanics*, Vol. 15, Part 4, 1972, pp. 773–779.

3 Vermeulen, P. J., Odgers, J., and Ramesh, V., "Acoustic Control of Dilution-Air Mixing in a Gas Turbine Combustor," ASME JOURNAL OF ENGINEERING FOR POWER, Vol. 104, Oct. 1982, pp. 844–852.

4 Crow, S. C., and Champagne, F. H., "Orderly Structure in Jet Turbulence," *Journal of Fluid Mechanics*, Vol. 48, Aug. 1971, pp. 547–591.

5 Binder, G., and Favre-Marinet, M., "Mixing Improvement in Pulsating Turbulent Jets," *ASME Symposium on Fluid Mechanics of Mixing*, Georgia Institute of Technology, Atlanta, GA, June, 20–22, 1973, pp. 167–172.

6 Anderson, A. B. C., "Structure and Velocity of the Periodic Vortex-Ring Flow Pattern of a Primary Pfeifenton (Pipe Tone) Jet," *The Journal of the Acoustical Society of America*, Vol. 27, No. 6, Nov. 1955, pp. 1048–1053.

7 Hill, W. G., and Greene, P. R., "Increased Turbulent Jet Mixing Rates Obtained by Self-Excited Acoustic Oscillations," ASME *Journal of Fluids Engineering*, Vol. 99, No. 3, Sept. 1977, pp. 520–525.

8 Vermeulen, P. J., and Yu, Wai Keung, "An Experimental Study of the Mixing by an Acoustically Pulsed Axisymmetrical Air-Jet," *30th ASME International Gas Turbine Conference*, Houston, TX, Mar. 18–21, 1985, Paper No. 85-GT-49, pp. 1–10.

9 Vermeulen, P. J., Odgers, J., and Ramesh, V., "Full Load Operation of a Gas Turbine Combustor With Acoustically Controlled Dilution-Air Mixing," *29th ASME International Gas Turbine Conference*, Amsterdam, The Netherlands, June 3–7, 1984, Paper No. 84-GT-106, pp. 1–8.

Study on Two-Phase Fuel Distributions in High-Speed Hot Transverse Air Stream

Yang Mao-lin
Gu Shan-jian
Li Xiang-yi
Beijing Institute of Aeronautics and Astronautics,
Beijing, People's Republic of China

It was found that fuel distribution in a hot high-speed transverse air stream differed greatly from that in a cold stream. In a hot air stream there exist two-phase fuel distributions, and hence, two mass center lines extending downstream. Experimental results of fuel distributions are presented. By using the model of trajectory with diffusion and also considering the fuel evaporation, a semi-empirical method to predict two-phase fuel distributions has been developed.

Introduction

Fuel distribution has profound influence on the performance of a combustor. It is necessary to understand the processes of fuel atomization, mixing, evaporation, and fuel distribution, both for designing a combustor and for improving its performance. Only when the fuel distribution can be predicted and controlled can we design a combustor properly and get good performance.

The actual process by which the fuel issuing from an injector forms the two-phase fuel distributions in a hot high-speed air stream is very complex. We know from experiments that when the relative velocity between fuel and stream is low, there exists a short liquid bar just outside the orifice of the injector, which is bent and deformed by aerodynamic forces. Usually there are some fuel droplets blown off from the surface of the bar. Later on, all the liquid fuel will break up in a region. When the relative velocity is high, the liquid fuel will break up at once after issuing from the injector. This results in a dense spray. The spray is shattered by the stream and the fuel droplets disperse into it, resulting in a thin fuel spray. Due to evaporation of the fuel droplets moving along their trajectories, two-phase fuel distributions are formed. The initial velocities of the droplets formed in the atomization process differ widely both in magnitude and direction [3]. The actual process is complicated by deformation of the droplets, a second breaking up and collision between droplets, the wakes behind droplets, evaporation, and turbulent mixing. It is difficult, therefore, to describe this process theoretically. However, to get a good understanding of the pattern of fuel distribution at real operating condition, a study on fuel distribution in simplified cases will be valuable.

Much work has been done on fuel distribution in an air stream at normal temperature. In a real afterburner or a ramjet combustor, the inlet air temperature is high, so we are more interested in fuel distributions in a hot air stream. We need to know the pattern of the fuel distribution and the effect of major variables.

Contributed by the Gas Turbine Division and presented at the 1985 Beijing International Gas Turbine Symposium and Exposition, Beijing, People's Republic of China, September 1-7, 1985. Manuscript received at ASME Headquarters June 14, 1985. Paper No. 85-IGT-118.

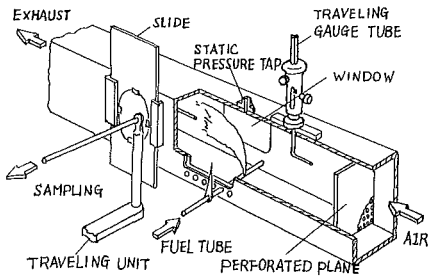

Fig. 1 Diagram of test section

It is known that when the inlet air temperature and the relative velocity between fuel droplets and air stream are low, the evaporation of liquid fuel can be neglected. But in a hot air stream, particularly at the operating condition in a real combustor, the evaporation of liquid fuel must be taken into account, and we have to deal with two-phase fuel distributions.

The main purpose of the present study is to study the features of two-phase fuel distributions in a hot air cross stream and to examine the effect of major variables. Based upon experimental work and considering evaporation, we develop the trajectory with diffusion method for predicting the two-phase fuel distributions.

The remarkable features of two-phase fuel distributions are described. The predictions of fuel distributions agree reasonably well with the experimental results.

Experimental Procedure

The experimental device is comprised of a test rig having a 300 mm × 170 mm rectangular test section with windows on both sides, as shown in Fig. 1. Air flow coming from the air supply was heated by an air preheater which consists of three tubular combustors. The heated air then enters the test section through a mixing chamber and two perforated planes. Uniform distribution of air temperature and velocity was then obtained.

In this investigation, air stream velocity ranged from 40 ~ 120 m/s, pressure drop across the fuel orifice, 5 ~ 30

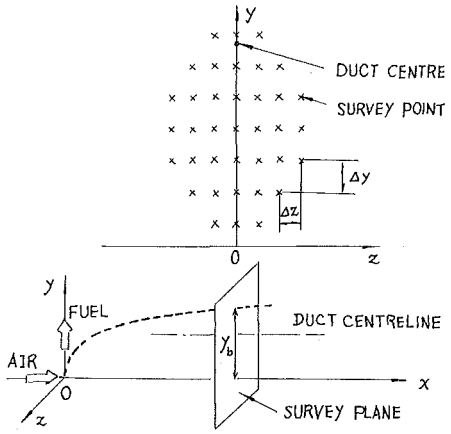

Fig. 2 Schematic drawing of survey point arrangement

kg/cm^2, diameter of the orifice, 0.5 ~ 0.9 mm, axial distance between the injector and the survey plane, 50 ~ 250 mm, and temperature of air stream, 283 ~ 473 K. Aviation kerosene was used in all experiments.

The schematic arrangement of survey points is shown in Fig. 2. The injector orifice center is taken as the origin of coordinates with the x axis parallel to the direction of fuel injection.

The fuel tube is mounted across the side walls of the duct upstream of the survey plane; the fuel injection direction could be changed by turning this tube. In this study 90 deg injection was used in all experiments.

The time-averaged total fuel concentration at a survey point was determined by an isokinetic sampling technique. After aspiration the sample was burned in the catalytic burner. By analyzing the volume contents of dry CO_2 in the dry gas, and after deducting the volume contents of CO_2 contributed by the preheater, the time-averaged total fuel-air ratio at the survey point was then determined. The sampling probe was placed on a traveling device, able to move in the x, y, z directions. The fuel-air distribution measurements can be achieved when the sampling probe finished scanning across one survey plane in a run. In each run, the variables of air and fuel were held constant while isokinetic samples were obtained at various points in the survey plane. The errors of total amount of fuel captured at the survey plane compared to the fuel mass flow rate taken from a flowmeter were in the range of ± 5 percent [8].

The Features of Fuel Distribution

1 Vertical spreading of the upper boundary of fuel spray, which is sometimes defined as spray penetration distance y_b,

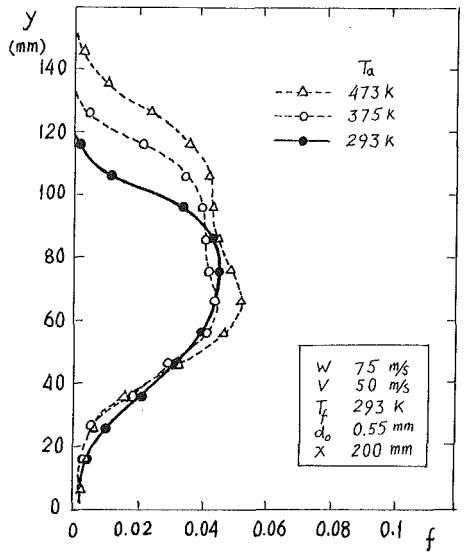

Fig. 3 Effect of air temperature on profile of total fuel-air ratio (experimental)

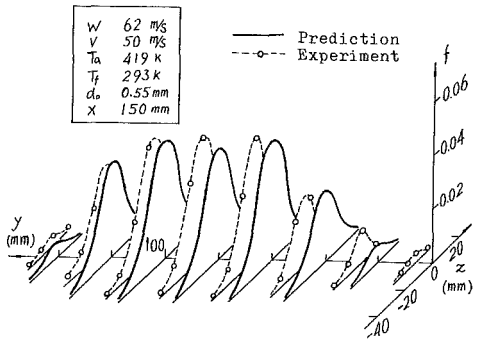

Fig. 4 Total fuel concentration distribution in the survey plane (a)

increases with the temperature of the air stream. Typical experimental data given in Fig. 3 show that the temperature of air stream has important influence on penetration of the fuel spray.

2 The profiles of fuel-air ratio along the lateral direction z at a survey plane were found from data reduction to approximate Gaussian curves. The dispersion range of fuel concentration along z was wider in a hot than in a cold air stream. This was probably due to the effect of higher air temperature on the trajectories of droplets, and of increased turbulence level on the diffusion of fuel particles (see Fig. 4).

3 The profiles of fuel concentration in the vertical direction

Nomenclature

a = drop diameter
a_m = drop diameter, maximum value of dF/da
a_{cp} = median diameter of droplets
B, k = coefficients
C_b = evaporation rate constant
C_d = drag coefficient
C_p = specific heat at constant pressure
d_0 = diameter of the orifice of fuel injector
D = equivalent diffusion coefficient
F = volume fraction of drops having diameter $< a$
f = fuel air ratio (time-averaged value)
G = mass flow rate
L = latent heat of evaporation
n = drop size distribution constant
q = mass flux
r = radius
Re = Reynolds number $= Ua/\nu_a$
S = length
T = temperature
U = relative velocity
V = velocity of fuel droplets
W = velocity of air stream
x, y, z = axes
Z = relative drop diameter $= a/a_{cp}$
α = heat exchange coefficient
λ = thermal conductivity
μ = viscosity
ν = kinematic viscosity
ρ = density
τ = time

Subscripts

a = air
b = boundary
f = fuel
l = liquid fuel
g = gaseous
0 = initial value

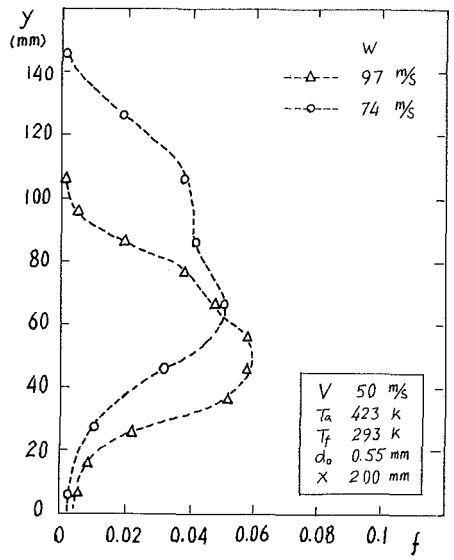

Fig. 5 Effect of air velocity on profile of total fuel concentration

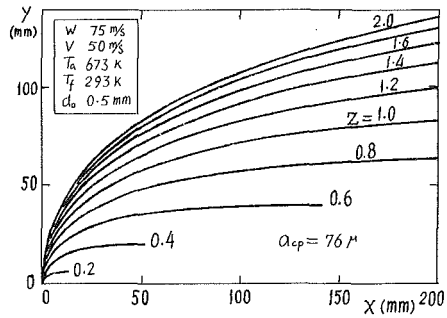

Fig. 6 Trajectories of droplets in a spray

y at a survey plane were found to be smoother in a hot than in a cold air stream. Particularly, in some cases, these profiles appeared to be double-humped curves, as shown in Fig. 3. This is a remarkable feature of fuel distribution in a hot air stream. Obviously, this is due to the evaporation of liquid fuel. Experiments showed that when air temperature was low, there existed only one hump. As air temperature was getting higher, the lower hump appeared and became larger while the upper hump became smaller. So, when the maximum fuel mass center line is to be determined, more attention should be paid to this complex situation.

4 Air velocity has a strong influence on the fuel concentration distribution, as shown in Fig. 5.

The Trajectory With Diffusion Method

The trajectory with diffusion method [3, 7], considering fuel evaporation, is used to predict the fuel distribution.

The assumptions are: The fuel jet breaks up immediately after being injected from the orifice of the injector; the motion of each group of fuel droplets is considered as a resultant motion of the droplets along their mean trajectories, which is calculated accounting for the evaporation of fuel droplets, with diffusion; the contribution by each group of droplets to the liquid fuel distribution in a target plane downstream may be expressed approximately by the contribution from an equivalent point source. Thus the time-averaged liquid fuel concentration at any point in the plane will be the summation of fuel concentrations contributed by all equivalent point sources. The contribution by each group of evaporated droplets in a small time period to the fuel vapor distribution in the plane may be expressed approximately by the contribution from an equivalent point source too. Thus the time-averaged fuel vapor concentration will be the summation of fuel concentrations contributed by all equivalent point sources, and the total fuel concentration will be the sum of liquid and vapor concentrations.

Fuel Drop Size Distribution. The Rosin–Rammler expression with $n=3$, which is approximately similar to the expression in [4], was used to describe the initial size distribution, while a_{cp} is determined by a_m, from the expression in [4], and a relative diameter was used in this study [7]. The drop size distribution and mean drop size given by Ingebo in NASA TP 1791 and NASA TM-83611 will be used in the next calculation, and better results would be expected.

Evaporation Rate of Fuel Droplet. To account for the forced convective evaporation of liquid fuel droplets, the thickness of the layer around the drop in which heat exchange is carried out is taken as

$$r_b = r_l/(1-2/\mathrm{Nu}) \tag{1}$$

where $\mathrm{Nu} = 2r_l\alpha/\lambda_m$.

The equation of heat exchange of a drop in the flow will be:

$$-4\pi r^2\lambda_m\frac{dT}{dr} = \frac{dG}{d\tau}[L + C_{pm}(T-T_l)] \tag{2}$$

where λ_m, C_{pm} are coefficient of thermal conductivity and specific heat of mixture of air and vapor in the equivalent layer around the drop, respectively.

Assuming the evaporation process to be a quasi-steady one, integrating equation (2) yields

$$\frac{dG}{d\tau} = \frac{2\pi r_l\lambda_m}{C_{pm}}\mathrm{Nu}\ln\left[1+\frac{C_{pm}}{L}(T_b-T_l)\right] \tag{3}$$

where

$$\mathrm{Nu} = 2 + 0.6\,\mathrm{Re}^{1/2}\mathrm{Pr}^{1/3} \quad [6] \tag{4}$$

For simplification, Pr = 1, $C_{pm} = C_{pa}$, $\lambda_m = \lambda_a$, and $T_b = T_a$; thus

$$\frac{da}{d\tau} = \frac{C_b}{2a}(1+0.3\mathrm{Re}^{1/2}) \tag{5}$$

where

$$C_b = \frac{8\lambda_a}{\rho_f C_{pa}}\ln\left[1+\frac{C_{pa}}{L}(T_a-T_l)\right] \tag{6}$$

Integration of equation (5), with C_b, Re, etc. considered as constants during the small time interval $\Delta\tau = \tau - \tau_0$, gives

$$a^2 = a_0^2 - C_b(1+0.3\,\mathrm{Re}^{1/2})(\tau-\tau_0) \tag{7}$$

where a_0 is the diameter of droplet at τ_0.

Temperature of Fuel Droplet. The time rate of change of the droplet temperature is given by the heat exchange equation

$$\frac{dT_l}{d\tau}\left(C_{pl}\rho_l\frac{\pi a^3}{6}\right) = \alpha\pi a^2(T_a-T_l) \tag{8}$$

thus

$$\frac{dT_l}{d\tau} = \frac{6\mathrm{Nu}\,\lambda_a}{C_{pl}a^2\rho_l}(T_a-T_l) \tag{9}$$

Integration of equation (9) gives

$$T_l = T_a - (T_a-T_{l0})\exp\left[-\frac{6\mathrm{Nu}\lambda_a(\tau-\tau_0)}{\rho_l a^2 C_{pl}}\right] \tag{10}$$

where $\Delta\tau = \tau - \tau_0$ is the small time interval.

Trajectory of Droplet Evaporating in a Flow. The equation of a droplet in the absence of all external forces except drag is

$$\frac{d\bar{V}}{d\tau} = -\frac{3\rho_a C_d}{4\rho_f a}U\bar{U} \tag{11}$$

where $\bar{U} = \bar{V} - \bar{W}$.

When written in component form this becomes

$$\begin{cases} \dfrac{dU_x}{d\tau} = -\dfrac{3\,\mu_a}{4\,\rho_f a^2} C_d \mathrm{Re} U_x \\ \dfrac{dU_y}{d\tau} = -\dfrac{3\,\mu_a}{4\,\rho_f a^2} C_d \mathrm{Re} U_y \end{cases} \tag{12}$$

Substituting equation (7) into this, and integrating, then

$$\begin{cases} \dfrac{U_x}{U_{x0}} = \left(\dfrac{a}{a_0}\right)^k \\ \dfrac{U_y}{U_{y0}} = \left(\dfrac{a}{a_0}\right)^k \end{cases} \tag{13}$$

and thus

$$\frac{U}{U_0} = \left(\frac{a}{a_0}\right)^k$$

where

$$k = \frac{6\mu_a C_d \mathrm{Re}}{4\rho_f C_b (1+0.3\mathrm{Re}^{1/2})} \tag{14}$$

thus

$$\begin{cases} V_x = W_x + U_{x0}\left(\dfrac{a}{a_0}\right)^k \\ V_y = W_y + U_{y0}\left(\dfrac{a}{a_0}\right)^k \end{cases} \tag{15}$$

Integration of equation (15) yields

$$\begin{cases} x = x_0 + W_x(\tau-\tau_0) - \dfrac{a_0^2}{B} U_{x0}\left[\left(\dfrac{a}{a_0}\right)^{k+2} - 1\right] \\ y = y_0 + W_y(\tau-\tau_0) - \dfrac{a_0^2}{B} U_{y0}\left[\left(\dfrac{a}{a_0}\right)^{k+2} - 1\right] \end{cases} \tag{16}$$

where

$$B = C_b(1+0.3\mathrm{Re}^{1/2})(1+0.5k) \tag{17}$$

The drag coefficient is given by the formula

$$C_d = \left(\frac{24}{\mathrm{Re}} + \frac{4.4}{\mathrm{Re}^2} + 0.32\right) \quad [3] \tag{18}$$

A modification factor K_d was introduced to account for the influence by other droplets in a spray on the drag coefficient of a single droplet [7].

The upper boundaries and penetration distances of fuel spray calculated with this modified drag coefficient are in good agreement with experimental results.

Calculation of Two-Phase Fuel Distributions. It is assumed that the liquid fuel concentration distribution in the target plane contributed by each group of droplets may be described by the distribution formed by an imaginary point source located upstream at a distance S_l, with dG_l as the source intensity, and D_l as the equivalent diffusion coefficient which is selected experimentally [7]. Thus

$$f_{li} = \frac{dG_l\, W}{4\pi D_l q_a S_l} \exp\left\{-\frac{W[z_p^2 + (y-y_p)^2]}{4D_l S_l}\right\} \tag{19}$$

where

$$S_l = \int_0^x \sqrt{\left(\frac{dy}{dx}\right)^2 + 1}\, dx \tag{20}$$

$$dG_l = G_f \frac{dF}{dZ} dZ \left(\frac{a}{a_0}\right)^3 \tag{21}$$

The time-averaged liquid fuel concentration distribution at a point p in the target plane donwnstream will be

$$f_l = \int_0^{Z_{\max}} \left(\frac{dF}{dZ}\right)\left(\frac{a}{a_0}\right)^3 \frac{G_f W}{4\pi D_l q_a S_l} \times \exp\left\{-\frac{W[z_p^2 + (y-y_p)^2]}{4\pi D_l S_l}\right\} dZ \tag{22}$$

The fuel vapor concentration distribution in the target plane contributed by each group of droplets at a short time interval $\Delta\tau$ may be described approximately by an imaginary point source located upstream at a distance S_g, with dG_g as the source intensity and D_g as an equivalent diffusion coefficient. Thus

$$f_{gi} = \frac{dG_g W}{4\pi D_g q_a S_g} \exp\left\{-\frac{W[z_p^2 + (y-y_p)^2]}{4D_g S_g}\right\} \tag{23}$$

where

$$dG_g = G_f \frac{dF}{dZ} dZ \left[\left(\frac{a_1}{a_0}\right)^3 - \left(\frac{a_2}{a_0}\right)^3\right] \tag{24}$$

a_0 is the initial drop diameter, a_1, a_2 are the drop diameter at τ_1 and τ_2, respectively, and $\Delta\tau = \tau_2 - \tau_1$.

S_g is the distance downstream of the imaginary vapor source and is determined by the path length of vapor jet plus an increment. This increment is proportional to the dispersion of the group of droplets.

The time-averaged fuel vapor concentration at a point in the target plane downstream may be determined as follows

$$f_g = \int_Z \int_{S_l} f_{gi} \tag{25}$$

and the total fuel concentration distribution will be

$$f = f_g + f_l \tag{26}$$

In this calculation the time interval was selected to be 0.0001 s.

The parameters, such as ρ, C_p, Re, etc., which are temperature dependent were calculated at the beginning of each time interval, and it was assumed that they remained constant during the small time interval.

The equivalent diffusion coefficients D_l and D_g depend on the initial dispersion and turbulent diffusion. It is difficult to determine them theoretically. In this calculation D_l was determined according to the same analysis and method in [7]

$$D_l = D_{l\max} K_e \tag{27}$$

$D_{l\max}$ was selected to be 0.03 m^2/s for $K_e = 0.5 \sim 1$, and depends on Z. For simplification, D_g was selected to be 0.015 m^2/s, at $T_a = 300$ K, for all conditions, and

$$D_g = 0.015\left(\frac{T_a}{300}\right) \mathrm{m}^2/\mathrm{s} \tag{28}$$

to account for the influence of air temperature on D_g.

These are generally accepted values, though they are not universal.

Calculation Results and Discussion

The two-phase fuel concentration distributions downstream of a plain orifice in a high-speed hot air stream were calculated in a wide range of variable by means of the trajectory with diffusion method.

Figure 6 shows the trajectories of fuel droplets in a spray. The larger the drop size, the higher the trajectory and the longer the lifetime. At high temperature, the small droplets evaporate completely in the vicinity of the injection point.

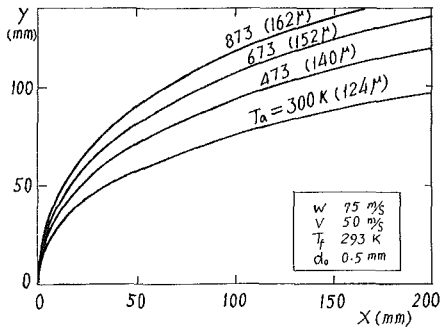

Fig. 7 Effect of air temperature on trajectories of droplets ($Z = 2$)

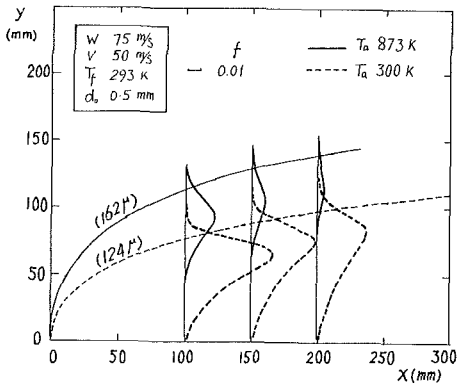

Fig. 8 Effect of air temperature on liquid fuel concentration distribution

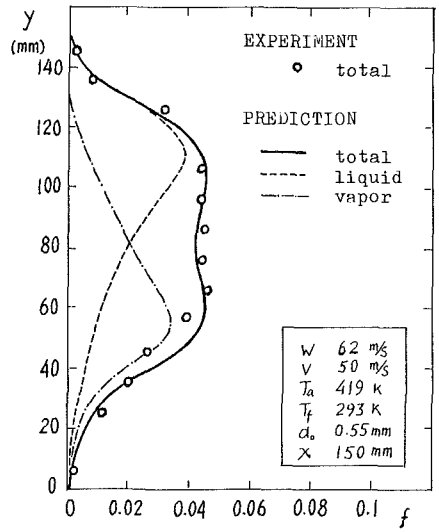

Fig. 9 Two-phase fuel distributions (*a*)

Figure 7 shows the influence of air temperature on the trajectory of droplets ($Z = 2$), and hence approximately on the upper boundary of the spray. When air temperature is higher, the aerodynamic force on the fuel spray will be smaller due to lower air density; furthermore, the initial drop size will be larger due to smaller air resistance, so the upper boundary of the spray will spread upward. However, when the air temperature is higher, the liquid droplets are gradually getting smaller due to evaporation. This will make the upper boundary shrink inward. In comparison, the effect of the former is stronger than that of the latter.

Figure 8 shows the liquid fuel concentration distributions and the effect of the major variables. When air temperature is low, the evaporation of liquid fuel may be neglected, but when air temperature is high, the evaporation of liquid fuel

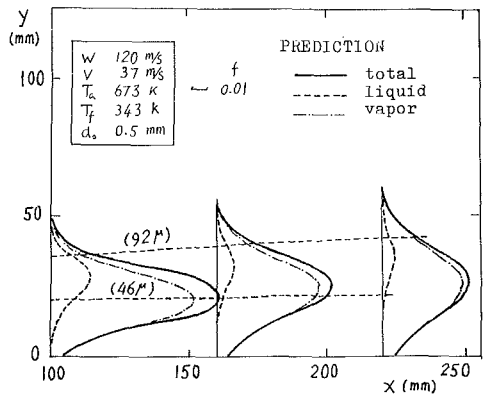

Fig. 10 Two-phase fuel distributions (*b*)

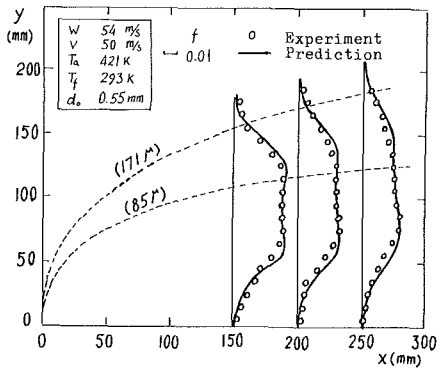

Fig. 11 Effect of downstream distance on profile of total fuel-air ratio

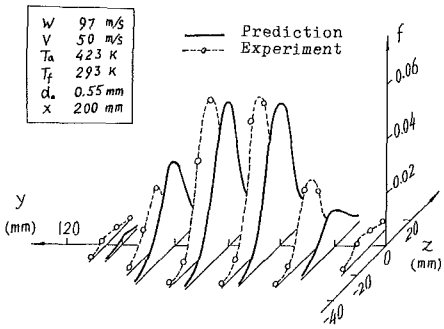

Fig. 12 Total fuel concentration distribution in the survey plane (*b*)

will be more significant, and the amount of liquid fuel will be getting smaller.

Figures 9 and 10 show the two-phase fuel concentration distributions. Figure 9 shows clearly that the solid curve of total fuel distribution resulting from the summation of the two dashed curves by calculation agrees reasonably well with the experimental data.

Figures 4, 9, 11, and 12 show a comparison of the prediction with the experimental results. The predicted total fuel concentration distributions agree very well with the experimental results.

The calculation and the experiment reveal the remarkable features of the fuel concentration distribution in a hot air stream which differ widely from those in a cold air stream. There is a transition region where the liquid and vapor phase coexist between the initial liquid fuel jet and the complete vapor phase region downstream.

In the transition region, the liquid mass center lies in the upper part of the spray plume. As the droplets move downstream, the amount of liquid fuel decreases. The liquid fuel region is reduced and the liquid mass center moves toward the upper boundary of the spray gradually (see Fig. 8).

However, the vapor fuel distribution has the opposite tendency. It moves toward the lower part of the spray. The amount of fuel vapor increases and the vapor region expands gradually with downstream distance.

It is obvious that the liquid fuel distribution peak doesn't generally coincide with the vapor peak, thus the resulting total fuel concentration distribution in a downstream plane appears to be flatter in a hot than in a cold stream. In certain conditions, there appears a double-humped distribution profile. Obviously, the upper hump is contributed mainly by the liquid fuel, and the lower hump is contributed mainly by the fuel vapor which has less penetration capability and is entrained by the crossflow. In other words, in the transition region there exist two mass centerlines in different phase. The liquid mass center line is above the vapor mass center line of a spray in hot cross flow. However, the calculation shows that the transition region decreases inversely with the air temperature. When the air temperature is high, most of the liquid fuel will vaporize in a short time.

The calculations also show that when both air velocity and air temperature are high and the fuel injection velocity is low, the spray cone will be slender and the liquid and vapor mass centerlines will be close to each other (see Fig. 10).

Conclusions

1 In a hot high-speed crossflow, there exists a two-phase fuel distribution region just downstream of the injector. The liquid fuel distribution zone becomes smaller gradually and tends toward the upper boundary of spray. On the other hand, the fuel vapor distribution zone increases gradually. Their mass center lines usually do not coincide with each other, resulting in a flatter profile and sometimes a two-humped profile of fuel distribution in the downstream plane.

2 Both the air temperature and initial fuel temperature have important influences on the two-phase fuel distribution; however, the air velocity is predominant.

3 The trajectory with diffusion method, also accounting for the evaporation of liquid fuel, may be used to predict the two-phase fuel distribution in a hot high-speed cross stream.

References

1 Longwell, J. P., and Weiss, M. A., "Mixing and Distribution of Liquid in High-Velocity Air Streams," *I.E.C.*, Vol. 45, No 3, Mar. 1953.

2 Mikhailov, A. I., et al., *Rabochii Protsess i Raschet Kamer Sgoraniya Gazoturbinnykh Dvigateli*, Moscow, 1959.

3 Raushchenbakh, B. V., et al., *Fizicheskie Osnovy Rabochego Protsessa v Kamerakh Sgoraniya Vozdushno-Reaktivnykh Dvigatelei*, Moscow, 1964.

4 Ingebo, R. D., and Foster, H. H., "Drop-Size Distribution for Cross-Current Breakup of Liquid Jets in Air Streams," NACA TN 4087, Oct. 1957.

5 Ning, H., "Combustor Aerodynamic Fudamentals," Sept. 1980.

6 Boyson, F., and Swithenbank, J., "Spray Evaporation in Recirculation Flow," AD A03606, 1978.

7 Yang, M. L., Gu, S. J., Liu, G. E., and Li, X. Y., "Trajectory With Diffusion Method for Predicting the Fuel Distribution in a Transverse Stream," AIAA 83-0336, Jan. 1983.

8 Yang, M. L., Gu, S. J., Liu, G. E., and Li, X. Y., "Experimental Investigation of Fuel Distribution in a Transverse Stream," ASME Paper No. 83-GT-207, Mar. 1983.

R. C. Adkins

D. Gueroui

Thermal Power Group,
School of Mechanical Engineering,
Cranfield Institute of Technology,
Cranfield, Bedford, England

An Improved Method for Accurate Prediction of Mass Flows Through Combustor Liner Holes

A theory is devised for predicting the coefficients of discharge for some types of combustor liner holes and for calculating the local quantity of airflow into the liner. The resulting equations are tested against reliable empirical data and they show an agreement of better than 99 percent. The new correlation is particularly amenable to the preliminary design and development of combustors and could usefully be incorporated into numerical modeling techniques. The theory is also used to devise a simple but very accurate method of correlating experimental data that has advantages over many of the methods in current use.

Introduction

The accurate prediction of mass flow and jet angle through the air admission holes in combustor liners is essential knowledge for both engine design and development. Numerous empirical data exist, much of which were generated in the early days of the gas turbine [1–4], but this is difficult to collate due to the various bases used for correlation. Even where correlation is common the data often are subject to large discrepancies due to differences in the techniques used during their acquisition.

Numerical modeling would seem to be the obvious approach to accurate prediction, but the great detail needed in the near-hole regions, coupled with numerous iterations, makes modeling of a complete combustor an expensive and time-consuming proposition. Added to this is the problem of where to prescribe the relevant boundary conditions since it is known that flow upstream of the liner can play a major role in dictating the flow pattern inside the liner.

The objective of this paper is to present a simple approach to the solution of flow through combustor liner holes which can be used by practicing combustor engineers as well as providing the specialist modeler with a convenient boundary condition. For modeling, suppose that all relevant details of the incoming jets can be readily predicted, then the computational boundary can be limited to the inner wall of the liner and to the jets themselves.

The scope of this paper is limited to the derivation of a simple analysis, the development of a reliable test technique, and to the correlation of data for plane holes having a diameter which is large when compared to the liner wall thickness. The effect of internal liner flow on the performance of the holes is neglected; this is considered to be justifiable because the analysis terminates at a short distance downstream of the hole and the significantly lower velocities inside the combustor have had little opportunity to have taken any effect. It is intended to extend the procedure to more complex hole forms and flow configurations in later papers.

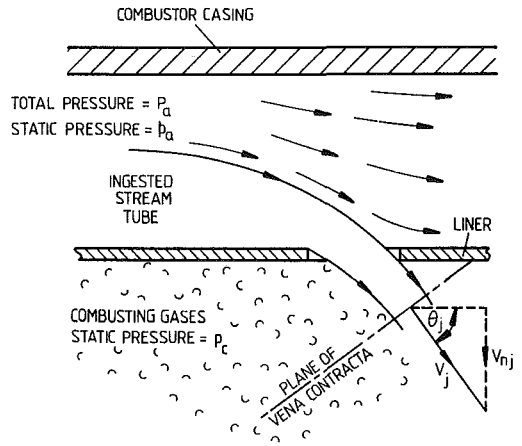

Fig. 1 Flow ingested into liner

Relevant Conditions

Flow typical to the neighborhood of combustor liner holes is sketched in Fig. 1. Upstream, it originates from flow which is parallel to the liner wall, but on approaching the hole its direction becomes influenced by the lower pressure inside the liner. A stream tube, originating from close to the wall, is drawn into the hole, and in doing so, it is both deflected and accelerated and also contracts in cross-sectional area. This contraction is so rapid that fluid dynamic forces cause it to continue contracting for some distance after it has passed through the hole. A position is reached where its cross section becomes a minimum and this is known as the vena contracta.

At the vena contracta there is no streamwise curvature of the streamtube and so the velocity and static pressure are uniform over the cross section. Static pressure at this plane

Contributed by the Gas Turbine Division of THE AMERICAN SOCIETY OF MECHANICAL ENGINEERS and presented at the 31st International Gas Turbine Conference and Exhibit, Düsseldorf, Federal Republic of Germany, June 8–12, 1986. Manuscript received at ASME Headquarters January 30, 1986. Paper No. 86-GT-149.

will now equal that of the surrounding gases. The vena contracta therefore provides a convenient location from which to assess the properties of the jet.

Analysis

With reference to the terms used in Fig. 1, the continuity equation yields an expression for the mass flowing through the hole where

$$m_h = \rho \cdot A_j \cdot v_j \tag{1}$$

By treating the flow as incompressible, the value of air density at the jet ρ can be conveniently calculated, using the ideal gas law and from the known conditions upstream of the hole. Here

$$\rho = p_a / R \cdot T_a \tag{2}$$

Furthermore, a simple expression for the jet velocity follows from a rearrangement of the Bernoulli equation

$$v_j = \sqrt{2 \cdot (P_a - p_c)/\rho} \tag{3}$$

By far the most difficult value to determine in equation (1) is that of the cross-sectional area A_j. In this, the problem is similar to that which arises in the use of orifice air meters in pipelines. Here, the minimum area of the jet is expressed as a fraction of the orifice area, the fraction being called the coefficient of contraction C_c. A typical value of this coefficient is in the order of 0.60 and it is dependent on several factors of which the most dominant is the contraction ratio. This relates to the contraction in cross-sectional area between the upstream pipe and the orifice plate. This contraction ratio is therefore simply based on geometric configuration.

Determination of the contraction coefficient C_c of combustor liner holes is fundamentally more complex, differing from the orifice flow meter in two ways. Firstly, the flow approaches the hole from a direction parallel to the liner wall and so it enters the hole obliquely rather than perpendicularly, the angle of entry being dependent on the velocity of approach and the pressure drop across the hole. Secondly, in most instances the hole only swallows part of the flow in the approach passage and so the upstream contraction ratio cannot be determined from solely geometric considerations.

The first problem, that of oblique entry, is addressed here again with reference to Fig. 1. This is based on observations made by the authors while conducting water flow visualization studies on various gas turbine combustors. It was noted that the angle of flow into a liner varied considerably across the section of the hole. In the present analysis, use is therefore made of the jet angle θ_j at the vena contracta where the angle is consistent over the cross section, and where the angle can be readily evaluated from the local vectors, here

$$\sin \theta_j = v_{nj}/v_j$$

The velocity normal to the liner v_{nj} is derived directly from the drop in static pressure across the hole and so the angle can be expressed solely in terms of pressure differences, viz.

$$\sin \theta_j = [(p_a - p_c)/(P_a - p_c)]^{1/2} \tag{4}$$

The ratio of pressure drops involved in equation (4) is later shown to be a major parameter and is denoted by ϕ, where

$$\phi \equiv (p_a - p_c)/(P_a - p_c) \tag{5}$$

The angle θ_j can now be expressed more conveniently by

$$\sin \theta_j = \sqrt{\phi} \tag{6}$$

Evaluation of Contraction Coefficient, C_c. As explained previously, it is not possible in the present configuration to derive C_c from an upstream contraction ratio based on geometric properties. It is therefore necessary to take recourse to an overall area contraction ratio C_r, which can be derived by one-dimensional considerations of the flow such that

$$C_r = A_j/A_a = v_a/v_j$$

Here A_a is the cross-sectional area of the approaching stream tube. Then expressing C_r in terms of pressure differences gives

$$C_r = \sqrt{\frac{P_a - p_c + p_c - p_a}{(P_a - p_c)}}$$

from which we obtain

$$C_r = \sqrt{1 - \phi} \tag{7}$$

It was successfully predicted that the relationship between contraction coefficient and overall contraction ratio would be an exponential function. This had to satisfy the following conditions relating to the flow:

(*i*) When $A_j/A_a = 1.0$ (i.e., the stream tube maintains a constant cross-sectional area), then $C_r = 1$ (also $\phi = 0$), and the value of C_c equals 1.0.

(*ii*) When $A_j/A_a \to 0$, then $A_a \to \infty$ and the pressure difference ratio ϕ tends to unity. This situation resembles that of a plenum chamber supplying an orifice air meter and for which it is indicated in [5] that C_c would be approximately equal to 0.62. (It is considered pertinent here that $1 - \exp(-1) = 0.632$.)

A suitable form of equation for present purposes is then likely to be

$$C_c = 1 - \exp(-1) + \exp(-1/C_r)$$

Nomenclature

A = cross-sectional area
c = length of curved surface
C_c = coefficient of contraction
C_d = coefficient of discharge
C_r = contraction ratio
C_f = correction factor
C_{fc} = corrected coefficient of contraction
D = diameter of liner
d = diameter of liner hole
f = area adjustment factor for liner curvature
H = height of approach duct
I = ingestion ratio (defined in text)
k = numerical constant
m = mass flow rate
n = number of holes in line across/around liner
P = total or stagnation pressure
p = static pressure
R = gas constant
T = absolute temperature
t = wall thickness
v = velocity
V_f = view factor
X = porosity ratio (defined in text)
x = perpendicular distance from center of hole
y = half length of cord
z = multiplier correction for Reynolds number effect
α = angular displacement of cordal element
β = angle projected to center of liner
θ = angle of jet
μ = absolute viscosity
ρ = density
ϕ = correlation parameter (defined in text)

Subscripts

a = denotes conditions in supply duct immediately upstream of test holes
c = conditions in liner downstream of hole
e = effective
h = conditions at liner hole
j = conditions at vena contracta of jet
n = distance normal to liner wall
s = denotes at same axial location

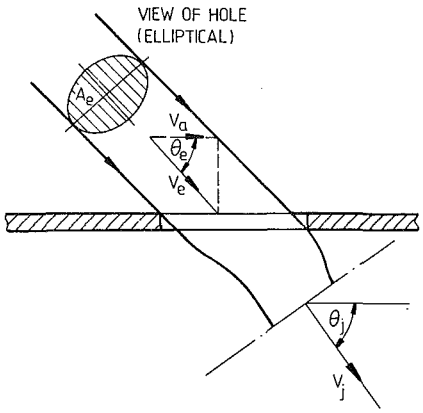

Fig. 2 Notional flow

Using equation (7) to express this in terms of ϕ

$$C_c = 1 - \exp(-1) + \exp(-1/\sqrt{1-\phi}) \tag{8}$$

Correction for Three Dimensionality. Due to the use of assumptions made it was considered necessary to include a multiplication factor to correct for true three dimensionality. The correction factor C_f, derived from the experiments described later, was found to vary slightly with ϕ but it remained very close to unity, thereby justifying the present theoretical assumptions.

In formulating the correction factor C_f, it was argued that at the extreme condition when there would be no contraction of the stream tube (i.e., $\phi \rightarrow 0$), then clearly there should be no need to correct for contraction and hence C_f would equal unity. Similarly, as $\phi \rightarrow 1.0$, then the upstream flow would resemble that from a plenum chamber and the stream tube would flow through the hole perpendicularly and so correction at this condition will also be unnecessary.

A suitable correction multiplier C_f was accordingly expected to take the form

$$C_f = 1 - \frac{\phi \cdot (1-\phi)}{k} \tag{9}$$

k was later found from experiment to be 3.0.

The corrected coefficient of contraction C_{fc} is then expressed as

$$C_{fc} = C_c \cdot C_f \tag{10}$$

Equivalent Area of Hole. In order to simplify the situation the jet angle at the vena contracta was related to a notional angle θ_e, defined as the angle made by the flow through the hole if all its streamlines were parallel (Fig. 2). A further simplification was to consider the liner as a flat plate; both of these simplifications will be corrected for later on.

The jet, as it approaches the circular hole at the angle θ_e, views it as an ellipse of cross-sectional area A_e, where

$$A_e = \pi \cdot d^2/4 \cdot \sin\theta_e \tag{11}$$

With this simplification, it is also possible to derive a simple expression for the velocity v_e, through the notional hole, where

$$v_e = v_j \cdot C_{fc} \tag{12}$$

The velocity of air v_a parallel to the liner is known and so the notional angle can be evaluated from the local velocity vectors, where

$$\cos\theta_e = v_a/v_e$$

and

$$\sin\theta_e = \sqrt{1-(v_a/v_e)^2}$$

Then in terms of pressure differences

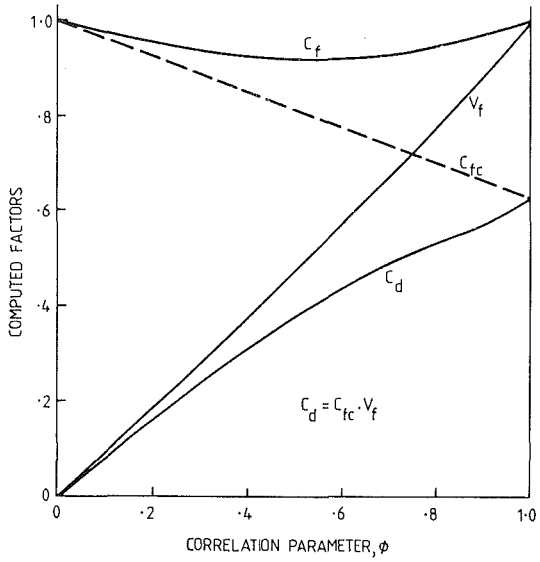

Fig. 3 Discharge coefficient

$$\sin\theta_e = \sqrt{1 - \frac{(P_a - p_a)}{(P_a - p_c) \cdot C_{fc}^2}}$$

or

$$\sin\theta_e = \sqrt{1 - \frac{(P_a - p_c - p_a + p_c)}{(P_a - p_c) \cdot C_{fc}^2}}$$

This can now be expressed in terms of previously defined parameters such that

$$\sin\theta_e = \frac{1}{C_{fc}} \cdot \sqrt{C_{fc}^2 - 1 + \phi} \tag{13}$$

Combining equations (11) and (13) leads to

$$A_e = A_{\text{geom}} \cdot \sqrt{C_{fc}^2 - 1 + \phi}/C_{fc}$$

A view factor V_f can now be defined where

$$V_f = A_e/A_{\text{geom}} = \frac{\sqrt{C_{fc}^2 - 1 + \phi}}{C_{fc}} \tag{14}$$

An Expression for Coefficient of Discharge. If effects of Reynolds number and compressibility are temporarily ignored, then a coefficient of discharge C_d can be defined

$$C_d = \frac{m}{\rho \cdot V_j \cdot \text{geometric area of hole}} \tag{15}$$

and where

$$C_d = C_{fc} \cdot V_f \tag{16}$$

C_d, together with its component factors C_{fc} and V_f, is shown in Fig. 3. The new discovery that C_d is a compound function, having factors with opposing trends, could explain why the previous investigators only met with partial success.

Adjustment for Liner Wall Curvature. Most combustor liners are cylindrical and this can lead to a small error in the assessment of cross-sectional area of the holes. The need for an adjustment factor depends on the manner in which the liner is manufactured. For instance, if circular holes are machined through a flat sheet before it is made cylindrical then no adjustment is necessary. Conversely, holes machined through the wall of a preformed cylinder will remove a surface area which is greater than the cross-sectional area of the boring tool. Reference to Fig. 4 makes the reason for this apparent: The arc AA is clearly longer than the chord AA. An area adjust-

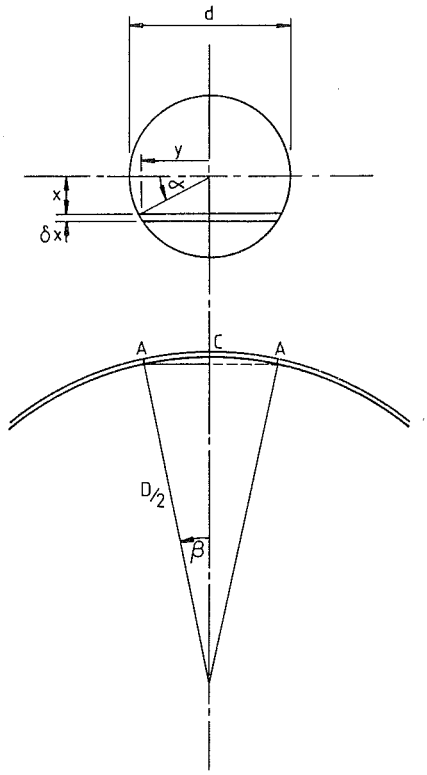

Fig. 4 Curvature correction

ment factor f was derived in order to convert the plan area into the cylindrical surface area through which the air supply passes into the liner.

The plan view in Fig. 4 shows an element of thickness δx which is at a distance of x from the center and which subtends an angle α with the transverse diameter. The projected distance y along the diametral line corresponds to an arc of length AC on the cylindrical surface which, in turn, subtends an angle β at the center of the liner. This arrangement leads to the following trigonometric relationships

$$y = d/2 \cdot \cos\alpha = d/2\sqrt{1-\sin^2\alpha}$$

or

$$y = d/2\sqrt{1-(2x/d)^2}$$

$$\beta = \sin^{-1}(2y/D)$$

$$\text{arc AA} = D \cdot \beta$$

Substituting for y and β gives

$$\text{arc AA} = D \cdot \sin^{-1}\left[\frac{d}{D}\sqrt{1-(2x/d)^2}\right]$$

Replacing the chord, length $2y$, by the length of arc AA leads to the integral expression for the curved surface area

$$2 \cdot D \cdot \int_0^{d/2} \sin^{-1}\left[\frac{d}{D}\sqrt{1-(2x/d)^2}\right] dx$$

The area of the circular plan $= \pi \cdot d^2/4$.

The adjustment factor f is defined as

$$f = \frac{\text{circumferential surface area}}{\text{circular plan area}}$$

Numerical integration was used to compute the curve of factor f shown in Fig. 5. In order to simplify the direct use of this factor, the quadratic equation (17), given in the figure, was fitted to the computed curve with an agreement of better than 0.1 percent.

Parameters Relating Directly to Mass Flow. Supposing

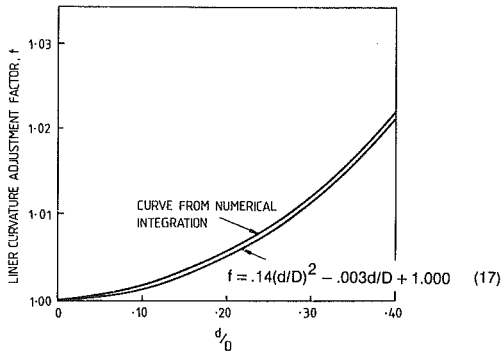

Fig. 5 Adjustment factor

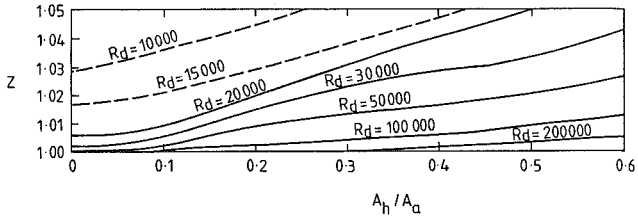

Fig. 6 Reynolds number correction (after [5])

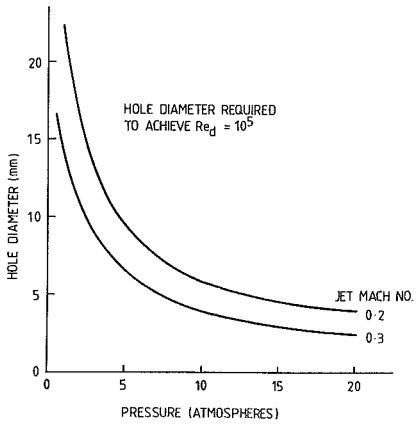

Fig. 7 Hole size for similarity

that there are n holes around the circumference at a particular axial location of the liner, then the total geometric area A_s available for flow ingestion at this station is

$$A_s = n \cdot A_h \tag{18}$$

A porosity ratio X was then defined as

$$X = A_s/A_a \tag{19}$$

Here, A_a is the area of the supply duct.

This factor X is used in conjunction with the ingestion ratio I which is the quantity of approach air ingested at the particular axial plane divided by the air mass flow immediately upstream of this plane, viz.

$$I = m_s/m_a \tag{20}$$

Typically, for gas turbine combustors, the value of I will vary from 0.3 for the secondary holes supplying the primary zone to unity for the final dilution holes.

The use of the ratio I/X is recommended for combustor design and development calculations since the mass flow entering the liner at a particular axial station can be determined without first obtaining a value for C_d. It is for this reason that some of the experimental data will be found correlated in terms of I/X.

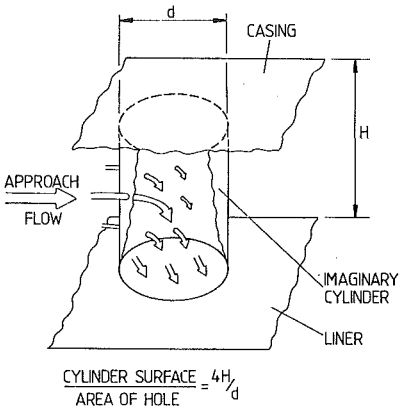

Fig. 8 Casing interference

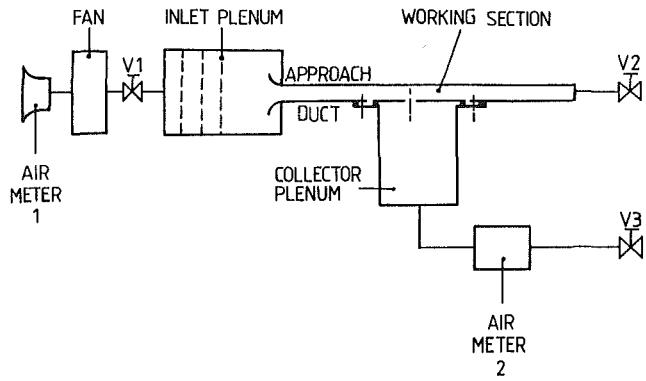

Fig. 9 Experimental arrangement

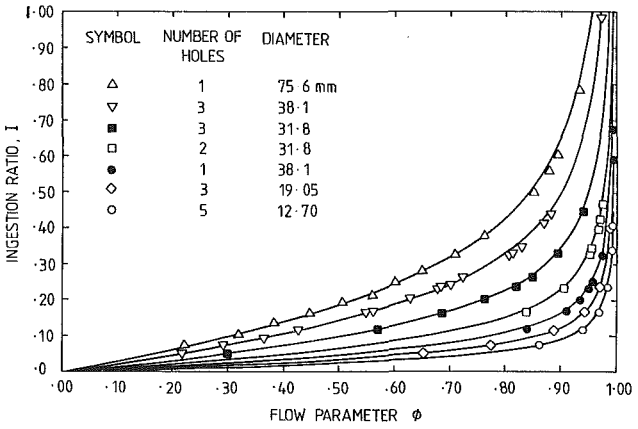

Fig. 10 Individual data

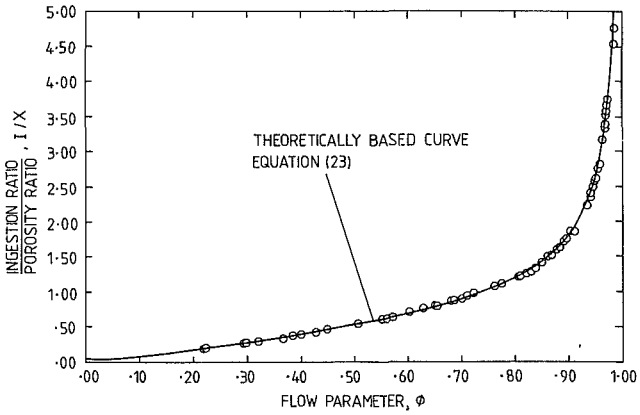

Fig. 11 Mass flow correlation

Practical Considerations

In the literature review given in [6], the author suggested that many of the discrepancies in previous data arose from the diversity of experimental techniques. Care was therefore taken to try and avoid the many practical pitfalls during his own experiments, the data from which are used later in this paper. Consideration was given to the following items:

(i) **Compressibility.** In his deliberations of flow through orifice plates, Ward Smith [7] stated that compressibility effects reduced the contraction downstream of the hole (i.e., compressibility increases the value of C_c).

To obtain high engine efficiency, combustor liner pressure drops are seldom allowed to exceed 6 percent of the total pressure of their supply air. This limits the ratio of total pressure upstream to static pressure downstream of the hole to around 1.064, giving a maximum jet Mach number in the order of 0.30. At these values compressibility effects will not be very significant. The present experimental data, however, were obtained at typical engine combustor Mach numbers.

(ii) **Reynolds Number R_d.** Hole diameter d was an obvious choice for the linear dimension in this parameter, such that

$$R_d = \rho_a \cdot v \cdot d/\mu_a \tag{21}$$

Figure 6, derived from data relating to orifice flow meters [5], shows how a correcting multiplier z varies with the ratio of upstream area contraction, assuming that this also applies to the present work and that the area ratio corresponds to parameter X. In practice, X is unlikely to exceed a value of 0.3. It can then be deduced from these curves that the correction multiplier will be lower than 1.01 so long as R_d exceeds 10^5; the high pressure ratio and mass flows used in current engines ensure values of R_d well in excess of this. Laboratory test conditions, however, which have to economize both on mass flow and pressure, could be significantly lower. Accordingly, Fig. 7 was generated to show how hole diameter must be increased in order to maintain a value of R_d of 10^5 and so compensate for test conditions. Two curves are shown representing the extremes of jet Mach number at the hole. The experiments in [6] were dissimilar to previous ones in that hole sizes were scaled up to avoid discrepancies arising from Reynolds number.

(iii) **Hole Proximity.** The holes were spaced at least two diameters apart to avoid interference between adjacent holes and also between their approach flows.

(iv) **Liner Thickness t.** Data published in [2] indicate that coefficient of discharge is independent of wall thickness so long as the fraction t/d does not exceed 0.10. Accordingly, this limitation was adhered to during the present investigation.

(v) **Approach Duct Height H.** If approach duct height is insufficient it will interfere with the flow as illustrated in Fig. 8.

Here, for simplicity, it is considered that the flow entering the hole must first pass through the wall of an imaginary tube, located between the hole and the casing wall. Clearly, if the flow area through the tube wall is less than or even comparable to the area of the hole, then interference must occur. At very low velocities of approach the flow may be considered as passing through the complete wall of the tube whereas at high approach velocities the flow would only pass through sections facing upstream and its effective flow area could then be less than one quarter of the tube surface.

Accordingly, the present tests were confined to values of the fraction H/d in excess of 1.00.

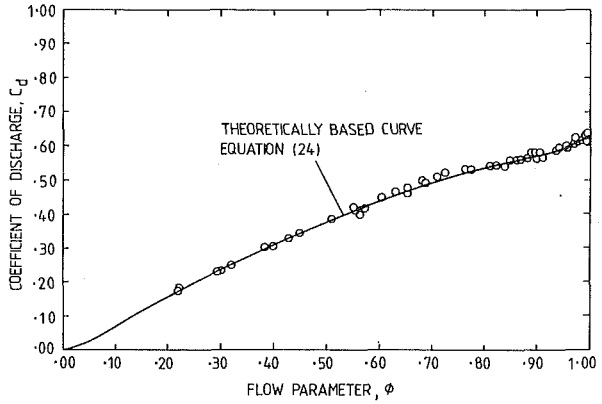

Fig. 12 Correlation for discharge coefficient

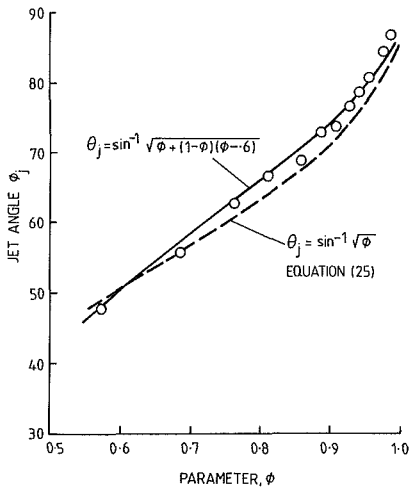

Fig. 13 Angle correlation

(*vi*) **Manufacture of Hole.** Particular care was taken to keep the edges of the holes perpendicular and sharp because it is known that any chamfer or radius on the edge of a hole will significantly increase the value of C_d.

Experimental Investigation

This is only described briefly here as a fuller description can be found in [6]. A line diagram of the test rig is shown in Fig. 9. The test holes were made in a set of interchangeable flat plates, 1.6 mm thick, which formed the floor of a small wind tunnel of section 227 mm wide by 56 mm high. The holes were located in a single row at a distance of 380 mm downstream from the beginning of the floor in order to ensure a fully developed turbulent boundary layer.

Air flowing through the holes was collected in a plenum chamber, made sufficiently large so as to avoid high recirculatory velocities which otherwise would interfere with both jet penetration and static pressure evaluation.

Air meters 1 and 2 were installed according to [5] so that they would have an individual accuracy of better than 1.5 percent. The accuracy was improved, however, by temporarily closing valve 2 so that all the air passed through both air meters so that they could be cross-calibrated.

Static pressure measurements from all tappings were made using a micromanometer which could discriminate down to 0.1 mm of water gauge. Total pressures in the test tunnel were derived from measurements of mass flow, static pressure, and the local airstream temperature.

A sliding plate, with seal, was later [8] located on the side of the plenum to act as a mounting point for a five-hole probe. The head of the probe was inserted so that it was 10 mm below the test hole and then the plate was slid axially until a maximum pressure signal was obtained. The probe was then rotated until a null differential between its two side holes indicated that it was in line with the jet direction. The jet angle was then measured from a protractor, attached to the mounting plate at the probe stem.

The following conditions were obtained during testing:

1 Reynolds numbers R_d greater than 10^5
2 Approach Mach numbers in the test tunnel of up to 0.10
3 Jet Mach numbers of up to 0.30
4 Values of porosity ratio X of up to 0.275
5 Values of ingestion ratio I in the range 0 to 1.00
6 Parameter ϕ in the range 0.2 to 1.00

Details of the test plate are tabulated below.

Plate number	Hole diameter d, mm	Number of holes	Ratio H/d	Ratio t/d	Porosity ratio X
1	12.7	5	4.41	0.126	0.0498
2	19.05	3	2.94	0.084	0.0673
3	31.75	3	1.76	0.050	0.1868
4	31.75	2	1.76	0.050	0.1246
5	38.1	1	1.47	0.042	0.0897
6	38.1	2	1.47	0.042	0.1794
7	38.1	3	1.47	0.042	0.2691

Data taken during testing were correlated against the pressure difference ratio ϕ and used to obtain the best value of constant k, which was subsequently found to equal 3.00.

All the test data, reduced to nondimensional parameters, are given in Figs. 10–13. Curves of ingestion ratio I are shown in Fig. 10, where data from the individual test plates are clearly identifiable and constitute smooth curves with a low level of experimental scatter.

All the data are then reduced to a single curve (Fig. 11) by use of the ratio I/X, and this curve is identical to that derived using the theoretical considerations where

$$I/X = f \cdot C_{fc} \cdot V_f \cdot (1-\phi)^{-0.5} \tag{22}$$

where $f = 1.00$ for a flat plate.

Alternatively this can be expressed in terms of the pressure difference ratio ϕ as follows

$$\frac{I}{X} = f \cdot \sqrt{\frac{C_{fc}^2 - 1 + \phi}{1-\phi}} \tag{23}$$

$$C_{fc} = \{1 - \exp(-1) + \exp(-1/\sqrt{1-\phi})\} \cdot \left[1 - \frac{\phi \cdot (1-\phi)}{3}\right]$$

In practice, equation (23) has been found particularly convenient because it does not involve calculation of intermediate quantities such as density or coefficient of discharge. The fraction I/X can be used directly to give the unknown quantity whether it is the area of holes in the liner (in the design case), or the local ingested mass flow (in the analysis case).

The steepness of the curve, for values of ϕ between 0.90 and 1.00, which correspond to dilution holes, is of interest. It indicates that a slight perturbation in the pressure difference ratio has the potential to significantly change the distribution of flow into the liner. Furthermore small pressure fluctuations that occur in engines could be amplified by this characteristic and result in combustor instabilities.

In Fig. 12 all the experimental data are compared with the theoretical curve for coefficient of discharge C_d and the agreement is well within experimental limits. The analysis is further supported by its ability to predict the inflection which was obtained for values of ϕ between 0.7 and 1.0. In terms of the pressure difference ratio ϕ, the equation for this curve is given as

$$C_d = f \cdot \sqrt{C_{fc}^2 - 1 + \phi} \tag{24}$$

C_{fc} and f were given previously.

Figure 13 was derived from measurements of jet angle as described in [8] and it relates to a single hole of 38.1 mm diameter. The data are compared to the theoretical equation for jet angle at the vena contracta θ_j where

$$\theta_j = \sin^{-1}\sqrt{\phi} \tag{25}$$

The difference probably arises due to the fixed location of the probe, at 10 mm downstream of the hole, where it was unlikely to coincide with the vena contracta over the whole range of the test conditions. A second curve, based on an empirical modification to the theoretical curve, is included in the figure.

Conclusion

The flow through plane circular holes with parallel approach flow has been the subject of a theoretical and experimental investigation. As a result, accurate equations for mass flow, the coefficient of discharge, and the angle of the jet have been established.

The above parameters are shown to be dependent on a single pressure drop ratio ϕ which is recommended as a basis for correlations.

References

1 Callaghan, E. E., and Bowden, D. T., "Investigation of Flow Coefficients of Circular, Square and Elliptical Orifices at High Pressure Ratios," NACA TN, 1947.

2 Dittrich, R. T., and Graves, C. C., "Discharge Coefficients for Combustor Liner Air Entry Holes, I. Circular Holes With Parallel Flow," NACA TN 3663, 1949.

3 Kaddah, K. S., "Discharge Coefficients and Jet Deflection Studies for Combustor Line Air Entry Holes," M.Sc. thesis, CIT, 1965.

4 Seglem, C. E., "The Discharge Coefficient of a Combustor Air Inlet Hole," M.Sc. thesis, Pittsburgh, 1952.

5 "Measurement of Airflow," British Standard Code of Practice No. BS 1042.

6 Gueroui, D., "The Performance of Combustor Liner Air Inlet Holes in Uniform and Distorted Flow," M.Sc. thesis, CIT, Sept. 1982.

7 Ward Smith, A. J., "Pressure Losses in Ducted Flows," Butterworth, London.

8 Coq, P., and Carcasses, A., "The Performance of Combustor Liner Air Admission Holes in Uniform and Distorted Flows," Unpublished report, SME CIT, June, 1983.

S. Lloyd
Department of Mechanical and Manufacturing Systems, University of Wales Institute of Science and Technology, Cardiff CF1 3NU, United Kingdom

A. Brown
School of Mechanical, Materials and Civil Engineering, Royal Military College of Science, Shrivenham, Swindon, Wiltshire SN6 8LA, United Kingdom

Velocity and Turbulence Fields in Pipe Entrance Regions in the Presence of Cross Flows

This paper reports on an experimental investigation into the velocity and turbulence fields in the entrance region of a circular pipe with cross flow at the entry. The pipe entry is a sharp square-edged type with air as the working fluid and measurements are made over the region $0<X/D<21$. Observations are presented for a range of cross flows with a maximum Reynolds number, based on pipe diameter, of 64,000. The hot-wire anemometer measurements show a separated nonaxisymmetric flow at entry followed by a skewed flow which progressively smooths out with distance along the pipe.

Introduction

The fluid flow characteristics in the entrance regions of a pipe at entry to which the fluid has some cross flow, that is, a transverse velocity at pipe entrance, are of particular relevance to cooled turbine blades whose internal passages are branched from the blade root. Although cooled turbine blades have been in service for about 30 years knowledge of the internal fluid mechanics is still limited in comparison with the amount of available data describing the external hot gas paths. Flow from a supply duct or manifold into branch tubes is a situation occurring in a wide variety of applications; however, despite the prevalence of this flow arrangement, an exhaustive literature search has failed to uncover previous studies into such fluid flows.

Metzger and Corado [1] are the only researchers to offer data to predict the enhanced heat transfer rates in a pipe fed with cross flow. Their investigation showed a significant effect of cross flow on the heat transfer in short tubes with the heat transfer enhancement increasing with the cross flow to pipe velocity ratio. Although not directly applicable, Sparrow and Kermink [2] observed the heat transfer rates in the supply duct downstream of a fluid withdrawal branch attributing the enhanced heat transfer to an induced secondary flow arising from the fluid extraction process. However, no detailed flow measurements were made.

The term "cross flow" usually encountered in the literature concerned with turbine blade components refers to either film cooling and/or impingement heat transfer. In such situations jet impingement on the inside of the suction or pressure surface is influenced by the cross-flowing "spent" fluid from the leading edge jets. However, such studies are concerned with a combining flow and should be distinguished from the observations reported in this paper where essentially the flow is dividing. The effect of cross flow at entry to film holes has been examined by a number of workers typical of which is the work reported by Florschuetz and Isoda [3] and Chu et al. [4]. However, film-cooling hole geometry is substantially different from that of convection cooling tubes and little is known of the flows inside the holes. The flow measurements for such holes are related to general flow characteristics and entry and exit plane distributions.

This paper presents experimental measurements of velocity and turbulence intensity fields within a pipe with cross flow and reveals the relative importance of the cross flow to pipe velocity ratio on their distributions. It is hoped that this work will act as a catalyst for further studies to provide further applicable design data for turbine blade internal cooling passages.

Experimental Rig and Experimentation

The apparatus used was modified from that employed in a previous investigation into the velocity profiles in the entrance region of a circular pipe with a sharp square-edged entrance [5]. A line drawing of the apparatus is shown in Fig. 1. Essen-

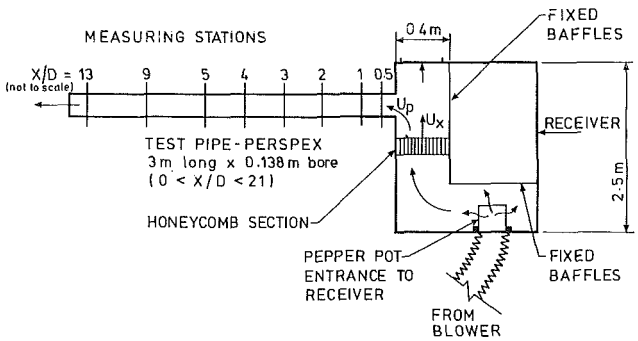

Fig. 1 Line diagram of the apparatus

Contributed by the Gas Turbine Division of THE AMERICAN SOCIETY OF MECHANICAL ENGINEERS and presented at the 31st International Gas Turbine Conference and Exhibit, Düsseldorf, Federal Republic of Germany, June 8–12, 1986. Manuscript received at ASME Headquarters January 22, 1986. Paper No. 86-GT-119.

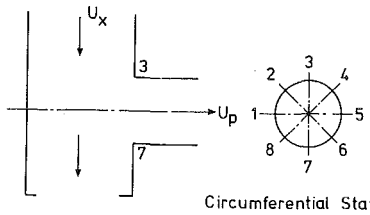

Fig. 2 Notation of circumferential measuring stations

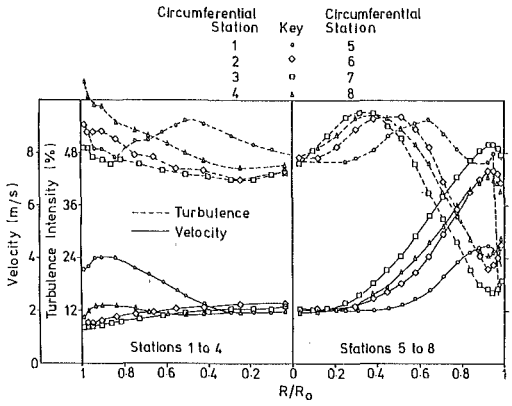

Fig. 3 Typical set of measurements

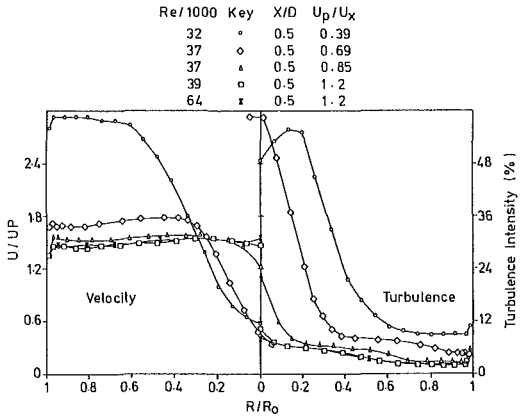

Fig. 4 Nondimensional velocity and turbulence profiles for circumferential station 7 at $U_r = 0.39$

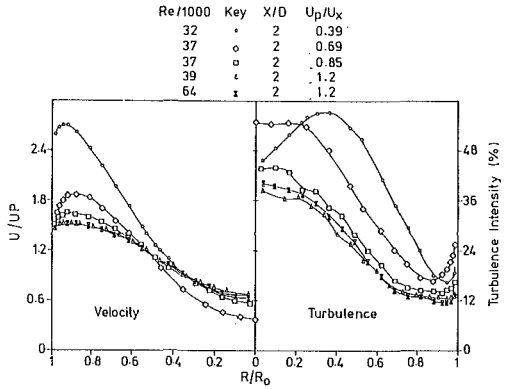

Fig. 5 Nondimensional velocity and turbulence profiles for circumferential station 7 at $U_r = 0.69$

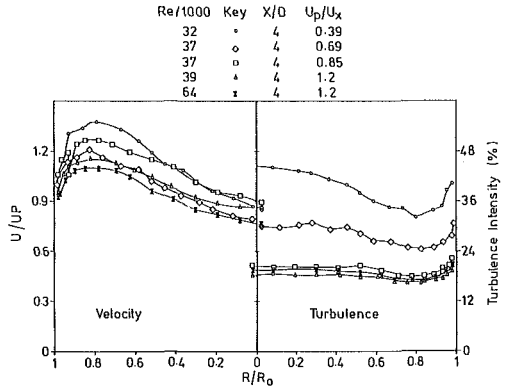

Fig. 6 Nondimensional velocity and turbulence profiles for circumferential station 7 at $U_r = 0.85$

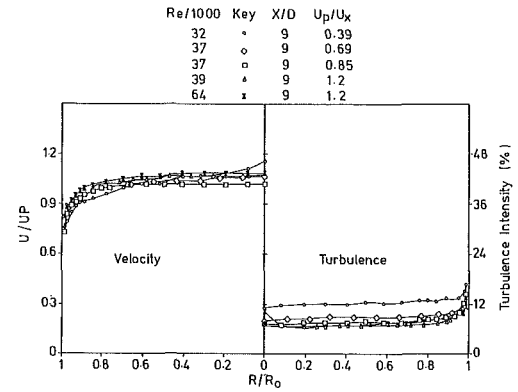

Fig. 7 Nondimensional velocity and turbulence profiles for circumferential station 7 at $U_r = 1.2$

tially the apparatus comprises three principal components: (*i*) a three-speed blower; (*ii*) a receiver; (*iii*) the test pipe.

The flow rate to the receiver was varied by selecting one of the three blower speeds and/or constricting the intake with one of a variety of specially made grids. This was found to give a more repeatable flow rate than could be achieved by throttling the blower's gate valve.

The pipe for velocity and turbulence measurements was made of perspex with measurement stations at X/D equal to 0.5, 1, 2, 3, 4, 5, 9, 13, 17, and 21. Measurement of velocity and turbulence intensity profiles was via a miniature single hot-wire anemometer which could be traversed along a radial line from wall to center line and turned around the probe axis. The ability to rotate the probe around its axis is very important when using a single hot wire to measure velocity in a three-dimensional flow situation. The pipe was flanged to the receiver wall in such a way that it was possible to index the pipe about its axis to give eight evenly spaced locations around its circumference in which to make velocity measurements.

For the study in the absence of cross flow, the receiver had a "pepper-pot" entrance, fixed baffle plates, and a honeycomb section to ensure a straight flow at pipe entry. The modified layout shown in Fig. 1 was arrived at so as to achieve a

Nomenclature

D = pipe diameter
R = radial position measured from the pipe center line
R_0 = pipe radius
Re = Reynolds number based on mean pipe velocity and pipe diameter = $U_p D/\nu$
U = local axial velocity
U_p = mean pipe flow velocity
U_x = supply flow velocity normal to the pipe axis
U_r = pipe flow velocity ratio $= U_p/U_x$
X = distance measured along the pipe from entry

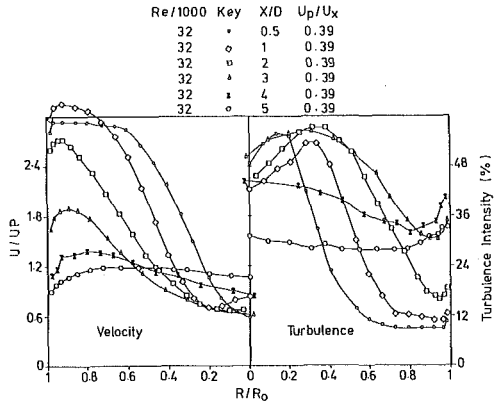

Fig. 8 Development of the flow over the first five diameters at circumferential station 7 for $U_r = 0.39$

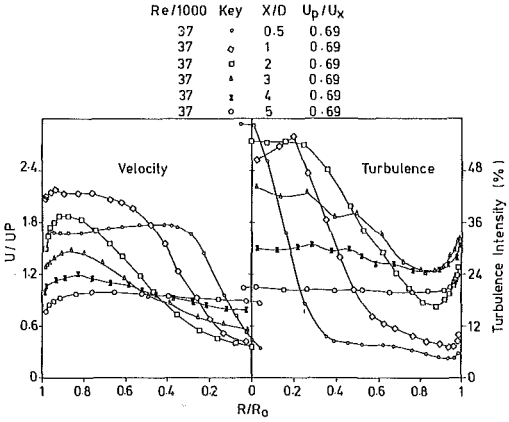

Fig. 9 Development of the flow over the first five diameters at circumferential station 7 for $U_r = 0.69$

representative cross flow velocity range. The range of cross flow velocity ratio U_r ($= U_p/U_x$) necessary to model engine conditions is $0 < U_r < 1$ and typical values of Reynolds number are $20{,}000 < \mathrm{Re} < 150{,}000$. The minimum velocity ratio used in the present investigation was limited to 0.4 which occurred at the highest delivery from the blower. This minimum cross flow ratio could have been further reduced by lessening the flow area within the receiver. However, this was thought imprudent as further reduction of this flow area would have resulted in the area of the supply manifold approaching that of the test pipe. In addition, with a smaller receiver flow area the boundary layer growth within the supply duct could become a significant factor and less representative of the situation in a turbine blade root.

The Reynolds number based on the mean pipe velocity at the minimum cross flow velocity ratio was approximately 32,000. The aim of the investigation was to measure the velocity and turbulence characteristics over a range of both Reynolds numbers and cross flow ratios. However, from the previous work undertaken by the authors in entrance region axial flows and reported in [5], it was thought that the velocity profiles within the pipe would be more sensitive to the cross flow velocity ratio than the pipe Reynolds number. Thus, for the initial observations it was decided to vary the cross flow ratio at a single pipe Reynolds number and then at one of the cross flow ratios, two pipe flow rates and, therefore, two values of pipe Reynolds number were used to assess the significance of Reynolds number on the flow.

At the nominal Reynolds number of 32,000, a range of velocity ratios was established, namely 0.39, 0.69, 0.85, and 1.2 with the highest velocity ratio also used at a Reynolds number of 64,000.

The notation adopted to describe measurement positions is shown in Fig. 2. The eight circumferential positions are

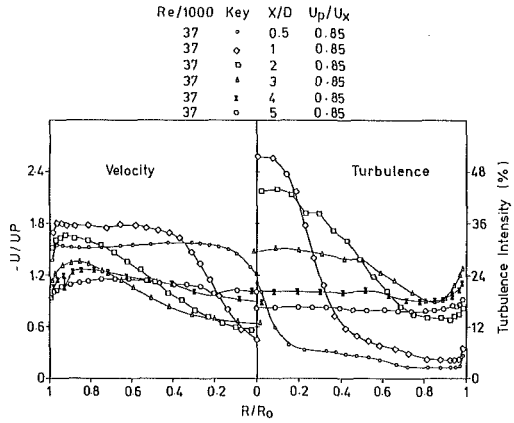

Fig. 10 Development of the flow over the first five diameters at circumferential station 7 for $U_r = 0.85$

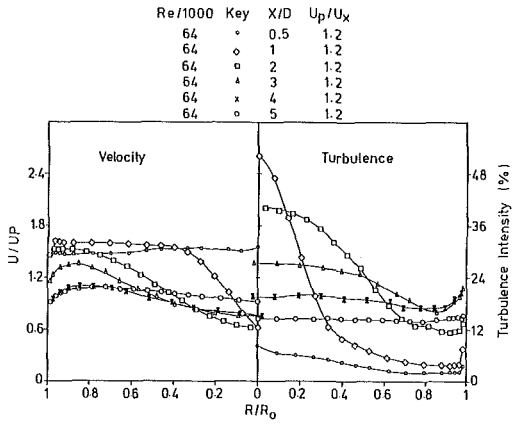

Fig. 11 Development of the flow over the first five diameters at circumferential station 7 for $U_r = 1.2$

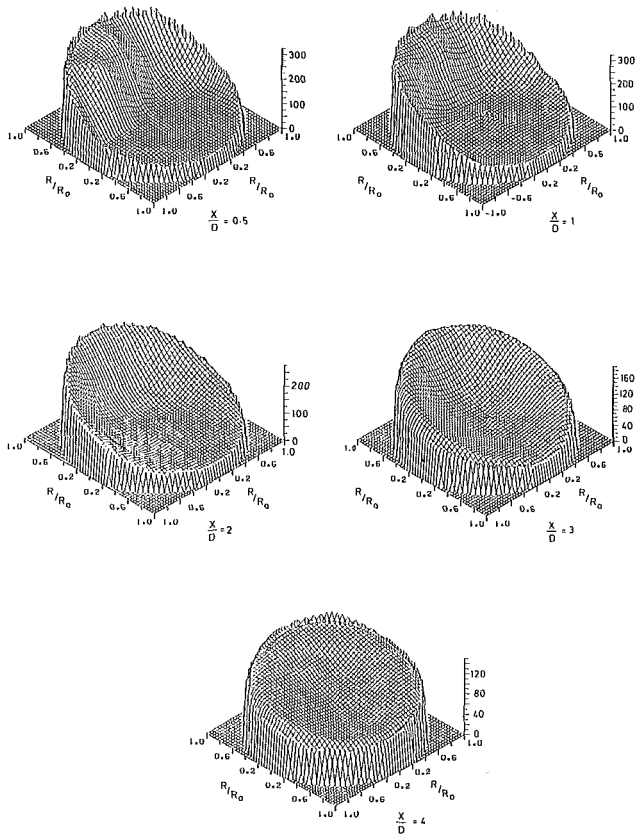

Fig. 12 Three-dimensional representation of velocity profiles over the first four diameters for $U_r = 0.39$

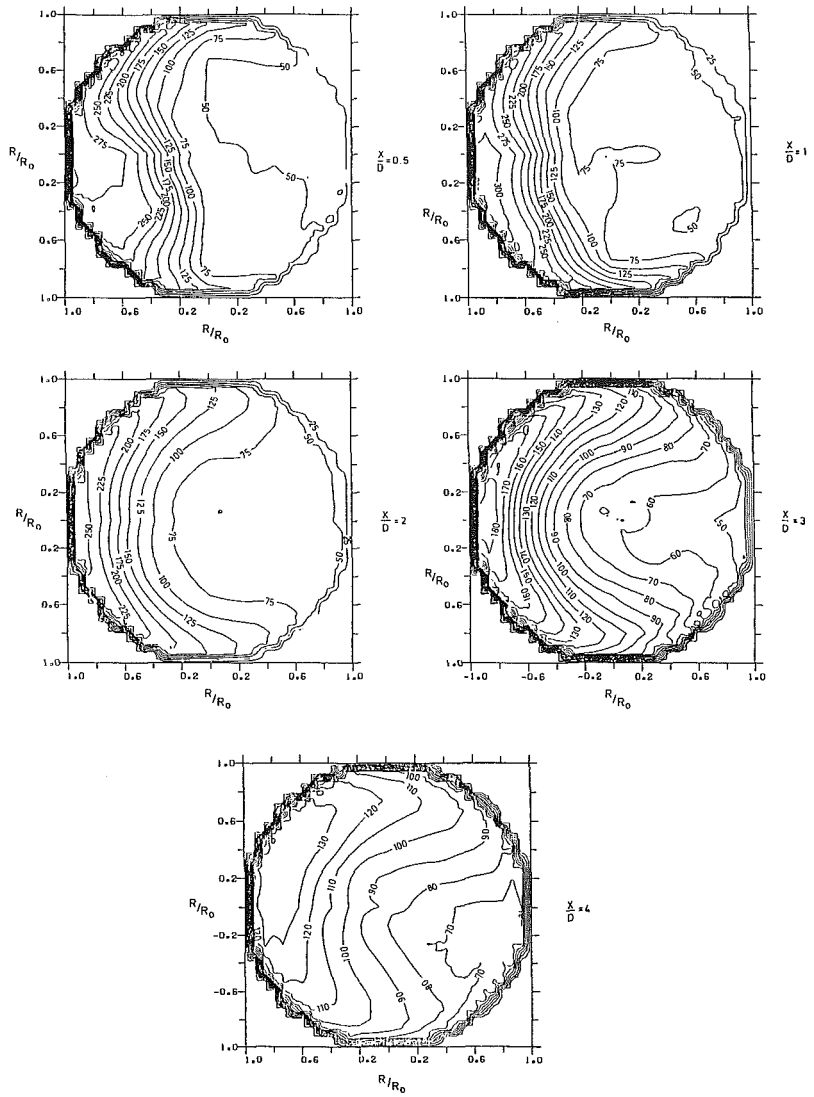

Fig. 13 Velocity contours of the first four diameters for $U_r = 0.39$

numbered clockwise from the top of the pipe, when viewed from the test pipe outlet.

Results and Discussion

A typical set of measurements is shown in Fig. 3 in the form of velocity and associated local turbulence intensity profiles at eight circumferential positions for a Reynolds number of 32,000 and cross flow ratio $U_r = 0.39$ at $X/D = 2$. As can be seen the maximum velocity occurs in the radial distribution for circumferential station 7 with the minimum in the station 3 distribution. The plot is basically symmetric about this 7-3 plane which is the plane parallel to the direction of the cross flow, that is, the velocity distributions for stations 6 and 8 are nearly equal as are those for 5 and 1, and 4 and 2. The local turbulence levels are extremely high approaching 55 percent over the majority of the pipe section, but falling sharply within the skewed jet at the wall for circumferential station 7. Such levels of turbulence are indicative of regions of flow reversal and recirculation. The hot-wire anemometry system will not yield accurate velocity measurements in such disturbed flows. As the signal from the hot wire is rectified it is to be expected that the indicated mean values should be high and the rms quantities low at indicated levels of turbulence greater than about 30 percent. In recirculating flows this phenomenon is even more prominent. However, as observed by Simpson et al. [6], the magnitude of the discrepancies need not preclude valid fluid mechanic conclusions.

With the peak velocity occurring in the radial distribution for circumferential station 7, the velocity profiles at this station were examined further. Figures 4 to 7 give nondimensional velocity and turbulence profiles for circumferential station 7 for the four cross flow ratios of 0.39, 0.69, 0.85, and 1.2 at X/D equal to 0.5, 2, 4, and 9, respectively, although measurements were also recorded for X/D of 1, 3, and 5. The mean velocity was determined from a graphic integration of the velocity profiles at X/D equal to 9 where the turbulence levels were relatively low, thus ensuring accurate velocity measurement. It was found that extremely high turbulence levels extended up to four diameters from entry before starting to subside. The effect of the cross flow velocity ratio on the velocity characteristic is considerable whereas, as anticipated, the Reynolds number dependence appears weak with the plots for $U_r = 1.2$ at Reynolds numbers of 39,000 and 64,000 being almost coincident. The measured peak velocity increased with reduced pipe to transverse velocity ratio for $X/D < 3$. At X/D equal to 4 and 5 this pattern of the velocity profiles was not so pronounced; the general levels of turbulence were higher than those at $X/D < 3$ although less peaky near the center line. At $X/D = 9$ the difference between the velocity profiles is slight although the turbulence levels are still higher for lower U_r.

The development of the flow over the first five diameters at circumferential station 7 for the four cross flow ratios is shown in Figs. 8–11. For each condition the jetlike profile is seen to contract from $X/D = 0.5$ to 1 where the maximum

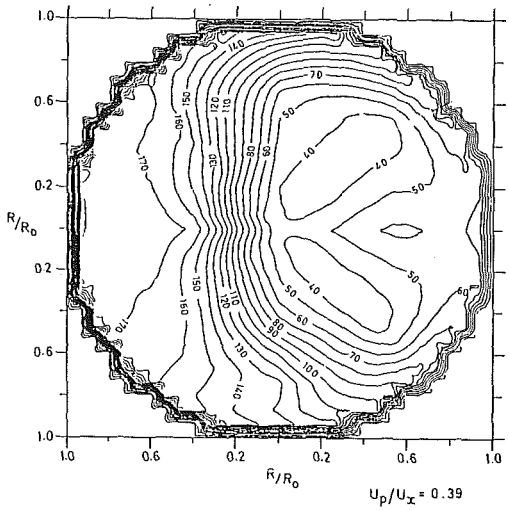

Fig. 14 Velocity contours at $X/D = 1$ for $U_r = 0.85$

velocity is achieved. The peak then reduces along the pipe but is still in evidence at $X/D = 4$. Initially when the fluid enters the pipe the turbulence levels at the apex of the jet are relatively low but increase as the jet narrows further under the influence of mixing with the neighboring fluid. The level of turbulence within the jet at entry increases with reduced cross flow velocity ratio.

The presentation so far has concentrated on the path and form of the fluid at a single circumferential station. However, further examination of the data revealed asymmetry in some instances. Interpretation of the flow was difficult and therefore a computer program was developed to promote a better feel for the situation. The program enabled two types of plots to be generated: (*i*) a "topographical" or three-dimensional plot, and (*ii*) a map of constant velocity contours. The plots can display both velocity and turbulence quantities but the velocity characteristics only will be considered here. Figure 12 gives the three-dimensional representations while Fig. 13 shows the corresponding velocity contours within the first four diameters at $U_r = 0.39$. The velocity contours are labeled as a percentage of the mean pipe velocity. These plots demonstrate that the regions of higher velocity emanating from the initial skewed jet develop around the walls of the pipe engulfing a pocket of lower velocity fluid. Although the magnitude of the jet varies with U_r these patterns are similar at the other cross flow ratios. Figure 14 shows the velocity contour plot at $X/D = 1$ and $U_r = 0.85$, the plot clearly shows two zones of relatively low velocity being enveloped. Such patterns are synonymous with strong secondary flow as was suggested by the levels of turbulence. Indeed there appears to be a vortex pair, a phenomenon prevalent for flow in curved pipes [7], which is similar to this area of investigation. Further along the pipe at $X/D = 4$ the flow field has changed significantly as can be seen from Fig. 15 for $U_r = 0.69$, 0.85, and 1.2. The zone of maximum velocity has moved toward circumferential station 8. It appears that the supply cross flow has induced a swirl within the pipe. This accounts for the observations at $X/D = 4$ for circumferential station 7 where it was noted that the maximum velocity did not follow the same pattern exhibited upstream, an inverse relationship with U_r. The maximum velocity position had shifted away from its original position at this distance along the pipe. To further illustrate the nature of the flow within the pipe some limited flow visualization studies were carried out which tended to agree with the hot-wire measurements.

The essential difference between the characteristics of the flows with and without cross flow at entry is the degree of secondary flow. Without cross flow at entry the core is irrotational and the pressure gradient from the core serves to promote secondary flow within the boundary layer (see Lloyd and Brown [5]). With cross flow at entry an additional secondary flow is set up as a result of the curved path of the incoming flow. Fluid particles at lower velocities tend to move toward the center of curvature under centripetal acceleration. The cross flow to pipe velocity ratio determines the size of the skewed jet and thus the curvature of flow from the supply manifold to the branch tube. Thus at lower cross flow ratios the curvature of flow is greater resulting in higher secondary flows and associated turbulence at entry. This is endorsed by the heat transfer measurements of Metzger and Corado [1].

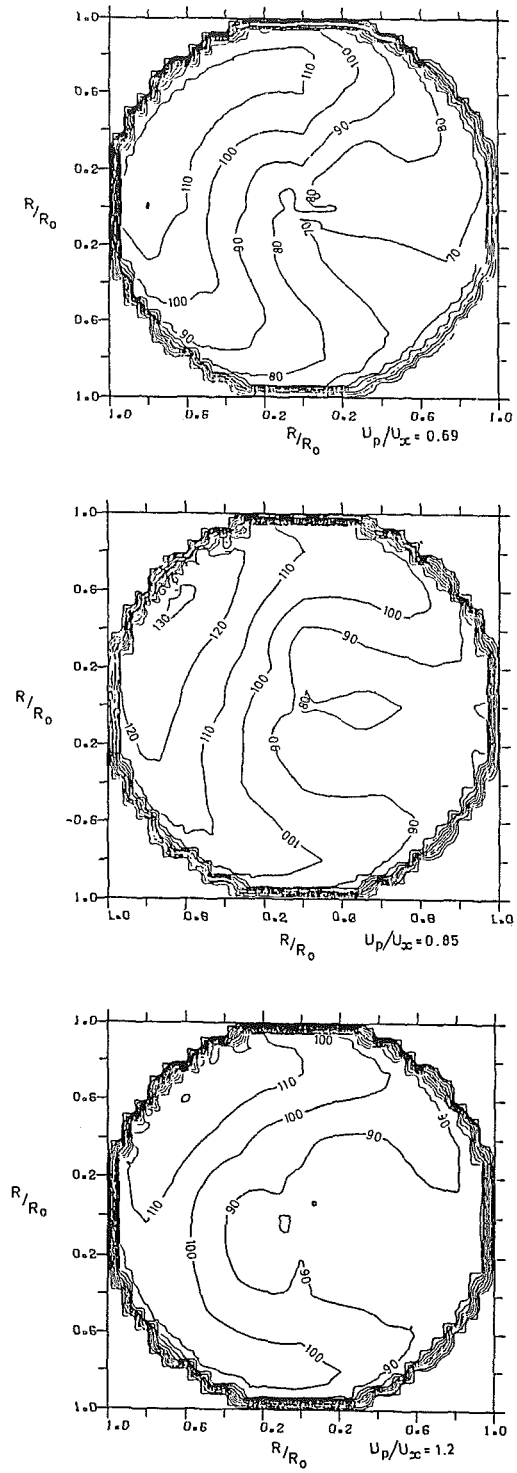

Fig. 15 Velocity contours at $X/D = 4$ for $U_r = 0.69$, 0.85, and 1.2

Conclusions

1 Over the range of experimentation the velocity characteristics are independent of Reynolds number although it is fair to say that this was not unexpected.

2 The velocity characteristics within the pipe are grossly affected by the cross flow to pipe velocity ratio. The velocity field is more peaky with reduced U_r as the size of the skewed jet at entry reduces with U_r.

3 At $X/D=4$ the position of maximum velocity has shifted by approximately 45 deg from that at $X/D=0.5$. There appears to be a swirling flow set up as the result of the cross flow at entry. The authors do not think that the swirling flow is the result of residual swirl in the approach flow in the receiver.

4 For lower U_r stronger secondary flows are evident in the first three diameters than further along the pipe.

5 Comparison between the velocity characteristics for entrance region flows with and without cross flow at entry show far greater disturbance when cross flow is present. The three-dimensional plots of Fig. 12 serve to show the gross distortion in the flow of the current investigation.

Acknowledgments

The authors are indebted to Dr. M. Ghassempory for his work during the development of the software to produce three-dimensional and velocity contour plots. The authors are also indebted to Mrs. S. Thompson, Mrs. J. Mosley, and Mrs. P. Jenkins for their help in preparing the article.

References

1 Metzger, D. E., and Corado, J. V., "The Effect of Cross Flow at the Entrance on Heat Transfer Enhancement in Tubes," ASME *Journal of Heat Transfer*, Vol. 103, 1981, pp. 178–179.

2 Sparrow, E. M., and Kermink, R. G., "Heat Transfer Downstream of a Fluid Withdrawal Branch in a Tube," ASME *Journal of Heat Transfer*, Vol. 101, 1979, pp. 23–28.

3 Florschuetz, L. W., and Isoda, Y., "Flow Distribution and Discharge Coefficient Effects for Jet Array Impingement With Initial Cross Flow," ASME JOURNAL OF ENGINEERING FOR POWER, Vol. 105, 1983, pp. 296–304.

4 Chu, T., Brown, A., and Garrett, S., "Discharge Coefficients of Impingement and Film Cooling Holes," ASME Paper No. 85-GT-81.

5 Lloyd, S., and Brown, A., "Fluid Flow and Heat Transfer Characteristics in the Entrance Region of Circular Pipes," ASME Paper No. 85-GT-121.

6 Simpson, R. L., Strickland, J. H., and Barr, P. W., "Features of a Separating Turbulent Boundary Layer in the Vicinity of Separation," *Journal of Fluid Mechanics*, Vol. 79, 1977, p. 553.

7 Bradshaw, P., *Topics in Applied Physics—Turbulence*, Vol. 12, 2nd ed., New York, p. 123.

Thermal Mechanical Fatigue Life Prediction for Advanced Anisotropic Turbine Alloys

P. N. Pejsa
Materials Engineer.

B. A. Cowles
Materials Project Engineer.

United Technologies,
Pratt & Whitney,
Engineering Division—South,
West Palm Beach, FL 33402

The most severe stresses that turbine airfoils encounter are thermally induced by extreme temperature gradients and rapid thermal transients. These thermally induced stresses combined with mechanical loading produce thermal mechanical fatigue (TMF) cracking in the airfoil. Analysis of and life prediction for the complex loading situation is further complicated by the use of advanced anisotropic alloys in high turbine sections of modern aircraft engines. In an effort to better understand TMF behavior of these materials, a test program was conducted to simulate turbine airfoil conditions at critical locations. A damage parameter containing terms thought to be essential to the description of material response to TMF cycling was developed. The damage parameter consolidated the data within a factor of approximately 1.5×.

Introduction and Background

Gas turbine airfoils, particularly those immediately adjacent to the combustor in the high-pressure turbine, experience increasingly severe temperature and stress cycles in advanced military fighter aircraft engines. The higher thrust-to-weight ratios of these engines, which are largely achieved by increasing combustor exit temperatures, enhance the maneuverability of these aircraft. Hence, turbomachinery components are cycled faster and more frequently. Consequently, lives of high-pressure turbine airfoils are limited by a combination of cyclic thermal, centrifugal, and gas bending loads, or thermal mechanical fatigue (TMF).

Life prediction for the complex thermal and mechanical loading situation is further complicated by the use of advanced anisotropic alloys and protective coating systems in these engines. A number of approaches to the life prediction problem have been proposed [1–5]. A common postulate is that damage in a TMF cycle may be approximated at some "equivalent" temperature (e.g., the maximum cyclic temperature). However, these approaches are frequently limited to specific test conditions, requiring a large data base for a successful generalized TMF life prediction system.

High-pressure turbine alloys experience a wide variety of thermal and mechanical loading cycles depending upon the speed of the particular power transient and location on the airfoil. In addition, the phasing of the thermal and mechanical cycles varies, the extremes being completely in phase (Fig. 1) and completely out of phase (Fig. 2). Life prediction analyses and test experience indicate that the most deleterious case is the completely out-of-phase cycle due to the high mean stresses developed as a result of stress relaxation at the maximum cyclic temperature. Hence, TMF characterization of turbine alloys is frequently performed using out-of-phase strain and temperature waveforms.

In an effort to reduce the number of data required for TMF characterization of turbine airfoils, a hysteretic energy-based life prediction model has been developed at Pratt & Whitney.

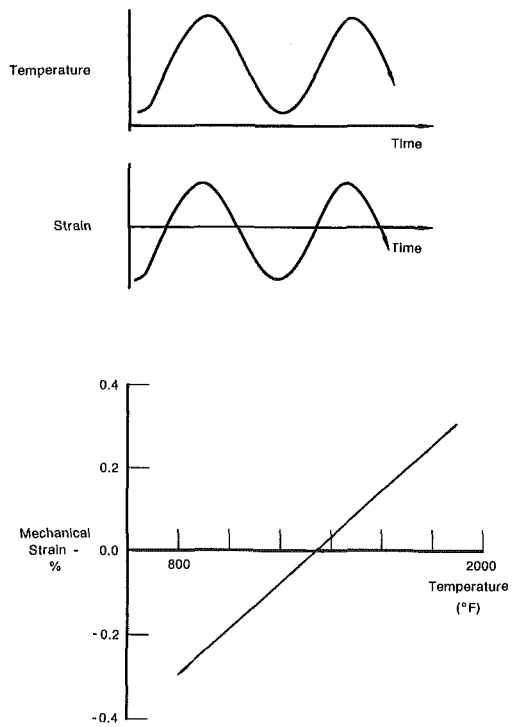

Fig. 1 In-phase strain and temperature waveforms

Contributed by the Gas Turbine Division of THE AMERICAN SOCIETY OF MECHANICAL ENGINEERS and presented at the 31st International Gas Turbine Conference and Exhibit, Düsseldorf, Federal Republic of Germany, June 8–12, 1986. Manuscript received at ASME Headquarters January 24, 1986. Paper No. 86-GT-124.

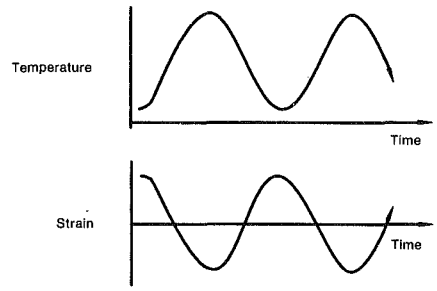

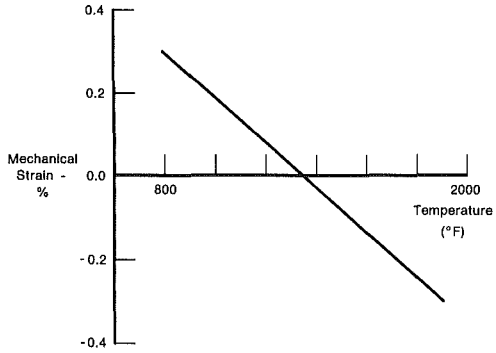

Fig. 2 Out-of-phase strain and temperature waveforms

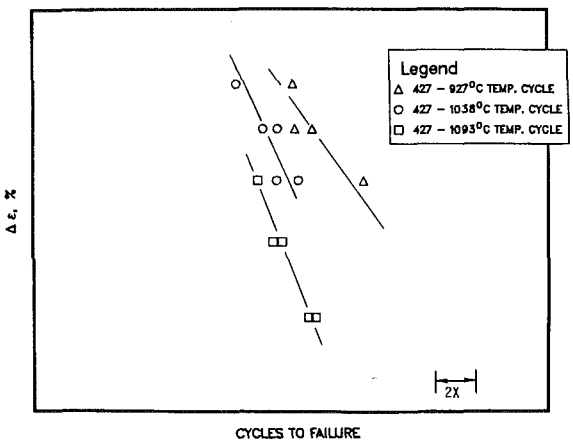

Fig. 3 TMF test results for out-of-phase strain-temperature testing

The model currently addresses the out-of-phase strain-temperature cyclic waveform (hereafter referred to as the Type 1 cycle), including variations in maximum cyclic temperature, total strain range, and associated changes in mean and peak stresses. Further development of the model is currently in progress under Air Force Materials Laboratory sponsorship [6].

Experimental Procedures

TMF data were collected using a system that features independent servocontrol of stress or strain and temperature. Test specimens were hollow and cylindrical. A low-frequency (10 kHz) 20 kW induction unit was used for heating, and desired cooling rates were achieved via conduction and both natural and forced convection. Temperature was maintained to within ±5°C of the command signal using closed-loop temperature control and an infrared pyrometer. A linear variable differential transformer (LVDT) was used to measure specimen deflection.

Since it is desirable to directly control mechanical strain rather than total strain in a nonisothermal test, a thermal expansion compensator was employed to subtract thermal strain voltages from the measured total strain feedback signal to produce the mechanical strain signal. Mechanical strains were controlled within ±2 percent of the operating range.

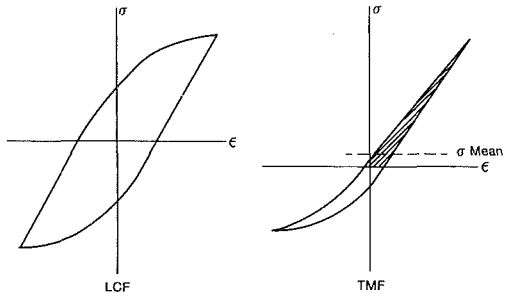

Fig. 4 Typical hysteresis loops for isothermal LCF and TMF testing

Experimental Results

Using the equipment described above, Type 1 TMF data were generated on PWA 1480, an advanced nickel-based single crystal alloy with an overlay coating. PWA 1480 turbine components are fabricated so that the primary loading direction coincides with the [001] axis of the alloy. Hence, test specimens were machined to the same specifications, with the angle between the longitudinal axis of the specimen and the [001] axis held to ±8 deg. Since alloying requirements for optimum strength and optimum oxidation resistance are not compatible, high-pressure turbine airfoils are typically coated to enhance the environmental stability of these high-strength materials. Hence, specimens were also coated. Although the coating essentially has no effect on the mechanical behavior of the substrate, coatings have been demonstrated to degrade TMF life. Future studies will investigate this behavior.

Three temperature ranges were investigated: 427–927°C, 427–1038°C, and 427–1093°C. Strain ranges varied from 0.4 percent and 0.8 percent. Testing frequency was 1 cycle per minute (cpm).

Test results are presented in Fig. 3, with observed lives plotted against total strain range (note: all data graphs are log scale on both axes). This method of presenting fatigue data has historically given good correlation for isothermal low cycle fatigue (LCF) data, and it is observed that data for any single TMF temperature range are well behaved and can be described using a typical power law relationship. However, when the three temperature ranges under study are compared, order-of-magnitude differences in life are observed at low strain ranges. Hence, a damage parameter based on strain range alone does not satisfactorily characterize TMF behavior, and alternative methods of quantifying damage must be investigated.

Discussion

To gain insight into the task of selecting a damage parameter capable of characterizing TMF behavior, it is useful to consider the stress–strain hysteresis loops that result from isothermal and nonisothermal strain controlled, $R = -1$ cyclic loading, as shown in Fig. 4. The isothermal loop (with a single frequency and no hold periods) is essentially completely reversed with respect to stress, while the TMF loop exhibits significant mean stresses, the magnitude of which depends on both strain range and temperature end points. Hence, a damage parameter that better describes the TMF cycle would comprise both stress and strain terms. A measure of cyclic damage containing both of these descriptors is hysteretic energy. This method of consolidating fatigue data has previously been proposed [7, 8] for elevated temperature, isothermal operating conditions. The model proposed here [9] for the consolidation of TMF data is based on some of this earlier work.

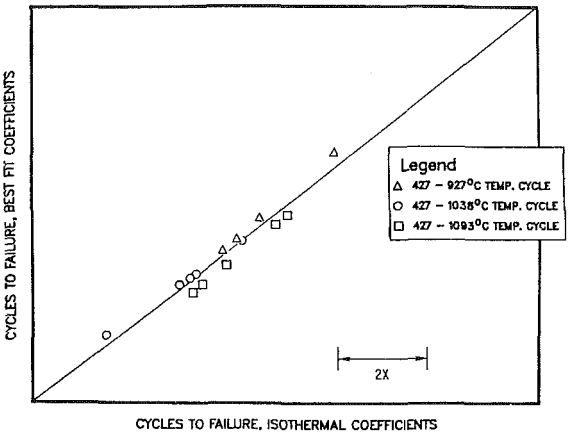

Fig. 5 Comparison of cycles to failure using isothermally determined and regressed inelastic strain constants

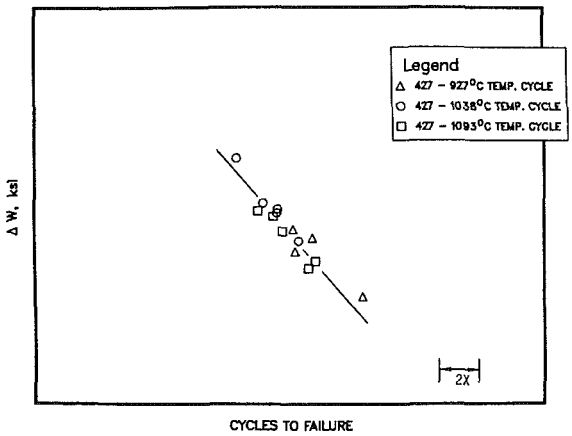

Fig. 6 Regression of cycles to failure using the hysteretic energy damage parameter ΔW

The cyclic hysteretic energy ΔW developed in the fatigue loading of a material may be expressed by the relationship

$$\Delta W = \int \sigma d\epsilon \tag{1}$$

It is postulated that damage is only incurred when micropores or other microstructural discontinuities in the cast material are pulled in tension. For the simplest case, with no closure effects, only the tensile portion of the energy contributes to damage. The relevant cyclic energy is then represented by the shaded portion of the TMF hysteresis loop depicted in Fig. 4, and the damage parameter takes the form

$$\Delta W = \int \sigma_T d\epsilon \approx (\sigma_T)(\Delta\epsilon_i) \tag{2}$$

where σ_T is the maximum stress ($=\sigma_{\text{mean}} + \Delta\sigma/2$), and $\Delta\epsilon_i$ is the inelastic strain range. ΔW is then assumed to be related to N_f, the number of cycles to failure, by

$$N_f = A(\Delta W)^B \tag{3}$$

where A and B are constants, which results in the equation

$$N_f = A((\sigma_{\text{mean}} + \Delta\sigma/2)(\Delta\epsilon_i))^B \tag{4}$$

The problem of determining the inelastic strain range developed in the TMF cycle is now addressed. Since Young's Modulus, E, is not constant but varies inversely with temperature, the portion of the total strain range that is inelastic is difficult to determine accurately. In an isothermal fatigue test, the inelastic strain range may be related to the applied stress range by

$$\Delta\epsilon_i = (\Delta\sigma/C)^D \tag{5}$$

and inelastic strains in the TMF cycles were approximated here using the isothermal data and this relationship. The inelastic strain coefficient C and exponent D were determined from completely reversed, strain-controlled fatigue data, and were evaluated at the midcycle temperatures: 677°C, 733°C, and 760°C for the 427–927°C, 627–1038°C, and 427–1093°C TMF temperature cycles, respectively.

The resultant expression for life depends *only* upon the stresses developed in the TMF mission cycle

$$N_f = A((\sigma_{\text{mean}} + \Delta\sigma/2)(\Delta\sigma/C)^D)^B \tag{6}$$

Furthermore, if the predominant effect of changing temperature endpoints or strain-temperature phasing in a TMF mission cycle is to cause a shift in the mean stress and stress range, then the proposed model will take into account variations in the thermal cycle imposed on the material. Time-dependent behavior that is reflected in changes in mean stress and stress range is also taken into account with this model.

A mathematical regression of the data presented in Fig. 3 was performed using equation (6) to best fit C and D, which were approximated here by mean cyclic temperature data. The values of these constants determined from the isothermal data were found to be reasonable approximations to the statistically best-fit values, as shown in Fig. 5.

Figure 6 shows the result of applying equation (6) (with the physically determined constants C and D) to the data in Fig. 3. It is observed that better than a factor of 1.5× life consolidation is possible, based on the stress range and mean stress that result from strain-controlled thermal mechanical fatigue cycling.

Conclusions

A hysteretic energy-based model was developed for the consolidation of thermal mechanical fatigue data. Out-of-phase, completely reversed, strain-controlled TMF tests were conducted at strain ranges from 0.4 percent to 0.8 percent and three temperature ranges: 427–927°C, 427–1038°C, and 427–1093°C. Using inelastic strains approximated at the midcycle temperature, better than a factor of 1.5× consolidation in the test data is possible. Statistical analyses of the data show that the strain approximations are reasonable, and the resultant equation for cyclic life depends only upon mean stress and stress range.

Further studies will investigate the effects of coatings, environment, and other factors on TMF lives and the current model will be modified to reflect this behavior.

References

1 Halford, G. R., and Manson, S. S., "Life Prediction of Thermal Mechanical Fatigue Using Strain Range Partitioning," *Thermal Fatigue of Materials and Components*, ASTM STP 612, D. A. Spera and D. F. Mowbray, eds., American Society for Testing and Materials, 1976, pp. 239–254.

2 McNight, R. L., and Laflen, J. H., "Turbine Blade Non-linear Structural and Life Analysis," Paper No. 82-1056, AIAA/SAE/ASME Joint Propulsion Conference, Cleveland, OH, June 21–23, 1982.

3 Fujino, M., and Taira, S., "Effect of Thermal Cycle on Low Cycle Fatigue Life of Steels and Grain Boundary Sliding Characteristics," *Mechanical Behavior of Materials*, Proceedings of the Third International Conference, Cambridge, England, Aug. 20–24, 1979.

4 Spera, D. A., "Calculation of Thermal-Fatigue Life Based on Accumulated Creep Damage," NASA TND-5489, National Aeronautics and Space Administration, Oct. 1969.

5 Jaske, C. E., "Thermal-Mechanical, Low-Cycle Fatigue of AISI 1010 Steel," *Thermal Fatigue of Materials and Components*, ASTM STP 612, D. A. Spera and D. F. Mowbray, eds., American Society for Testing and Materials, 1976, pp. 170–198.

6 "Thermal Mechanical Fatigue of Coated Blade Materials," AFWAL/MLLN Contract No. F33615-84-C-5027.

7 Morrow, J., "Cyclic Plastic Strain Energy and Fatigue of Metals," *Internal Friction, Damping and Cyclic Plasticity*, ASTM STP378, American Society for Testing and Materials, 1965.

8 Ostergren, W. J., "A Damage Function and Associated Failure Equations for Predicting Hold Time and Frequency Effects in Elevated Temperature, Low Cycle Fatigue," *Journal of Testing and Evaluation*, Vol. 4, No. 5, Sept. 1976.

9 Pejsa, P. N., and Cowles, B. A., "TMF Behavior of an Anisotropic Turbine Airfoil Alloy," NASA TMF Workshop, Cleveland, OH, Nov. 15–16, 1984.

Comparison of Methods for Lifetime Calculations of Highly Loaded Aero-Engine Discs

R. Hefele

G. Kappler

D. Rist

Lehrstuhl fur Flugantriebe,
Technische Universität München,
Munich, Federal Republic of Germany

The requirement for low weight-to-thrust ratios of modern aero-engines has led to high structure loads and design of parts in the range of low cycle fatigue. In order to ensure high reliability and optimized TBO's (time between overhaul), methods to calculate accurately the durability of parts are of great interest. For a highly loaded compressor disc of a fighter engine the lifetime was calculated using the nominal stress method and the maximum local strain concept. The nominal and maximum local stresses and strains were calculated with a finite-element program which was extended to consider plastic deformation of materials. The reference load cycle, which was the same for both methods, was derived from actual load measurements during flight missions. The comparison of the results shows the region of validity of both methods and suggests the application of a modified nominal stress method. Two proposals for improving the nominal stress method by superseding the Neuber-Hyperbolic rule and modifying the mean stress influence in the Goodman diagram are discussed.

Introduction

The nominal stress method is generally applied for the determination of the cumulative fatigue damage and lifetime calculation of aero-engine discs [1, 2]. The method employs Wöhler lines, i.e., curves of component part stress versus maximum number of load cycles, that have to be established from cyclic spin tests of the actual manufactured rotor discs. Using the nominal stress distribution as the relationship between the load and the durability avoids the necessity of complicated stress and strain calculations in the parts region of high local stresses such as notches and bores. It requires, however, for each critical design feature a specific Wöhler line, since lifetime determining factors like the local stress distribution in grooves are not fully considered by nominal stresses. The determination of Wöhler lines through cyclic spinning of fabricated discs is very expensive [3] because of the required test facilities and the long test durations until the cyclic loading generates the first cracks.

Another method for determining durability of parts is based on the calculation of the maximal local stresses and strains (notch root method) in conjunction with the assumption that the stresses and strains in the highest loaded parts region behave similar to those of uniform test specimens subjected to the same loads. Although this method requires intricate calculations of stress and strain distributions by finite elements which account for elastic and plastic material behavior at notch roots, it bears the potential for reducing the bulk of cyclic material tests. The method has been successfully applied for durability calculations of power transmission shafts [4].

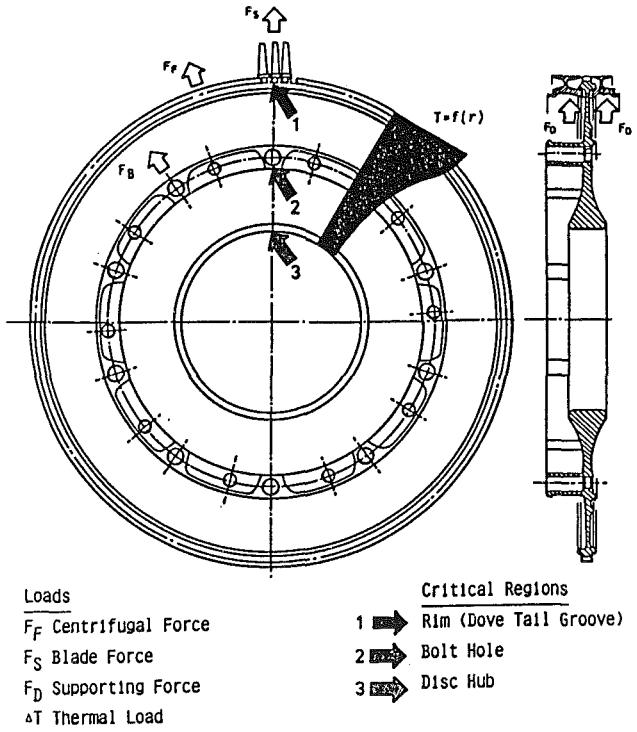

Fig. 1 Compressor disc with acting loads and critical design regions

In this paper the two lifetime calculation methods were applied for the rotor disc of a compressor stage using duty cycles

Contributed by the Gas Turbine Division of The American Society of Mechanical Engineers and presented at the 31st International Gas Turbine Conference and Exhibit, Düsseldorf, Federal Republic of Germany, June 8–12, 1986. Manuscript received at ASME Headquarters January 20, 1986. Paper No. 86-GT-102.

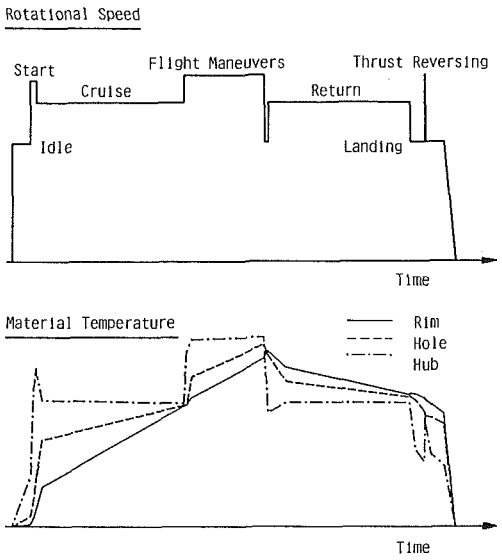

Fig. 2 Load variation during a simplified flight mission

derived from actual measurements during fighter engine missions. Analysis of the results should determine if the knowledge of the local stress and strain distribution in the critical regions of the disc, especially in the dovetail groove, leads to a more accurate lifetime prediction and a reduction of cyclic tests.

The rotating disc of a fighter engine compressor has basically three critical regions for which lifetime certification is necessary. As shown in Fig. 1 the critical design regions of the disc are the dovetail grooves for the blade attachment around the outer rim, the bore holes for the assembly bolts, and the inner center hole. The forces acting on the disc are the centrifugal forces of the blades and those self-generated, the thermostresses and the loads implied by the spacers and the bolts. These mechanical loads and thermostresses are not constant, but vary considerably during the engine flight mission. Figure 2 illustrates the variation of the rotational speed during a typical flight mission consisting of the engine start, the climb and cruise section, the engagement with a multitude of fast flight maneuvers, the aircraft return, and landing during which the thrust reverser is activated for reduction of roll out on the runway. The disc material temperature variation for this flight mission is also shown in Fig. 2 for the critical regions: rim, bolt holes, and disc hub. Due to the different heating and cooling rates of the outer and inner part of the disc, high thermal gradients occur during the transition phases which lead to high thermal stresses [5].

Stress Calculation of the Compressor Disc

The calculation of the stress distribution of the disc at different load conditions was made with the finite element method because the complicated disc geometry, the variation of the material properties with temperature, and the nonlinear strain behavior make analytical closed-form solutions highly impractical. In order to account for the different geometric shapes of the critical regions, three different meshes were generated. As illustrated in Fig. 3, isoparametric elements with four nodal points were used for the description of the plane stress conditions. Because of geometric symmetry, it was sufficient to apply the mesh to one half of the disc sector comprising half of the dovetail groove and half of the assembly bolt bore. The boundary conditions were adjusted to allow only deformations similar to that of the full disc. As shown in Fig. 3, the third dimension is considered for this two-dimensional mesh by assigning a corresponding thickness to each element. For the stress calculations presented in Fig. 4, each of the

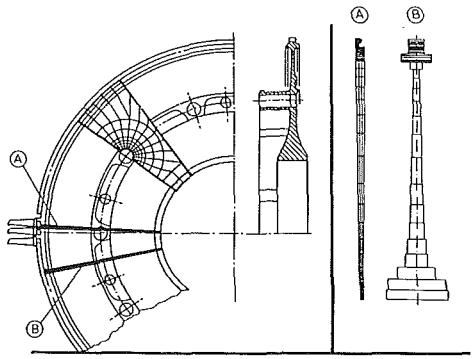

Fig. 3 Finite element mesh of the compressor disc

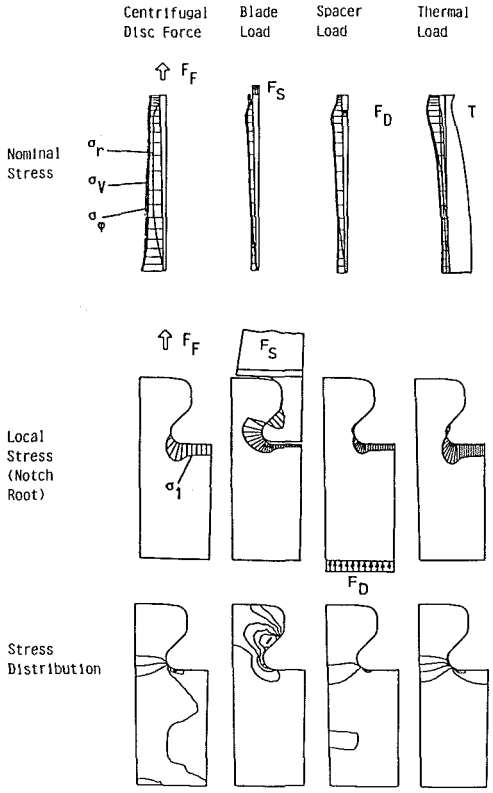

Fig. 4 Stress calculations for each of the disc loads

typical loads was introduced into the finite element mesh. At rotational speeds of 20,000 rpm and circumferential velocities of 350 m/s at the rim the centrifugal force of the disc itself becomes the predominant load. The calculated nominal stresses are plotted along the disc radius in the top row of Fig. 4. Because of the suitable chosen disc thickness distribution, the circumferential stress component σ_φ due to the centrifugal disc force has an almost uniform distribution along the radius. The typical steep increase at the disc hub has been omitted by making a compromise between the disc thickness and the higher permissible stress level at the inner regions. The radial stress σ_r is zero in the absence of blade loads, at the rim and other radial loads at the disc hub. The equivalent stress in the dovetail groove, plotted in the middle section of Fig. 4, corresponds to the tangential stress at the notch root. The stress field shown in the last row of that figure presents lines of equal stress values. It shows that the highest stresses concentrate in the dovetail in a very narrow area.

The blade loading is imposed to the disc over the dovetail groove sides. The centrifugal force of the blade F_s was transformed into a pressure loading for the finite-element

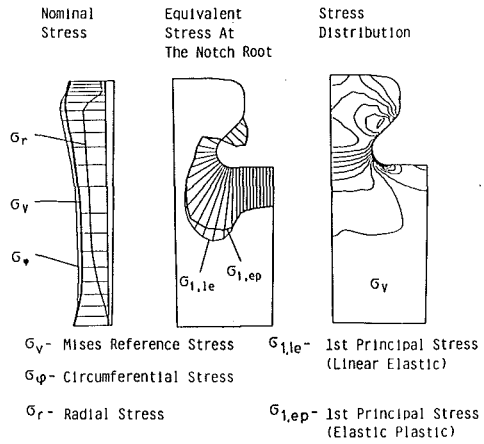

Fig. 5 Calculation of the total stresses for the case of highest loading

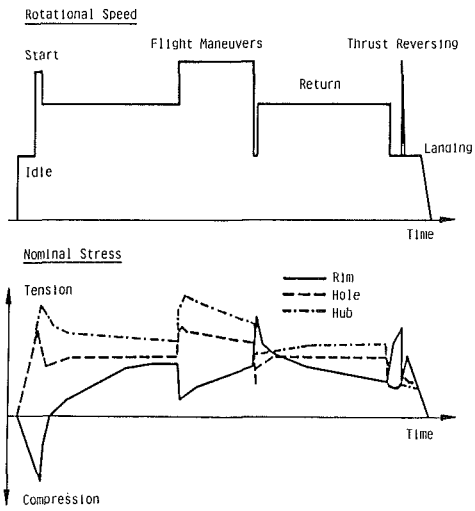

Fig. 6 Nominal stress variation over the simplified flight mission

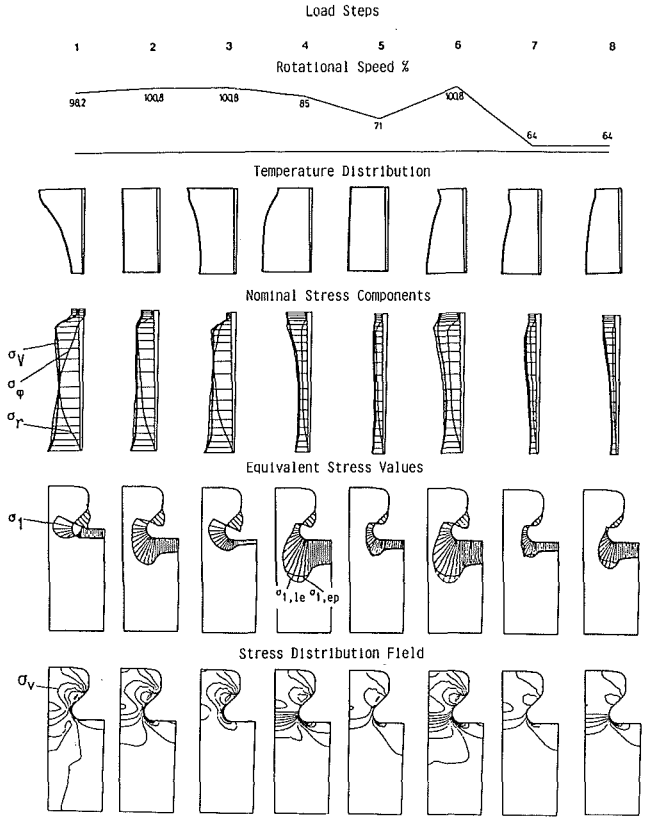

Fig. 7 Stress calculations at the rim for several load conditions

calculations and introduced into the mesh along two element sides. The nominal stress is calculated by transforming the centrifugal force exerted by the blades into a tension acting uniformly over the rim boundary. The radial stresses on the disc rim calculated with the finite element method are, of course, in equilibrium with this tension. For this manner of loading, the highest equivalent stresses occur in the smallest cross section of the dovetail groove as shown in Fig. 4.

The spacer loads act upon the disc as compressions in the area of contact because of their different thermal expansion. While the forces reach a maximum during engine acceleration, the spacer can shrink when the engine is decelerated and no forces will act on the disc. The loads are introduced into the finite element calculations along those elements in contact with the spacer. As shown in Fig. 4 the highest nominal stresses resemble those due to the blade tension and the stress distribution exhibits a high local stress concentration in the dovetail groove.

The temperature distribution along the compressor disc is shown on the right side of Fig. 4. It was calculated for the flight mission at the point where the thrust reverser is activated during the landing phase. This condition implies the highest stresses because the disc rim is being cooled by the gas flow whereas the hub is still hot. From the stress distribution it can be seen that the peak values are concentrated in a narrow region of the dovetail groove.

The stresses produced by these four separate loadings can be added up as illustrated in Fig. 5. This represents the case of highest stresses because the engine operates at full power when the thrust reverser is used producing high thermal stresses when the centrifugal tensions are at a maximum. At the bottom of the dovetail groove the high equivalent stresses surpass the yield strength. Its maximum value exceeds the nominal stress by a factor of 2.1. The stress distribution shows that the critical region of the dovetail groove is very localized.

Calculation of Total Stress Distribution for Various Flight Missions

During the flight mission the rotational speed, the temperatures, and hence the disc loads are continuously changing. The highest loads occur during transient operations because of the high temperature gradients. In order to determine all of the stress peaks the simplified flight mission has to be partitioned into small time increments together with its corresponding temperature variations. As a first step aimed at determining critical duty events, the nominal stresses for the rim, bore holes, and disc hub were calculated. The results of these calculations, which require less computing time and storage volume than the local stress calculations, are represented in Fig. 6. They show that the curves of the nominal stresses for the disc hub and the bore holes are similar because they are mainly determined by centrifugal forces. The nominal stresses at the hub behave different because they are mainly influenced by thermal stresses [6]. During acceleration the hot rim and the "cold" hub produce compressions which turn into tensions as the disc warms up. During engine operations with an almost uniformly heated disc, the nominal stresses at the hub become dominated by centrifugal loads as well. During deceleration the situation is reversed and tensions occur in the hub which is still hot whereas the rim is cool.

The peaks of the nominal stresses which appear at different times for the rim, the bore holes, and the disc hub are of importance for the disc lifetime calculation. For eight relevant

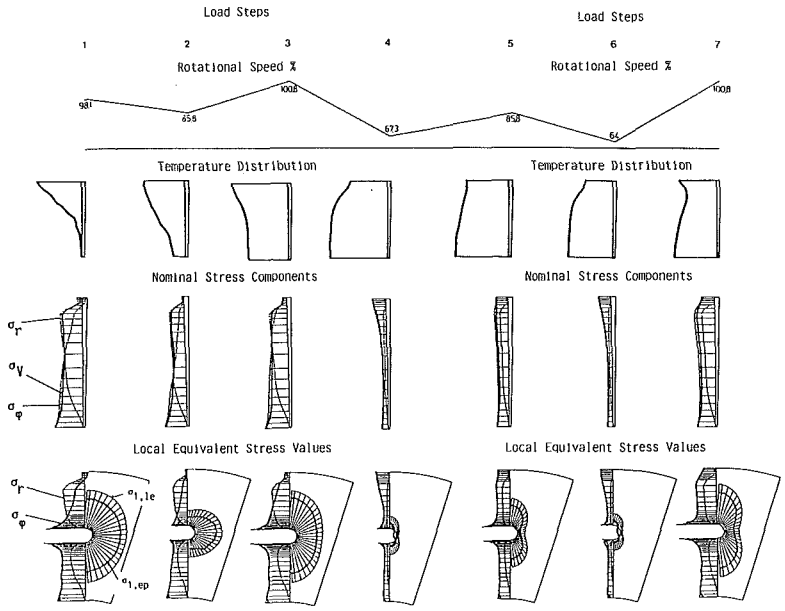

Fig. 8 Stress calculations at the assembly bore hole for several load conditions

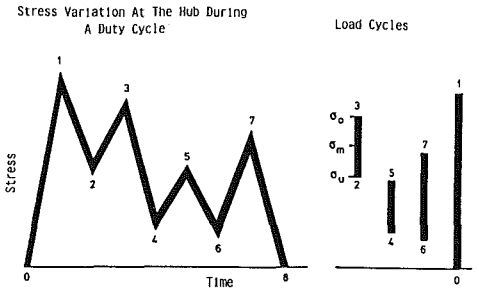

Fig. 9 Load cycles derived from one simplified duty cycle

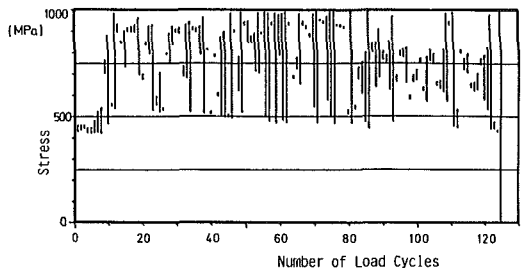

Fig. 10 Load cycles of a real flight mission

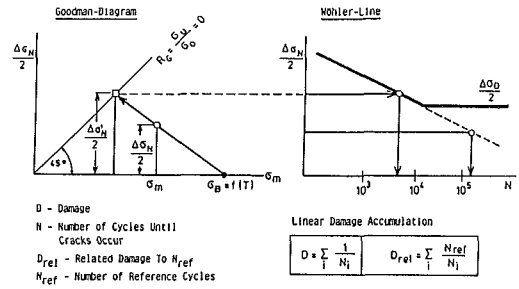

Fig. 11 Nominal stress method used for linear accumulation of damage

peaks the stress distribution at the rim was calculated and the results are shown in Fig. 7. The calculations were first made with a linear-elastic and then repeated with an elastic-plastic stress–strain relationship because the yield point was surpassed at some loads. At the first load step the previously described thermally induced compressions appear in the notch root whereas tensions are produced in the smallest dovetail groove section by the centrifugal blade forces. At the second step, the temperature distribution along the disc radius is almost uniform and centrifugal stresses prevail. The acceleration at the third step causes a change of the thermal stresses again, but their magnitude does not suffice to induce compressions in the dovetail groove.

The first plastic deformation takes place at the fourth step, where the sudden reduction of the gas temperature from full power to idle leads to a temperature reduction at the rim. Its shrinking is opposed by the hot disc hub leading to an overlay of tensions. The combined tension stress is higher than the yield strength which causes deformation at the bottom of the dovetail notch. Another plastic deformation occurs at the sixth load step because of similar reasons. The stress distribution field shown in the last row of Fig. 7 reveals the high stress concentration inside a very narrow location of the dovetail groove.

Besides the nominal load values, notch root components and the equivalent stresses at the assembly bore hole of the disc over the duration of a mission were also calculated and are presented in Fig. 8. Plastic deformations in the bore appear at the first load step. The difference between the equivalent stresses calculated with the linear elastic and the elastic-plastic stress–strain relationship, referred to as residual deformations, cover uniformly the whole bore circumference. The circumferential σ_φ and radial σ_r stresses are at this location almost equal due to the high-temperature gradients. The residual deformation, i.e., the difference between plastic and fictive elastic deformation, remains in the disc unchanged during all of the following load steps. At the seventh load step, which corresponds to the thrust reverser operation, plastic material deformation again arises. The maximum stress for this case lies in the upper half of the bore because the circumferential stresses are larger than the radial stresses.

Determination of Load Cycles

The duty cycle of the compressor disc during flight mission is composed of irregular alternating loads. Fatigue lives of specimen discs are however determined with load cycles of constant amplitudes. In order to relate the endurance of actual

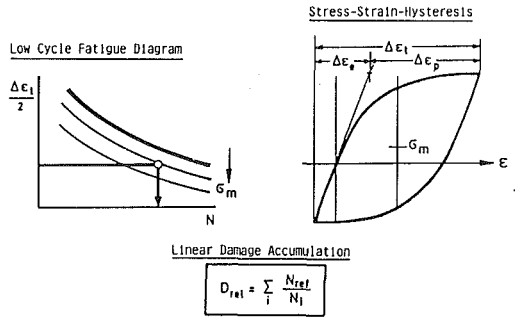

Fig. 12 Maximum local stress (notch root) method

discs to simplified spin test results, the irregular duty cycle shown in Fig. 9 must be broken down in a number of constant amplitude load cycles. By using a certain cycle counting scheme, the cumulative fatigue damage of the constant amplitude cycles corresponds to the actual fatigue damage or endurance, respectively.

The well-known rainflow counting was used because it defines cycles as closed stress-strain hysteresis loops and the algorithm described in [7] has the advantage that the counting of single cycles can begin before the entire history is known and without missing large overall cycles. The load cycles derived with the rainflow counting from the duty cycle are shown on the right side of Fig. 9. Each cycle is represented by a vertical line which spans the lowest σ_u and the highest σ_o stresses. This representation enables it to readily determine the stress amplitude and the mean stress σ_m of each cycle. Flight missions are characterized by a large cycle generated by the start and the engine shut off, medium cycles induced by changes in operation conditions, and many small cycles caused by speed and thrust control. For real flight missions the number of individual load cycles is very high. Figure 10 illustrates the counting of a duty cycle measured for a 1.5-hr flight mission which amounts to more than 120 load cycles.

Cumulative Fatigue Damage Calculations

For the nominal stress method, the circumferential nominal stress component σ_φ is used to establish the relationship between the load and the endurance. The effect of local stress concentrations, in the notch root, resulting in residual plastic material deformations, is considered by a reduction of the allowable nominal stress. Therefore, for each critical spot of the disc a nominal stress range versus maximum number of load cycles, i.e., a Wöhler line represented in Fig. 11, had to be established. It determines how many load cycles at constant nominal stress amplitude can be endured by the disc before cracks appear. The cyclic spin tests for setting up Wöhler lines require ready-designed and manufactured discs having even the surface finish equal to those of the production line. Since the experimental determination of the mean stress influence on endurance was too involved, an analytical estimation was applied. The modified Goodman diagram [9], shown on the left side of Fig. 11, enables one to transform the equivalent stress amplitudes from one mean cycle stress to another. Both cycles produce the same cumulative fatigue damage. The reference cycle for the transformation to $\Delta\sigma'_N/2$ was taken from the Wöhler line for which the stress ratio R_σ is zero, corresponding to a 45-deg line in the Goodman diagram. With the transformed nominal stress range amplitude $\Delta\sigma_N/2$ the number of load cycles N until damage was determined from the Wöhler line. The lifetime numbers of each cycle were linearly cumulated to yield the fatigue damage D_{rel} for the complete duty cycle [9].

The maximum local stress concept (notch root load method) uses, as shown in Fig. 12, the so-called LCF (low cycle fatigue) diagram, a relationship between the mean strain range at the

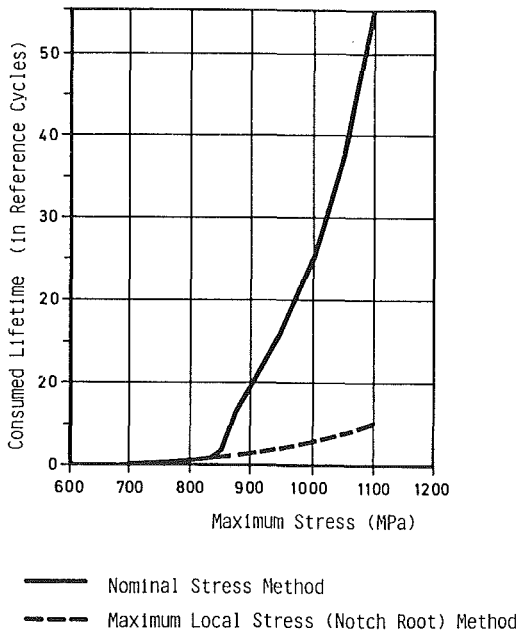

Fig. 13 Lifetime consumption during the flight mission

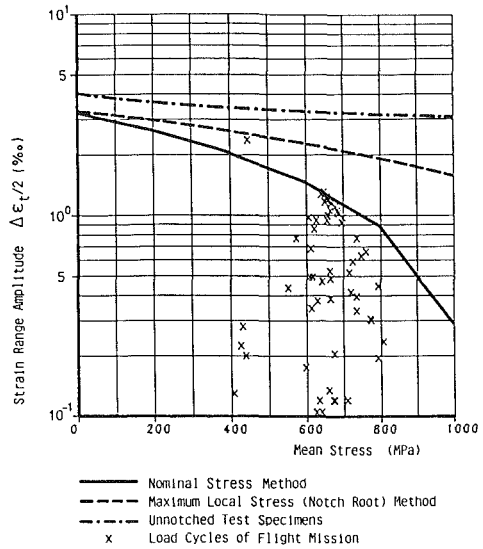

Fig. 14 LCF curves for $N = 10^4$ and varying mean stresses: comparison of calculated and experimental results

critical region $\Delta\varepsilon t/2$, the mean cycle stress σ_m, and the number of cycles N until crack initiation. The finite-element program applied for stress-strain calculations is based on ADINA [10]. The program initially made for calculations of civil engineering structures was extended for our goals. A program was introduced to enable centrifugal force calculations and second order form functions were used to extrapolate incremental changes from the element integration point to the nodal mesh points [11]. This new procedure was necessary to calculate the deformation and stresses in the very narrow critical regions of the dovetail groove. Further extensions of ADINA enabled a more useful consideration of the element thickness along the disc radius and a more efficient input and output data processing. Finally a program for graphic presentation of data was linked to it.

The calculated local strains for each load cycle were considered to be proportional to the logarithmic scale of the disc lifetime according to the LCF diagram shown on the left side of Fig. 12. Such lifetime curves can be obtained from ex-

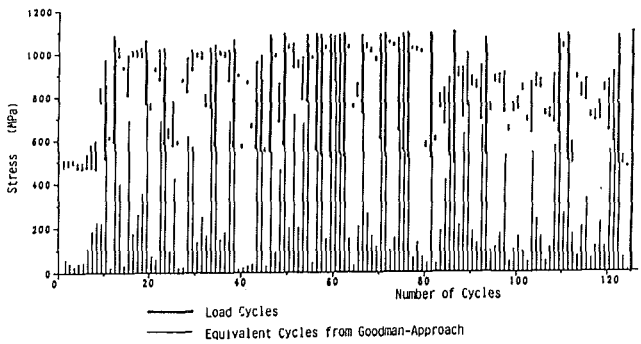

Fig. 15 Equivalent load cycles

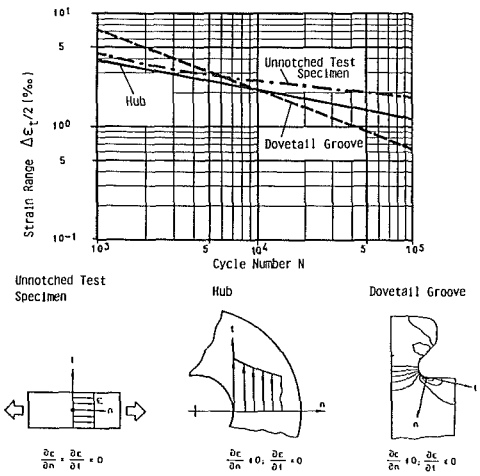

Fig. 16 LCF curves at $R_\sigma = \sigma_u/\sigma_o = 0$

perimental tests of unnotched test specimens in advance of the disc design. Since it is assumed that under equal loads, the total strains in the unnotched test specimen behave similar to those at the critical region, it is possible to assign to each critical region a lifetime curve. The total strain range is composed of the elastic $\Delta\epsilon_e$ and the plastic $\Delta\epsilon_p$ strain ranges as shown in the stress–strain hysteresis curve in Fig. 12. From the lifetime curves the linear damage accumulation D_{rel} was determined to be similar to the nominal stress method.

Comparison of Lifetime Calculation Results

The cycles of the measured flight mission were evaluated with the nominal stress and the maximum local stress method. The linear damage accumulation results according to Miner's rule are presented in Fig. 13. The lifetime consumption is expressed as number of reference cycles per flight hour plotted over the maximum stress of the mission. One reference cycle spans the load range produced through start, flight, and landing.

The results show that at low stresses only the large cycle of the mission is counted. In this event the results obtained from both methods are very similar, the values from the maximum local stress method being lower than those of the nominal stress method. From a certain maximum stress onward the medium to large load ranges of some cycles surpass the endurance strength limit and the lifetime consumption increases. Although the accumulated results of the nominal stress method exhibit a steep gradient there is only a slight rise for the results obtained by the maximum local stress method. The differences between the two methods, the largest appearing at the disc hub, were analyzed.

One of the reasons is the stronger mean stress influence of the nominal stress method. The lifetime curves for a constant cycle number of $N = 10^4$ are plotted in Fig. 14 as strain range

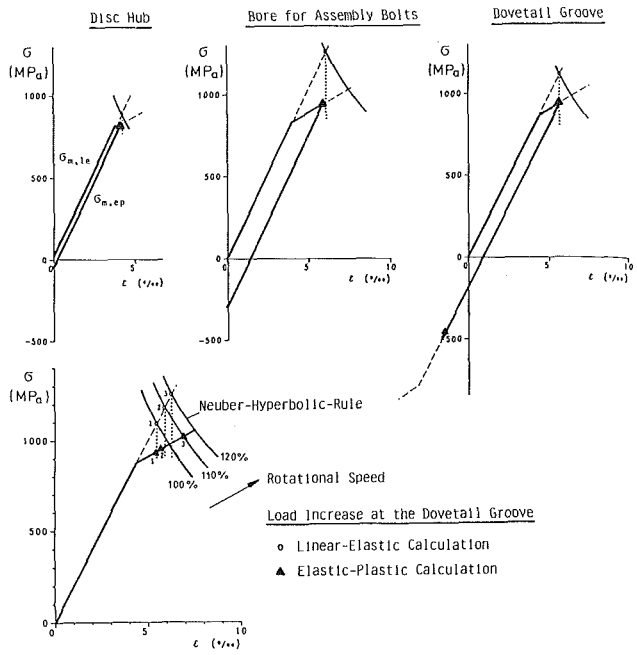

Fig. 17 Cyclic loads at three critical regions of the disc

amplitudes versus mean stress. The higher lifetime consumption with increasing mean stress is evident and the overaccentuation of that fact by the nominal stress method becomes clear. The values of the load cycles derived from the flight mission are represented in Fig. 14 by crosses and they are in the region of high mean stresses where the discrepancies appear. To determine which of the methods is more realistic the results of low cycle fatigue tests with notched test specimen were used [12]. Their lifetime curve for the cycle number $N = 10^4$ is plotted in Fig. 14. Accordingly, the mean stress influence of unnotched test specimen on lifetime is even smaller. It was assumed, therefore, that the stress amplitude transformation according to the Goodman approach is unrealistically high. This becomes obvious when the equivalent cycles with the stress ratio zero are plotted in Fig. 15 into the load cycles of the flight mission. Mean sized cycles with a stress ratio of 0.5 are transformed into equivalent cycles with a stress range equal to the main cycle yielding nominal stresses close to the maximum stress and the fracture strength σ_B. The Goodman transformation approach is not valid in the region close to the fracture strength. The maximum local (notch root) stress method describes, therefore, the mean stress dependence more realistically and uncovers a potential for additional lifetime.

Another reason for the calculated lifetime discrepancies of the two methods lies in the different material behavior of unnotched test specimens. The lifetime curves of an unnotched test specimen, the disc hub, and the dovetail groove are presented in Fig. 16 for a stress ratio of zero. The curves have different gradients which suggest different damage accumulations for small and large strain range amplitudes and different behavior of the material adjacent to the highest loaded region. Small strain changes at the unnotched test specimen lead to considerable lifetime variations. The local strain gradient is zero in both directions, i.e., the strain ranges are equal and small load changes are well endured because they are uniformly distributed over the cross section. At large loads, where the yield point is exceeded, plastic material deformation occurs in the whole cross section and the lifetime is considerably reduced. At the disc hub only the strain gradient in tangential direction is zero because of rotational symmetry. The strain decreases in the radial direction and the material close to the hub has to support the higher strains. The supporting action is even more pronounced in the notch root of the dovetail groove

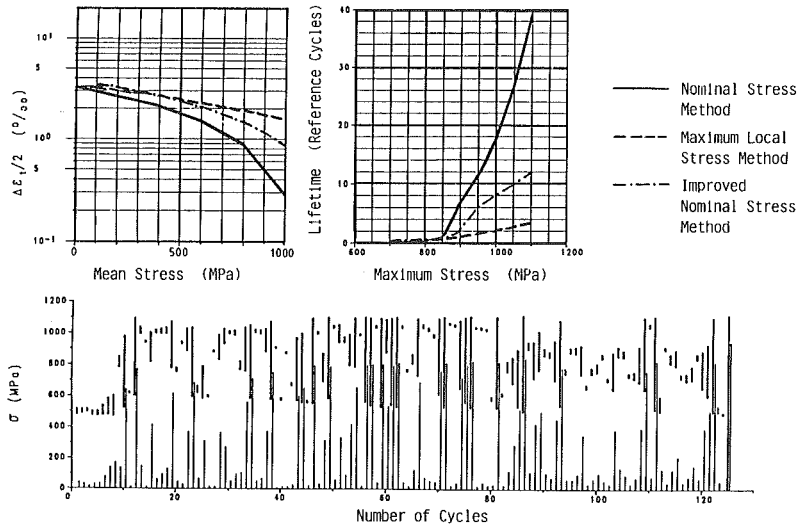

Fig. 18 Results with the modified nominal stress method

where strain gradients in normal and tangential direction prevail. Relative large changes of strain range amplitudes do not lead to large lifetime consumptions because maximum stresses in the notch bottom are diminished by plastic material flow and carried into adjacent regions. Since the strain range amplitudes are small for the greatest part of the single load cycles, the maximum local stress notch root method underestimates the cumulative fatigue damage. Lifetime test results from unnotched test specimens do not properly account for the three-dimensional stress and strain conditions in notched roots. Therefore the maximum local stress method in the present form cannot be used as a substitute for the nominal stress method. Spin testing of manufactured discs provides additional data of great importance.

Proposals for a Modified Nominal Stress Method

If the maximum stresses exceed the yield strength of the material and plastic flow takes place the approximation formula usually applied to determine the real state of stress and strain is the Neuber-Hyperbolic rule. In Fig. 17 the Neuber-Hyperbolic rules are presented in comparison with the finite-element calculation results at three critical disc regions. The comparison shows that the Neuber-Hyperbolic rule determines higher strains and stresses for all critical regions as evaluated with the more accurate finite element calculation method. Since the Neuber-Hyperbolic rule was established for test probes with large strain amplitudes, it overestimates the local load conditions for the rotating disc where small plastic deformations prevail. The deformations can be more realistically determined by an approximation method illustrated in the lower graph of Fig. 17. From the calculated linear-elastic point at the Hooke line, a vertical line is drawn and its intersection with the strength curve of the disc material determines the highest state of the actual stress and strain.

In order to test the validity of this approximation, the loads at the dovetail groove were increased. At the same thermal stress condition the rotational speeds and therefore the centrifugal forces were increased up to 120 percent. At 120 percent of rated rotation the deformation calculated with the finite element method is somewhat larger than the proposed approximation but still smaller compared to the one estimated with the Neuber-Hyperbolic rule. At higher loads, the more precise calculated deformation approaches and even surpasses the Neuber-Hyperbolic rule; however, the maximal stresses lead to short lifetimes and even disc burst. In the region of small strains, the proposed estimation using the simple linear-elastic relation represents a realistic description of the actual stress–strain conditions in the notch root.

The results of the linear-elastic and elastic-plastic finite-element calculations have shown that plastic material deformations are produced by critical load conditions during the first duty cycle. After load relief they induce a residual state of compression in the compressor disc, which causes a reduction of the mean stress during the following load cycles. If the nominal mean load cycle stress reduced by this residual compression stress is used in the Goodman transformation approach, the lifetime curve in the strain range mean stress diagram shown in Fig. 18 for a cycle number of $N = 10^4$ shifts toward the lifetime curve obtained with the maximum local stress method. The degree of shifting is proportional to the magnitude of the residual stress.

For the disc hub in the lower diagram of Fig. 18 the load cycles of the simplified flight mission are represented together with the equivalent loads of the same cycles, calculated with the proposed improvement. As can be seen, the relatively high stress values of the smaller cycles which caused unrealistically high life consumption are greatly reduced. Accordingly, the linear damage accumulation plotted in the right diagram is between the curves for the unmodified nominal stress method and the maximum local stress method. The reduced mean stresses are more realistic and no longer close to the fracture strength for which the Goodman transformation approach is, strictly taken, not valid. Their reduction becomes larger with the increase of the maximum stresses and hence the local plastic deformation during the first duty cycle.

Conclusions

The comparison of lifetime calculation methods for highly loaded engine discs has shown that the nominal stress method cannot be substituted at higher stress loads with the maximum local stress (notch root) method. Cyclic lifetime curves of unnotched test specimens do not account for the three-dimensional state of stress and the resulting redistribution in the adjacent material during plastic deformation. Spin tests of manufactured discs are further required for lifetime evaluation.

The analysis of the results has led to two proposals for the modification of the nominal stress method. The first concerns the maximum stress of component parts which are exposed to plastic deformations during the first duty cycle. The real stress peak can be found by using the extended Hooke line for the calculation and then to determine the stress value on the material strength curve at the same strain condition. The second involves the mean stress level estimation of the cyclic loadings. It is essentially diminished by the residual compres-

sion stresses remaining after the plastic deformation. With the modified nominal stress method lower lifetimes of discs are calculated which are much closer to the general and particular experience. The utility of the linear damage accumulation from experimental spin test results will be the subject of further investigation. The methods for lifetime calculations have to be still improved and simplified in order to use them for in-flight lifetime monitoring of critical engine parts.

Acknowledgments

The authors want to thank M. Roemer of MTU–München GmbH for his scientific and practical cooperation.

References

1 Edmunds, T. M., and Lawrence, R. A., "Monitoring Engine Thermal Stresses," *Engine Cyclic Durability by Analysis and Testing*, AGARD Conference Proceedings No. 368, 1984.

2 Breitkopf, G. E., and Speer, T. M., "In-Flight Evaluation of LCF Life Consumption of Critical Rotor Components Subjected to High Transient Thermal Stress," AGARD Conference Proceedings No. 368, 1984.

3 Fresco, J., "Exigence de conception et d'essai pour developper les moteurs d'aujourd'hui," AGARD Conference Proceedings No. 368, 1984.

4 Buxbaum, O., et al., "Vergleich der Lebensdauervorhersage nach dem Kerbgrundkonzept und dem Nennspannungskonzept," Paper No. FB-169, 1983.

5 Koff, B. L., "Designing for Durability in Fighter Engines," ASME Paper No. 84-GT-164.

6 Manson, S. S., *Thermal Stress and Low-Cycle Fatigue*, McGraw-Hill, New York, 1985.

7 Downing, S. D., and Socie, D. F., "Simple Rainflow Counting Algorithms," *Int. J. Fatigue*, Jan. 1982.

8 Dubuc, J., and Vanasse, J. R., "Effect of Mean Stress and Mean Strain," ASME Paper No. 69-pVP1, No. 92, Feb. 1970.

9 Miner, H. A., "Cumulative Damage in Fatigue," ASME *Journal of Applied Mechanics*, Vol. 12, 1945, pp. 159–164.

10 "ADINA – Automatic Dynamic Incremental Nonlinear Analysis Users Manual," Report No. AE 81-1, ADINA Engineering Inc., 1983.

11 Hefele, R., "Zur Berechnung der Schädigung hochbelasteter Fluggasturbinen-Scheiben unter realen Flugbedingungen," Dissertation, Technische Universitat München, Nov., 1985.

12 Schütz, W., et al., "Einfluss von Mittelspannungen auf die Lebensdauer im LCF-Bereich," IABG TF-871, 1978.

A Simplified Thermal Mechanical Fatigue (TMF) Test Method

J. R. Warren
Assistant Materials Project Engineer.

B. A. Cowles
Materials Project Engineer.

United Technologies,
Pratt & Whitney Group,
Engineering Division—South,
West Palm Beach, FL 33402

The thermal fatigue environment of gas turbine engine airfoils is severe and is often a life-limiting mode of failure. Alloy and coating system evaluation and accurate service life predictions for advanced turbine blades and vanes are dependent upon realistic laboratory simulation of the engine service environment. Engine conditions are best simulated in the laboratory by mechanical testing capable of imposing simultaneous, independently controlled temperature and strain cycles, or thermal mechanical fatigue (TMF) tests. Historically, TMF tests are expensive and usually require computer-controlled laboratory equipment. Consequently the cost of TMF testing has been prohibitively expensive for airfoil material and coating system evaluation. A simplified, low-cost TMF test method has been developed which is useful for alloy/coating system research and screening. This method, referred to as "load-adjusted TMF" (LATMF), uses load and temperature as the primary test control parameters. Test results using the simplified TMF test method show good correlation (within a factor of two) with the full computer-automated strain control TMF test results.

Introduction and Background

Military fighter aircraft require engines with rapid acceleration and deceleration capabilities for maneuverability. Coupled with requirements for engines with higher thrust-to-weight ratios, and correspondingly higher combustor exit temperatures, the severe turbine airfoil thermal fatigue environment has become a life-limiting degradation mode of turbine airfoils. Alloy and coating system evaluation and accurate service life predictions for advanced turbine blades and vanes are dependent upon realistic laboratory simulation of the engine service environment. Figure 1 illustrates a strain-temperature transient cycle representative of a critical location on a turbine blade under service conditions. For laboratory testing and analysis of material behavior, these engine conditions are best simulated by mechanical testing capable of imposing simultaneous, independently controlled temperature and strain cycles, or thermal mechanical fatigue (TMF) tests. Historically, TMF tests have required expensive test specimens and sophisticated, usually computer-controlled laboratory equipment. As a result, the cost of TMF testing has often been prohibitively expensive for turbine airfoil alloy/coating system selection, and for alloy orientation and processing optimization.

Experience has shown that isothermal fatigue data are not a reliable basis for life prediction of a coated turbine material system [1]. At high temperature (above 760°C) the crack initiation life is independent of the coating due to high coating ductility. At low temperature (below 760°C) the capability of a coated material system is highly dependent on the coating; however, low-temperature isothermal fatigue testing is not generally applicable to engine experience since there is little of the oxidation, corrosion, and interdiffusion associated with high-temperature service. Furthermore, the additional contribution of thermal expansion mismatch strain (between coating and substrate material) cannot readily be handled in an isothermal fatigue test.

In summary, the change in the coating behavior with temperature and the complicated interaction of the coating/substrate system under realistic turbine airfoil operating conditions severely limit the usefulness of isothermal fatigue data for predicting turbine blade airfoil life. Consequently the objective of the current research was to develop and evaluate a flexible, low-cost laboratory TMF test method suitable for use in alloy/coating system research and screening.

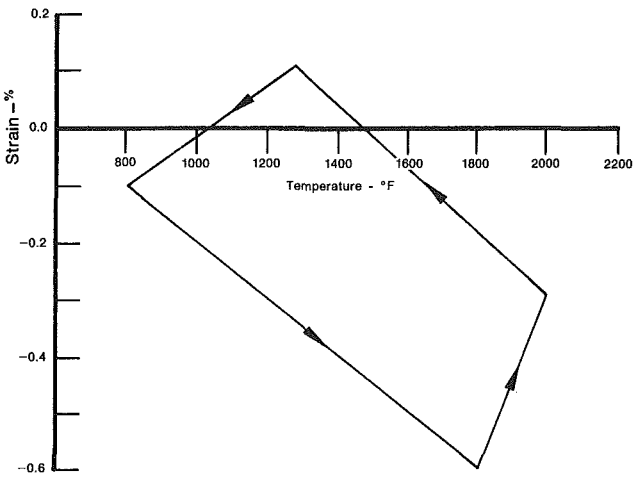

Fig. 1 Predicted TMF transient cycle shape

Contributed by the Gas Turbine Division of THE AMERICAN SOCIETY OF MECHANICAL ENGINEERS and presented at the 31st International Gas Turbine Conference and Exhibit, Düsseldorf, Federal Republic of Germany, June 8–12, 1986. Manuscript received at ASME Headquarters January 24, 1986. Paper No. 86-GT-120.

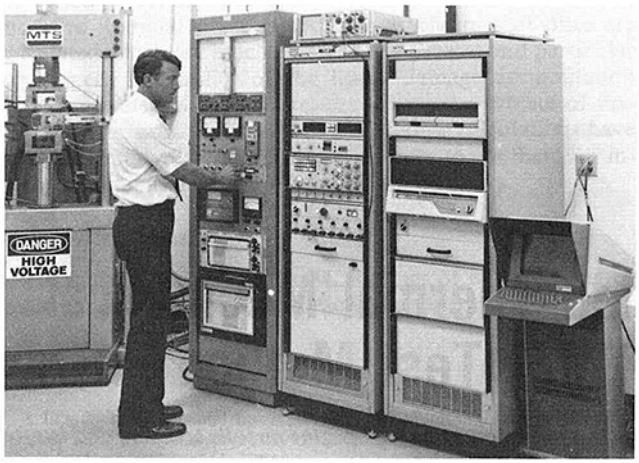

Fig. 2 Computer-automated strain-control TMF machine

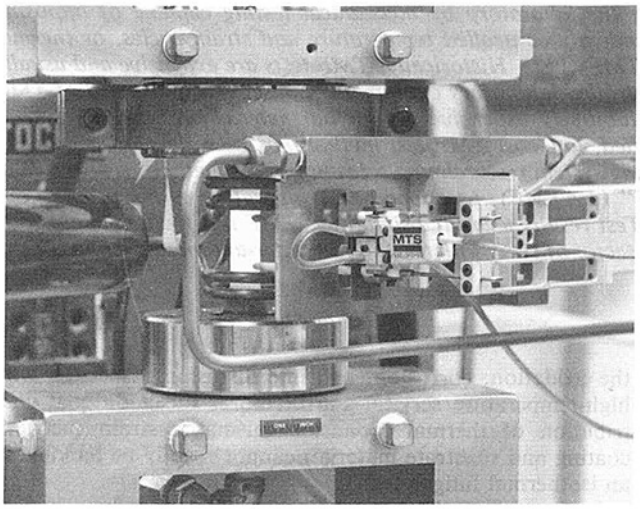

Fig. 3 Strain-control TMF test in progress

Discussion

Since the gas turbine engine airfoil environment is primarily thermally driven, strain rather than stress is the independent mechanical variable. The optimum laboratory testing technique would be the strain-control TMF (SCTMF) test method. In this method true mechanical strain is extracted and controlled from the total strain measured from extensometry by separating out the instantaneous free thermal strain. This type of testing requires a sophisticated computer and associated software. The SCTMF test machine shown in Fig. 2 contains two computer-controlled servosystems: One is a hydraulic system for closed-loop control of strain, load, or displacement; the other servosystem is for simultaneous closed-loop control of temperature. The computer generates the test waveforms, monitors and controls the test, gives status reports on a line printer, stores test data, performs analyses, and presents graphic results using a CRT display.

The test specimen has a hollow cylindrical gage geometry which conforms generally to ASTM recommended practice. A typical test running under strain-contolled TMF is shown in Fig. 3. The test specimen is heated by induction and/or direct resistance under closed-loop control. Cooling is controlled by servo-metered air directed through the inside diameter of the hollow test specimen. Temperature feedback is obtained from an infrared pyrometer. Strain is measured axially using an MTS Model 632 water-cooled, spring-loaded extensometer with ceramic (alumina) rods for specimen contact.

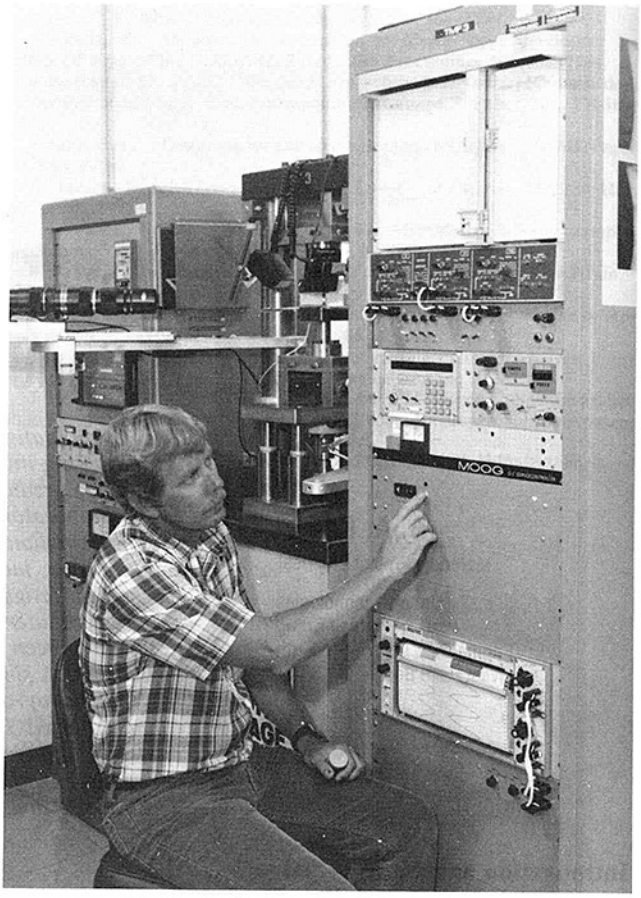

Fig. 4 Load-adjusted TMF test machine

An alternate test method, referred to as load-adjusted TMF (LATMF), is a relatively simple and inexpensive means to determine the comparative TMF capability of various alloy/coating systems under simulated aircraft engine operating conditions. The test equipment and test specimen are significantly less complex than those required to conduct a computer-automated and controlled TMF test using the "strain-control" test method.

The test machine shown in Fig. 4 is a conventional low cycle fatigue (LCF) test machine which has been modified to simultaneously ramp and control temperature, thereby extending its capability to include thermal mechanical fatigue. The machine incorporates a microprocessor-based, two-channel programmer to command load on one channel, and temperature on the second channel. The command waveforms for each parameter are independent and can easily be programmed into the microcomputer to conduct almost any TMF test cycle within the ramp rate capacity of the hydraulic and thermal servosystems. The test machines are equipped with automated cameras to photograph test specimen gage areas at preprogrammed intervals for documentation of crack initiation and surface condition during the test.

The temperature-control system utilizes direct resistance heating from a low-voltage high-current transformer. For temperature measurement and control, an infrared pyrometer is sighted on the specimen gage for TMF tests in the 260 to 1370°C range. Various test specimen designs are compatible with this test equipment including thin sheet, solid cylindrical gage, and cylindrical tubular designs which use internal air cooling for simulation of thin-walled airfoils. Figure 5 illustrates a typical specimen during an LATMF test.

The LATMF method [2] uses load rather than strain as the primary mechanical control parameter. This method is based upon the fact that the stress endpoints in a computer-

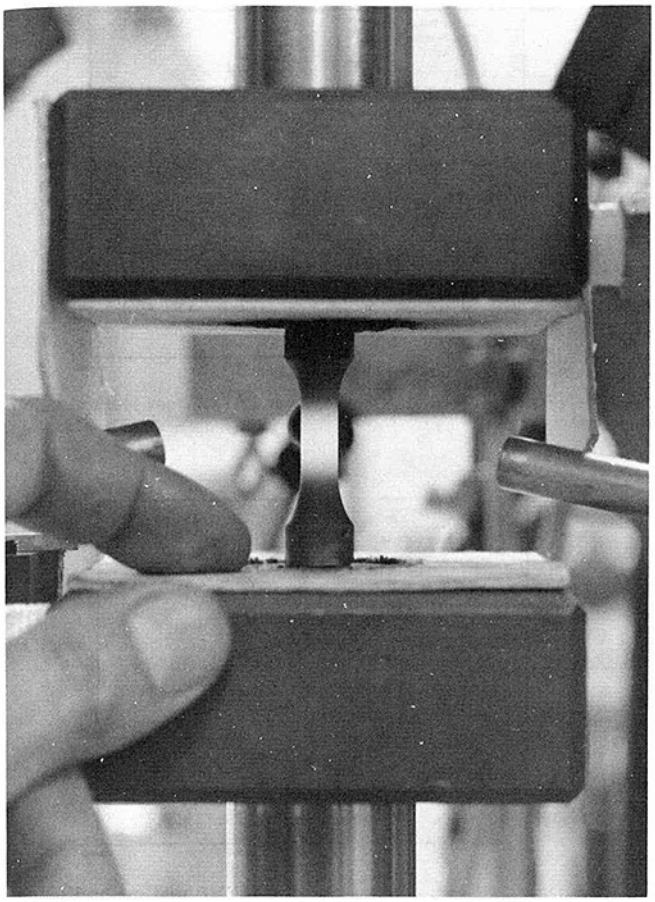

Fig. 5 Load-adjusted TMF test in progress

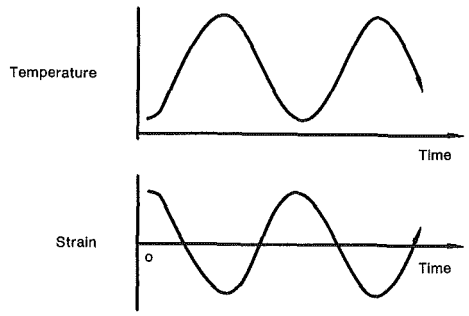

Fig. 6(*a*) Time waveforms

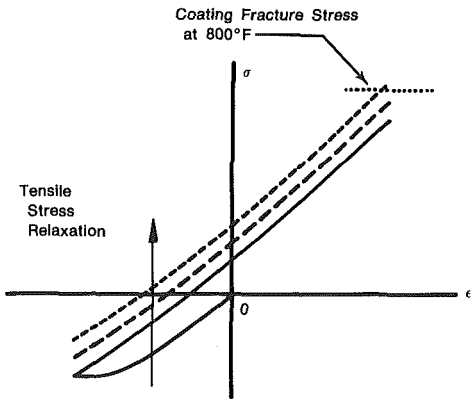

Fig. 6(*b*) Stress-strain response

Fig. 6 *Stress-strain mechanical behavior for an out-of-phase TMF test*

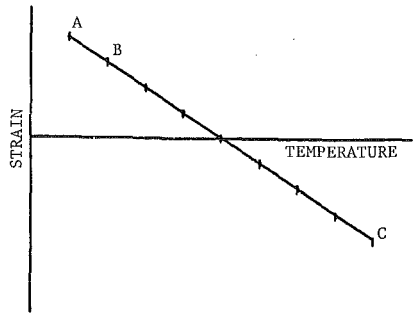

Fig. 7(*a*) Strain versus temperature excursion

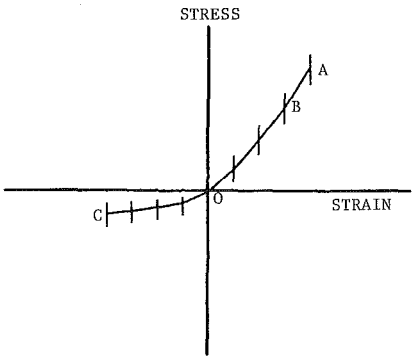

Fig. 7(*b*) Calculated stress-strain hysteresis loop

Fig. 7 Stress approximation method by incremental modulus summation

automated SCTMF test quickly stabilize and remain essentially constant until near failure. This can be illustrated by the mechanical behavior of a turbine airfoil alloy during a simple out-of-phase TMF cycle (Fig. 6). This cycle imposes maximum strain at the minimum temperature, and minimum strain at the maximum temperature. These conditions are of primary concern in a coated system because tensile stress can approach or exceed the fracture stress of the coating at low temperature, thus promoting nucleation and propagation of fatigue cracks. In this cycle, plastic deformation occurs in compression while approaching the maximum temperature of the cycle. This plastic deformation is most severe during the initial cycle, with subsequent cycles behaving nearly elastically. In addition, significant stress relaxation due to creep occurs on the initial cycle. This stress relaxation continues in a cyclic manner until a stabilized condition having a tensile mean stress is attained. This "shakedown" period occurs generally over the first 10 percent of life, and the test then continues to failure at nearly constant load limits.

Using the LATMF method, overall specimen gage axial displacement is measured and provides an approximation of the sum of both mechanical and thermal cyclic strains. Since the thermal component of cyclic strain is essentially constant (from the fixed temperature endpoints of the temperature cycle) throughout the test, any deviation in the measured cyclic displacement would be attributed to unreversed creep or strain hardening/softening and therefore would indicate a drift in the strain endpoints of the TMF test. If the displacement cycle is closely monitored on a stripchart recorder and the commanded load waveform (mean stress) is periodically adjusted to maintain constant displacement endpoints, a "simulated strain-control" test can be achieved. This mean stress shift in the load waveform is analogous to that which occurs inherently on the computer-automated SCTMF test run at similar test conditions.

A prerequisite for conducting the LATMF test is a knowledge of the stress endpoints which correspond to the

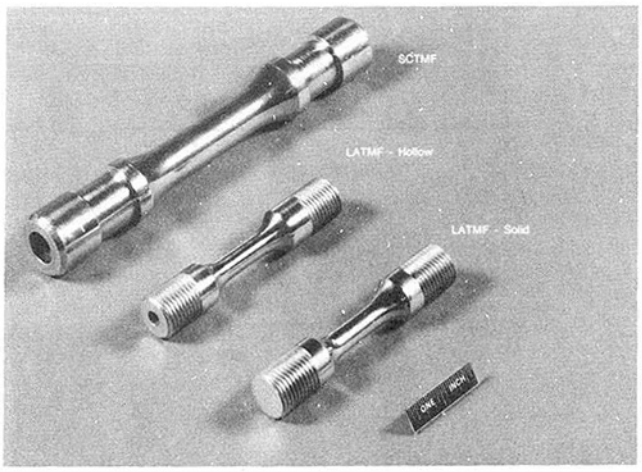

Fig. 8 TMF test specimen configurations

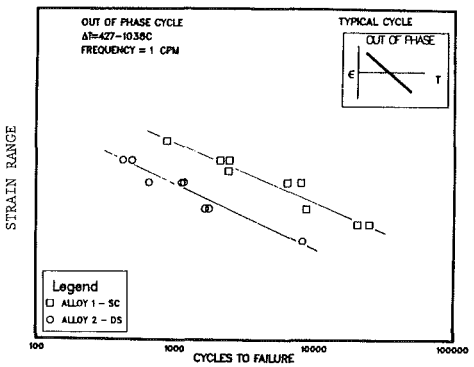

Fig. 9 Strain-control TMF test results

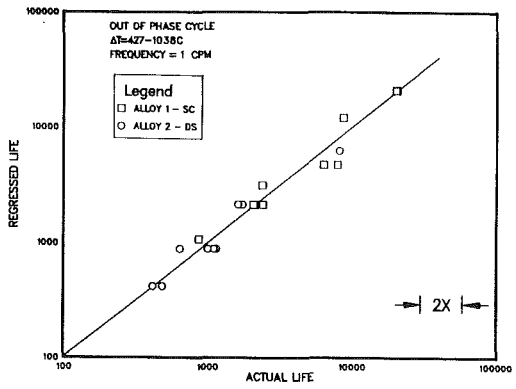

Fig. 10 Regressed versus actual life for SCTMF testing

strain limits of the cycle. These can be obtained from prior strain control TMF testing if available, or by using a simple incremental modulus approximation (Fig. 7). Here, the temperature/strain excursion is divided into 60°C increments, and using an elastic modulus for each strain increment, a stress segment is computed. Summation of the stress segments over the entire cycle yields the overall stress range. This approximation assumes the cyclic stress-strain hysteresis loop to be essentially elastic.

The LATMF test method is limited to those test cycles which do not introduce gross cyclic plasticity. Tests which incorporate significant stress relaxation, creep, or reversed inelastic strain should be conducted in the strain-control mode since constant strain limits would be difficult to maintain accurately using the load-control method. However the load-

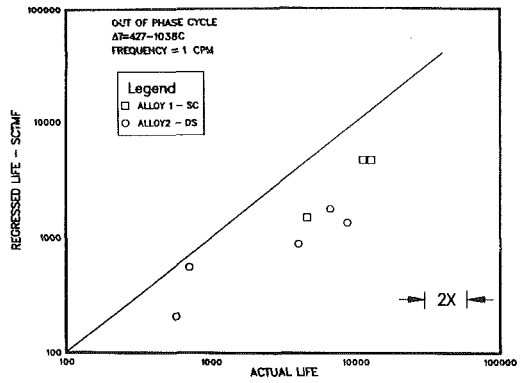

Fig. 11 Regressed versus actual life for LATMF test method using solid specimens

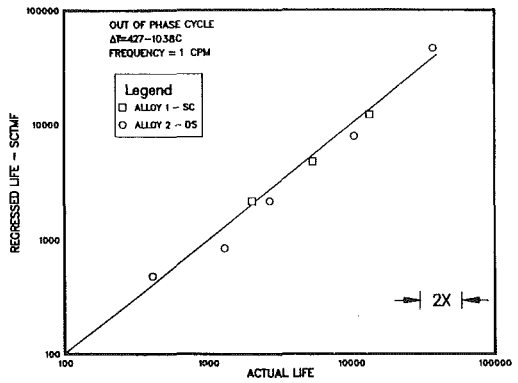

Fig. 12 Regressed versus actual life for LATMF test method using hollow specimens

control methodology is applicable for many gas turbine engine-representative TMF conditions, where elasticity assumptions are valid. Strain-control TMF testing at strain ranges of interest for turbine airfoils indicates that cyclic inelasticity is indeed small, and the computed stress range using the incremental modulus approximation agrees with the measured stress range in the strain-control test within 3 to 5 percent.

Experimental Results

A series of TMF experiments was conducted to evaluate the simple "load-adjusted" TMF (LATMF) method. Comparisons of test data were made between both strain-control TMF (SCTMF) and LATMF methods using solid and hollow test specimens depicted in Fig. 8. Strain-controlled TMF data and mean regression curves, used as the reference for all comparisons, are shown in Fig. 9 for two alloys using an out-of-phase temperature/strain cycle (Fig. 6). The two alloys include advanced single crystal and directionally solidified columnar-grain nickel-based alloys. These data are nondimensionalized on a predicted (from the SCTMF data regression) versus actual basis in Fig. 10 so that any bias due to test method could be assessed.

Load-adjusted TMF tests were initially conducted using the solid cylindrical test sample for both alloys at strain ranges that would produce a variation in cyclic life of one to two orders of magnitude. Test results presented in Fig. 11 indicate a bias, with the LATMF data showing greater cyclic life, especially in the low-strain/high-life regime when compared to the cyclic life predicted from SCTMF results. Several explanations were postulated for this effect. A surface area/volumetric effect has been observed for turbine disk alloys under isothermal fatigue testing [3] and may be active in the present case. A second plausible reason for the observed

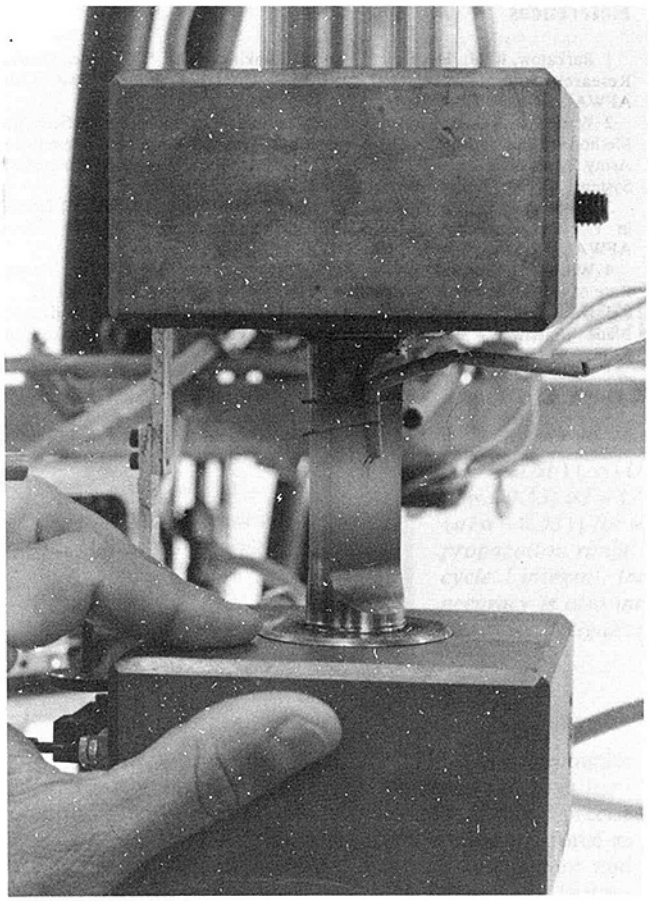

Fig. 13 TMF crack growth test

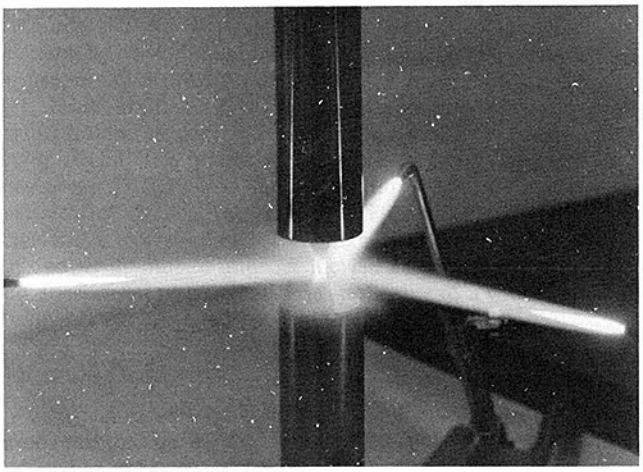

Fig. 14 TMF specimen heated by servocontrolled flame impingement

differences in life is a geometry effect. The hollow SCTMF specimen has a 1.27-mm wall thickness. Fatigue cracks thus have only a short distance to propagate until the specimen wall is cracked through. In the LATMF specimen the gage section is solid and a larger fraction of life is spent in crack propagation of the dominant cracks prior to failure. This was evidenced by visual detection of crack initiation at the surface in the coating, subsequent monitoring of crack growth to failure, and final fracture surface examination revealing well-developed thumbnail cracks.

To evaluate the geometry effect hypothesis, a number of test samples were machined to the same overall dimensions as the solid LATMF specimen, but having a hole machined through the center to obtain a hollow gage section with a wall thickness of 1.27 mm. Data generated using the hollow LATMF specimen configuration for both alloys (Fig. 12) were in good agreement with SCTMF data at all strain ranges. Examination of failed hollow LATMF specimens revealed that crack morphologies were very similar to those observed in SCTMF specimens where long but shallow circumferential surface cracks were prevalent. It is concluded therefore that the geometry effect is the primary explanation for the disparity in the TMF data between the SCTMF and LATMF test methods. Furthermore, using the LATMF method with hollow test samples should provide useful TMF information for design, screening processing optimization, and coating system evaluation under typical turbine airfoil operating conditions.

Future Directions

The load-control TMF testing method also has applications to crack propagation testing [4]. Figure 13 illustrates a TMF crack propagation test in progress using an ASTM standard center cracked tension (CCT) specimen. Other designs may also be tested, including surface flaws, sheets, and tubular shapes. Telemicroscopes are generally employed to measure crack lengths; however crack growth may be further documented using crack opening displacement (COD), electrical potential drop (EPD), or an automated camera system. Recent investigation of the TMF crack growth behavior of turbine airfoil alloys [5] has shown that compressive loading and TMF cycle type significantly affect both growth rate and fracture mechanism (i.e., Mode I/Mode II propagation).

An additional system for more realistic engine environment testing is currently under development which uses an array of three servocontrolled flame heating units for temperature control as shown in Fig. 14. Mechanical loading is simultaneously applied by a servo-hydraulic loading system similar to those shown previously. With this system it is possible to create an environment similar to that seen by turbine engine gas path components in service and it may be used for the investigation of a number of environmental damage modes (e.g., corrosion effects in which the combustion gases may be seeded with representative corrosion elements). This heating method will allow practical TMF evaluations of insulative ceramic coatings. Conventional rapid heating methods (i.e., induction and direct resistance) operate on the bulk substrate material with a heat flux from the substrate material outward to the coating. Engine service conditions are reversed with hot combustion gases impinging on the coated hardware with the heat flux from the coating into the airfoil substrate. This direction of heat flow becomes important for ceramic coatings where the coating serves as a thermal insulator. The flame heating method will enable better simulation of these engine service conditions.

Conclusions

The objective of this investigation was to evaluate the "load-adjusted TMF" (LATMF) test method as a simplified, economical technique for alloy/coating system research and screening. Results are summarized below:

1 The load-adjusted TMF test method produces excellent agreement with the more expensive computer strain-controlled TMF approach when conducted with similar specimen geometries (i.e., hollow).

2 Specimen geometry has a large effect on TMF life, indicating a substantial part of the total specimen life is spent in subcritical crack growth.

3 The LATMF method using hollow test specimens offers a

flexible means to evaluate the TMF behavior of alloys and coatings for turbine airfoil applications with substantially lower cost and equipment requirements.

4 Limitations of the LATMF tests method include test conditions which incorporate significant plasticity (e.g., tests having large cyclically reversed inelastic strain, creep or stress relaxation, or hardening/softening). These cases should be studied using the strain control method.

5 The general "load-adjusted" TMF approach is also applicable for TMF crack growth evaluations, and appears suitable for further development to obtain TMF data in extreme environments (e.g. vacuum, inert, or high-pressure hydrogen), and to better simulate the engine service environment using direct flame impingement heating.

References

1 Barkalow, R. H., Hecht, R. J., and Shamakian, R. L., "Advanced Coating Research and Development," USAF Contract F33615-78-C-5206, AFWAL-83-4086. Final Report, Feb. 1985.

2 Warren, J. R., and Cowles, B. A., "Thermal Mechanical Fatigue Screening Method for Gas Turbine Engine Applications," AMMRC MS 82-4, presented at Army Symposium on Solid Mechanics, 1982 Critical Mechanics Problems in Systems Design, Bass River, Cape Cod, Mass., Sept. 1982.

3 Ensberg, N. G., Annis, C. G., Jr., and Cowles, B. A., "Effects of Defects in Powder Metallurgy Superalloys," USAF Contract F33615-79-C-5074, AFWAL-TR-81-4191, Feb. 1982.

4 Wilson, D. A., and Warren, J. R., "Thermal Mechanical Crack Growth Rate of a High Strength Nickel Base Alloy," ASME Paper No. 85-GT-12.

5 DeLuca, D. P., and Cowles, B. A., "Fatigue and Fracture of Advanced Blade Materials," Final Report, AFWAL-TR-84-4167, USAF Contract F33615-80-C-5109, Aug. 1984.

Improvement of a Cycle J Integral for CT Specimens

Liu Shao-Lun

Xie Ji-Zhou

Institute of Aeronautical Materials, Beijing, People's Republic of China

The cycle J integral formula for CT specimens has been improved as follows: $\Delta J=(2/Bb)(\alpha_1 \cdot U+\alpha_2 \cdot \Delta P \cdot \Delta\delta)+(2/Bb)U_e-1.2025\ a/w+0.6233$ *for* $0.3 \le a/w \le 0.53$; $\Delta J=(2/Bb)(\alpha_1 \cdot U+\alpha_2 \cdot \Delta P \cdot \Delta\delta)+(2/Bb)U_e-0.02\ \sin[(\pi/0.23)(a/w-0.53)]$ *for* $0.53<a/w<0.95$. *This formula is applicable to the fatigue crack propagation range of* $0.3 \le a/w<0.95$. *In comparison with other formulae of the cycle J integral, the application range of the above expression is enlarged and its accuracy is also increased to a certain extent. Key words: cycle J integral, elastic-plasticity, fatigue crack propagation, strain energy release rate.*

Introduction

CT specimens are extensively used in fracture mechanics test, especially in the case of measuring da/dN at high temperature. Merkle and Corten [1] deduced a more precise formula of J_{Ic} for CT specimens, considering axial force as well as bending moment effects. In order to measure and calculate ΔJ conveniently, Clark and Landes [2] further reduced it. In the condition of elastic-plasticity as well as a large-scale yield, stress field near the crack tip depends on the J integral. Thus fatigue crack propagation rate can be considered as being dependent on the cycle J integral ΔJ. According to this, Sadananda and Shahinian [3] deduced an approximate expression of the cycle J integral on the basis of [1], and applied it to high-temperature fatigue crack propagation. In fact, their formula has still a considerable error when the value of a/w is in the range of $0.3 \le a/w \le 0.53$. Liu and Xie [4] obtained a more precise expression of cycle J integral for CT specimens, but it is inconvenient for application at high temperature. Therefore, this paper intends to improve a cycle J integral expression for CT specimens, so that it can be applicable to a wider range of fatigue crack propagation, i.e., $0.3 \le a/w < 0.95$.

Formula Deduction

In the case of load-controlled fatigue crack propagation, according to the method calculating cycle J integral in [3], i.e., when the cycle stress-strain hysteresis loop is stable and the displacement corresponding to minimum loading is taken as a reference point, all variables of the J_1 formula in [2] can be replaced by the corresponding increment. Thus, referring to Fig. 1, the cycle J integral expression for CT specimens can be obtained [4]

$$\Delta J=\frac{2}{Bb}(\alpha_1 \cdot U+\alpha_2 \cdot \Delta P \cdot \Delta\delta)+\Delta G_l-\frac{2}{Bb}(\alpha_1+2\alpha_2)U_e \quad (1)$$

where

$$\alpha=2[(a/b)^2+(a/b)+1/2]^{1/2}-2[(a/b)+1/2]$$

$$\alpha_1=\frac{1+\alpha}{1+\alpha^2}-\frac{1-2\alpha-\alpha^2}{(1+\alpha^2)^2}, \qquad \alpha_2=\frac{1-2\alpha-\alpha^2}{(1+\alpha^2)^2}$$

The coefficients α_1, α_2 change with a/w [3].

From [2] it can be seen that

$$\Delta G_l \cong(\alpha_1+\alpha_2)\frac{2U_e}{Bb} \quad (2)$$

This formula is approximately satisfied only in the case of $a/w \ge 0.53$. Then the formula (1) can be expressed as

$$\Delta J=\frac{2}{Bb}(\alpha_1 \cdot U+\alpha_2 \cdot \Delta P \cdot \Delta\delta) \quad (3)$$

However, in [1, 2], the formulae of fracture toughness J integral have been taken into consideration in the range $a/w \ge 0.53$. Nevertheless, in order to reform these formulae to be suitable for a cycle J integral over a range of $0.3 \le a/w \le 0.95$, they should be evaluated. For this purpose, let the difference of the last two terms in formula (1) be

$$\Delta G_l-\frac{2}{Bb}(\alpha_1+2\alpha_2)U_e=er \quad (4)$$

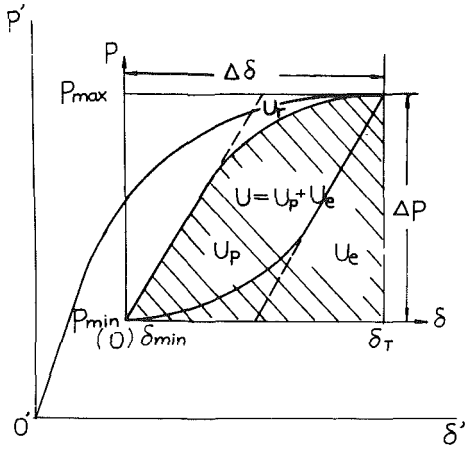

Fig. 1 Load-displacement hysteresis loop

Contributed by the Gas Turbine Division and presented at the 1985 Beijing International Gas Turbine Symposium and Exposition, Beijing, People's Republic of China, September 1-7, 1985. Manuscript received at ASME Headquarters May 31, 1985. Paper No. 85-IGT-66.

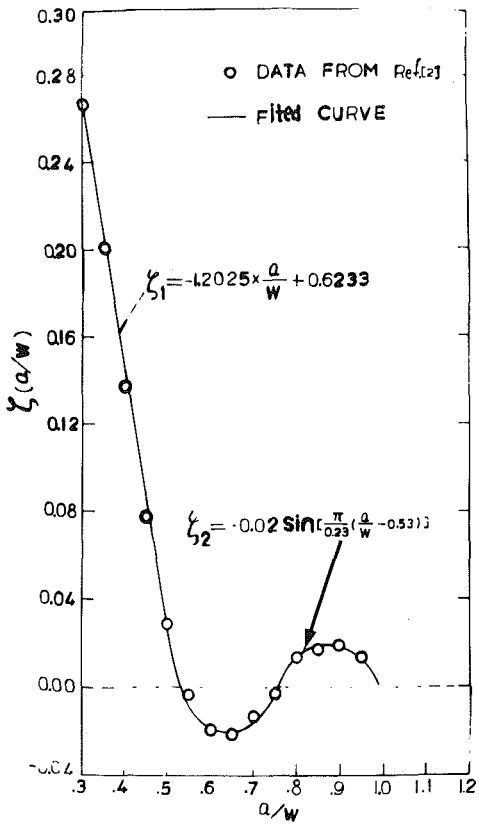

Fig. 2 The curve $\zeta(a/w)$-a/w

In accordance with compliance analysis in [2], expression (4) is equivalent to

$$\left[\frac{K(1-a/w)Y}{EB}\right]\frac{2U_e}{Bb}-(\alpha_1+2\alpha_2)\frac{2U_e}{Bb}=er \tag{5}$$

Let

$$\lambda_e=\frac{K(1-a/w)Y}{EB},\qquad \lambda_1=\frac{1+\alpha}{1+\alpha^2},\qquad \lambda_2=\alpha\frac{1-2\alpha-\alpha^2}{(1+\alpha^2)^2}$$

where K is rigidity coefficient; Y is geometry shape factor.

Since λ_1, λ_2 change with a/w, we will now analyze how the difference er changes with a/w.

Let

$$\zeta=\lambda_e-(\lambda_1+\lambda_2) \tag{6}$$

Thus, formula (5) can be written as

$$\zeta\cdot\frac{2}{Bb}\cdot U_e=er \tag{7}$$

We can plot the ζ-a/w curve, as shown in Fig. 2.

For the values of a/w within 0.3 to 0.53, by means of the least-squares method, we can obtain

Table 1 Comparison of ζ, ζ_1, ζ_2

$\frac{a}{w}$	α	λ_e	$\zeta=\lambda_e-(\lambda_1+\lambda_2)$	ζ_1	ζ_2
0.3	0.25212	1.5405	0.2669	0.26255	--
0.35	0.2282	1.4703	0.2016	0.20243	--
0.4	0.20525	1.3792	0.13722	0.14230	--
0.45	0.18328	1.32519	0.077455	0.08218	--
0.5	0.16227	1.2608	0.02835	0.02205	--
0.51	--	--	--	0.01003	--
0.52	--	--	--	--	0.002724
0.53	--	--	--	--	0.000000
0.54	--	--	--	--	0.002724
0.55	0.14222	1.20975	-0.00483	--	0.005396
0.6	0.1231	1.1744	-0.0203	--	0.016340
0.65	0.10489	1.1526	-0.02023	--	0.019953
0.7	0.087558	1.13715	-0.0126	--	0.014615
0.75	0.07106	1.12141	-0.00427	--	0.002719
0.76	--	--	--	--	0.000000
0.80	0.05538	1.1147	0.013762	--	0.010396
0.85	0.040474	1.0924	0.01662	--	0.018847
0.90	0.026297	1.0701	0.01965	--	0.018843
0.95	0.01281	1.0376	0.01247	--	0.010385

$$\zeta_1=-1.2025a/w+0.6233 \qquad 0.3\le a/w\le 0.53 \tag{8}$$

For the values of a/w between 0.53 to 0.95, taking a sinusoidal function we can obtain

$$\zeta_2=-0.02\sin\left[\frac{\pi}{0.23}(a/w-0.53)\right] \qquad 0.53<a/w<0.95 \tag{9}$$

Corresponding to each value of a/w, the results of ζ_1, ζ_2 compared with their real values ζ are listed in Table 1.

From the Table 1 it is found that the values of ζ can be replaced by the values of ζ_1 and ζ_2 with good accuracy. Thus a general form of the formula (1) can be obtained as follows

$$\Delta J=\frac{2}{Bb}(\alpha_1\cdot U+\alpha_2\cdot\Delta P\cdot\Delta\delta)+\frac{2}{Bb}U_e\begin{cases}-1.2025\dfrac{a}{w}+0.6233 & \left(0.3\le\dfrac{a}{w}\le 0.53\right)\\[2ex] -0.02\sin\left[\dfrac{\pi}{0.23}\left(\dfrac{a}{w}-0.53\right)\right] & \left(0.53<\dfrac{a}{w}<0.95\right)\end{cases} \tag{10}$$

Experimental Results and Discussion

Material and Experimental Procedure. The material used in this investigation was a directionally solidified alloy K5 (D.S. alloy K5), whose chemical composition and mechanical properties are listed in Table 2 and Table 3, respectively. The specimens were heat treated at 1210±10°C/4 h, air cool; 870±10°C/32 h, air cool.

The specimens used were WOL type, 10 mm thick, with growth orientation parallel to the principal stress axis [5]. The tests were carried out in a low-cycle electrohydraulic fatigue

Nomenclature

a = crack length
B = specimen thickness
b = specimen ligament size = $w-a$
D = material constant
E = elastic modulus
K = rigidity coefficient
N = number of cyclic loading
U = total area under load displacement hysteresis loop, i.e., total deformation work
W = specimen width
Y = geometry shape factor
γ = material constant
ΔG = increment of strain energy release rate
ΔJ = a cycle J integral
ΔK = stress intensity factor range
U_e = elastic portion of total deformation work
U_p = plastic portion of total deformation work

Table 2 Chemical composition of D.S. alloy K5, wt. percent

C	Cr	W	Co	Mo	Ti	Zr	Al	B	Ce	Ni
0.12	10.41	4.69	9.84	3.93	2.61	0.098	5.42	0.029	0.0038	Bal

Table 3 Mechanical properties of D.S. alloy K5

Temp	Tensile strength	elongation	area reduction	σ_{100h} endurance	σ_{200h} endurance	σ_{500h} endurance
°C	σ_b, kg/mm²	δ, %	ψ, %	kg/mm²	kg/mm²	kg/mm²
20	103-107	6-8	8-16			
700	100-110	6-10	10-11	93.5	92	90
800	108-110	7-12	10-11	64	62	60
850	102-104	9-12	13-19	52	50	47
900	85-91	12-18	14-19	34	33	30
950	68-72	20	32-40	25	23	20
1000	54-56	20	50	18	16	13-14.5

machine with tension-tension load control. The loading wave was a triangular wave. The stress ratio was 0.23. The loading frequency was about 20 cpm. The temperature during the tests was 950°C ± 2°C.

The fatigue crack length was measured by electrical potential drop method. The fatigue crack propagation rates were obtained by locally differentiating the a–N curves by means of a seven-point incremental polynomial.

In order to record each of the load-displacement hysteresis loops with an x–y recorder, the special extensometer was designed and manufactured [6].

The expression [7] of stress intensity factor for CT specimens is

$$\Delta K = \frac{\Delta P}{BW^{0.5}} F(a/w) \tag{11}$$

where

$$F(a/w) = 30.96(a/w)^{1/2} - 195.8(a/w)^{3/2}$$
$$+ 730.6(a/w)^{5/2} - 1186.3(a/w)^{7/2} + 754.6(a/w)^{9/2}$$

It has been shown that fatigue crack propagation rate in an elastic-plastic regime depends on the cycle J integral ΔJ, i.e.

$$da/dN = D(\Delta J)^{\gamma} \tag{12}$$

Analysis and Discussion. The results obtained are shown in Fig. 3. It can be seen that the values da/dN can be expressed by ΔK and $\sqrt{\Delta J \cdot E}$, respectively, where $\sqrt{\Delta J \cdot E}$ is converted from ΔK and they are nearly equal, and the ΔJ was calculated by formula (1) [4]. The latter is smaller than the former. Thus K and J can be considered as nearly equivalent under this experimental condition, since linear-elastic fracture mechanics does not consider the effects of plastic zone on stress intensity factor (SIF), but the J integral does. Therefore, in accordance with the method of crack-tip parallel movement proposed by Irwin [8], it is known that the effect of a small-range plastic zone is equivalent to an increase in crack length, and SIF increases with it as well. That is why the da/dN expressed by $\sqrt{\Delta J \cdot E}$ aren't quite equal to, but are slightly smaller than those expressed by ΔK in Fig. 3. Nevertheless, in the second stage of fatigue crack propagation the curves da/dN–ΔK and da/dN–$\sqrt{\Delta J \cdot E}$ appear to intersect at the middle in the plot in [3] (see Fig. 4). This is due to the use of formula (3) which is obtained by neglecting the last two terms in the formula (1).

From Fig. 2, when $a/w \le 0.53$ and then $\zeta \ge 0$, combining formulas (4), (5), and (7), it can be shown that

$$\Delta G_l \ge \frac{2}{Bb}(\alpha_1 + 2\alpha_2) U_e$$

$$\Delta G_l - \frac{2}{Bb}(\alpha_1 + 2\alpha_2) U_e = er > 0$$

Thus the ΔJ expressed by the formula (3) is smaller than that

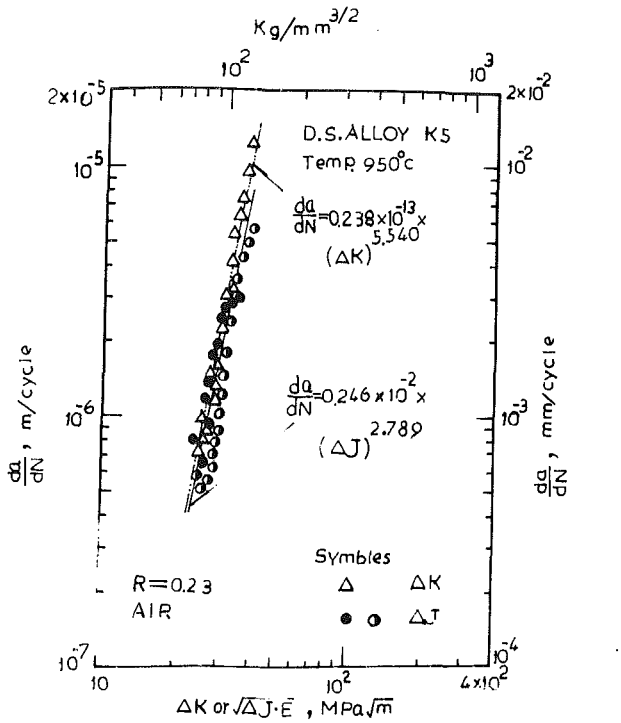

Fig. 3 Comparison of the dependence of da/dN on ΔK with that on $\sqrt{\Delta J \cdot E}$

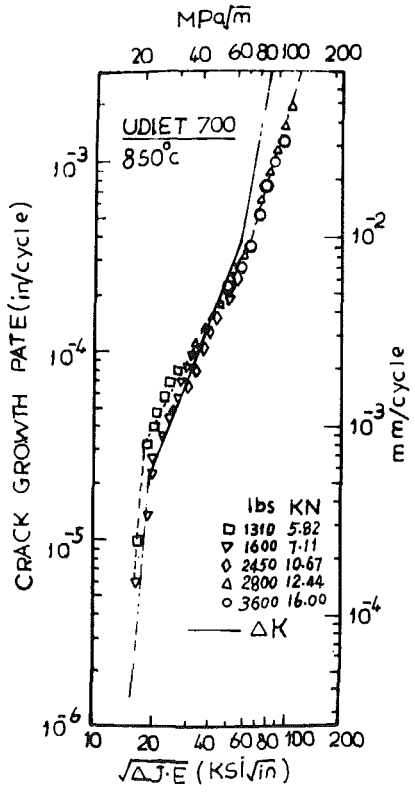

Fig. 4 Comparison of the dependence of crack growth rate on ΔJ with that on ΔK [3]

in formula (1). In order to distinguish the ΔJ between formulas (1) and (3), we denote the ΔJ in formulas (1) and (3) as ΔJ_1 and ΔJ_3, respectively. It is obvious that

$$\Delta J_3 < \Delta J_1 \qquad (a/w \le 0.53) \tag{13}$$

From [3], it is found that the two curves in Fig. 4 intersect near $a/w = 0.53$ (about $\Delta K = 40$ Ksi $\sqrt{\text{in}}$). Since $\sqrt{\Delta J_1 \cdot E} = \Delta K$

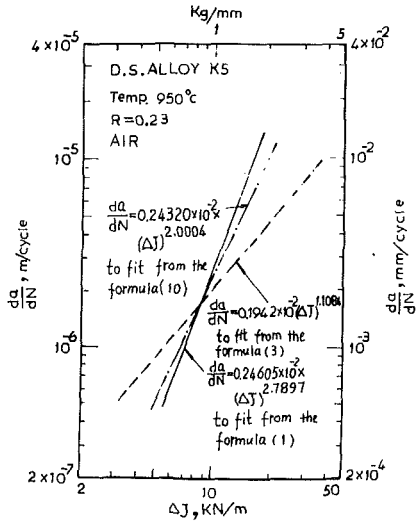

Fig. 5 The curves $da/dN - \Delta J$

(see Fig. 3), the measured values da/dN corresponding to each test point are unchanged. According to inequality (13) it can be seen that the curve da/dN-$\sqrt{\Delta J \cdot E}$ is above the da/dN-ΔK curve. On the contrary, for $0.53 < a/w < 0.95$, it can be obtained that

$$\Delta G_I \leq \frac{2}{Bb}(\alpha_1 + 2\alpha_2)U_e$$

Thus

$$\Delta J_3 > \Delta J_1 \quad (0.53 < a/w < 0.95) \tag{14}$$

Similarly, from inequality (14), it can be recognized that for $0.53 < a/w < 0.95$ in Fig. 4 the curve da/dN-$\sqrt{\Delta J \cdot E}$ is under the da/dN-ΔK curve.

Therefore, the phenomenon in Fig. 4 is caused by the approximate formula (3), not by notch effects as well as strain energy input or output at all.

It is not difficult to show that formula (3) does not bring a larger error only when $a/w > 0.53$, i.e., in elastic-plasticity until full yield. However, when $a/w \leq 0.53$, it will bring a larger error from the above analysis. Furthermore, this can be verified by lifetime estimation. For comparison, the dependences of da/dN on ΔJ by taking the experimental data of D.S. alloy K5 at 950°C in air were plotted in Fig. 5 by using (1), (3), and (10), respectively. The lifetime estimation is listed in Table 4.

The changing trends appearing in Fig. 4 and Fig. 5 are quite similar (stage II of fatigue crack propagation).

From Table 4 and Fig. 5 it can be seen that formula (1) is more accurate, but it contains the increment of the strain energy release rate, which correlates with the elastic modulus E. Thus it is inconvenient to use this formula at high temperatures. Since the elastic modulus changes with temperature, the values of elastic modulus at various temperatures have to be determined by additional experiments. Although the accuracy of formula (10) is not better than that of formula (1), it is much better than that of formula (3), and its relative error is allowable in engineering applications. Furthermore, it does not contain the elastic modulus E, and is rather convenient to use at high temperature.

Table 4 Comparison of lifetime estimation

formula	D	γ	estimated lifetime N, cycle	measured lifetime N, cycle	relative error δ, %
formula (1)	0.24605×10^{-2}	2.7897	3205		1.05
formula (3)	0.19423×10^{-2}	1.1084	2922	3239	9.79
formula (10)	0.24320×10^{-2}	2.0004	3125		3.54

D, γ are the coefficients in the formula (12)

Conclusions

In this paper the cycle J integral expression for CT specimens was improved. Formula (10), derived in present study, is able to be used in large crack growth range of $0.3 \leq a/w < 0.95$. Furthermore, the estimating accuracy of this formula increases 1.7 times than that of the previous formula.

Acknowledgments

The authors are grateful to Prof. Yan Minggao for his guidance in this work.

References

1 Merkle, J. G., and Corten, H. T., "A J Integral Analysis for the Compact Specimen, Considering Axial Force as Well as Bending Effects," ASME *Journal of Pressure Vessel Technology*, Vol. 96, Nov. 1974, pp. 286–292.

2 Clark, G. A., and Landes, J. D., "Evaluation of the J Integral for the Compact Specimen," ASTM *Journal of Testing and Evaluation*, Vol. 7, No. 5, Sept. 1979, pp. 264–269.

3 Sadananda, K., and Shahinian, P., "A Fracture Mechanics Approach to High Temperature Fatigue Crack Growth in Udimet 700," *International Journal of Engineering Fracture Mechanics*, Vol. 11, No. 1, 1979, pp. 73–86.

4 Liu Shao-Lun and Xie Ji-Zhou, *J. of Aeronautical Materials*, Beijing, Vol. 1, 1981, pp. 58–62 (in Chinese).

5 Group of Directional Alloy Research, "Effects of Directional Solidification on Organizations and Properties of Cast Superalloy K5," Institute of Aeronautical Materials, Beijing, No. 2, 1978, pp. 18–32 (in Chinese).

6 Group of Low-Cycle Fatigue Research, "Measurement of High Temperature Low Fatigue Crack Propagation Rate da/dN," *J. of Aeronautical Materials*, No. 6, 1979 (in Chinese).

7 Zhu Wu Yang et al., *Measurement of Fracture Toughness*, Science publisher, 1979, p. 78 (in Chinese).

8 Irwin, G. R., *Handbuch der Physik*, Vol. VI, Springer, Berlin, 1958, p. 551.

A. V. Srinivasan
Manager, Applied Mechanics Research.

B. N. Cassenti
Senior Analytical Engineer.

United Technologies Research Center,
East Hartford, CT 06108

A Nonlinear Theory of Dynamic Systems With Dry Friction Forces

Structural systems with interfaces where one component may rub against another are not uncommon in aircraft and other engineering structures. The dynamic characteristics of such systems need to be calculated for use in design and such calculations depend on the law of friction used to represent the interacting boundaries. This paper proposes a nonlocal law of dynamic friction and establishes a procedure to incorporate such laws in a general structural dynamic analysis.

1 Introduction

One of the most important sources of energy dissipation in built-up structures pertains to dry friction at joints and at interfaces in contact with each other. When materials with very low inherent damping are used in environments offering essentially no aerodynamic damping (such as, for example, in space structural systems), the ability of the structures to withstand resonant vibration depends almost entirely on the extent of friction damping. Even in the design of components which can generate certain levels of aerodynamic damping, it is essential to be able to estimate accurately the levels of nonaerodynamic sources of damping because unlike the latter, the former can be either positive or negative. For example, the aeroelastic instabilities of aircraft structures such as airplane wings or turbomachinery blades are attributed to negative aerodynamic damping developing in the system as a result of its interaction with the air forces causing the system to vibrate. In such situations, escalation of vibratory stresses to dangerous levels is prevented only through the contribution to damping from sources such as friction. In some instances, artificial devices are designed and introduced into the structural system with the sole purpose of developing friction forces leading to damping when the dynamics of the component demands it. Thus, there is a clear need to enhance the level of understanding in the broad area of dynamics of surfaces in contact.

Among the multitude of factors contributing to the dynamics of elastic bodies that come into contact with each other at interfaces, the most significant factor is the governing law of friction. It is the law of friction that accounts for the characteristics of contacting surfaces and the environment, and establishes the relationship among forces and resulting motion. Success in predicting the dynamic response of a structural component depends, to a large extent, on the choice of a realistic friction law that accurately portrays the interfaces. The laws of friction so constructed must be adaptable in a dynamic analysis of the structural system and directly verifiable in a carefully controlled test.

In the context of vibration engineering, the basic requirements are to (*a*) quantify the nature and magnitude of friction forces that are manifest between contacting interfaces of vibrating components, (*b*) quantify the nature and magnitude of vibratory motion at these interfaces, and (*c*) predict the extent of damping that may be present. Within this context, friction forces are considered to be useful, i.e., they control vibratory amplitudes which otherwise may escalate. On the other hand, any consideration of friction forces cannot ignore the influence of these forces on wear of the components resulting in loss of useful life of machines. The phenomena of friction and wear are inseparable. The emphasis in this study, however, is in outlining those aspects of friction forces that pertain to vibration damping.

This paper is aimed at examining different characterizations of friction forces at interfaces. A general nonlinear theory of dynamic systems is proposed in such a way that a local or nonlocal law guided by experimental data may be incorporated. Solution procedures are presented and discussed.

A general structural system with an arbitrary number of interfaces is considered. The friction forces developing at these interfaces during vibration are treated in such a way that the influence of different laws of friction may be examined. The solution procedure leads to a calculation of time history of the vibratory motion either under arbitrary transient loading or as the driving frequency is swept over a given range so that the dynamic response as well as the nature of its stability can be evaluated.

The primary purpose of proposing this approach is to be able to solve real structural systems with a large number of interfaces. The success of obtaining reliable solutions to such systems may depend upon the representation of friction forces. For example, it is shown that the use of the Coulomb law of friction can lead to numerical instabilities even for an apparently simple problem of a two-degree-of-freedom system. It is recognized that alternate numerical algorithms and/or extremely fine time steps may alleviate the numerical instability. But the more important point to be made is that realistic and physically meaningful laws of friction do not appear to have such inherent problems. Therefore they are more amenable to obtaining numerical solutions. One such law, a dynamic nonlocal law, confirms that this important, practically useful methodology can be applied to dynamic problems of engineering interest in which friction forces play an important role.

Contributed by the Gas Turbine Division of THE AMERICAN SOCIETY OF MECHANICAL ENGINEERS and presented at the 31st International Gas Turbine Conference and Exhibit, Dusseldorf, Federal Republic of Germany, June 8–12, 1986. Manuscript received at ASME Headquarters December 26, 1985. Paper No. 86-GT-8.

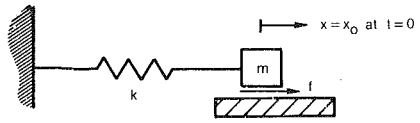

Fig. 1 A single-degree-of-freedom model

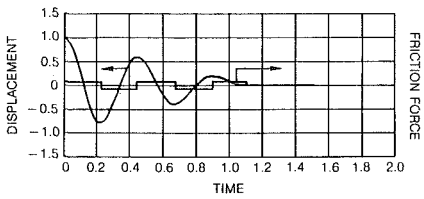

Fig. 2 Displacement history and friction force

A Formulation. The governing equations of motion for the structural system may be represented in matrix form as

$$[m]\{\ddot{x}\} + [c]\{\dot{x}\} + [k]\{x\} = \{f\} + \{F\} \tag{1}$$

where $\{x\}$ represents physical displacements; $\{f\}$ represents forces of friction; $\{F\}$ represents external forces; $[m]$, $[c]$, and $[k]$ are the mass, damping, and stiffness matrices.

It may be noted that some of the elements of $\{f\}$ and $\{F\}$ may be zero. Also, if $\{f\}$ represents forces at internal interfaces only, the arithmetic sum of the elements of $\{f\} = 0$.

Let $[\Phi]$ represent the matrix of eigenvectors $\{\varphi\}$, obtained from the solution of equation (1) in which $[c] = 0 = \{f\} = \{F\}$ and $[\omega^2]$ represents the corresponding eigenvalues.

Successive transformations lead to

$$\{\ddot{z}\} + [\omega^2]\{z\} = \{g\} + \{G\} - [H] \tag{2}$$

where

$$\begin{aligned} \{z\} &= [\Phi]^T\{y\} \\ \{y\} &= [\sqrt{m}]\{x\} \\ \{g\} &= [\Phi]^T[1/\sqrt{m}]\{f\} \\ \{G\} &= [\Phi]^T[1/\sqrt{m}] \\ [H] &= [\Phi]^T[c][\Phi]\{\dot{z}\} \\ [\sqrt{m}][\sqrt{m}] &= [m] \\ [1\sqrt{m}][1\sqrt{m}] &= [m]^{-1} \end{aligned} \tag{3}$$

The elements of $\{G\}$ are functions of time and the elements of $\{g\}$ represent the nature of friction forces.

The ith row of equation (2) can be written as

$$\ddot{z}_i + \omega_i^2 z_i = g_i + G_i - H_i \tag{4}$$

and $g_i = g_i(z_1, z_2, z_3, \ldots; \dot{z}_1, \dot{z}_2, \dot{z}_3, \ldots)$, in view of equation (3), represents the influence of friction forces in mode i; $G_i = G_i(t)$ represents the generalized force in the ith model and $H_i = H_i(\dot{z}_i, z_2, \ldots)$ represents the influence of viscous type damping forces in the ith mode.

B Solution. The solution to equation (4) can be written as

$$\begin{aligned} z_i &= C_i^{(1)} e^{i\omega_i t} + C_i^{(2)} e^{-i\omega_i t} \\ &- \frac{i}{2\omega_i}\int_0^t (g_i + G_i - H_i) e^{i\omega_i(t-\tau)}\, d\tau \\ &+ \frac{i}{2\omega_i}\int_0^t (g_i + G_i - H_i) e^{-i\omega_i(t-\tau)}\, d\tau \end{aligned} \tag{5}$$

where $g_i = g_i\{z_1(\tau), \dot{z}_1(\tau), z_2(\tau), \dot{z}_2(\tau), \ldots\}$; $H_i = H_i\{\dot{z}_1(\tau), \dot{z}_2(\tau), \ldots\}$; $G_i = G_i(\tau)$; $C_i^{(1)}$ and $C_i^{(2)}$ are arbitrary constants.

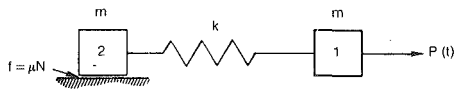

Fig. 3 Two-degree-of-freedom system

It may be noted that $C_i^{(1)}$ and $C_i^{(2)}$ are calculated from prescribed initial conditions, i.e., $\{x\}$ and $\{\dot{x}\}$ at $t = 0$. With $\{x\}$ and $\{\dot{x}\}$ prescribed at $t = 0$, z_i can be calculated from equation (3); i.e.,

$$\begin{aligned} \{z\}_{t=0} &= [\Phi]^T[\sqrt{m}]\{x\}_{t=0} \\ \{\dot{z}\}_{t=0} &= [\Phi]^T[\sqrt{m}]\{\dot{x}\}_{t=0} \end{aligned} \tag{6}$$

which transforms the physical coordinates to modal coordinates. Because the friction forces are brought under the integral sign, the numerical solution should tend to be more stable.

C Numerical Application. The implicit integration, i.e., equation (5), has been coded on a P.C. (HP9816) and several example problems were run to verify the procedure and the program. Two examples are shown below to illustrate certain aspects of the procedure.

The first example chosen to obtain numerical results is a simple single-degree-of-freedom system with a Coulomb type of friction interface (see Fig. 1) whose solution can be shown to be

$$x = \begin{cases} \left[x_0 - (2N+1)\dfrac{F}{k}\right]\cos\ \omega_0 t + (-1)^N \dfrac{F}{k} & N < N_0 \\ (-1)^{N_0}\left[x_0 - 2N_0\dfrac{F}{k}\right] & N \geq N_0 \end{cases} \tag{7}$$

and N = number of half-cycles completed, truncated to the greatest integer less than $\omega_0 t/\pi$ and $N_0 = 1/2(kx_0/F - 1)$.

The following numerical values are prescribed for the parameters

$$k = 1, \quad x_0 = 1, \quad m = 0.5, \quad F = 0.1$$

Clearly the ratio of spring force to friction force, i.e., kx_0/F, is 10 and therefore the force in the spring exceeds F at $t = 0$ and continues to be so at all times, *except* when x changes direction in the course of oscillation. At those instants of time when $x = 0$, the inertial forces are such that the block does not come to rest until approximately a quarter cycle later when $\dot{x} = 0$. At instances of time when $\dot{x} = 0$ the spring force is still large enough to permit continuing motion. However at each such cycle the motion gets damped (see Fig. 2) because of the presence of friction. After four half-cycles the block comes to complete rest. The time history shown in Fig. 2 agrees entirely with the analytical solution. At instances of time when the block completely comes to rest, numerical instability occurs. This feature is demonstrated more clearly in the following example.

The second example chosen is a two-degree-of-freedom system which tests some important aspects of frictionally damped systems.

Figure 3 is the analytical model of a two-degree-of-freedom system which has a rigid body mode and a flexible system mode. When mass 2 is fully stuck, the system degenerates into a single-degree-of-freedom model. With $P = P_0 \sin t$ *and* an assumed friction force of $\mu N = 3P_0$, the system would respond as a single-degree-of-freedom model as long as the driving frequency is not close to the natural frequency $\sqrt{k/m}$. As the frequency approaches the natural frequency, the spring force would gradually build up to overcome $3P_0$ and mass 2 will begin to slip. At $= 1.14\sqrt{k/m}$ and $N = 3P_0$, calculations were made using the displacement at each time as the criterion for convergence. For the example discussed below: $k = 1$, $m = 1$,

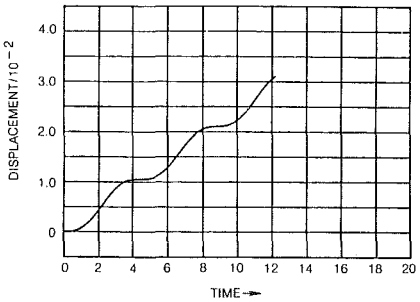

Fig. 4 Displacement of mass 2 using Coulomb friction law and displacement convergence test

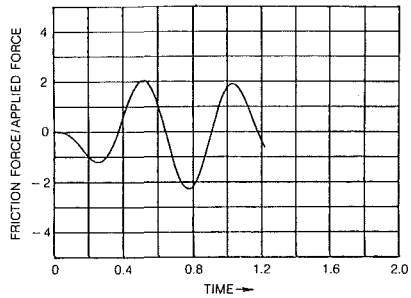

Fig. 5 Friction force using Coulomb friction law and displacement convergence test

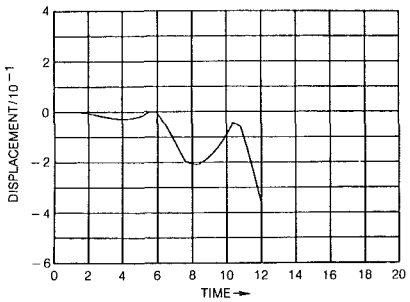

Fig. 6 Displacement of mass 2 using Coulomb friction law and velocity convergence test

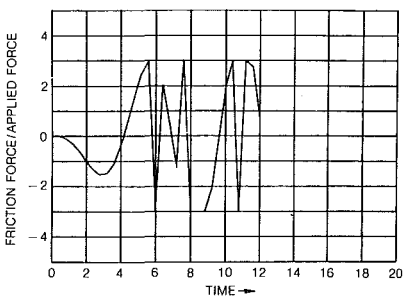

Fig. 7 Friction force using Coulomb friction law and velocity convergence test

$p = 1$. The resulting time history for the displacement of mass 2 and the friction force at the interface are shown in Figs. 4 and 5, respectively. These results are clearly unacceptable because the mass 2 cannot begin to move since the friction force at the interface has not reached $3P_0$ as can be seen from Fig. 5. This is an illustration of the influence of numerical analysis on the solution and suggests the need to examine (1) the numerical algorithm, (2) the computer code, (3) the step size, and (4) the choice of convergence criterion, as possible sources for the error.

The convergence criterion was changed to a check on velocity at each step and the results show some improvements as can be observed from Figs. 6 and 7. Mass 2 moves but there is no steady drift. However, the frictional force is quite erratic. Certain obvious checks were made to verify the accuracy of the program. A single-degree-of-freedom system with Coulomb friction checked exactly with the corresponding analytical solution as can be seen from Fig. 2. Other checks with various types of damping compared well with corresponding exact solutions. Altering time steps did not improve the results. Alternate numerical integration schemes also had little effect.

The numerical integration was performed using only one trapezoidal increment over each interval from t to $t + \Delta t$. This is equivalent to a one-step Euler implicit integration. Various approximations of the Coulomb friction law were tried. These included

$$f = -\mu N \operatorname{sgn}(\dot{x}) \tag{8}$$

$$f = -\mu N \tanh\left(\frac{\dot{x}}{v_0}\right) \tag{9}$$

$$f = \begin{cases} -k(x_1 - x_2) & |x_1 - x_2| < \dfrac{\mu N}{k} \\ -\mu N \operatorname{sgn}(\dot{x}) & |x_1 - x_2| \geq \dfrac{\mu N}{k} \end{cases} \tag{10}$$

$$f = \begin{cases} -\dfrac{\mu N}{v_0}\dot{x} & |\dot{x}| < v_0 \\ -\mu N \operatorname{sgn}(\dot{x}) & |\dot{x}| \geq v_0 \end{cases} \tag{11}$$

where v_0, k are parameters used to represent the friction law. The law represented by equation (8) was the most unstable. Equation (10) which is the physically consistent version was also unstable. Equations (9) and (11) were more stable but have no physical basis.

The discontinuity inherent in the representation of the Coulomb force is the principal source of the numerically unstable calculation. If one were to pursue this problem further, other numerical schemes including constructing piecewise linear solutions could be shown to lead to satisfactory solutions. However, the aim of this work is to illustrate that the use of more realistic friction models, such as the one discussed in the section below, are not only more appropriate for engineering use but also their numerical solution is not prone to the type of problems discussed above.

D Nonlocal Laws of Friction. The approach presented below is based on the concept of nonlocal nature of deformations introduced by Oden and Pires [1]. A brief discussion of the concept is included here for the sake of completeness and is followed by the formulation of a modified law proposed by the present authors. This section will conclude by applying the proposed modified nonlocal law to the two-degree-of-freedom system and will demonstrate the resulting improvements in the numerical solution.

Recognizing the continuum nature of bodies in contact, the friction force at a point $\bar{x}$ is represented as the sum total of the influence of normal stresses over a neighborhood as shown schematically in Fig. 8. Thus, unlike the local law

$$\tau(\bar{x}) = \mu\sigma_n(\bar{x}) \tag{12}$$

a nonlocal law represents

$$\tau(\bar{x}) = \mu \int_{A_c} W_\rho(\bar{x} - \bar{y})\sigma_n(\bar{y})\, dA_c \tag{13}$$

where W_ρ is a weighting function that distributes the influence of σ_n in a circle of characteristic radius ρ. Further, as the friction (shear stress) vector is always opposed to the direction of relative motion

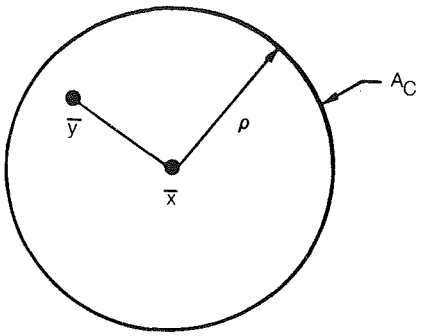

Fig. 8 Concept of nonlocal laws of friction (Olden and Pires)

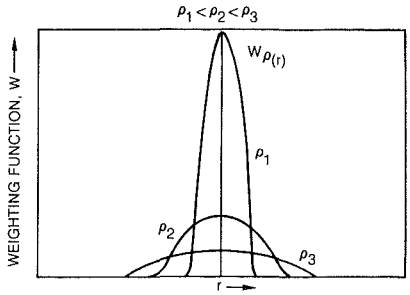

Fig. 9 Nonlocal effects

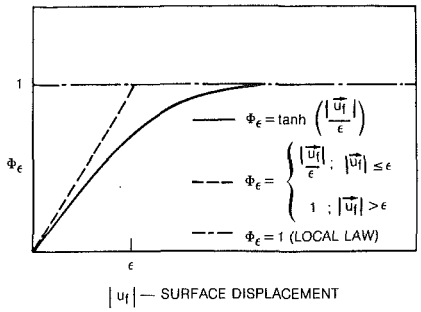

Fig. 10 Nonlinear effects

$$\bar{\tau}(\bar{x}) = -\mu \bar{n}_f \int_{A_c} W_\rho(\bar{x}-\bar{y})\sigma_n(\bar{y})dA_c$$

$$\bar{n}_f = \frac{\bar{u}_f}{|\bar{u}_f|} \tag{14}$$

where $\bar{u}_f$ is the vector of relative displacement along the surface. The requirement that the friction force be dependent on the motion (displacement or velocity) leads to

$$\bar{\tau}(\bar{x}) = -\mu \bar{n}_f \Phi_\epsilon(|\bar{u}_f|)\int_{A_c} W_\rho(\bar{x}-\bar{y})\sigma_n(\bar{y})dA_c \tag{15}$$

Figures 9 and 10 show possible representations of the weighting function W and the nonlinear function Φ_ϵ which allows for a dependence of the force on the motion.

An extension to the above law is proposed in this paper and includes velocity dependence for the forces at the interface and an integration along the path followed by the points at the interfaces undegoing relative motion. The velocity dependence accounts for the dynamics of relative motion at interfaces and the type of integration proposed recognizes a nonisotropic weighting function. The nature of this extension is presented below.

Consider two elastic bodies A and B in relative motion at an interface and assume that body B is stationary. Let $V_1(t)$ be the velocity of a point A in surface A that was initially in contact with B at position X_1 and at time t_1. Then the relative motion of A may be written as

$$\mathbf{X}_{A_1} = \mathbf{X}_1 + \int_{t_1}^{t} \mathbf{V}_1 dt \tag{16}$$

The total distance traveled between t_1 and t is

$$R = \int_{t_1}^{t} |\mathbf{V}_1| dt$$

$$\dot{R} = \begin{cases} |\mathbf{V}_1| & t \ge t_1 \\ 0 & t < t_1 \end{cases} \tag{17}$$
$$R = 0 \qquad \text{at } t = t_1$$

As stated earlier the point under consideration came into contact with a corresponding point in B in time t_1. As the point A moves over the contact surface a bond may develop. The adhesive strength of this bond will depend on many factors including the extent of time the two points remain in contact with each other and is proportional to the area of the bond. The elapsed time of this bond in turn depends upon the relative speed of the two points at the time of contact. Let ϵ represent the dimension of the bond in the direction of motion. Before the two points come in contact $\epsilon = 0$. After they are in contact, the surfaces will deform together until the contact is broken. The growth of this bond may be represented by an evolution law as follows

$$\dot{\epsilon}(x_1,t) = \begin{cases} 0 & t < t_1 \\ \dfrac{a_s}{|\mathbf{V}_1|}(\epsilon_0 - \epsilon) + \dfrac{|\mathbf{V}_1|}{l_k}(\epsilon_k - \epsilon) & t \ge t_1 \end{cases} \tag{18}$$

where a_s, l_k, ϵ_0, ϵ_k are constants that can be chosen to represent a given condition (pressure, temperature, etc. and static, subscript s or kinematic, subscript k condition). The above form is chosen to allow for a realistic growth of bond both at low and high relative velocities.

This is illustrated by considering the steady-state values for ϵ which are given by

$$\bar{\epsilon} = 0$$

or

$$\epsilon = \frac{\dfrac{a_s}{|\mathbf{V}_1|}\epsilon_0 + \dfrac{|\mathbf{V}_1|}{l_k}\epsilon_k}{\dfrac{a_s}{|\mathbf{V}_1|} + \dfrac{|\mathbf{V}_1|}{l_k}} \tag{19}$$

For low speeds (i.e., V_1 very small)

$$\frac{a_s}{|\mathbf{V}_1|} \gg \frac{|\mathbf{V}_1|}{l_k} \text{ and } \epsilon \approx \epsilon_0 \tag{20}$$

For high speeds

$$\frac{a_s}{|\mathbf{V}_1|} \ll \frac{|\mathbf{V}_1|}{l_k} \text{ and } \epsilon \approx \epsilon_k \tag{21}$$

As relative motion begins and the two points move apart, the shear force at the bond will change. At first, the shear force will increase, reach a maximum, and as the bond begins to break, the force will decrease. The above characteristics can be represented by a function ϕ as follows

$$\phi = \phi(R/\epsilon) = \frac{1}{\Gamma(p+1)}(R/\epsilon)^p e^{-(R/\epsilon)} \tag{22}$$

where the ratio R/ϵ represents the extent of relative motion in terms of bond length. This function is shown in Fig. 11 for several values of the parameter p. R is along the path of motion and $R \ge 0$ by definition. Hence the integral of ϕ over R is finite if $p > -1$.

Perpendicular to the path, a second weighting function is allowed to represent the bond length. This has been taken to be (see Fig. 12)

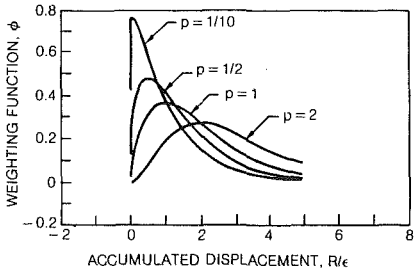

Fig. 11 Weighting function along direction of motion (see equation (23))

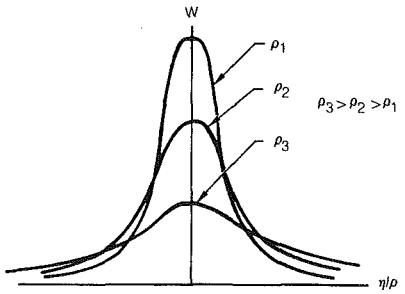

Fig. 12 Weighting function perpendicular to direction of motion (see equation (24))

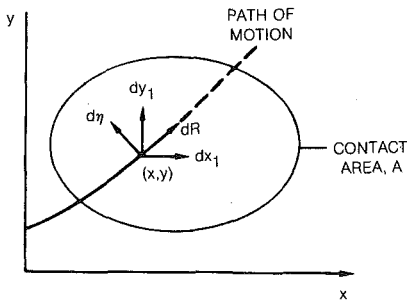

Fig. 13 Coordinate systems for modified nonlocal law

$$W\left(\frac{\eta}{\rho}\right)=\frac{e^{-(\eta^2/2\rho^2)}}{\sqrt{2\pi}} \tag{23}$$

where η is the distance perpendicular to the path and ρ along with ϵ represents a measure of the area of bond. The shear force acting between the two points is now made proportional to the product of ϕ and W. Further, the strength of the bond must also depend upon the normal stress $\sigma_n(X_1)$ at X_1. Therefore, the proposed nonlocal law for the shear force at x_1 is essentially complete with the following representation

$$\tau(\mathbf{X})=\mu_s\int_{-\infty}^{\infty}\int_{-\infty}^{\infty}\phi(R/\epsilon)W(\eta/\rho)\sigma_n(\mathbf{X}_1)\frac{dX_1dY_1}{\epsilon_0\rho} \tag{24}$$

See Fig. 13 for the corresponding coordinate system. Recognition of the fact that the frictional shear at X will be in a direction opposite to the relative displacement $\mathbf{u}$ completes the required representation as follows

$$\tau(\mathbf{X})=-\mu_s\int_{-\infty}^{\infty}\int_{-\infty}^{\infty}\phi(R/\epsilon)W(\eta/\rho)\sigma_n(\mathbf{X}_1)\frac{\mathbf{u}}{|\mathbf{u}|}\frac{dX_1dY_1}{\epsilon_0\rho} \tag{25}$$

The constants present in this formulation (ϵ_0, ϵ_k) can be shown to be related to the static and kinetic coefficients of friction [2]. The total friction force at the interface is

$$\mathbf{f}=\int_A\tau(\mathbf{X})dA \tag{26}$$

where A is the total area of the interface. The fourfold integration evident in equation (26) averages the local effects and therefore there is no need to model individual asperities on the surface.

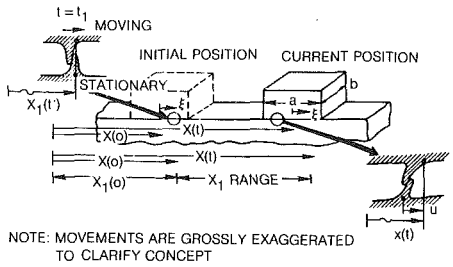

Fig. 14 One-dimensional simplification of the modified nonlocal law

The formulation presented above is of sufficient generality to permit its use in specific engineering problems in which rubbing at interfaces influences the dynamics of components. However, an examination of equation (26) reveals that the real time calculation of friction at a point on an interface requires computing fourfold integrals. Therefore computing time becomes an important factor in solving problems of practical interest. This particular issue will be discussed in another paper. In the context of this paper however, a simple example is chosen to illustrate the validity of the principles involved in dynamic friction problems.

Consider a block moving over another block (see Fig. 14). It is assumed that the normal stresses over the interface are uniform and that the characteristic dimension $\rho \ll b$.

With reference to Fig. 14, ξ = location of a point in the block; X = the location of the center of the block in global coordinates; x = the location of point ξ in global coordinates.

The assumption of uniform distribution of normal stress on the surface simplifies the integral of σ_n over the area to N/ab in equation (25). Similar simplification occurs in the integration of $W(\eta/\rho)$ in the direction perpendicular to the path of motion with the assumption $\rho \ll b$. The integral of $W(\eta/\rho)$ with respect to dY_1/ρ becomes unity while the integration over the limits $-b/2$ to $+b/2$ leads to b.

Thus, equation (26) reduces to

$$f=\frac{-\mu N}{a\,\epsilon}\int_{-a/2}^{a/2}\int_{x(0)}^{x(t)}\phi(R/\epsilon)\frac{|X-X_1+\xi|}{X-X_1+\xi}dX_1d\xi \tag{27}$$

$$X_1=X \text{ at } t=0<t_1<t$$

where

$$R=\int_{t_1}^{t}|\dot{X}(\tau)|d\tau=R(t,\quad x,\quad \xi)$$

$$X(t)=x-\xi \tag{28}$$

$$X_1=X(t_1)$$

ϕ is given by equation (22), and t_1 is the time at which two asperities first came into contact, as shown in Fig. 14.

Note that the displacement u is given by

$$u=X(t)-X_1(t_1)+\xi$$

The above equations were coded on a computer and the results for the dynamic system of Fig. 3 were encouraging since the numerical instabilities were much reduced. However, the execution times were excessive because of the double integration that had to be performed in equation (27).

A further simplification appeared necessary and was achieved by considering two limiting cases: (1) small displacements in only one direction (i.e., there are no reversals), and (2) large displacements in one direction.

Consider the first case where

$$\frac{|X+\xi-X_1|}{\epsilon}\ll 1$$

then the friction force

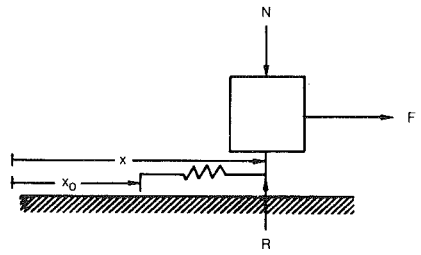

Fig. 15 Model representing equation (37)

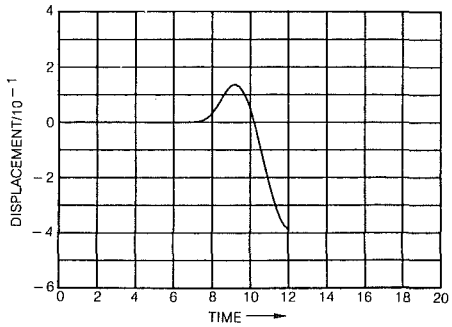

Fig. 16 Displacement of mass 2 using elastic-plastic friction law and velocity convergence test

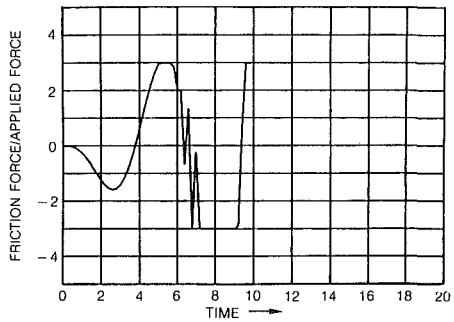

Fig. 17 Friction force using elastic-plastic friction law and velocity convergence test

$$f=-\frac{\mu N}{\epsilon a}\int_{-a/2}^{a/2}\int_{X_0}^{X}\phi\left(\frac{u}{\epsilon}\right)\frac{u}{|u|}\,du\,d\xi \tag{29}$$

For small $|u|/\epsilon$

$$\phi\left(\frac{|u|}{\epsilon}\right)\approx\frac{|u/\epsilon|^P}{\Gamma(p+1)} \tag{30}$$

Assuming $u>0$, and $a \gg \epsilon$

$$f\approx-\frac{\mu N}{\epsilon}\int_{X_0}^{X}\frac{u^P}{\Gamma(p+1)}\frac{du}{\epsilon^p} \tag{31}$$

which can be integrated to yield

$$f=-\frac{\mu N}{\Gamma(p+2)}\left(\frac{X-X_0}{\epsilon}\right)^{p+1} \tag{32}$$

For $p=0$

$$f=-\mu N\left(\frac{X-X_0}{\epsilon}\right) \tag{33}$$

a linear force displacement relationship results. If the motion is large, but in one direction only, and if $a \gg \epsilon$

$$f\approx\mu N\int_{X_0/\epsilon}^{X/\epsilon}\frac{z^p}{\Gamma(p+1)}e^{-z}dz \tag{34}$$

Since $(X-X_0)/\epsilon \gg 1$, and taking p to be zero

$$f\approx-\mu N \tag{35}$$

These two limiting cases are equivalent to representing the friction force by a nonlinear spring (see Fig. 15).

The force in the spring can now be taken from the two limiting cases, i.e., equations (33) and (35)

$$f=-\begin{cases}\dfrac{\mu N}{\epsilon}(X-X_0) & |X-X_0|<\epsilon\\ \mu N\,\mathrm{sgn}(\dot{X}) & |X-X_0|\geq\epsilon\end{cases} \tag{36}$$

where $|X-X_0|<\epsilon$ is now equivalent to $|u|/\epsilon \ll 1$.

Note that reversals are automatically included. The end of the spring must move according to

$$\dot{X}_0=\begin{cases}0 & |X-X_0|<\epsilon\\ \dot{X} & |X-X_0|\geq\epsilon\end{cases} \tag{37}$$

These equations approximate the effects of asperities on the surfaces. As motion begins the asperities are locked together between the two surfaces and they act as linear springs. At sufficiently large displacements the asperities begin to shear or yield. As the asperities fail new asperities become locked which is represented by the motion of the new reference X_0 when the displacement becomes sufficiently large.

This simplified friction law can also be represented by an elastic-perfectly plastic rod subjected to a uniaxial stress. This concept has been used in the past in finite element modeling of structures with friction present.

This simplified version of the formulation was used in the simulation of the system shown in Fig. 3. A convergence criterion based on velocities was used in the numerical analysis. The results obtained are shown in Figs. 16 and 17. Clearly, the displacement of mass 2 is essentially zero until the friction force exceeds μN. Although the friction force shows some instability, the characteristic is clearly superior to that seen earlier in Fig. 7.

Conclusion

An analytical approach to solving dynamic systems with many friction interfaces is proposed. It is shown that the numerical analysis is feasible when nonlocal laws of dynamic friction are used. The latter are realistic and physically meaningful, and do not lead to numerical instabilities common with the use of Coulomb type representation.

References

1 Oden, J. T., and Pires, E. B., "Nonlocal and Nonlinear Friction Laws and Variational Principles for Contact Problems in Elasticity," ASME *J. App. Mech.*, Vol. 50, 1983.

2 Srinivasan, A. V., Cassenti, B. N., and Cutts, D. G., "Study of Characteristics of Dry Friction Damping," Final Report to the Air Force Office of Scientific Research, R85-956479-2, Apr. 1985.

Reliability Evaluation of Ceramic Rotor for Passenger-Car Turbochargers

Y. Hamano

N. Sagawa

H. Miyata

Kyocera Corporation,
Kagoshima, Japan

A performance advantage is expected when the rotors of turbochargers are made out of ceramics. In order to qualify as commercially produced engine components, ceramic rotors must demonstrate confirmed reliability because the operation conditions are severe and the behavior of ceramic components under such conditions is not well understood. By the progress of related technologies such as designing, shape-forming, and ceramics-to-metal joining, ceramic rotors having high enough reliability levels as confirmed by NDE methods are produced.

Introduction

Ceramic turbine wheels offer a remarkable improvement in the rotational response of turbochargers [1, 2]. This is especially advantageous for passenger-car turbochargers, since transient engine boosting is their main function.

Unfortunately, however, the use of ceramic materials for such high-stress applications is still very limited, because of their brittleness and susceptibility to mechanical and thermal shocks. Ceramics have been regarded as relatively unreliable for such high-stress applications. So, in order to qualify for commercial production as engine components, ceramic turbine wheels must demonstrate confirmed reliability within a given cost limit.

In the production of gas turbine ceramic rotors, the reliability could be confirmed by the proof-spin test. Because of the cost limitation, proof testing is not feasible in the case of turbocharger production. The reliability has to be confirmed by the spot-check and in process NDE.

With the progress of the ceramic gas turbine development programs and with a few successes in commercial ceramic component production [3] – such as glow plugs and swirl chambers for small diesel engines – we have accumulated substantial test data on the production and engine testing of ceramic components of complex shapes. Related technologies, such as raw materials processing, shape-forming, sintering, finish machining, ceramics-to-metal joining, NDE, and design, have been improved. Ceramic turbine wheels and rotor assemblies designed and produced with these technologies now have performance capabilities and reliability levels high enough to be confirmed by NDE methods.

This paper covers the development and current status of related technologies such as designing, shape-forming, joining, and NDE and test results of ceramic turbine wheels and rotor assemblies.

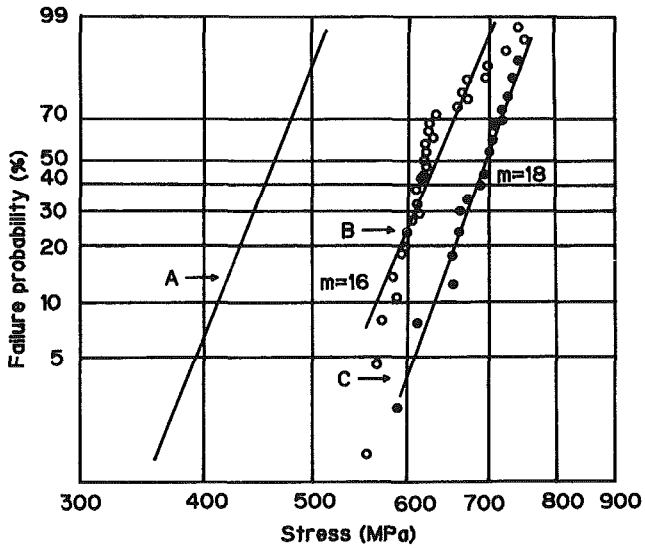

Fig. 1 Failure probabilities of silicon nitride (SN220M) test specimens and turbine wheels: (A) Spin burst stress calculated for turbine wheels made by slip-casting and sintering; (B) four-point bending (cross section: 3 × 4; inner span: 10, outer span: 30 mm) test result of test specimens cut from turbine wheels and surface ground; (C) four-point bending test result of dry-pressed, sintered, and surface-ground specimens

Ceramic Turbine Wheel Design

Because of their brittle nature, ceramics can be abruptly fractured when subjected to excessive stress. While metals deform under similar conditions, ceramics are limited by this relatively low fracture resistance. Consequently, small defects inside a ceramic component or on its surface are very undesirable for high-stress components. Thus, metals have traditionally been considered more attractive for these applications.

Recently, however, the mechanical characteristics and structural reliability of ceramic materials have been remarkably improved. The intrinsic bond strength of silicon nitride and

Contributed by the Gas Turbine Division of THE AMERICAN SOCIETY OF MECHANICAL ENGINEERS and presented at the 31st International Gas Turbine Conference and Exhibit, Düsseldorf, Federal Republic of Germany, June 8–12, 1986. Manuscript received at ASME Headquarters December 26, 1985. Paper No. 86-GT-10.

Table 1 Material properties of SN220M

Bulk Density	3.19 (3.16)
Flexural Strength*	
R.T.	679MPa (627MPa)
800°C	679MPa
1000°C	598MPa
1200°C	390MPa
Young's Modulus	293GPa
Poisson's Ratio	0.28
Hardness HRa	92.0
Toughness K_{IC}**	7.4MN/$m^{3/2}$ (7.3MN/$m^{3/2}$)
Coefficient of Linear Thermal Expansion (40~900°C)	3.1×10^{-6}/°C
Thermal Conductivity	25W/mK

( ):The properties of specimens cut from slip-cast rotors

*4-Point bendings (Cross section : 3×4, inner span : 10, Outer span : 30 mm)

**Indentation method

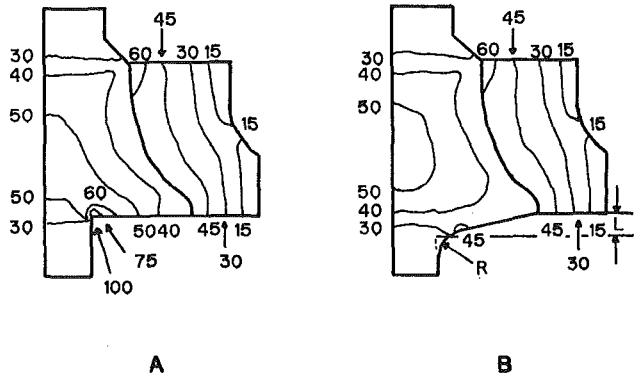

Fig. 2 Comparison in steady-state principal stress contours of turbine wheels: (A) with no back face taper or corner radius; (B) with 2.5 mm back face taper and 3 mm corner radius

silicon carbide bodies have been increased substantially and maintained at higher temperatures. The size and number of strength-limiting defects diminish with every additional processing experience and each refinement in processing.

Today, the relationship between the strength of test specimens and the strength, life, and failure probability of actual ceramic components can be formulated by the fracture mechanics [5] and Weibull statistics [4]. Figure 1 shows the Weibull distribution of the fracture stress of silicon nitride test specimens which were dry-pressed and sintered in the shape of small bars as well as specimens which were cut from turbine wheel hubs made by slip-casting and sintering the same material. The failure probability of ceramic wheels (in spin test) was also calculated, based upon the effective volume [5].

Table 1 shows physical properties of the silicon nitride (Kyocera Corporation designation: SN220M) which has been chosen for this application in view of fracture toughness, thermal shock resistance, and process capability.

FEM stress analyses are now widely applied to ceramic components to show the stress distribution of given component designs at given operating conditions, and to improve the component design with a view to minimizing and optimizing stresses. Figure 2 shows steady-state principal stress contours in ceramic turbine wheels and Table 2 shows the effect of back face taper and corner radius on the maximum stress of each wheel. A small change in wheel design reduced the maximum stress by more than 40 percent.

Table 2 Effect of back face taper (L) and corner radius (R) on the maximum stress in the ceramic wheel

R \ L	0	1	2.5	4 mm
0	100	69	57	40
2	81	66	50	—
3	78	66	50	—
4 mm	72	64	50	—

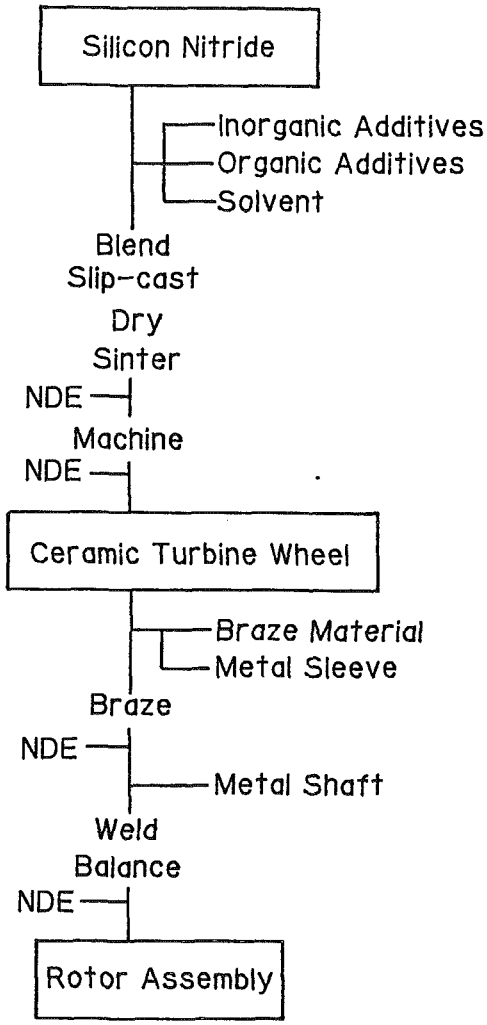

Fig. 3 Process flow sheet for ceramic turbine wheels and rotor assemblies

Ceramic Turbine Wheel Production

In order to produce ceramic turbine wheels commercially, every step of the production process must be well controlled and performed with skilled hands. Among many processes

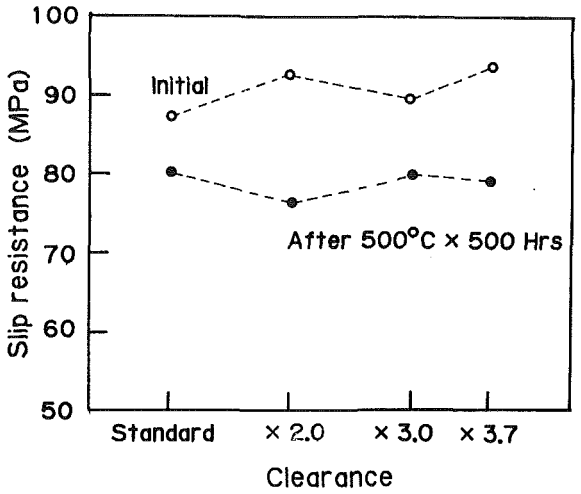

Fig. 4 Axial slip resistance at 500°C of braze-bonded joints versus clearances between ceramic shafts and metal sleeves; test specimen size: metal sleeve o.d.: 17.5; i.d.: 12, *L*: 6.3 mm

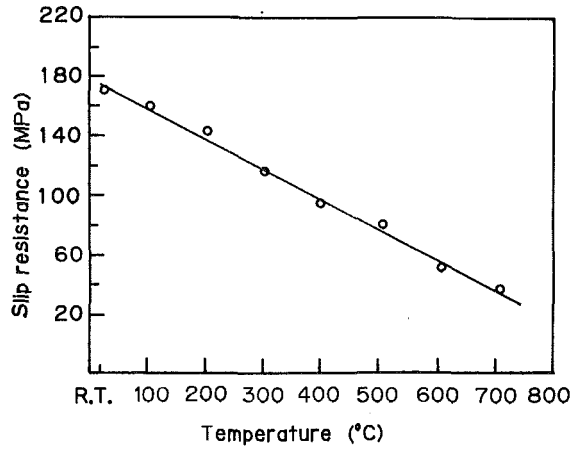

Fig. 5 Slip resistance of braze-bonded joints versus temperatures

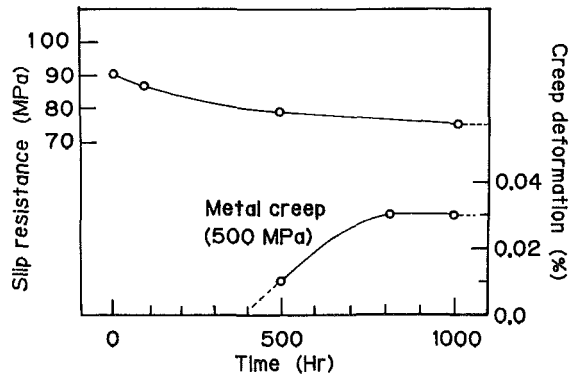

Fig. 6 Tensile creep deformation of the sleeve metal and 500°C slip resistance of braze-bonded joints versus 500°C heating hr

beginning from raw material synthesis to final inspection, the shape-forming process has the strongest influence on production cost. Near-net-shape forming such as injection molding and slip-casting are needed to produce such complex-shaped ceramic components as turbine wheels.

In injection molding, ceramic powders are blended with organic binders (thermoplastic resins and plasticizers) of almost equal volume at elevated temperatures and forced to flow through an orifice into the cavity of a preheated tool. After the binder burnout, ceramics sinter to near-net-shape.

In slip-casting, a slurry of uniformly dispersed ceramic powder mixture is cast into plaster molds. Liquidity and viscosity can be lowered through the selection of organic additives such as binders, wetting agents, and deflocculents. Uniform and dense particle packing with no particle agglomeration is achieved in carefully made slurries. The slip-casting process is believed to have a better chance of forming defect-free wheels than injection molding, because of slip-casting's higher casting fluidity and lower amount of organic binders. Because of uniform and dense particle packing, higher green density, and lower firing shrinkage, fired wheels have uniform mechanical properties and good dimensional accuracy. Careful fabrication of plaster molds minimizes machining after firing.

Figure 3 shows the process flow sheet for ceramic turbine wheels and rotor assemblies.

Table 3 NDE methods for various types of defects

NDE Timing	Type of Defects	NDE Method
After Sintering	Surface Crack	Fluorescent Dye Penetrant
	Inside Crack	Ultrasonic
	Inside Void	X-ray Radiography
After Machining	Chip	Visual
	Machining Flaw	Fluorescent Dye Penetrant
After Brazing	Braze Stagnancy	Ultrasonic C-scan
Before Shipping	Chip	Visual
	Crack	Visual

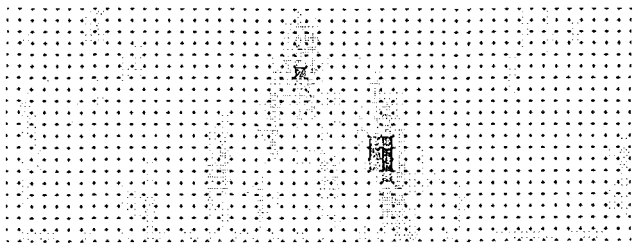

Fig. 7 Ultrasonic C-scan map of a ceramics-to-metal joint

Ceramics-to-Metal Joint

It is more complicated and difficult to clarify the optimum design and reliability of the ceramics-to-metal joint than that of the ceramic wheel itself. Many important questions arise:

- Shrink-fitting or brazing?
- Joint configuration?
- Braze material?
- Shrink-fit temperature?

In search of a joining technique, the following characteristics were examined at elevated temperatures:

1 Resistive force against axial slip
2 Cantilever bend strength
3 Cyclic loading life

Because of thermal expansion mismatch, radial and axial thermal stress are unavoidable at a ceramics-to-metal interface, especially axial tensile stress at the end of a metal sleeve. Long and challenging experimental and theoretical analyses were necessary to minimize the tensile spike and evaluate the estimated reliability of the joint under cyclic loadings and temperature cycles.

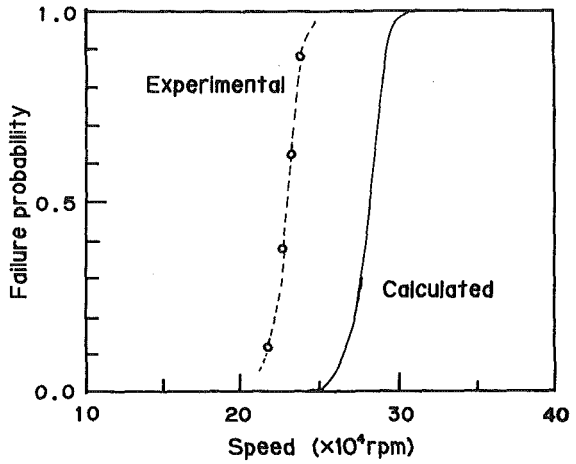

Fig. 8 Comparison of calculated failure probability of ceramic turbine wheels with 900°C hot-spin test results of 56-mm-dia rotor assemblies

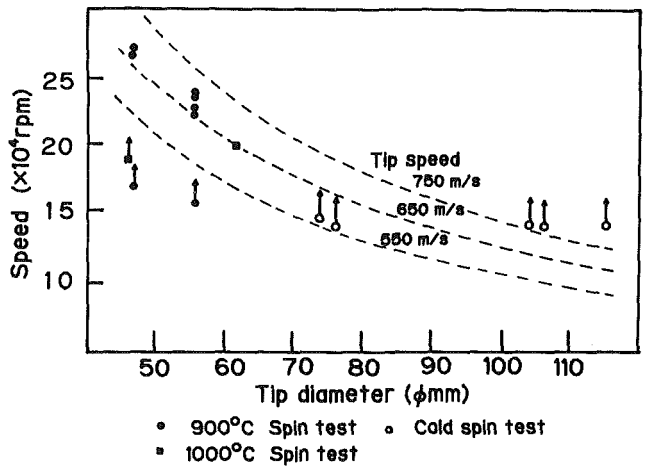

Fig. 9 Hot and cold-spin test results of rotor assemblies with various tip diameters

After many different joining techniques and configurations were evaluated, a braze-bonded cup-joint was finally adopted. A refractory alloy was selected for the sleeve material to minimize creep deformation and to maintain high-temperature joint strength. A relatively low-temperature braze material was selected because its hardness and brazing temperature are more favorable for reliable joints.

Figure 4 shows the axial slip resistance of the braze-bonded joint with different clearances between ceramic shafts and metal sleeves. The slip resistance of braze joints was found to be less sensitive to the clearance than that of shrink-fit joints. Figure 5 shows the slip resistance of the braze-bonded joint at elevated temperatures. Figure 6 shows the creep deformation of the sleeve metal and the slip resistance of the joint at 500°C. The change in the slip resistance in 1000 hr was relatively low.

Nondestructive Evaluation

In order to ensure the reliability of ceramic wheels and rotor assemblies based on the fracture mechanics and Weibull statistics, it is very important to maintain the mechanical properties of ceramic material and ceramics-to-metal joint above constant levels. As mentioned above, mechanical properties of ceramics are very sensitive to defects which have been introduced accidentally during processing. Major causes of defects are as follows:

1 Nonhomogeneity in the casting slurry
2 Pores in the slurry
3 Nonhomogeneity in drying shrinkage and firing shrinkage
4 Flaws and chips in machining and handling
5 Nonuniform distribution of the braze material

The number of defects could be minimized by a careful process control, but it is impossible to eliminate all the defects from commercially produced rotors. Therefore, it is very important to detect all the strength-limiting defects nondestructively and remove defective parts from the process.

The maximum allowable size (A_{max}) of defects can be calculated from the following relationship:

$$KIC = Y \cdot S_{max} \sqrt{A_{max}}$$

where KIC is the critical stress intensity factor or the fracture toughness of the material and S_{max} is the maximum stress.

For example, in the case of a 56-mm-dia wheel with the maximum design speed of 170,000 rpm. S_{max} is equal to 240 MPa at 120 percent overspeed. By replacing KIC with 7.4 from Table 1, A_{max} was calculated to be 180 μm.

Defects larger than 180 μm can be detected by existing NDE methods. Table 3 shows basic NDE methods for various types of defects. Figure 7 shows an example of ultrasonic C-scan maps of defects of ceramics-to-metal joints.

Rotor Spin Test

Figure 8 shows hot-spin test results of 56-mm-dia rotor assemblies at turbine inlet temperature of 900°C, compared with the theoretically calculated failure probability (Line A in Fig. 1) of ceramic wheels.

The discrepancy between experimental and theoretical failure probabilities was about 20 percent in tip speeds. Possible explanations for this are:

1 thermal stress in the ceramic wheel
2 the difference in strength between the ceramic wheels and joints
3 predominance of effective surface area over effective volume, etc.

which are not understood yet.

An average failure speed of 230,000 rpm is well over (135 percent) the maximum design speed of 170,000 rpm, and from the Weibull number of 18, the failure probability at the maximum design speed was calculated to be 0.00001.

Figure 9 shows spin-test results of various types of ceramic wheels and rotor assemblies. Failures were observed at tip speed over 650 m/s.

Conclusion

Ceramic turbine wheels were produced and tested with the intention of bringing them into mass production. The most critical problem was the means to confirm their reliabilities within the cost limitation. With the improvements of related technologies, ceramic turbine wheels and rotor assemblies of high enough capability were produced whose reliabilities could be confirmed by existing NDE methods. Following are major findings.

1 The failure probability of the ceramic wheel can be calculated from that of test specimens based upon the fracture mechanics and Weibull statistics.

2 FEM study revealed that more than 40 percent reduction of the maximum stress of a wheel could be achieved by a small design change.

3 The slip-casting process to form defect-free wheels was established.

4 In order to obtain highly reliable ceramics-to-metal joint, optimum sleeve materials and braze materials were determined.

5 NDE methods were investigated to eliminate wheels with accidental process defects.

6 In 900°C test of rotor assemblies (56 mm diameter), failure took place at 230,000 rpm on average. The average failure speed was 20 percent lower than that calculated for wheels, and 35 percent higher than the maximum design speed.

7 In the spin test of various types of ceramic rotors, failures were observed at tip speeds over 650 m/s.

References

1 Lasker, M. F., et al., "Evaluation of Ceramics for Passenger-Car Turbocharger," 1985 Beijing International Gas Turbine Symposium and Exposition.

2 Okazaki, Y., et al., "Ceramic Turbine Wheel Developments for Mitsubishi Turbocharger," SAE Paper No. 850312, 1985.

3 Hamano, Y., et al., "Ceramic Engine Components Under Commercial Production," ASME Paper No. 84-GT-165.

4 Weibull, W., "A Statistical Distribution Function of Wide Applicability," ASME *J. Appl. Mech.*, Vol. 18, No. 293, 1951, p. 293.

5 Davies, D. G. S., "The Statistical Approach to Engineering Design in Ceramics," *Proc. Brit. Ceram. Soc.*, Vol. 22, 1973, p. 429.

G. Bandyopadhyay

K. W. French

GTE Laboratories Incorporated,
Waltham, MA 02254

Fabrication of Near-Net-Shape Silicon Nitride Parts for Engine Application

Significant advances have been made at GTE for fabrication of near-net-shape silicon nitride parts by injection molding. The technology is now in place to fabricate high-quality, high-density small cross-section ($\cong 0.25$ in.) parts such as axial flow gas turbine blades and vanes with state-of-the-art silicon nitride properties. New methods have been developed to fabricate large cross-section (> 0.5 in) complex parts with good mechanical properties and reliability.

Introduction

Development of near-net-shape fabrication methods is critical for application of ceramics in heat engines. Recognizing this need, several companies in the United States, Europe, and Japan have invested significant resources to develop injection molding and slip casting for fabrication of complex cross-section structural ceramic parts. These technologies are mostly considered proprietary. Thus a meaningful evaluation of the current status of capabilities is difficult. Occasional press releases from various companies regarding their progress further cloud these technologies with an air of mystery. Despite these uncertainties, it is clear from several U.S. Government programs (e.g., CATE and AGT) [1–3] that high-quality complex cross-section silicon nitride and silicon carbide parts can be fabricated by injection molding and slip casting to dimensional tolerances as required for heat-engine applications. While the fabricability and high quality of ceramics have been demonstrated, ceramics manufacturers continue to work to improve the reliability and yield of the product in manufacturing.

Among the shapemaking techniques, slip casting is believed to be a method appropriate for prototypes, whereas injection molding is ideally suited for high-volume, cost-effective production of complex parts. For the last several years, GTE Laboratories Incorporated (GTE Labs) has been involved in developing injection-molding technology for ceramics and has applied this technology extensively for fabrication of silicon nitride components for heat-engine applications [4–7]. Several components having a variety of cross sections and complexities have been fabricated and evaluated. The status of GTE Labs' injection-molding technology and the properties and reliability of some of the test parts are described in this paper.

Injection Molding of Silicon Nitride

Success of the injection-molding process is critically dependent on starting powder, binder, and the process parameters such as molding and binder removal conditions and subsequent densification. Details of the powder and binder system and the injection-molding process steps used at GTE Labs have been described in several earlier publications [4–7]. A summary is presented in this paper.

Silicon Nitride: Powder and Alloy Composition. GTE SN-502 silicon nitride powder has been used for all injection-molding programs. This powder is characterized by its high purity and reactivity, and it is a fine, high-surface area powder with crystalline and amorphous phases.

Densification of silicon nitride requires addition of minor phases which combine with the SiO_2 present in Si_3N_4 to form a liquid phase which, in turn, allows sintering to high densities. Silicon nitride alloys containing Y_2O_3 and Al_2O_3 are of primary interest to GTE. While GTE injection-molding technology is not limited to any particular material composition, two specific materials [AY6 (Si_3N_4 + 6 w/o Y_2O_3 + 2 w/o Al_2O_3) and PY6 (Si_3N_4 + 6 w/o Y_2O_3)] have been selected based on an extensive optimization effort in relation to composition, densification, strength, and oxidation resistance [7–9]. GTE AY6 is the material with superior strength properties from room temperature to 1200°C. The other material, GTE PY6, has a grain boundary phase composed of a more refractory composition (no Al_2O_3). Consequently, it exhibits improved strength maintenance to temperatures at or above 1200°C [7].

In GTE Lab's program, both AY6 and PY6 powders have been injection molded and densified. These powders are prepared in a ball-milling operation where SN502 Si_3N_4 is blended with appropriate amounts of Al_2O_3 and Y_2O_3 or Y_2O_3 alone.

Binder Selection. The selection of a binder system is one of the most critical factors in silicon nitride part fabrication by injection molding. In general, the binder system must (1) have the capability of supporting solids loading levels sufficient to allow sintering to high final density; (2) exhibit sufficient thermoplastic flow at these loadings to uniformly fill complex-shaped mold cavities with thin sections; (3) impart sufficient

Contributed by the Gas Turbine Division of THE AMERICAN SOCIETY OF MECHANICAL ENGINEERS and presented at the 31st International Gas Turbine Conference and Exhibit, Düsseldorf, Federal Republic of Germany, June 8–12, 1986. Manuscript received at ASME Headquarters December 26, 1985. Paper No. 86-GT-11.

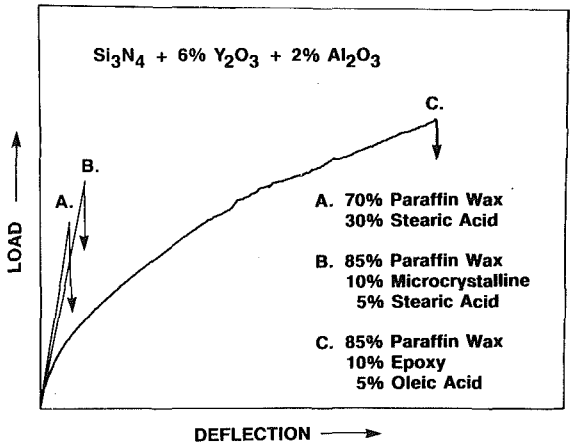

Fig. 1 Strength behavior of as-molded bars as a function of binder composition

green strength and flexibility to produce flaw-free as-molded parts; and (4) allow complete nondisruptive removal.

The requirement for thermoplastic behavior dictates much higher concentrations of binder than normally associated with the more traditional ceramic shapemaking processes such as uniaxial pressing or isopressing. Thus nondisruptive binder removal becomes a serious processing issue.

The binder system used for injection molding of Si_3N_4 parts contains a paraffin wax (90 w/o), a liquid epoxy (5 w/o), and a surfactant (5 w/o) [10]. A paraffin-type wax with a melting temperature of $\cong 60°C$ was chosen primarily to minimize the differential between the barrel and mold temperatures and thus limit part shrinkage in the mold. Additional advantages of this wax are the low melt viscosity, which results in high flow, and the ease of removal from a molded part in a thermal binder removal process. The disadvantages are lower green (as-molded) strength of the parts and bleeding and segregation of the binder from the ceramic powder during molding. The additon from 5 to 15 percent epoxy results in several beneficial changes in the rheological properties of the powder/binder system. The epoxy acts as a plasticizer, imparting greater flexibility to the powder/binder mixtures at room temperature. Green strength of the parts is also improved. These observed properties have been confirmed by room temperature modulus of rupture (MOR) testing of green (as-molded) bars (see Fig. 1). The segregation of the binder, which is a serious problem with paraffin-wax-based systems, is also reduced by the addition of epoxy. This combination of lower melt temperature and flexibility allows the molding of crack-free complex shapes with thin and thick sections.

Stearic or oleic acid is added as a surfactant. This addition results in more uniform compounding as well as slight improvements in flow and green strength.

The resulting powder/binder system possesses good molding properties and produces fully packed visually and radiographically flaw-free green parts (both small and large) with excellent surface finish.

Injection-Molding Process Steps. Injection molding of ceramics and metal powders has been described in the literature by various authors. The general process routing is well known [4–6, 11–13]. It includes (*a*) compounding, which involves mixing the high-surface-area powder with molten organic binder; (*b*) injection molding, by which the powder/binder mix is formed into a given shape in a metallic mold; (*c*) binder removal, which must be accomplished without disrupting the ceramic structure; and (*d*) consolidation of the part by sintering and/or hot isostatic pressing (HIPing). Each of these process steps is critical for fabrication of a defect-free part. A thorough understanding of material characteristics, process parameters, and final properties is required to achieve the yield and reliability necessary for heat-engine applications.

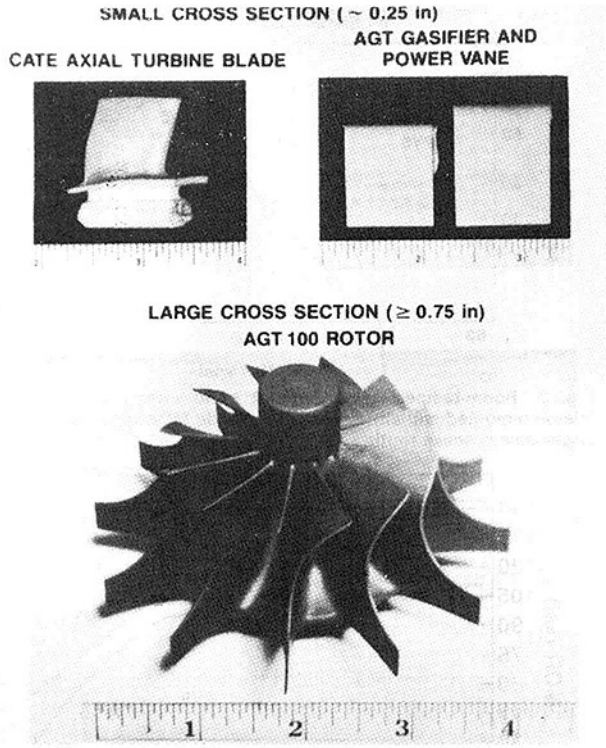

Fig. 2 Examples of some injection-molded silicon nitride parts

A fundamental characteristic of the injection-molding process is the ability to obtain highly uniform green microstructure, primarily because the soft agglomerates present in the starting material can easily be broken up during high shear compounding and during the molding process [6]. The green microstructural homogeneity, in general, leads to a reliable sintered product. In a systematic laboratory study [14], injection-molded and sintered bars, machined to a size of 1.27 × 2.54 × 25.4 mm and surface ground to a 320 grit finish, showed an average strength of 130 ksi with a Weibull modulus of 14 for a sample size of 50.[1] The challenge is to maintain the green microstructural homogeneity through the binder removal and densification process.

Component Fabrication

Typical examples of injection-molded components fabricated by GTE Labs under subcontract to Allison Gas Turbine Division (AGTD) of General Motors Corporation are shown in Fig. 2. These fabrication efforts were part of CATE and AGT, projects which are administered by the NASA Lewis Research Center and funded by the U.S. Department of Energy (DOE). The AY6 CATE axial turbine blades, and AY6 and PY6 gasifier and powder turbine vanes, are representative of typical small cross-section parts, whereas the AGT 100 rotor is considered a complex large cross-section component. It is this size and cross-section difference which dictates the ease with which the part can be injection molded and densified.

Small cross-section parts such as those shown in Fig. 2 have been routinely injection molded and sintered to greater than 98 percent of theoretical density (3.26 g/cc) with excellent dimensional control and with state-of-the-art properties. Eighteen CATE blades were cold spin tested to failure by

[1] All strength data discussed in this paper were obtained in four-point bend tests in a SiC fixture [7] whose inner and outer loading points were 1.016 and 2.286 cm, respectively. Crosshead speed was constant at 0.05 cm/min for all tests.

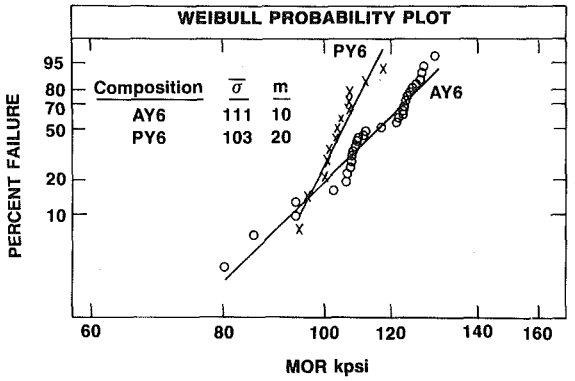

Fig. 3 Room-temperature four-point bend strength distribution of injection-molded and sintered silicon nitride MOR bars fabricated by a large-scale process routing

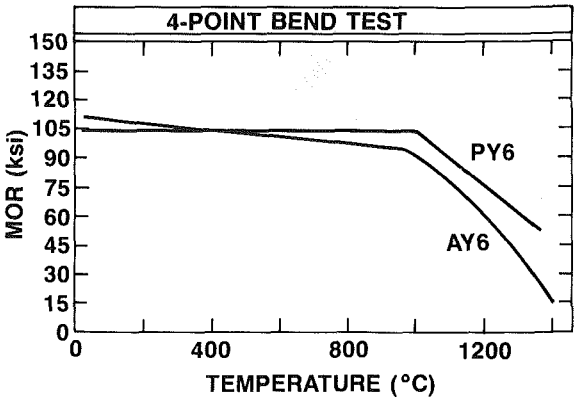

Fig. 4 Strength as a function of temperature of injection-molded and sintered nitride MOR bars fabricated by a large-scale processing route

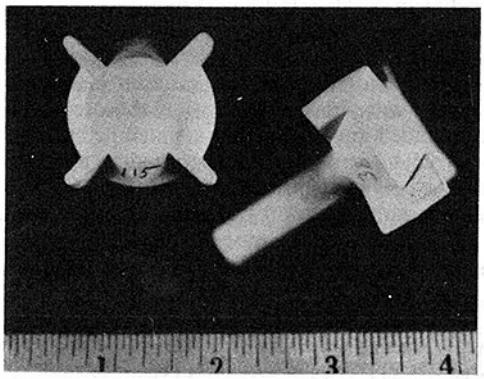

Fig. 5 Injection-molding basic studies test part

AGTD [15] to an average of 136 percent of design speed (36,900 rpm). Typical room-temperature and high-temperature strength values that can be achieved in injection-molded and sintered AY6 and PY6 MOR bars fabricated by large-scale process routing are shown in Figs. 3 and 4. These results clearly indicate that technology now exists at GTE to manufacture high-quality, small cross-section injection-molded and sintered parts in large quantities.

The difficulty of fabrication of large cross-section injection-molded parts became evident when efforts were initiated to fabricate AGT 100 rotors. These rotors were molded and sintered to >96 percent of theoretical density with good maintenance of geometry. However, they were prone to internal and external cracking during the binder removal step. A basic study was initiated at GTE Labs to understand the cracking mechanisms in large cross-section parts (>0.5 in.). Figure 5 shows the test part used for this study. The part contained the thin and thick cross sections typical of a turbocharger, and

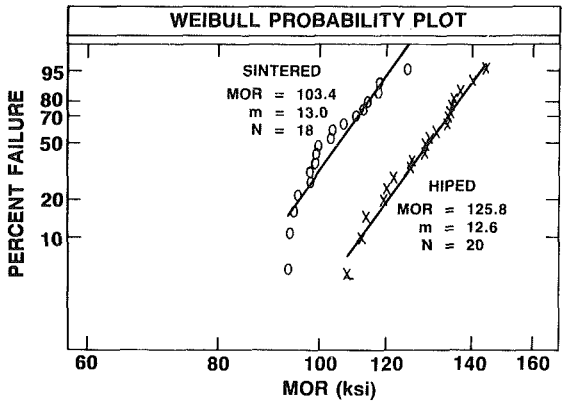

Fig. 6 Room-temperature four-point bend strength distribution of MOR bars machined from sintered and HIPed basic studies test part

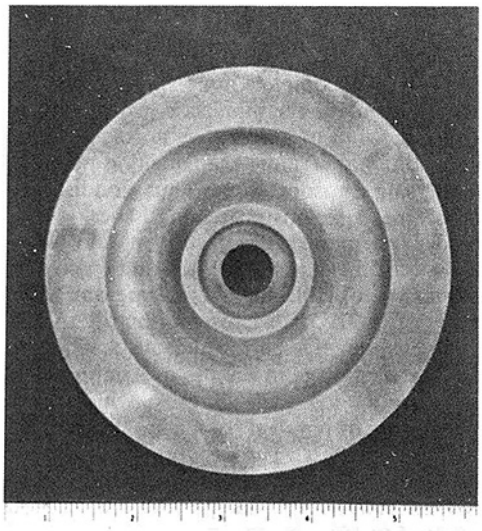

Fig. 7 Daimler Benz unbladed disk; scale shown is in inches

generally showed internal and external cracking problems similar to those observed in AGT rotors. As a result of this basic study, cracking mechanisms were identified, and a new proprietary processing method has been developed for fabrication of large cross-section parts. Figure 6 shows the room-temperature strength of MOR bars machined from sintered and HIPed test parts fabricated by the new process routing. The HIPing of partially sintered injection-molded parts was done by ASEA Cerama using their proprietary glass particle encapsulation process [16]. While the HIPed bars were clearly stronger than the sintered MOR bars, the strength and Weibull modulus of both sets of samples are as good as those observed in small cross-section parts.

The new processing route has also been used successfully to fabricate much larger volume parts, such as Daimler Benz unbladed rotor disks (Fig. 7). Figure 8 shows the room-temperature strength of MOR bars machined from sintered and HIPed disks. Although the sintered disks showed somewhat lower Weibull modulus, the HIPed material strength is equivalent to that observed for smaller cross-section parts. Several of these sintered and HIPed disks are now being evaluated by Daimler Benz.

Several injection-molded and HIPed AY6 AGT 100 rotors were fabricated and evaluated. The cold spin test data as obtained byAGTD from five injection-molded and HIPed rotors are shown in Fig. 9. The average burst speed of these rotors was 91,040 rpm or 105.6 percent of the design speed (86,240 rpm). The average strength of MOR bars machined from individual HIPed rotors varied from 114 ksi to 122 ksi. Strength as a function of temperature for an HIPed rotor is shown in

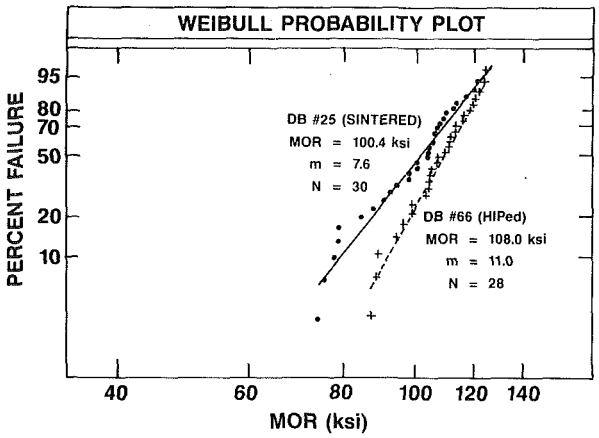

Fig. 8 Four-point bend strength of MOR bars machined from sintered and HIPed injection-molded Daimler Benz disks

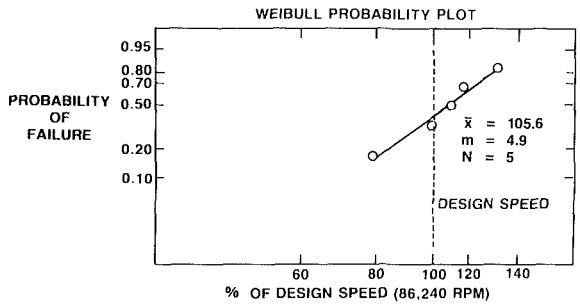

Fig. 9 Injection-molded and HIPed silicon nitride AGT 100 rotor cold spin test results

Fig. 10, which also shows typical strength values for GTE isopressed sintered AY6 and PY6 MOR bars. Oxidation resistance of the HIPed rotor material is shown in Fig. 11, which compares very well with standard GTE materials.

The results, as presented above, show that complex large cross-section silicon nitride parts can be fabricated by injection molding and sintering or HIP with good state-of-the-art properties. Efforts are continuing to improve the yield and reliability of these products through elimination of process-related contamination (e.g., metallic contamination via abrasion) and through process optimization.

Acknowledgments

The authors gratefully acknowledge Paul Fuce, Jean Gagne, and Peter Okun for experimental assistance at various stages of the experimental program.

References

1 Groseclose, L. E., "Status of the AGT100 Advanced Gas Turbine Program," ASME Paper No. 85-GT-205.

2 Boyd, G. L. et al., "Ceramic Design Methodology and the AGT 101," ASME Paper No. 85-GT-199.

3 Thrasher, S. R., "Ceramic Applications in Turbine Engines (CATE)-Program Summary," *Proc. of the Twenty-First Automotive Technology Development Contractors' Coordination Meeting*, Dearborn, MI, Nov. 14-17, 1983, pp. 255-262.

4 Quackenbush, C. L., French, K. W., and Neil, J. T., "Fabrication of Sinterable Silicon Nitride by Injection Molding," Automotive Technology Development Contractors Coordinating Meeting, Oct. 26-29, 1981.

5 Neil, J. T., French, K. W., Quackenbush, C. L., and Smith, J. T., "Fabrication of Turbine Components and Properties of Sintered Silicon Nitride," ASME Paper No. 82-GT-252.

6 Bandyopadhyay, G., and French, K. W., "Near Net Shape Fabrication and Densification of Silicon Nitride," *Proc. of Workshop on Conservation and Substitution Technology for Critical Metals in Bearings and Related Components for Improved Bearing Performance*, Vanderbilt University, Nashville, TN, Mar. 12-14, 1984.

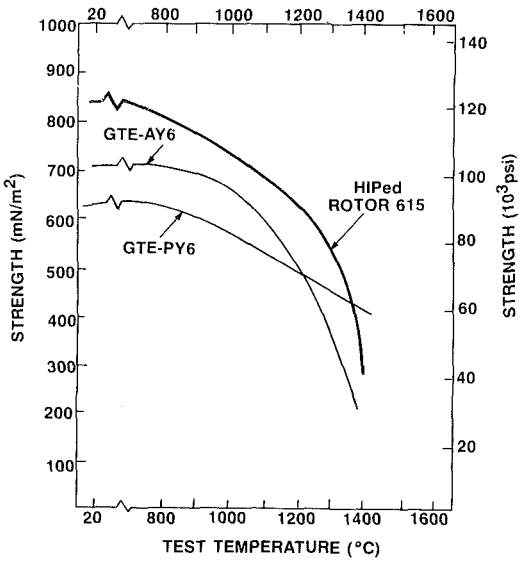

Fig. 10 Strength versus test temperature for silicon nitride

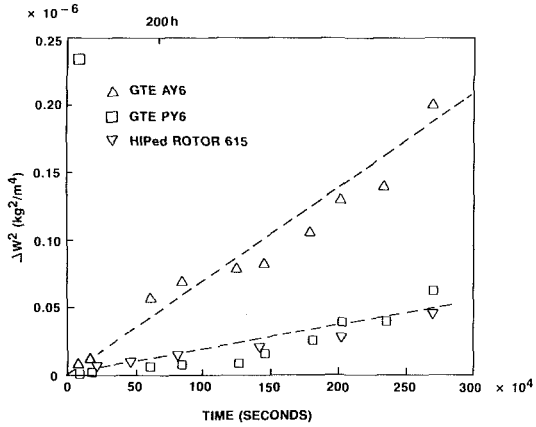

Fig. 11 Oxidation of silicon nitride at 1000°C

7 Smith, J. T., and Quackenbush, C. L., "Phase Effects in Si_3N_4 Containing Y_2O_3 or CeO_2: I. Strength," *Bull. Am. Ceram. Soc.*, Vol. 59, No. 5, 1980, pp. 529-532.

8 Quackenbush, C. L., and Smith, J. T., "Phase Effects in Si_3N_4 Containing Y_2O_3 or CeO_2: II. Oxidation," *Bull. Am. Ceram. Soc.*, Vol. 59, No. 5, 1980, pp. 533-537.

9 Quackenbush, C. L., Neil, J. T., and Smith, J. T., "Sintering, Microstructure, and Properties of Si_3N_4 and SiC Based Structural Ceramics," ASME Paper No. 81-GT-200.

10 French, K. W., Neil, J. T., and Turnbaugh, L. T., "Composition for Injection Molding," U.S. Patent No. 4,456,713, 1984.

11 Schnittgrund, G. D., "Injection Molded Ceramic Rocket Engine Components," *SAMPE Quarterly*, July 1981, pp. 8-13.

12 Mangels, J. A., "Development of Injection Molded Reaction Bonded Silicon Nitride," in: *Ceramics for High Performance Applications—II*, J. J. Burke, E. N. Lenoe, and R. N. Katz, eds., Brook Hill Publishing Co., 1978, pp. 113-129.

13 Whalen, T. J., Noakes, J. E., and Tuerner, L. L., "Progress of Injection Molded Reaction-Bonded SiC," Ibid, pp. 179-189.

14 Pasto, A. E., Neil, J. T., and Quackenbush, C. L., "Microstructural Effects Influencing Strength of Silicon Nitride," *Proc. of Int. Conf. on Ultrastructure Processing of Ceramics, Glasses and Composites*, L. L. Hench and D. R. Ulrich, eds., Wiley, New York, 1984, pp. 476-489.

15 Groseclose, L. E., Heitman, P. W., and Jenn Chang, "Development of Ceramic Components for Gas Turbine Engines," *Proc. of the Twentieth Automotive Technology Development Contractors' Coordination Meeting*, Dearborn, MI, Oct. 25-28, 1982, pp. 181-188.

16 Larker, H. T., "Hot Isostatic Pressing of Ceramics," in: *Progress in Nitrogen Ceramics*, F. L. Riley, ed., Martinns Hijhoff Publishers, 1983, pp. 717-724.

SCARE: A Postprocessor Program to MSC/NASTRAN for Reliability Analysis of Structural Ceramic Components

J. P. Gyekenyesi
NASA Lewis Research Center,
Cleveland, OH 44135

A computer program is developed for calculating the statistical fast fracture reliability and failure probability of ceramic components. The program includes the two-parameter Weibull material fracture strength distribution model, using the principle of independent action for polyaxial stress states and Batdorf's shear-sensitive as well as shear-insensitive crack theories, all for volume distributed flaws in macroscopically isotropic solids. Both penny-shaped cracks and Griffith cracks are included in the Batdorf shear-sensitive crack response calculations, using Griffith's maximum tensile stress or critical coplanar strain energy release rate criteria to predict mixed mode fracture. Weibull material parameters can also be calculated from modulus of rupture bar tests, using the least-squares method with known specimen geometry and fracture data. The reliability prediction analysis uses MSC/NASTRAN stress, temperature, and volume output, obtained from the use of three-dimensional, quadratic, isoparametric, or axisymmetric finite elements. The statistical fast fracture theories employed, along with selected input and output formats and options, are summarized. A sample problem to demonstrate various features of the program is included.

Introduction

The attractive physical and mechanical properties of modern ceramics—high-temperature strength, light weight, excellent erosion, corrosion and oxidation resistance, low thermal conductivity, low cost, and wide availability—have made ceramics an increasingly important structural material. The potential of ceramics in demanding structural applications is especially attractive when resistance to high temperatures, such as in heat engines, is the main concern. With today's needs for more fuel-efficient transportation, multifuel engine capability, and reduced emissions, advanced engines, operating at much higher temperatures with ceramic components, appear to be mandatory to meet economically these national objectives.

However, ceramics, like all other brittle materials, display linear stress-strain behavior from zero to fracture. The lack of ductility and yielding capability gives ceramic materials their most undesirable characteristics such as low strain tolerance, low fracture toughness, and large variation in observed fracture strength. This wide variation of material strength is due to the nature and distribution of intrinsic microscopic flaws, which are unavoidably present as a result of materials processing operations. Failure in ceramics usually initiates at a single weakest flaw when the local stress there reaches a critical value. Because of the large scatter in strength, designers today use statistics and reliability analysis for the failure prediction of brittle material components, which may be subject to arbitrary loadings and multidimensional stress states.

The first probabilistic approach used to account for the scatter in fracture strength of brittle materials was introduced by Weibull [1]. His analysis was based on the weakest link theory (WLT) and assumed a unique strength cumulative distribution for the uniaxial fracture data obtained from simple specimen tests. Weibull also proposed a method for calculating the failure probability in multidimensional stress fields when using material parameters obtained from uniaxial tests. His approach basically involves calculating the risk of rupture by averaging the tensile stress in all directions. This is intuitively plausible but not rigorous, and consequently other models were introduced. The most widely used among them is the assumption that principal stresses act independently (PIA) [2]. This is a very convenient formulation because of its simplicity. However, as shown by several investigators these models can lead to unsafe estimates of failure probability, since they both neglect the shear force, and in the case of the PIA hypothesis, the effects of combined local principal stresses [3].

An important element of failure predictive theories is the crack extension criterion. In the classic Weibull formulation, a normal stress criterion is used, which is likely to be correct when the dominant crack is normal to a uniaxial tensile stress. However, in a multiaxial stress field with flaws orientated at

Contributed by the Gas Turbine Division of THE AMERICAN SOCIETY OF MECHANICAL ENGINEERS and presented at the 31st International Gas Turbine Conference and Exhibit, Dusseldorf, Federal Republic of Germany, June 8–12, 1986. Manuscript received at ASME Headquarters January 8, 1986. Paper No. 86-GT-34.

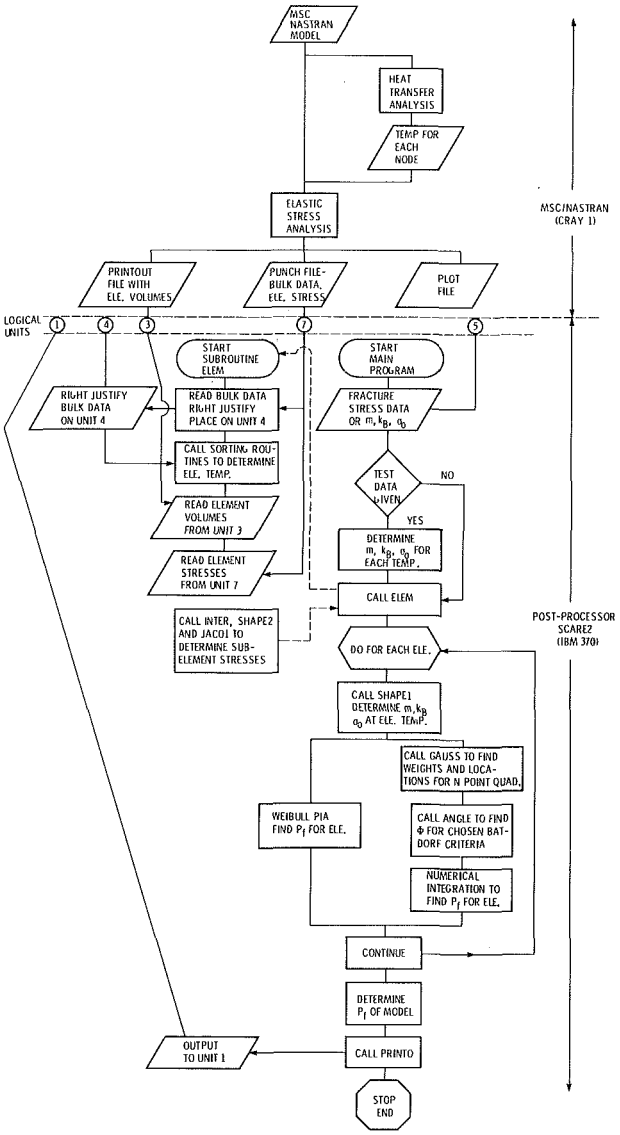

Fig. 1 Computational elements of the SCARE2 reliability analysis program

arbitrary angles to the applied stresses, both normal tensile stresses and in-plane shear stresses will influence the deformation and fracture processes [4–6], and lead to a different fracture response than that of the uniaxial case. Several fracture criteria have been proposed [7–9], with the critical coplanar strain energy release rate G_c criterion, among those available in this study, leading to the best agreement with available brittle material experimental data.

The primary objective of this report is to develop a public domain computer program which will be coupled to a general purpose finite element code, such as MSC/NASTRAN [10], to predict the fast fracture failure probability of ceramic components due to the presence of volume type flaws. The user is given various options to select currently available fracture models in addition to calculating statistical material parameters. Two versions of the program are presently available which are designated as SCARE1 (Structural Ceramics Analysis and Reliability Evaluation) and SCARE2, respectively [11]. In SCARE1, the finite element centroidal principal stresses are taken as constant throughout the element volume and the convergence of the mesh for accurate stress analysis leads to convergence for volume type flaw reliability analysis. However, previous results from higher order isoparametric finite elements with permissible internal stress

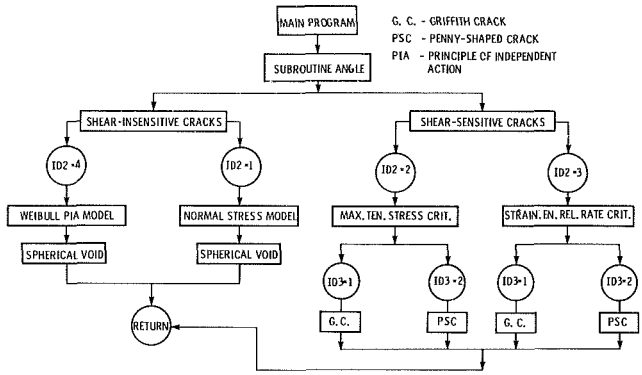

Fig. 2 Flowchart for subroutine ANGLE

gradients showed that the accuracy of failure predictions is significantly improved when the finite element volumes are further subdivided. In the SCARE2 version, all six-sided HEXA MSC/NASTRAN elements are further discretized into 27 subelements, which are then used with interpolated principal stresses to perform all analysis.

Program Capability and Description

The basic computational elements of the postprocessor program for the reliability analysis of structural ceramic components using the SCARE2 version of the code are shown in Fig. 1. Clearly the NASTRAN part is totally independent of SCARE, and output data from other general purpose analysis programs could also be used as long as similar elements are available for the thermal and stress analysis of the structure. For computational efficiency, all the experimental fracture stresses used to calculate material parameters, as well as the elemental principal stresses, are normalized. Initially, the normalizing stress used is the average of all experimental fracture data when specimen test results are available. When material parameters are known, an appropriate value of the Weibull scale parameter σ_0 is used to normalize all stresses.

As shown in Fig. 1, executing the SCARE program requires FORTRAN logical units 1, 3, 4, 5, and 7 in addition to those generally used in performing NASTRAN analysis (such as units 5, 6, and 14). The program uses these tape drives for intermediate storage of large amounts of data, so that the transfer of information from NASTRAN to SCARE is done internally rather than manually. MSC/NASTRAN bulk data including required nodal temperatures, and element centroidal as well as selected corner node stresses, are stored on logical unit 7 where NASTRAN punch files are saved for access and further processing in SCARE. Since element volumes are obtained through a NASTRAN parameter call, the required volume data are taken from the printout files on unit 6 and stored on logical unit 3. The input to SCARE is handled through logical unit 5, but the output from SCARE had to be placed on unit 1 to avoid potential terminal problems. In addition to NASTRAN output files and analysis data, input to SCARE includes control indices specifying various fracture models, temperature-dependent material parameters if available, specimen geometry and ordered (in ascending order for a given temperature) fracture strength data when required statistical parameters are internally calculated.

In order to use WLT, no principal compressive stress is permitted to exceed three times the maximum principal tensile stress in absolute value. If this criterion is violated in an element, compressive stress state predominates and the corresponding reliability is set equal to unity. Additionally, when using the PIA model in conjunction with Weibull statistics, only tensile principal stresses can contribute to failure and fracture due to compression is inadmissible.

The program has broad capabilities which allow the user to

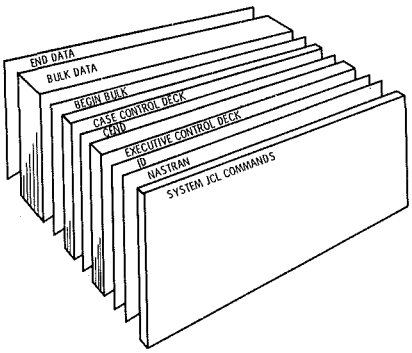

Fig. 3 NASTRAN input file arrangement

specify temperature-dependent statistical material parameters, several crack configurations, and four fracture criteria. Uniaxial fracture data along with specimen geometry from four point modulus of rupture (MOR) bar tests can be used to calculate Weibull parameters and the Batdorf crack density coefficient. Figure 2 contains the flowchart summarizing the available options in fracture criteria and flaw configurations used to model the volume imperfections. Note that two of the failure criteria are for shear-insensitive cracks, even in polyaxial stress states. The other two criteria are used for the more general shear-sensitive model. The available three crack configurations include the spherical void, which is isotropic or direction independent, and is inherently assumed in the Weibull PIA and normal stress failure theories. However, imperfections in high-density, sintered ceramics are best represented by the structural response of penny-shaped and Griffith cracks. Among the available criteria and crack configurations shown in Fig. 2, the penny-shaped crack (PSC) with the G_c criterion gives the highest failure probability for a given case, while the PIA approach yields consistently the lowest failure estimate. It should also be noted that the Batdorf shear-insensitive fracture model, although in slightly different form, gives identical results to the originally proposed Weibull normal stress-averaging method.

Input Information

NASTRAN (NASA Structural Analysis) is a large, comprehensive, general purpose finite-element computer code for structural analysis, which was developed under NASA sponsorship to fill the need for a universally available analysis program. In addition to the government-supported version, there are several greatly enhanced, proprietary versions of this program, the most widely known of which is called MSC/NASTRAN. This program is used throughout the world in large corporations, government laboratories, and most commercial data centers. The SCARE program utilizes results from only a very small fraction of available NASTRAN analysis capability. Since fast fracture mechanical design of ceramic components requires only the temperature and stress distributions, static analysis results from rigid formats 61 and 47 (in case of cyclic symmetry) are most often used. Ceramics are also extremely sensitive to geometric discontinuities, requiring the use of isoparametric three-dimensional and quadratic axisymmetric finite elements. Within MSC/NASTRAN, these elements are denoted as HEXA, PENTA, and TRIAX6, respectively. Although the midedge nodes of HEXA elements in NASTRAN are optional, their use when analyzing with SCARE is required. It is assumed here that analysts using the SCARE program would be fully familiar with MSC/NASTRAN, and its input requirements in creating the executive control, case control, and bulk data decks. Preceding the entire NASTRAN input file is the system operating JCL (job control language) set of commands, which usually identify the job, user, set time and memory requirements, and define NASTRAN input, punch, plot, and printout files. If the self-contained, solid modeling processor, called MSGMESH, is used to discretize the structure, the SCARE program includes a number of sorting routines to permit arbitrary numbering of elements and nodes. Figure 3 shows the arrangement of a typical NASTRAN input file.

COLUMNS	VARIABLE	ENTRY (FORMAT - 11I5)
1 - 5	ID1	CONTROL INDEX FOR EXPERIMENTAL DATA 1: PURE BENDING TEST DATA 2: 4-pt BENDING TEST DATA 3: ALL THE MATERIAL PARAMETERS VMT, VKT AND VSPT ARE KNOWN AS INPUT
6 - 10	ID2	CONTROL INDEX FOR FRACTURE CRITERIA 1: SHEAR-INSENSITIVE, NORMAL STRESS CRITERION 2: MAXIMUM TENSILE STRESS CRITERION 3: ENERGY RELEASE RATE CRITERION 4: WEIBULL PIA SHEAR-INSENSITIVE MODEL
11 - 15	ID3	CONTROL INDEX FOR CRACK SHAPES 1: GRIFFITH TYPE CRACK 2: PENNY-SHAPED CRACK
16 - 20	NE	TOTAL NUMBER OF ELEMENTS IN MODEL
21 - 25	NH	NUMBER OF HEXA ELEMENTS IN MODEL
26 - 30	NP	NUMBER OF PENTA ELEMENTS IN MODEL
31 - 35	NA	NUMBER OF TRIAX6 ELEMENTS IN MODEL
36 - 40	NT	TOTAL NUMBER OF SPECIMENS IN EACH SET AT A GIVEN TEMPERATURE
41 - 45	NGP	NUMBER OF GAUSSIAN QUADRATURE POINTS
46 - 50	NS	NUMBER OF SEGMENTS IN CYCLIC SYMMETRY PROBLEMS
51 - 55	JT	NUMBER OF TEST TEMPERATURES AT WHICH MATERIAL DATA IS SPECIFIED

Fig. 4 SCARE master control deck data requirements

The MSC/NASTRAN program at the Lewis laboratory runs on the CRAY 1-S/2200 computer in a batch mode. Input and output to and from the CRAY is handled through an IBM 370 mainframe computer, which serves as the front-end processor for the CRAY. Consequently, an additional set of JCL commands is required to handle the involved data sets, compiler, FORTRAN logical units, and execution commands. Both versions of the SCARE source program are permanently stored on the IBM in the user's library, where all reliability calculations are eventually made. Details of the system JCL for executing MSC/NASTRAN first, and then the SCARE program, can be found in [11]. These instructions are unique to the computer system existing at Lewis, but are representative of the required commands in performing reliability analysis at other installations.

SCARE input requirements can be grouped into three categories. The first category, called master control deck, defines control indices, information on the finite element mesh, and some integer data describing crack configurations, fracture criteria, and material parameter format. Figure 4 shows the details of the required information, with explanatory notes and size limitations available in the program user's manual [11]. The second category, called the specimen deck, summarizes fracture specimen results needed in calculating statistical fracture parameters, or direct material properties, including Poisson's ratio, when available. There are five different entries required in this category. The first entry includes the material Poisson's ratio, which is used in the reliability calculations when PSC's are selected for volume imperfections. The second entry defines the MOR specimen geometry, which was used in generating fracture data. The third entry includes experimental, extreme fiber fracture stresses, arranged in ascending order for a given temperature. For multiple temperature tests, the temperatures must also be ordered according to ascending values, since calculated material parameters are interpolated within SCARE. At a specified temperature, fracture readings must be unique and multiple values of identical magnitudes are not permitted. The

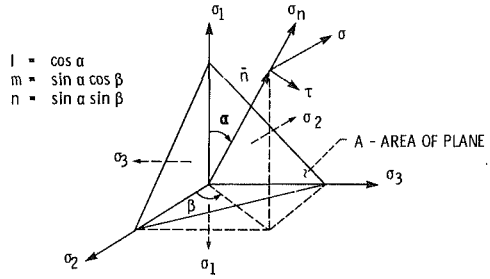

Fig. 5 Stresses on Cauchy infinitesimal tetrahedron in principal stress space

number of available fracture readings for all temperature tests must be the same. The fourth entry is used when material statistical parameters are directly available as a function of temperature. The three required parameters are the Weibull modulus or shape parameter m, the Batdorf normalized crack density coefficient or flaw parameter k_B, and the Weibull scale parameter σ_0. These material parameters must be so arranged that they correspond to ascending order of discrete temperatures. The last entry in the specimen deck category lists the discrete temperatures at which fracture data or material parameters are known. Additional explanation of the required input, including size limitations, can be found in [11].

The last SCARE input category, called the structures deck, contains results of the finite element structural analysis needed for failure probability predictions. These include element volume, element or nodal temperatures, and element principal stresses along with the appropriate identification numbers. In the present version of SCARE, which relies on MSC/NASTRAN output files, all of these data are internally manipulated through subroutine ELEM, and the structure deck requires no specific input by the user. It is these input data, however, that have to be carefully catalogued if another general purpose program were to be used or element data were to be directly read, instead of using temporary storage devices.

Output Information

The results of MSC/NASTRAN thermal analysis are the grid point temperatures, which can be obtained at transient or steady-state conditions. After solution of the component temperature distribution, the most severe thermal gradients can be selected and combined with the mechanical loads to obtain an elastic solution (rigid formats 47 or 61). The usual output from these rigid formats includes the nodal displacements along the global coordinate directions and the element stresses. Depending on the element type, normal and shear stresses in the local element or material coordinate system are always available at element centroids. Additionally, element principal stresses are calculated there for the HEXA and PENTA elements. Corner node stresses are also printed for these elements. For available stress recovery options, users should consult [10] and the appropriate program manuals. In addition to the displacements and stresses, useful parameters such as element volumes, element areas, component center of gravity, moments of inertia, etc. can be calculated through the parameter call feature of the program. For volume flaw reliability analysis, the element volumes are essential, since in the weakest link model, integration of the stress distribution over the material volume is needed.

The first part of all SCARE output data contains an echo of important NASTRAN finite element analysis results. Identifying labels, element type, and number of elements in the model are noted. A table of element centroidal principal stresses with appropriate element identification numbers is given. For the SCARE2 version, the 27 centroidal subelement principal stresses within each HEXA element are listed. Element volumes and calculated element temperatures are summarized in another output table. Next, the selected fracture model is identified and the room temperature (70°F) statistical fracture parameters are listed. Additionally, a table of discrete temperatures with corresponding material parameters, which were either internally calculated or directly supplied, is printed. For the shear-sensitive fracture models, the crack shape is identified along with a more specific description of the fracture criterion. The last table in the SCARE output file contains an element results summary, listing the element number, corresponding element survival probabilities and material parameters. Finally, the overall component probability of failure as well as the component probability of survival are printed.

Theory

The statistical nature of fracture in engineering materials can be viewed from two distinct and extreme models. The first was presented by Weibull and is termed the weak link model. With it a structure is characterized as a series of links connected in such a manner that the structure fails whenever any of the links fractures. In contrast the second model is referred to as the bundle or parallel model for which failure is defined only when all links in parallel have fractured. Structural ceramics have been observed to approach the weakest link hypothesis and fail when the stress intensity factor at any one flaw reaches a critical value. In view of its pessimism, WLT design is in most cases conservative. Other important features of WLT are that it predicts size effect and that failure of a complex component may not be initiated at the point of highest nominal stress. A particularly severe flaw may be located at somewhat less highly stressed points and may still be the first crack to become critical. It is for this reason that the entire field solution of the stresses must be obtained and examination of the most highly stressed point, as in ductile materials, is no longer adequate.

Experimental fracture strength data obtained from uniaxially loaded simple specimens, when arranged in ascending order, can be represented in two different forms. The probability density function of a random variable (fracture strength) is a mathematical function that best represents the data in a relative frequency histogram, that is failure stress versus number of failures. The result, typically, would be a bell-shaped curve [12]. Alternatively, fracture data can be plotted as stress versus failure probability which leads to an S-shaped curve, called the cumulative distribution function of this random variable. Various distribution curves have been used to characterize the material's fracture property. The two most commonly used distribution functions are the Gaussian (normal) distribution and Weibull's distribution. The Weibull distribution is selected to characterize ceramic strength variations, since the Gaussian distribution is intrinsically associated with the bundle model and is incompatible with WLT. Consequently, the uniaxial fracture data are approximated by the three-parameter Weibull distribution, defined by

$$P_f = 1 - \exp\left[-\int_V \left(\frac{\sigma - \sigma_u}{\sigma_0}\right)^m dV\right] \tag{1}$$

where P_f is the probability of failure, σ_0 is the scale parameter with dimensions of stress $\times$ (volume)$^{1/m}$, σ_u is the threshold stress which is usually taken as zero, m is the Weibull modulus which measures the degree of strength variability, σ is the applied tensile stress, and V the stressed volume.

In the analysis of failure of brittle materials subject to multiaxial stress states, the Weibull model, when combined with the PIA hypothesis, yields

$$P_f = 1 - \exp\left\{-\int_V \left[\left(\frac{\sigma_1}{\sigma_0}\right)^m + \left(\frac{\sigma_2}{\sigma_0}\right)^m + \left(\frac{\sigma_3}{\sigma_0}\right)^m\right] dV\right\} \tag{2}$$

where σ_1, σ_2, and σ_3 are the principal stresses and it was

assumed that $\sigma_u = 0$. Equation (2) has been widely used in the past to estimate failure probabilities of ceramic structures [13]. The failure probability using the normal tensile stress-averaging method, as proposed early by Weibull [1], and described later through an integral formulation [14] can be calculated from

$$P_f = 1 - \exp\left\{-\int_V \left[k_{wp}\int_A \sigma_n^m dA\right] dV\right\} \tag{3}$$

where k_{wp} is the polyaxial Weibull crack density coefficient given by

$$k_{wp} = \left(\frac{2m+1}{2\pi}\right)\left(\frac{1}{\sigma_0}\right)^m \tag{4}$$

This constant can be obtained by making the result of integrating equation (3), using the normal stress σ_n distribution on an arbitrary plane, obtained from the Cauchy infinitesimal tetrahedron in principal stress space as shown in Fig. 5, for uniaxial stress cases, agree with the results obtained from the uniaxial, two-parameter Weibull equation. The area integration is performed on the surface of the unit sphere where the normal stress is tensile and neglecting regions where the normal stress is compressive. The cracklike flaws can then be regarded as located in these arbitrary planes which are tangent to the sphere and are acted upon by σ_n which is induced by the principal stresses σ_1, σ_2, and σ_3. Since equation (3) is just the shear-insensitive case of the more general Batdorf [15] polyaxial stress fracture model, its SCARE implementation follows a somewhat different format. The polyaxial Weibull equation has also been extensively used in the past [14], but since it neglects the effects of shear loads, it also underestimates failure for the more general loading condition.

In the previously described two multidimensional stress fracture models no direct use was made of the hypothesis that fractures are due to crack growth. In [4, 5], attention is focused on the cracks and their failure under stress. Since there is not as yet a consensus regarding how to treat mixed mode fracture, even in ductile materials, the SCARE program includes several fracture criteria and flaw shapes. Rufin et al. [16] recently compared results obtained from various fracture models and experimental tests, with similar work being reported in [5].

Consider now a small uniformly stressed material element of volume ΔV. The probability of failure under an applied state of stress can be written as [16]

$$P_f = P_1 P_2 \tag{5}$$

where P_1 is the probability of existence in ΔV of a crack having a critical stress in the range of σ_{cr} to $\sigma_{cr} + d\sigma_{cr}$, and P_2 denotes the probability that a crack of critical stress σ_{cr} will be oriented in a direction such that an effective stress σ_e equals or exceeds σ_{cr}. σ_{cr} is defined as the remote, uniaxial, normal fracture stress of a given crack. Failure will occur when the effective stress (a function of chosen crack configuration and fracture criterion) exceeds σ_{cr} for a particular crack. P_1 has the form

$$P_1 = \Delta V \frac{dN}{d\sigma_{cr}}(\sigma_{cr})\, d\sigma_{cr} \tag{6}$$

and

$$P_2 = \frac{\Omega}{4\pi} \tag{7}$$

where $N(\sigma_{cr})$ is the crack density function (the density of cracks having a critical stress $\leq \sigma_{cr}$) and Ω is the solid angle in principal stress space containing all the crack orientations for which $\sigma_e \geq \sigma_{cr}$. Using the weakest link theory, the overall failure probability can be calculated from [15]

$$P_f = 1 - \exp\left[-\int_V dV \int_0^{\sigma_1} \left(\frac{\Omega}{4\pi}\right)\frac{dN}{d\sigma_{cr}}\, d\sigma_{cr}\right] \tag{8}$$

The crack density function $N(\sigma_{cr})$ is a material constant and is independent of stress state. It is usually expressed as a power function of σ_{cr}, that is, $N(\sigma_{cr}) = k_B \sigma_{cr}^m$, where the flaw distribution parameters k_B and m can be evaluated from experimental data using uniaxial or equibiaxial tension specimens. Batdorf [15] initially proposed a Taylor series expansion for $N(\sigma_{cr})$, but this method had computational difficulties. Recently, a more convenient integral equation approach was formulated and extended to the use of data from four-point MOR bar tests [16].

The statistical analysis of fracture is greatly simplified by assuming that cracks are shear-insensitive. For this case fracture occurs when $\sigma_e = \sigma_{cr} = \sigma_n$ and there is no need to specify the crack shape or the material's Poisson's ratio. Note that the crack size is never used in statistical fracture theories and is always eliminated from the analysis. Since for uniaxial loading shear-insensitive cracks are assumed to dominate the fracture process, σ_e is defined such that in the absence of shear on the crack plane, $\sigma_e = \sigma_n$. In a similar manner, when the G_c criterion is used, we define σ_e as the uniaxial normal stress that would induce the same energy release rate as the actual stress. The same ideas can be extended to noncoplanar crack growth criteria, such as the maximum G or strain energy density, to define σ_e for those applications. In any event, for polyaxial stress states, the effective stress σ_e is a function of both σ_n and τ, where τ is the shear stress in the crack plane. Similarly to calculating σ_n at any point, the Cauchy infinitesimal tetrahedron of Fig. 5 can also be used to obtain τ on the same arbitrary crack plane. Reference [4] gives effective stress expressions for two crack shapes using the maximum tensile stress and G_c fracture criteria. The same four options for shear-sensitive cracks are available in SCARE, as can be seen in Fig. 2. The best choice among them is σ_e for PSC's, given by

$$\sigma_e = \sqrt{\sigma_n^2 + \tau^2/(1 - 0.5\,\nu)^2} \tag{9}$$

where ν is Poisson's ratio.

The solid angle Ω depends on the fracture criterion selected, the assumed crack configuration, and on the applied stress state. Closed form expressions for Ω can be derived for analytically simple fracture criteria in uniaxial and balanced biaxial stress states [15]. Assuming a uniaxial stress σ and the normal stress (shear-insensitive) fracture criterion, we obtain [5]

$$P_2 = \frac{\Omega}{4\pi} = \left[1 - \left(\frac{\sigma_{cr}}{\sigma}\right)^{1/2}\right] \tag{10}$$

Note that when a shear-sensitive fracture criterion is used, the crack shape must also be specified. In general for three-dimensional stress states, Ω must be determined numerically. Using the shear-insensitive case as an example, we obtain at fracture [15]

$$\sigma_e = \sigma_n = \sigma_{cr} = \sigma_3 + (\sigma_1 - \sigma_3)\cos^2\alpha + (\sigma_2 - \sigma_3)\cos^2\beta\,\sin^2\alpha \tag{11}$$

where from Fig. 5 angles α and β define the crack plane in principal stress space, on which σ_n and τ act. Using direction cosines l, m, and n, the equilibrium of forces on the Cauchy tetrahedron yields values of σ_n and τ in terms of the principal stresses and the angles α and β [11]. It is computationally convenient to define $\varphi = \cos^2\beta$. Then equation (11) can be rewritten as

$$a_1\varphi^2 + a_2\varphi + a_3 = 0 \tag{12}$$

where $a_1 = 0$, $a_2 = (\sigma_2 - \sigma_3)\sin^2\alpha$, and $a_3 = (\sigma_1 - \sigma_3)\cos^2\alpha + \sigma_3 - \sigma_{cr}$. Solving for φ gives

$$\varphi = \frac{-a_3}{a_2} = \frac{\sigma_{cr} - \sigma_3 - (\sigma_1 - \sigma_3)\cos^2\alpha}{(\sigma_2 - \sigma_3)\sin^2\alpha} \tag{13}$$

If we define $\beta = \cos^{-1}\sqrt{\varphi}$, then P_2 can be calculated from [15]

Table 1 Forms of P_2 for various shear-sensitive fracture criteria and selected crack configurations ($\sigma_2 \neq \sigma_3$)

Fracture criterion	Crack configuration	P_2
Maximum tensile stress	Griffith crack (G.C.)	$\frac{\Omega}{4\pi} = \frac{1}{\pi}\int_0^{\pi} \cos^{-1}\sqrt{\varphi}\,\sin\alpha\,d\alpha$ where $\varphi = \cos^2\beta = \frac{-a_2 \pm \sqrt{a_2^2 - 4a_1a_3}}{2a_1}$ and $a_1 = (\sigma_2 - \sigma_3)^2 \sin^4\alpha$ $a_2 = (\sigma_2 - \sigma_3)\sin^2\alpha\,(2(\sigma_1\cos^2\alpha + \sigma_3\sin^2\alpha) - 4\sigma_{cr} - \sigma_3 - \sigma_2)$ $a_3 = (\sigma_1\cos^2\alpha + \sigma_3\sin^2\alpha)^2 - 4\sigma_{cr}(\sigma_1\cos^2\alpha + \sigma_3\sin^2\alpha) - (\sigma_1^2\cos^2\alpha + \sigma_3^2\sin^2\alpha) + 4\sigma_{cr}^2$
	Penny-shaped crack (PSC)	$a_1 = D_1(\sigma_2 - \sigma_3)^2\sin^4\alpha$ $a_2 = D_1(\sigma_2 - \sigma_3)\sin^2\alpha\,(2(\sigma_1\cos^2\alpha + \sigma_3\sin^2\alpha) - \frac{4}{D_1}\sigma_{cr} - \sigma_3 - \sigma_2)$ $a_3 = D_1(\sigma_1\cos^2\alpha + \sigma_3\sin^2\alpha)^2 - 4\sigma_{cr}(\sigma_1\cos^2\alpha + \sigma_3\sin^2\alpha) - D_1(\sigma_1^2\cos^2\alpha + \sigma_3^2\sin^2\alpha) + 4\sigma_{cr}^2$
Strain energy release rate	Griffith crack (G.C.)	$\varphi = \frac{\sigma_{cr}^2 - \sigma_1^2\cos^2\alpha - \sigma_3^2\sin^2\alpha}{(\sigma_2^2 - \sigma_3^2)\sin^2\alpha}$
	Penny-shaped crack (PSC)	$a_1 = D_2(\sigma_2 - \sigma_3)^2\sin^4\alpha$ $a_2 = D_1(\sigma_2^2 - \sigma_3^2)\sin^2\alpha + 2D_2(\sigma_2 - \sigma_3)\sin^2\alpha \cdot (\sigma_3\sin^2\alpha + \sigma_1\cos^2\alpha)$ $a_3 = D_1(\sigma_1^2\cos^2\alpha + \sigma_3^2\sin^2\alpha) + D_2(\sigma_1\cos^2\alpha + \sigma_3\sin^2\alpha)^2 - \sigma_{cr}^2$ where $D_1 = \frac{1}{(1 - 0.5\,\nu)^2}$, $D_2 = \frac{-\nu(1 - 0.25\,\nu)}{(1 - 0.5\,\nu)^2}$

$$P_2 = \frac{\Omega}{4\pi} = \frac{1}{\pi}\int_0^{\pi} \bar{\beta}\,\sin\alpha\,d\alpha \tag{14}$$

Following an analogous procedure to the above shear-insensitive case, similar expressions for P_2 in terms of φ and variables a_1, a_2, and a_3 can be developed using other fracture criteria and selected crack configurations. Results of this analysis are summarized in Table 1 and details are given in [11]. Equation (13) and those listed in Table 1 are not valid for all stress states, since at $\sigma_2 = \sigma_3$, an obvious singularity occurs. When component volumetric elements are exposed to this selected stress state, including the uniaxial case when $\sigma_2 = \sigma_3 = 0$, the normal and shear stresses are independent of β and the previously derived equations for P_2 change. However, at fracture a similar equation to (12) is obtained where φ now is defined as $\cos^2\alpha_{cr}$, with equation (14) no longer applicable. Reference [11] contains analogous equations to those listed in Table 1 for the case $\sigma_2 = \sigma_3$, in addition to defining P_2 for special stress states, such as the uniaxial, equibiaxial, and equitriaxial element loadings.

In the SCARE program the required integration is performed through the application of Gaussian quadratures. By using the power function form of $N(\sigma_{cr})$ and equation (14) in equation (8), the failure probability using the Batdorf approach for volume flaws can be calculated. Assuming that the stress state is constant in any given element (SCARE1 version) or subelement (SCARE2 version), the volume integration over the stressed material becomes trivial. For component reliability analysis, all that remains is that we sum the elemental survival probabilities according to established probability theory axioms, that is evaluate the product of all the individual, constant stress state elemental reliabilities. For two mutually exclusive events, such as the calculation of P_f and P_s, it is well known that for a given volume increment their sum is always unity, where P_s denotes reliability.

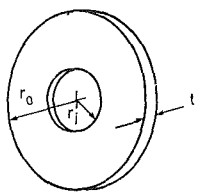

DATA:
NC - 132 HOT PRESSED Si_3N_4
m = 7.65
σ_0 = 74.82 MPa $m^{.3922}$
k_B = 16.30
r_i = 6.35 mm (.25 in)
r_0 = 41.275 mm (1.625 in)
t = 3.80 mm (.15 in)
RPM RANGE - 70K TO 114K

Fig. 6 Example 1—rotating annular disk [14]

Material Strength Characterization

Uniaxial ceramic strength data are usually obtained from flexure testing of simple geometry specimens. The Weibull parameters σ_0 and m as well as the Batdorf crack density coefficient k_B are evaluated in SCARE using four-point MOR data with known geometry. If we express the uniaxial flexure failure probability in terms of the maximum extreme fiber fracture stress σ_f or MOR using the Weibull form, that is

$$P_f = 1 - \exp\left[-C\sigma_f^m\right] \tag{15}$$

then after evaluating C and m by the least-squares method, σ_0 and k_B can be calculated. Note that in equation (15) we have used the two-parameter Weibull distribution and P_f is known along with σ_f. Details of evaluating C and m by the least-squares approach are given in [11]. In order to determine the relationship between C and σ_0, the stress distribution σ has to be expressed in terms of σ_f and the beam height h, and substituted into equation (1) with $\sigma_u = 0$. The volume integration is then performed over only the tensile portion of the beam, including the effect of the changing stress state along the beam span. After performing the necessary integration, results from equation (1) are compared to the expression given by equation (15), and the relationship between σ_0 and C is derived by making P_f from the two equations agree. For a rectangular beam of width w, length L_1 between symmetrically placed outer loads, and length L_2 between inner loads, the result is

$$\sigma_0 = \left[\left(\frac{wh}{2}\right)\frac{(L_1 + mL_2)}{C(m+1)^2}\right]^{1/m} \tag{16}$$

In addition to obtaining σ_0 and m, the SCARE program requires knowledge of k_B. We can evaluate k_B from four-point flexure data by substituting equation (10) into equation (8). Integration by parts of the results gives

$$P_s = \exp\left[-\int_V\int_0^{\sigma_1}\frac{N(\sigma_{cr})}{2\sqrt{\sigma_{cr}\sigma_1}}d\sigma_{cr}dV\right] \tag{17}$$

We again utilize the power function form of $N(\sigma_{cr})$ in equation (17) and carry out the stress integration. Similarly to the Weibull analysis, σ_1 is expressed in terms of σ_f and the beam height. The volume integration is then performed over the tensile portion of the beam, including effects of changing σ_1 along the beam length. Results from this integration are compared to equation (15) and the relationship between k_B and C is derived by setting P_f equal from the two equations. For a four-point loaded beam specimen having a rectangular cross section, we obtain

$$k_B = (2m+1)\left[\frac{2C(m+1)^2}{wh(L_1 + mL_2)}\right] \tag{18}$$

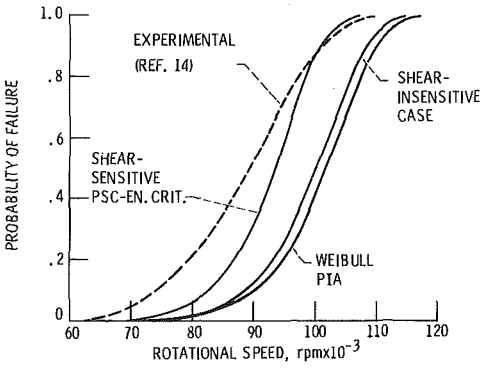

Fig. 7 Example 1 probability of failure versus disk rotational speed for various fracture models (SCARE2 data)

***Table 2* Example 1 failure probabilities as a function of rotational speed for various fracture models [m = 7.65; σ_0 = 74.82 MPa (m)$^{0.3922}$; $k_B\sigma_0^m$ = 16.30; NGP = 5]**

Angular speed (rpm)	SCARE2 (HEXA elements)			SCARE1 (HEXA elements)	Ford (Ref. 14) (axisymmetric elements)	Ford (Ref. 14)
	Weibull PIA	Batdorf shear-insensitive	Batdorf shear-sensitive PSC G_c criterion	Batdorf shear-insensitive	Shear-insensitive	Experimental
70 000	0.0021	0.0026	0.0078	0.0022	0.0023	0.0583
75 000	.0061	.0075	.0222	.0064	.0067	.1121
80 000	.0163	.0201	.0584	.0170	.0179	.2017
85 000	.0412	.0505	.1426	.0426	.0446	.3367
93 000	.1530	.1850	.4549	.1579	.1650	.6321
100 000	.3954	.4623	.8410	.4074	.4223	.8714
104 000	.6000	.6763	.9649	.6124	.6321	.9514
110 000	.8847	.9301	.9996	.8931	.9055	.9949
114 000	.9736	.9900	1.0000	.9792	.9830	.9994

By comparing equations (16) and (18), we conclude that when using the normal stress failure criterion, k_B and σ_0 are related by

$$k_B = (2m+1)\left(\frac{1}{\sigma_0}\right)^m \tag{19}$$

However, equation (19) changes when the G_c criterion is used [5].

Example

In order to validate SCARE, a number of sample problems were analyzed from the open literature [11]. Among them failure probability predictions were made, using Batdorf's shear-insensitive fracture model, for a silicon nitride disk rotating at various angular velocities [14]. The dimensions of the disk along with appropriate material statistical parameter data are given in Fig. 6. Because of the simple geometry, only eight HEXA elements were used in one 15 deg sector MSC/NASTRAN model of the disk. The calculated NASTRAN stresses and volumes both were within approximately 1 percent of the available closed form answers. Both SCARE1 and SCARE2 predictions were generated and the results were compared to those listed in [14]. Reliability calculations were also made at various speeds using other fracture theories. Selected results from these analyses are shown in Fig. 7 and Table 2. For a given speed, the Weibull PIA model yields clearly the lowest failure estimate, while the shear-sensitive PSC with the G_c criterion gives the highest. The agreement between SCARE2 results and those in [14] was within 10 percent, with the difference probably due to the different stress-volume data used in solving the reliability problem. Laboratory measurements agree best with the selected shear-sensitive fracture model, as can be noted, especially in the high failure probabilities range. Since only seven disks were fracture tested compared to 85 MOR specimens, there is some concern about the accuracy of the experimental disk Weibull modulus of 4.95, which causes the greater difference between experimental and predicted P_f at lower failure probabilities.

Conclusions

A general purpose, statistical, fast fracture failure probability code has been generated, which is coupled with MSC/NASTRAN, and can be used to design structural ceramics components. The program includes a number of widely used polyaxial fracture models, appropriate extreme value statistics, and the ability to calculate material failure distribution parameters, all for volume-distributed flaws. Current work includes extension of this same capability to bimodal flaw populations, where failure due to extrinsic defects is a concurrent possibility. The addition of more advanced failure criteria which permit out-of-plane crack extension is also planned. Finally, the problem of a transversely loaded circular plate will be investigated, both analytically and experimentally, to resolve some of the contradictory trends reported in [5, 16].

References

1 Weibull, W., "A Statistical Theory of the Strength of Materials," *Ingeniors Vetenskaps Akademien Handlinger*, No. 151, 1939.

2 Freudenthal, A. M., "Statistical Approach to Brittle Fracture," in: *Fracture, Vol. 2: An Advanced Treatise, Mathematical Fundamentals*, H. Liebowitz, ed., Academic Press, 1968, pp. 591–619.

3 Batdorf, S. B., "Some Approximate Treatments of Fracture Statistics for Polyaxial Tension," *Int. J. Fract.*, Vol. 13, No. 1, Feb. 1977, pp. 5–11.

4 Batdorf, S. B., and Heinisch, H. L., Jr., "Weakest Link Theory Reformulated for Arbitrary Fracture Criterion," *J. Am. Ceram. Soc.*, Vol. 61, No. 7–8, July–Aug. 1978, pp. 355–358.

5 Shetty, D. K., Rosenfield, A. R., and Duckworth, W. H., "Statistical Analysis of Size and Stress State Effects on the Strength of an Alumina Ceramic," in: *Methods for Assessing the Structural Reliability of Brittle Materials*, ASTM-STP-844, S. W. Freiman and C. M. Hudson, eds., American Society for Testing and Materials, 1984, pp. 57–80.

6 Lamon, J., and Evans, A. G., "Statistical Analysis of Bending Strengths for Brittle Solids: A Multiaxial Fracture Problem," *J. Am. Ceram. Soc.*, Vol. 66, No. 3, Mar. 1983, pp. 177–182.

7 Petrovic, J. J., "Mixed-Mode Fracture of Hot-Pressed Si_3N_4," *J. Am. Ceram. Soc.*, Vol. 68, No. 6, June 1985, pp. 348–355.

8 Alpa, G., "On a Statistical Approach to Brittle Rupture for Multiaxial States of Stress," *Eng. Fract. Mech.*, Vol. 19, No. 5, 1984, pp. 881–901.

9 Batdorf, S. B., "Comparison of the Best Known Fracture Criteria," *Proceedings of International Symposium on Absorbed Specific Energy and/or Strain Energy Density Criterion*, G. Sih, E. Czoboly, and F. Gillemot, eds., Martinus Nijhoff Publishers, 1982, pp. 243–251.

10 Schaeffer, H. G., *MSC/NASTRAN Primer: Static and Normal Modes Analysis*, rev. ed., Schaeffer Analysis Inc., Mount Vernon, NH, 1982.

11 Gyekenyesi, J. P., "SCARE—A Post-Processor Program to MSC/NASTRAN for the Reliability Analysis of Structural Ceramic Components," NASA TM-87188, 1986.

12 Shih, T. T., "An Evaluation of the Probabilistic Approach to Brittle Design," *Eng. Fract. Mech.*, Vol. 13, No. 2, 1980, pp. 257–271.

13 Wertz, J. L., and Heitman, P. W., "Predicting the Reliability of Ceramic Turbine Components," *Advanced Gas Turbine Systems for Automobiles*, SAE-SP-465, Society of Automotive Engineers, 1980, pp. 69–77.

14 Swank, L. R., and Williams, R. M., "Correlation of Static Strengths and Speeds of Rotational Failure of Structural Ceramics," *Am. Ceram. Soc. Bull.*, Vol. 60, No. 8, Aug. 1981, pp. 830–834.

15 Batdorf, S. B., and Crose, J. G., "A Statistical Theory for the Fracture of Brittle Structures Subjected to Nonuniform Polyaxial Stresses," ASME *J. Appl. Mech.*, Vol. 41, No. 2, June 1974, pp. 459–464.

16 Rufin, A. C., Samos, D. R., and Bollard, R. J. H., "Statistical Failure Prediction Models for Brittle Materials," *AIAA J.*, Vol. 22, No. 1, Jan. 1984, pp. 135–140.

H. Zimmermann

A. Firsching

MTU München,
Munich, Federal Republic of Germany

G. H. Dibelius

M. Ziemann

Institute for Steam and
Gas Turbines,
TU Aachen,
Aachen, Federal Republic of Germany

Friction Losses and Flow Distribution for Rotating Disks With Shielded and Protruding Bolts

The friction losses of rotating disks in turbomachines are often increased by protruding bolt heads and surface imperfections, especially at the rim. This can significantly influence the heat production and flow distribution in disk cooling systems. A detailed knowledge of losses and local cooling flows is required to improve the accuracy of both performance and disk life predictions. To this end a thorough experimental study of various disk, bolt, and bolt cover configurations has been carried out. Some of the important test results are presented, and recommendations are given for minimizing windage losses. Empirical influence coefficients based on von Kármán's equations for disk friction losses have been derived for different geometries. Furthermore, empirical correlations are proposed for the windage losses of various disk/bolt configurations.

1 Introduction

It is necessary to take into account secondary effects from cooling air flows, windage losses, etc., in order to improve the thermal efficiencies of advanced gas turbines in addition to the basic aerodynamic improvements which are presently pursued. Therefore these parasitic losses have to be much better analyzed and taken into consideration in the design stage. Bookkeeping methods of individual losses are required, and only with a good understanding of the physical mechanism will it be possible to reduce the resultant performance penalties. If in addition the heat sources and heat transfer coefficients are better known, a more reliable prediction of disk life could be achieved. So far the publications exclusively deal with plain disks, and there is little information available on real disks with surface imperfections such as protruding bolts or rim sealing configurations.

Detail measurements inside engines are nearly impossible, and numerical solutions of the problem are not yet available to the designer. Therefore some representative rotor housing configurations have been modeled and investigated on a special test rig. The experimental results are also used in attempts to set up analytical loss correlations with maximal general applicability, which could considerably reduce the test expenditure in future turbomachine development.

2 Experiments

2.1 Test Apparatus. The overhanging disk of radius 0.4 m is mounted in two ball bearings. It is surrounded by the housing as illustrated in Fig. 1. The disk is driven by a 65 kW d-c motor with a speed range of 0–6000 rpm. The shafts of the disk and the electric motor are both mounted in cradle bearings to measure the ventilation torque acting on the disk. The pressure of the air inside the housing ranges from 0.5 to 6.0 bar. The ducts between the shafts and the housing are sealed off by a complex air barrier. The heat produced by friction in the gap is transferred to the cooling water in the passages within the side walls of the disk housing.

For superimposed throughflow in the centrifugal direction, the air is supplied axially, passing the cone fixed to the front

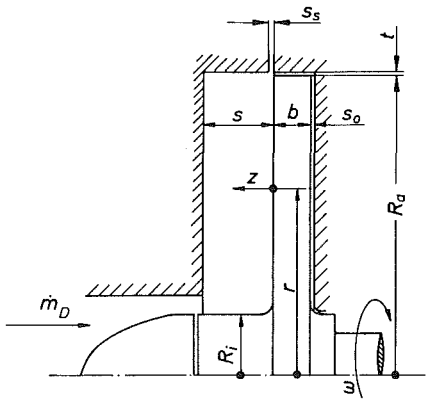

Fig. 1 Scheme of the test apparatus, the coordinate system, and notation:

$$\left(\frac{s}{R_a} = 0.2375 \quad \frac{b}{R_a} = 0.1250 \quad \frac{s_s}{R_a} = 0.0125\right)$$
$$\left(\frac{t}{R_a} = 0.0075 \quad \frac{s_0}{R_a} = 0.0125 \quad \frac{R_i}{R_a} = 0.2000\right)$$

Contributed by the Gas Turbine Division of THE AMERICAN SOCIETY OF MECHANICAL ENGINEERS and presented at the 31st International Gas Turbine Conference and Exhibit, Düsseldorf, Federal Republic of Germany, June 8–12, 1986. Manuscript received at ASME Headquarters February 7, 1986. Paper No. 86-GT-158.

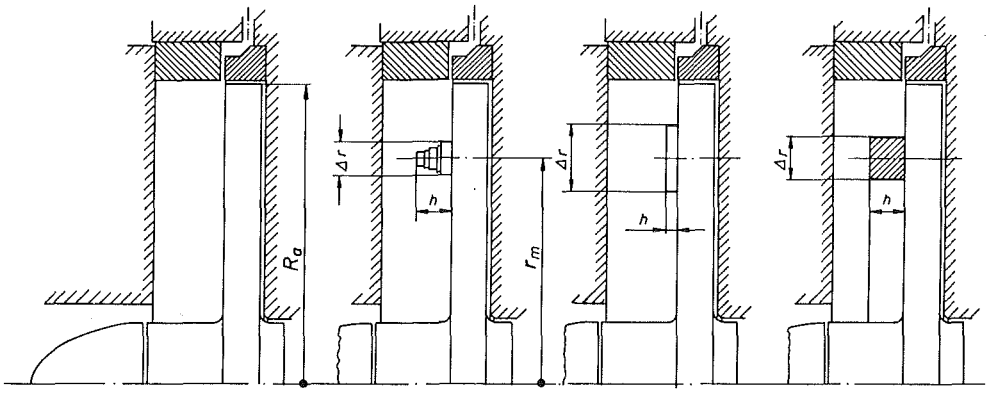

	Smooth	Staged Bolts	Cylindrical Bolts	Covered Bolts
$\Delta r/R_a$	-	0.1125	0.2250	0.1425
h/R_a	-	0.1150	0.0423	0.1150

Fig. 2(a) Configurations for the tests: $r_m/R_a = 0.75$, $R_a = 0.4$ m

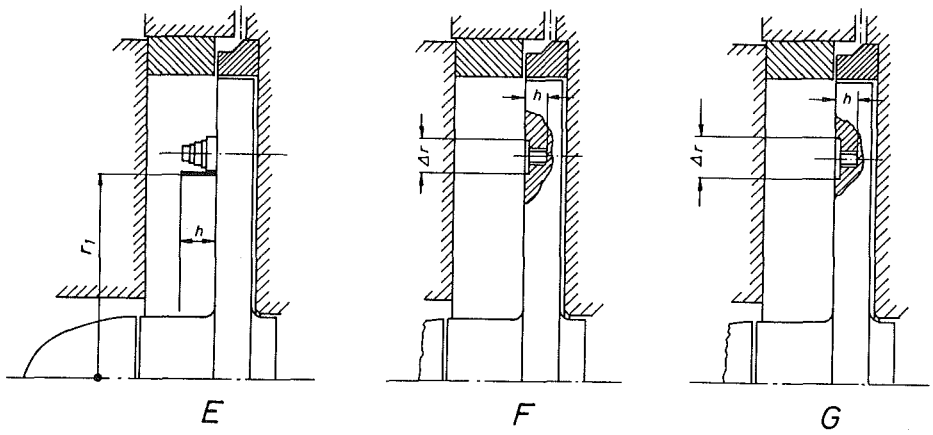

	Partially Covered Bolts		Smooth, with 18 Holes	Groove, with 36 Holes
r_1/R_a	0.6788	$\Delta r/R_a$	0.1125	0.1425
h/R_a	0.1150		0.0825	0.0825

Fig. 2(*b*) Configurations for the tests

Nomenclature

b = thickness of the disk, m
C_D' = $\dot{m}_D/R_a \cdot \mu$ = throughflow Reynolds number
C_{MS} = $M_S/(\rho/2 \cdot \omega^2 \cdot R_a^5)$ = frictional torque number
ΔC_{MS} = incremental friction torque number in comparison to the smooth disk
C_{W0} = drag coefficient of bolts in undisturbed flow
ΔC_W = drag coefficient of holes in the smooth disk
c_r = radial velocity component, m/s
c_u = circumferential velocity component, m/s
F = form drag correction factor
h = height of bolt or cover, depth of holes or grooves, m
K = $c_u/r \cdot \omega$ = core rotation factor at $z = s/2$
$\dot{m}$ = mass flow pumped by bolts, kg/s
$\dot{m}_D$ = superimposed cooling or sealing air flow, kg/s
M_S = frictional torque on one face of the disk, Nm
n = number of bolts or holes
P = power (windage losses), W
r = coordinate in radial direction, m
Δr = diameter of bolts or holes, m
r_m = bolt circle radius, m
R_a = outer radius of the disk, m
Re = $R_a^2 \cdot \rho \cdot \omega/\mu$ = rotational Reynolds number
R_i = inner radius of the disk, m
s, s_0 = axial clearance between disk and housing on the front side and on the back side, respectively, m
s_s = axial clearance of the housing, m
t = radial tip clearance of the disk, m
z = distance normal to the disk, m
μ = dynamic viscosity, kg/m•s
ρ = density of the fluid at the radius R_a, kg/m^3
ω = angular velocity of the disk, 1/s

Subscripts

a = outer
i = inner
F = form drag
1 = at inner side of the bolts
2 = at outer side of the bolts

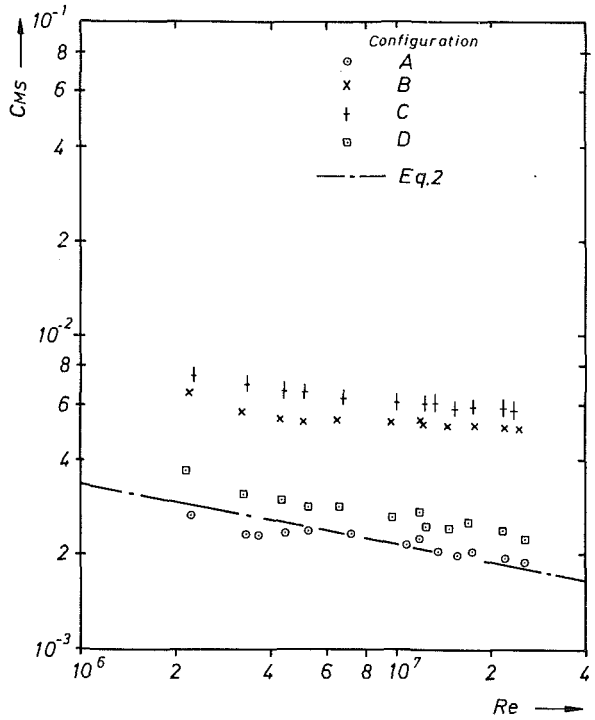

Fig. 3 Frictional torque number as a function of Reynolds number without throughflow ($C_D' = 0$)

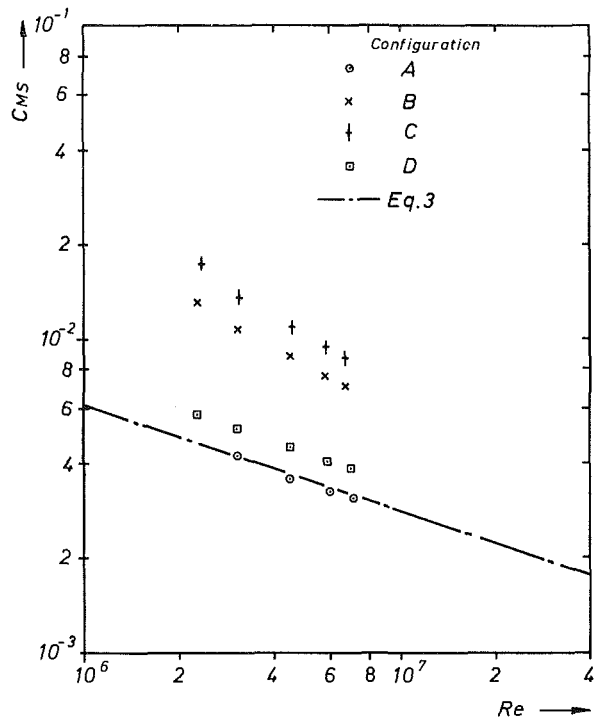

Fig. 5 Frictional torque number as a function of Reynolds number, superimposed throughflow in centrifugal direction ($C_D' = 2.6 \cdot 10^4$)

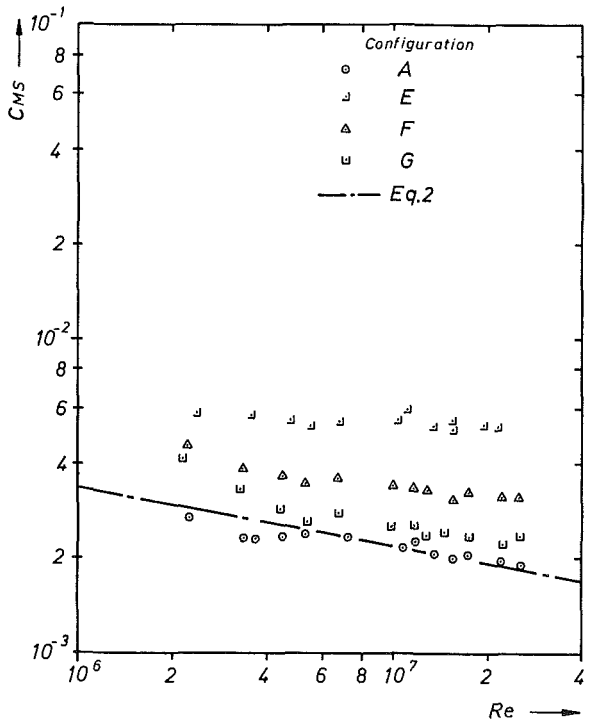

Fig. 4 Frictional torque number as a function of Reynolds number without throughflow ($C_D' = 0$)

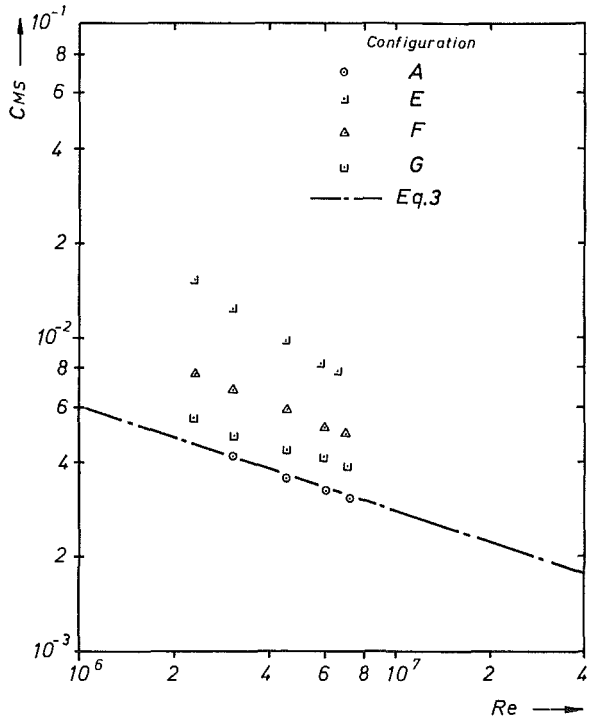

Fig. 6 Frictional torque number as a function of Reynolds number, superimposed throughflow in centrifugal direction ($C_D' = 2.6 \cdot 10^4$)

cover plate, and then leaves the casing at its outer circumference.

The geometry of the gap and the throughflow were modified only on the side facing the front cover plate. The frictional torque acting on the front side of the disk is determined as the difference between the measured torque and that part of the torque acting on the back side and the cylindrical surface of the disk. These parts of the total torque were determined by additional experiments in good agreement with other experimenters.

Detailed information on the test setup is given in [1].

2.2 Tested Configurations. The different configurations are shown in Fig. 2: (*A*) smooth disk; (*B*) 18 staged bolts with maximum diameter $d = \Delta r$ equally spaced; (*C*) 18 cylindrical bolts with the same area of projection in the circumferential direction as the bolts of configuration (*B*), but of smaller height and larger diameter Δr; (*D*) bolts fully covered by a

perfect ring of the same height as the staged bolts but with a somewhat larger difference of the radii Δr (without any holes in the cover); (*E*) 18 staged bolts partly covered at the inner radius by a fin of thickness 5 mm; (*F*) smooth disk with 18 holes, each one consisting of two cylindrical parts: one of diameter Δr and a depth of 4 mm; the second with a metrical thread *M* 22 × 1.5 and 29 mm deep; (*G*) smooth disk with a circumferential groove of depth 8 mm, and 36 holes with a metrical thread *M* 22 × 1.5 and 25 mm deep. Bolts, grooves and holes are positioned at the same radius. Staged bolts and bolt covers are of the same height.

2.3 Experimental Results. For facilitating general application the experimental results are expressed in dimensionless terms. The friction torque number and the tangential and radial velocity of the air in the gap related to the circumferential speed of the disk and the core rotation factors are mainly a function of the rotational Reynolds number, the throughflow Reynolds number, and the dimensionless geometry of the gap.

In Figs. 3-6 the frictional torque number is plotted versus the rotational Reynolds number.

Bolts on the disk increase the torque substantially, by a factor of 2.5. For flat bolts of the same circumferential projection area (configuration *C*), the frictional torque number exceeds that for staged bolts.

A full cover over the bolts increases the friction forces only by 25 percent. In order to keep weight and design complexity small, the partly covered bolt configuration (*E*) was tested. This should prevent the bolts at least from pumping. However, the test data deviate substantially from those for fully covered bolts (*D*). There is nearly no difference between this case and the uncovered bolts.

The separated holes of configuration (*F*) result in a larger torque than the circumferential groove of configuration (*G*), even though there are more holes in (*G*).

The superimposed throughflow of $C'_D = 2.6 \cdot 10^4$ increases the frictional torque number by at least 50 percent. There is a stronger influence of the rotational Reynolds number than without throughflow. In an aim to understand the difference in frictional torque number of configurations (*D*) and (*E*), the velocity of the flow in the gap was measured with a conventional hook-shaped pressure probe having three holes. Representative results of velocity traverses at radii below the cover and above the bolts are plotted for configuration (*E*) in Figs. 7 and 8. Because of the bolts and the cover, the core rotation is increased in comparison to the smooth disk of configuration (*A*).

Without superimposed throughflow, the fluid recirculation is restricted to a small part near the housing at the inner traverse, while it occupies the whole gap width at the outer traverse. The circumferential velocity component seems to be independent of the radius, as indicated by the peaks in the velocity profile.

If there is a superimposed throughflow of $C'_D = 2.6 \cdot 10^4$, the secondary flow is obstructed. At the inner traverse the recirculated mass flow is negligible. At the outer traverse the flow direction changes near the surface of the disk, which indicates a local recirculation.

3 Theoretical Results

3.1 Theory of the Smooth Disk. In the early 1920s von Kármán investigated the friction losses of a smooth disk without a casing [2]. In this type of "free" disk configuration fluid is continuously sucked in at its center, accelerated radially outward near the disk surface by friction and centrifugal forces, and transported over the disk rim. The energy is thus lost and has to be reproduced continuously by the disk.

These covering processes have been explained theoretically by von Kármán and can be described in one equation

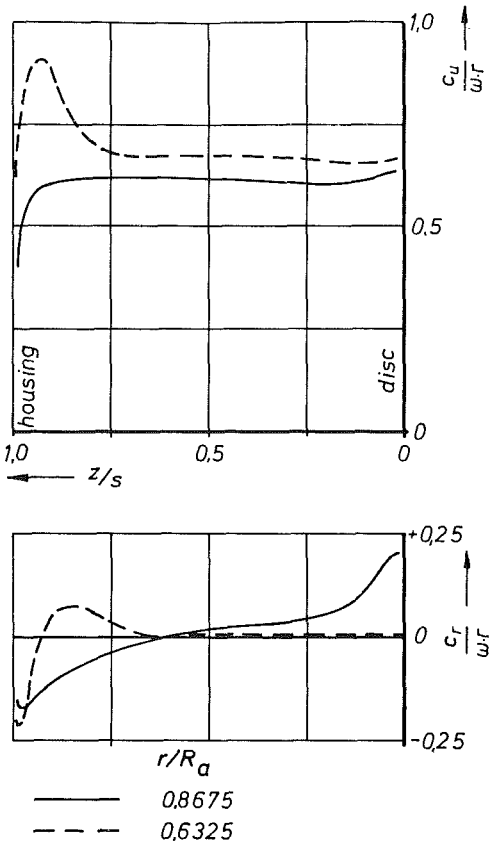

Fig. 7 Velocity profiles of the circumferential and the radial component in the gap of configuration (*E*) at different radii ($Re = 4 \cdot 10^6$, $C'_D = 0$)

$$C_{MS} = 0.073 \cdot \mathrm{Re}^{-0.2} \cdot \left[1 - \left(\frac{R_i}{R_a}\right)^{5.7}\right]^{0.8} \tag{1}$$

The term in brackets takes into account the fact that the beginning of the boundary layer could be out from the center of the disk because of the diameter of the disk shaft.

If the free disk is enclosed by a sealed casing, the fluid circulation is changed substantially: The fluid moving radially outward is recirculated on the static wall of the casing, as can be derived from Fig. 7, and the circumferential velocity component of the fluid, induced by frictional effects of the rotating disk, is developed into a stationary core rotation.

Both effects partly keep the energy produced by the disk inside the casing and reduce the disk friction losses considerably. An empirical correction factor to equation (1), including the effects of the axial width of the gap, is in good agreement with test data. This is plotted as a dash-and-dot line in Fig. 3 for configuration (*A*), and is given by equation (2)

$$C_{MS} = 0.073 \cdot \mathrm{Re}^{-0.2} \cdot (1 - 0.39 \cdot \mathrm{Re}^{0.11 \cdot s/R_a}) \cdot \left[1 - \left(\frac{R_i}{R_a}\right)^{5.7}\right]^{0.8} \tag{2}$$

A superimposed throughflow increases the relative speed between the disk and the fluid. Its influence on the friction torque number is also determined by an empirical correction factor to equation (1)

$$C_{MS} = 0.073 \cdot \mathrm{Re}^{-0.2} \cdot [1 + 10^{-4} \cdot C'_D \cdot (4.1 \cdot \mathrm{Re}^{-0.16} - 0.32)] \cdot \left[1 - \left(\frac{R_i}{R_a}\right)^{5.7}\right]^{0.8} \tag{3}$$

Within the range of tested axial gaps *s*, the frictional torque number appears to be independent of the axial clearance *s*. This function is plotted as a dash-and-dot line in Fig. 5 for configuration (*A*).

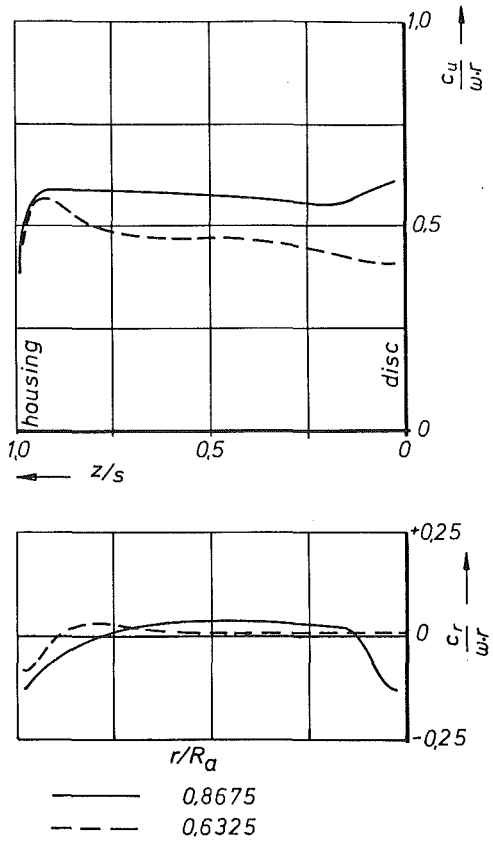

Fig. 8 Velocity profiles of the circumferential and the radial component in the gap of configuration (E) at different radii, superimposed throughflow in centrifugal direction ($Re = 6 \cdot 10^6$, $C_D' = 2.6 \cdot 10^4$)

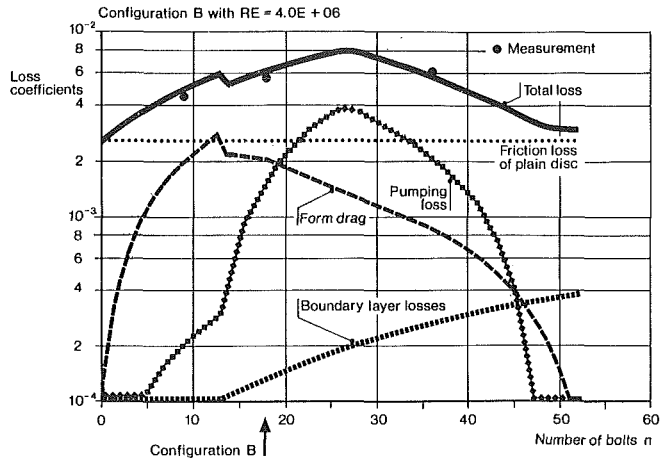

Fig. 9 Loss coefficient of configuration (B) as a function of bolt number, uncovered staged bolts, $Re = 4 \cdot 10^6$, $C_D' = 0$

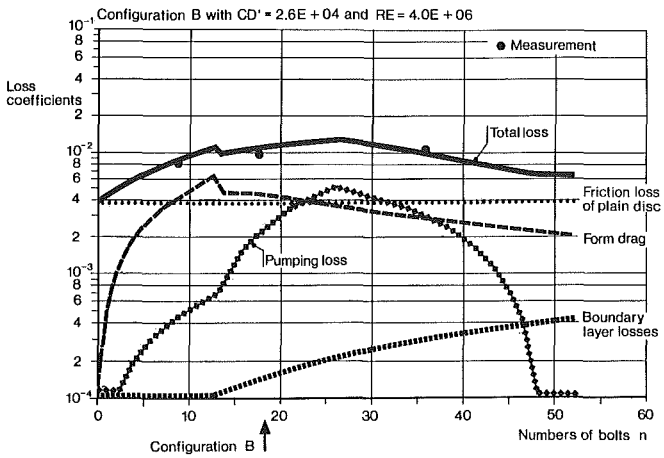

Fig. 10 Loss coefficients of configuration (B) as a function of bolt number, uncovered staged bolts, $Re = 4 \cdot 10^6$, $C_D' = 2.6 \cdot 10^4$

3.2 Theory of Protruding Bolts. If protruding bolt heads are fixed on the smooth disk, additional losses are to be expected. They are subdivided into three phenomena:

Form Drag. The circumferential velocity of the bolts on the smooth disk is larger than the speed of the fluid core in the gap, causing a relative speed between the bolts and fluid. This results in a drag loss, which can generally be calculated as

$$\Delta C_{MS_F} = n \cdot C_{W0} \cdot (1-K)^2 \cdot \left(\frac{r_m}{R_a}\right)^3 \cdot \frac{h \cdot \Delta r}{R_a^2} \cdot F \qquad (4)$$

Here C_{W0} is the basic drag coefficient of the bolt, F a drag correction factor due to the interference with the wakes from adjacent bolts [3], and K the core rotation factor.

Boundary Layer Losses. Bolt heads interrupt the boundary layer developing near the surface of the rotating disk. Behind the bolt heads the boundary layer will be rebuilt, causing boundary layer losses. These will vary with the geometry of the setup and with the rotational Reynolds number.

In accordance with von Kármán [2] the boundary layer losses of a circular ring of outer radius r_a and inner radius r_i are generally

$$C_{MS} = 0.073 \cdot \mathrm{Re}^{-0.2} \cdot \left(\frac{r_a}{R_a}\right)^{4.6} \cdot \left[1 - \left(\frac{r_i}{r_a}\right)^{5.7}\right]^{0.8} \qquad (5)$$

The total boundary layer loss can then be determined by adding up the losses from individual sections.

Pumping Losses. The protruding bolt heads on the smooth disk act as a radial compressor, depending on the number and shape of the bolts. The lost amount of power is derived from the Euler turbomachine equation

$$P = \omega \cdot \dot{m} \cdot (c_{2u} \cdot r_2 - c_{1u} \cdot r_1) \qquad (6)$$

In this equation, $\dot{m}$ is the mass flow pumped by the bolt heads, and c_u is the tangential velocity of the bolt driven fluid at the outer (2) and inner bolt radius (1), respectively. The total additional loss of the protruding bolt heads can be obtained by adding the three loss components.

3.3 Theory of Fully Covered Bolts, Holes, and Grooves. If the rotating bolt heads are totally covered by a rotating shielding, the pumping losses are nearly zero. The form drag is reduced to a friction term occurring at the side walls of the covering, resulting from the different rotational speeds of the bolt cover and fluid. It can be evaluated by an analogy to the derivations in [2].

$$\Delta C_{MS_F} = 0.157 \cdot (1-K)^{1.8} \cdot \frac{h}{R_a^{4.6}} \cdot \mathrm{Re}^{0.2} \cdot \left[\left(r_m - \frac{\Delta r}{2}\right)^{3.6} + \left(r_m + \frac{\Delta r}{2}\right)^{3.6}\right] \qquad (7)$$

The boundary layer losses can be evaluated according to equation (5), the disk being split up into three disk ring elements:

- ring 1: $r_i = R_i$, $r_a = r_m - \Delta r/2$
- ring 2: $r_i = r_m - \Delta r/2$; $r_a = r_m + \Delta r/2$
- ring 3: $r_i = r_m + \Delta r/2$; $r_a = R_a$

The three contributions, each computed from equation (5), are to be added.

If the bolt heads are replaced by holes in the smooth disk, the computation can be performed as indicated above, with pumping losses neglected. The boundary layer losses can be

evaluated according to equation (5), and the form drag according to Schlichting [4] as

$$\Delta C_{MS_F} = \frac{\pi}{4} \cdot n \cdot \Delta C_W \cdot (1-K)^2 \cdot \left(\frac{r_m}{R_a}\right)^3 \cdot \left(\frac{\Delta r}{R_a}\right)^2 \cdot \sqrt{1+2\cdot\frac{\Delta r}{r_m}} \quad (8)$$

The drag coefficient ΔC_W is a function of the flow conditions adjacent to the rotating disk [4]. The complete losses of rotating holes in the smooth disk can be obtained by adding form drag and boundary layer losses, as above. A rotating groove in the smooth disk can be treated in the same way as the rotating cover, see above, but the form drag at the side parts of the groove is small and can be neglected because of the small relative speed between disk and fluid.

3.4 Comparison of Test Data and Theoretical Data. In Figs. 9 and 10 some theoretical results on uncovered bolts with and without superimposed throughflow are plotted and compared to test results. Corresponding to representative engine conditions, the rotational Reynolds number was set to Re = $4 \cdot 10^6$ and the superimposed throughflow to $C_D' = 2.6 \cdot 10^4$. The core rotation factor K was assumed from test evidence to be $K = 0.6$ without, and $K = 0.42$ with, a superimposed throughflow of $C_D' = 2.6 \cdot 10^4$.

Comparison of Figs. 9 and 10 shows some very important trends:

1 At small bolt numbers ($n \leq 13$) the additional friction losses are mainly form drag; at large bolt numbers ($n \geq 28$) mainly pumping losses. Up to 13 bolts, form drag is only dependent on the bolt number; at higher numbers interference effects from bolt wakes occur, which strongly decrease drag losses with increasing bolt numbers (see also [3]). These wake effects are reduced at superimposed throughflow (see Fig. 10, "blown-away wake effects").

At about 16 bolts the distance between the bolts becomes small enough to excite pumping effects, which initially increase with growing bolt numbers, but these then are reduced again because of the smaller mass flow which can pass between the bolts (see also equation (6)).

2 Boundary layer losses increase linearly with the bolt number, but are always relatively small.

3 Superimposed mass flows heavily increase all loss components and hence total loss.

4 Conclusions

1 Fully covered bolts, or arrangements with maximal number of bolts, are the only low loss configurations tested and should be used wherever possible. As a consequence, the generated heat can be reduced and this has positive effects on the disk life.

2 With the geometries chosen, the maximum of the total losses always occurred with half of the maximum possible number of bolts.

3 Partly covered bolts, especially with superimposed throughflow, have high losses, and can yield even higher power losses than uncovered bolts.

4 The friction losses strongly depend on the core rotation factor K, which in itself is influenced by the shape of the surface imperfections, the axial clearance s, and the housing configuration. This should be investigated further.

5 Grooves and holes, i.e., inward surface imperfections, could be described with the same loss mechanism. For the tested configurations the friction torque numbers were in the same order as for outward surface imperfections.

6 The presented empirical correlations and simple physical models used allow one to calculate individual loss components and the total losses with reasonable accuracy.

5 References

1 Dibelius, G., Radtke, F., and Ziemann, M., "Experiments on Friction, Velocity and Pressure Distribution of Rotating Discs," D. E. Metzger and N. H. Afghan, eds., *Heat and Mass Transfer in Rotating Machinery*, Hemisphere, Washington, 1984.

2 von Kármán, Th., "Hauptaufsätze über laminare und turbulente Reibung," *Zeitschrift für angewandte Mathematik und Mechanik*, Vol. 1, No. 4, 1921, pp. 233–252.

3 Taniguchi, S., Sakamoto, H., and Arie, M., "Interference Between Two Circular Cylinders of Finite Height Vertically Immersed in a Turbulent Boundary Layer," *Journal of Fluids Engineering*, Vol. 104/529, Dec. 1982.

4 Schlichting, H., *Grenzschicht-Theorie*, G. Braun-Verlag, Karlsruhe, 1965, p. 606.

Effects of Honeycomb-Shaped Walls on the Flow Regime Between a Rotating Disk and a Stationary Wall

T. Uzkan[1]
General Motors Corp.,
Electromotive Division,
LaGrange, IL 60525

N. J. Lipstein
General Electric Company,
Corporate Research and Development,
Schenectady, NY 12301

In gas turbines there are many circumstances where coolant flows are introduced between the rotor disk and the stationary housing. This flow serves not only to supply coolant flow to the disk face, but also to restrict the radial inflow of hot gases to be ingested into the clearance from the turbine blade flow field. The amount of the hot radial inflow is influenced by the difference of the disk pumping capacity and the coolant flow supplied near the center. In order to cool the turbine disk with limited supply of coolant air, some means of reducing the radial inflow of hot gases is needed. It is thought that the use of different surface shapes on the stationary housing would inhibit the disk pumping capacity and, therefore, reduce the radial inflow of hot gases into the clearance. To validate the concept, an experimental study was undertaken. The basic geometry investigated was the flow field between a smooth cylindrical rotating disk parallel to a plain circular coaxial wall open to the free space at the disk periphery. Coolant flow is simulated by supplying air through the bore of the stationary wall into the gap. In addition to the base data obtained with the plain stationary wall, a duplicate series of experiments were run with an open honeycomb facing the stationary wall. The effects of the stationary wall surface geometry is assessed by comparing the data with honeycomb facing against the data with plain stationary wall. The flow field is studied through measurements of the static pressure on the stationary wall, radial and tangential velocity measurements in the clearance, the torque on the drive motor, and coolant flow rates. Flows were studied over a gap spacing to disk radii ratio of 0.01 and 0.10, disk Reynolds numbers from 5×10^5 to 2.2×10^6, and throughflow rates from 0 to 3.2 cfs. The results are presented in terms of the tangential and radial velocity profiles in the gap, the static pressure measurements, and the disk torque coefficients. The use of honeycomb on the stationary wall surface grossly altered the ingestion of external flow into the gap from the disk periphery. Important conclusions are: (1) The vacuum in the gap generated by the disk rotation is reduced by a factor of 0.4 to 0.6, depending on the radial location of the point; (2) the core tangential velocity is reduced by a factor of 0.6 to 0.7, depending on the axial spacing and the throughflow number; (3) the critical coolant flow rate is about 63 percent less for the honeycombed surface, as compared to the plain wall case. (4) for a given coolant flow rate, the penetration distance of the radial inflow is much larger for the plain disk than the honeycomb surface.

Introduction

In turbomachinery, there are many circumstances where coolant flows are introduced between a rotor disk and stationary housing. This flow serves not only to supply coolant to the disk face, but also to restrict and mix with any ingested hot gases from the turbine blade flow field, and thereby reduce the gas temperature in this interspace. The amount of the hot radial outflow is influenced by the difference of the disk pumping capacity and the coolant flow supplied near the center. In order to cool the turbine disk with limited supply of coolant air, some means of reducing the radial inflow of hot gases is needed. It is thought that the use of different surface shapes on the stationary housing would inhibit the disk pumping capacity and, therefore, reduce the radial inflow of hot gases into the clearance.

[1]This work was completed when the first author was with the GE Research and Development Center.

Contributed by the Gas Turbine Division of THE AMERICAN SOCIETY OF MECHANICAL ENGINEERS and presented at the 31st International Gas Turbine Conference and Exhibit, Düsseldorf, Federal Republic of Germany, June 8–12, 1986. Manuscript received at ASME Headquarters February 7, 1986. Paper No. 86-GT-161.

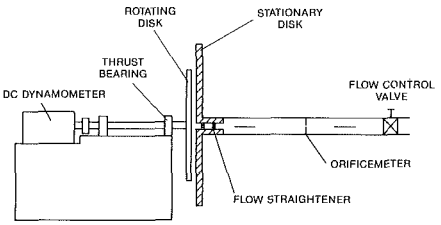

Fig. 1 General arrangement of test apparatus

There has been continuing interest in the ingestion of hot gases in the gap between a rotating disk and a stationary enclosure because of its application to turbine disk cooling. A good review of these studies dating from the early 1950s is available in [1]. Daily and Nece [2] have presented a systematic classification of flow regimes between a rotating disk and its casing. Bayley et al. [3] used a plane disk and a shrouded stationary wall to study the problem. From the pressure measurements they presented a correlation for the minimum dimensionless flow rate required to prevent ingress. Sokolov [4] presented an approximate integral method of calculating the air temperature with radial cooling of the rotor disk from known amount of ingress. Uzkan [5] presented an integral method of calculating the radial ingestion rates and the separation streamlines between the outflow and inflow regions in the gap. Owen and Pincombe [6] studied the flow between two rotating disks shrouded with throughflow and presented correlations for the tangential velocity in the central core. Phadke et al. [7] presented empirical correlations for the minimum amount of coolant necessary to prevent ingress for the radial clearance seal geometry. Moreover, comparing their data with those of plane disk case [3] and the axial seal case [8], they concluded that the radial clearance seals require less coolant to prevent ingress than that required for an axial clearance seal.

To reduce the amount of coolant flow necessary to prevent the ingress into the gap (and thus to improve the disk cooling), radial and sometimes axial seals are commonly used. On the other hand, reducing the ingress by using different stator surface geometry is also possible. This method is not well known, not reported in the literature, and its full potential is not fully realized. This paper presents an example in this direction.

Although the use of different stator surface geometry to reduce ingress is not reported in the literature, there is considerable information about the drag of rotating disks with different stator surface geometries, which may be useful for making intelligent engineering choices of disk friction results for different surface geometries. The data for radial, concentric, and logarithmic spiral blades on the stator or on the disk are available in [9] and [10]. Experiments on a rotating disk enclosed in a grooved casing for several geometric combinations are reported in [11]. Data for the stator geometry roughened up by using different grades of sand are available in [12]. Similar data obtained by using different wire-mesh sizes, both on the rotating disk or on the housing, are given in [13].

Experimental Apparatus and Instrumentation

The test apparatus was designed to study the flow in the gap between a rotating disk and stationary wall, and the ingestion of flow into this gap from the disk periphery. For this purpose, a 30-in-dia aluminum disk was directly shaft mounted and driven by a d-c dynamometer and located concentric to a 36 inch diameter stationary circular wall to form the gap of interest. The general arrangement is shown in Fig. 1. The stationary wall was fitted with a central 3-3/4 inch diameter flanged hole through which air could be supplied to the gap from an air supply to study the effects of throughflow. Test data are reported for disk Re from 5×10^5 to 2.2×10^6, nondimensional gap spacings of $\bar{S}=0.01$, 0.0166, 0.0666, and 0.10, and intergap throughflow $Q=0$, 1.75, 3.45 ft^3/s which corresponds to a nondimensional throughflow parameter of 0 to 0.27.

One of the principal interests in this investigation was to determine the effect of honeycomb on the stationary wall in reducing the radial pressure gradient within the gap and the throughflow required to prevent ingestion. For this investigation, honeycomb of one fixed design, resin impregnated cloth with 1/4 × 1/2 in. rectangular cells, 1 in. deep, was mounted on the stationary wall and the axial gap is measured between the open face of the honeycomb and the opposing rotating disk surface. Static pressure was measured on the stationary wall only. Flush wall taps were installed at 6, 8, 9-7/8, 11-1/4, 12-5/8, 14, and 15-3/8 in. radii along three equally spaced radial directions. The pressure at the outermost tap was always found to be equal to surrounding pressure. Overall uncertainty in pressure readings is less than ±0.02 in. H_2O.

The total velocity vector in the gap is based on total pressure traverses, as measured by a Kiel probe and wall static pressures. To measure the flow angle, a wedge probe was used in combination with a nulling type differential pressure reading method. Using this angle, the velocity vector could be decomposed into its radial and tangential components.

Velocity profiles are measured by these probes only at $r=13.32$ in. ($\bar{r}=0.8875$). Axial locations of the probes are

Nomenclature

C_M = disk torque coefficient $= 2M/\rho\omega^2 r_1^5$
K = core velocity ratio $= \beta/\omega$
K_1, K_2, K_3 = parameter values of equation
M = torque on one side of the disk, ft lb
P = static pressure at a point in the gap, lb /ft^2
$\bar{P}$ = dimensionless pressure $= P/\frac{1}{2}\rho\omega^2 r_1^2$
$\Delta\bar{P}$ = dimensionless vacuum in the gap $= \bar{P}_{\text{rim}} - \bar{P}$, in. of water
ΔP = vacuum in the gap
Q = through flow rate, ft^3/s
Q_{crit} = critical flow rate
Re = disk Reynolds number $= \omega r_1^2/V$
r_1 = disk radius, ft
$a = r$ = radial coordinate, from axis of rotation, ft
$\bar{r}$ = dimensionless radial coordinate $= r/r_1$
R_u = ratio of core tangential velocities for honeycomb to plain wall surface
S = axial distance between disk and stationary wall, ft
$\bar{S}$ = dimensionless axial distance $= S/r_1$
T = through flow number $= Q/\omega r_1^2 S2\pi$
u = tangential velocity, ft/s
VR = vacuum ratio, ratio of vacuum in the gap for honeycomb to plain wall surface
z_0 = axial location of zero radial velocity, ft
$\bar{z}_0$ = dimensionless axial location of zero radial velocity $= z_0/S$
z = axial coordinate, distance from the disk, ft
V = radial velocity, ft/s
V_r = average radial velocity based on volume flow rate $= Q/2\pi rs$, ft/s
β = tangential velocity in the core region or in the middle of the gap, ft/s
ω = disk speed, 1/s
ν = kinematic viscosity, ft^2/s
ρA = density, slugs/ft^3

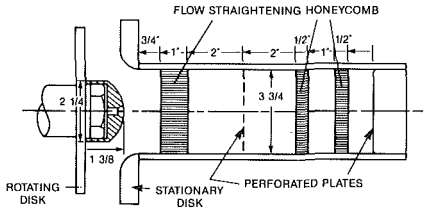

Fig. 2 Details of throughflow air inlet section

measured through a micrometer mechanism which is zeroed by touching the tips of the probe to the rotating disk. The overall uncertainties in axial location and the flow angles were estimated to be within ± 0.010 in. and ± 1 deg, respectively.

As mentioned, the throughflow is ducted to the center of the stationary wall via a 3-3/4 in. pipe and fed to the gap through a reduced inlet, as shown in Fig. 2. Perforated plates and honeycomb were inserted in the pipe to remove any swirl from the inlet flow and provide a reasonably uniform velocity profile. The flow was measured by a 2-1/2-in.-dia standard sharp-edged ASME orifice in an enlarged section of pipe leading to the inlet section.

A d-c dynamometer drive was used to provide a spectrum of disk rpms, as well as measure drive torque. It was possible to maintain a constant speed within ± 0.15 percent. Rpm was measured by a strobotac and checked against tachometer readings. Natural frequencies of the system were encountered at 400 and 1900 rpm and, therefore, these speeds were avoided for data runs.

For this program, the interest was in examining the flow field between a rotating and stationary disk. Therefore, to approximate the torque of the disk due to the gap flow field, a calculation of the torque from the total flow over the free face of the disk was subtracted from the measurement. A dimensionless torque coefficient presented in this report is based on twice the difference of the total measurement less the calculated free disk torque on one face. The system parasitic torque was evaluated by removing the disk and measuring the torque over the range of rpm of the test program. Three such tests were run and the average used to correct the disk torque measurements. Due to these corrections, the uncertainty in the disk data presented is estimated as ± 10 percent and should be used only for comparative evaluation of trends.

The axial clearance between plates was measured at eight points circumferentially, with the maximum difference among them less than 0.02 in. This variation was due to warpage of the lucite stationary disk. The deflection of the lucite plate due to the gap static pressure was investigated and found to be negligible. When honeycomb was fixed to the stationary disk the axial distance was measured from the tip of the honeycomb to the rotating disk surface.

Test Data and Discussion

The test data supporting the conclusions and detailing the physical trends are presented in this section. Due to space limitations only the trends about the effects of honeycomb wall geometry are described in detail.

Tangential Velocity Profile Measurements. The tangential velocity profiles were obtained at $\bar{r}=0.8875$ for throughflows $Q=0$, 1.75, and 3.43 ft^3/s at axial spacings $\bar{S}=0.0166$, 0.0333, 0.0666, and 0.10 for both the smooth and honeycomb-faced stationary wall. The results are given in Fig. 3 for no throughflow and Fig. 4 with throughflow. Consider first the no throughflow data in Figs. 3(*a*) and 3(*b*).

1 As the axial spacing $\bar{S}$ increases, the tangential velocities decrease at corresponding locations in the gap, the slope of the velocity profile changes and approaches a character where the bulk of the flow is rotating at almost constant velocity.

2 At the largest axial spacing, $\bar{S}=0.10$, the slope becomes slightly positive toward the stationary wall. This indicates that the fluid, which is flowing inward on this wall, and thus carries higher angular momentum from larger radii, is not as well mixed as at similar gap spacings. This profile overshoot is also observable in the measurements of Daily and Nece [2].

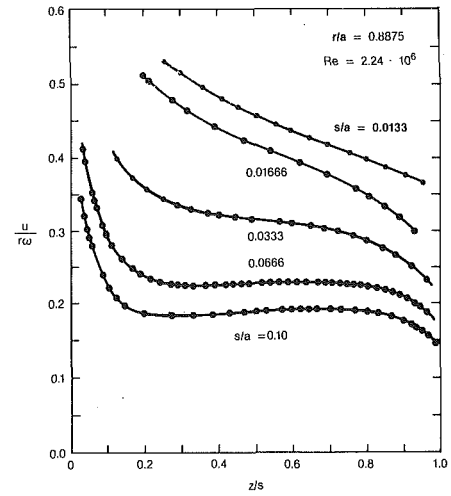

Fig. 3(*a*) Tangential velocity distribution, plain wall

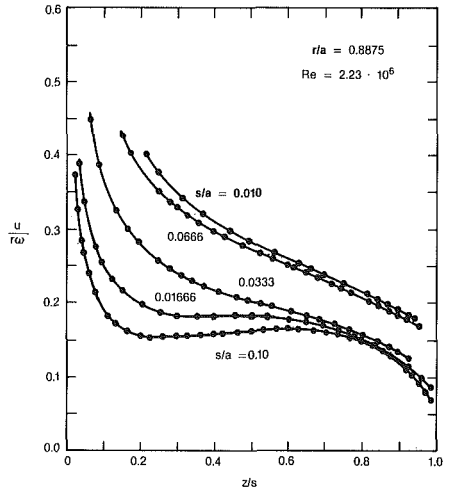

Fig. 3(*b*) Tangential velocity distribution with honeycomb

3 Comparison of the tangential velocity profiles with plain and honeycomb surfaces with and without throughflow (Figs. 3 and 4) indicates that the use of honeycomb:

- Reduces the velocity at all corresponding values of $\bar{S}$
- Decreases the tangential velocity at every point in the gap
- Increases the boundary layer thickness on the disk and decreases the boundary layer thickness on the wall
- Increases the overshoot of the velocity profile near the stationary wall

The ratios of core tangential velocities for honeycomb and plain wall surfaces are shown in Fig. 5 as a function of throughflow parameter T which indicates that the use of honeycomb decreases the core rotation by a factor of 0.6 to 0.75.

Static Pressure Measurements

No Throughflow. The pressure difference ΔP between a point at the disk rim (at r_i) and at a point $r(r<r_i)$ is shown on Figs. 6(*a*) and 6(*b*) in dimensionless coordinates for plain and honeycomb surface geometry, respectively. Pressure difference indicates the vacuum in the gap is increasing from the rim toward the center. On these figures, the least square error

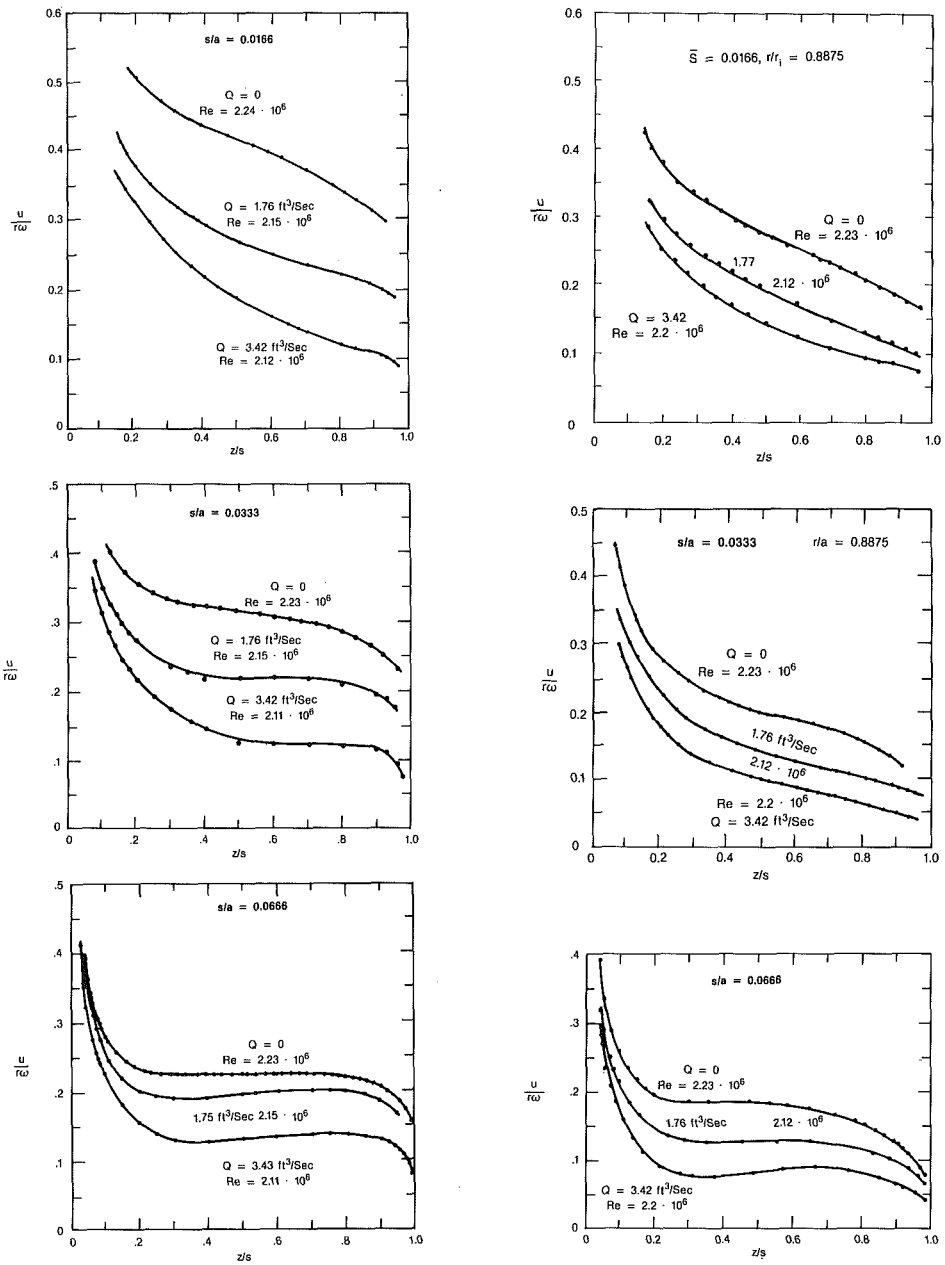

Fig. 4 Tangential velocity profiles in the gap, with and without throughflow

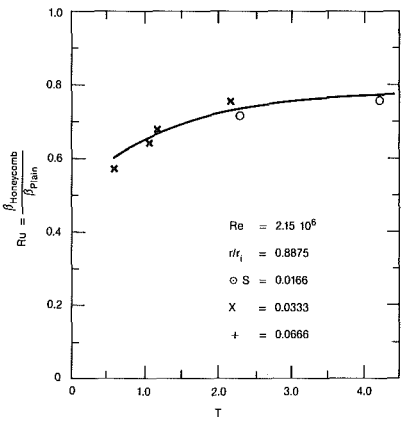

Fig. 5 Ratio of core tangential velocities for honeycomb over plain stationary disks

fit curve is drawn through the data taken at seven to nine different Reynolds numbers in the range $0.8\text{–}1.2\times 10^6$. (The scatter in the data with Re is also presented.) An equation of the following type

$$\Delta\bar{P} = k_1 + k_2(1-\bar{r}^2)^{k_3} \tag{1}$$

is fitted to the data. The values of the coefficients k_1, k_2, and k_3 are also shown on Figs. 6(*a*) and 6(*b*) for the four values of the parameter $\bar{S}$ covered in the tests. The data for plain wall (Fig. 6(*a*)) indicate the following trends.

a The pressure distribution in the gap, as represented in terms of dimensionless parameters $\Delta\bar{P}$ and $\bar{r}$, is independent of disk Reynolds number. This trend is in conformance with the widely used assumption that vacuum in the gap increases parabolically with the disk speed (2). This is further shown in the log-log plots of Fig. 7 where vacuum versus rpm and radial position is given for one gap spacing. The data for both honeycomb and smooth wall are well represented by straight lines of 1.98 slope.

b When there is no throughflow, the approximation is

often made that the radial pressure field can be represented as equation (2)

$$dP = -\rho\beta^2 r dr \tag{2}$$

In terms of dimensionless coordinates, equation (2) can be written

$$d\bar{P} = K^2 d\bar{R}^2 \tag{3}$$

where K is defined as the ratio of the representative fluid rotational velocity in the core to the disk rotational speed ω.

Hence, the slope of the curves of $\Delta\bar{P}$ versus $(1-\bar{r}^2)$ on Figs. 6(*a*) and 6(*b*) represent the square of the K ratio at each radial position. Only for the narrowest gap $\bar{S}=0.0166$ in the plain wall case, Fig. 7(*a*), is this slope constant over the bulk of the radial extent of the disk. For the honeycomb-faced wall, Fig. 6(*b*), the widest gap $\bar{S}=0.10$ approaches constant slope. This condition indicates the core is rotating as a solid body over the major extent of the disk.

The core velocity ratio (K) as calculated from pressure data and the use of equation (3) are given on Fig. 8 for plain and honeycomb geometry as a function of radial coordinate, for three different axial spacings. The data also indicate that the use of honeycomb reduces the core rotation considerably. The core rotation data calculated from the Kiel and wedge probe measurements at one radius ($\bar{r}=0.8875$) are also shown and are reasonably close to calculations from pressure data.

The effect of reduced core rotation reflects in a reduced vacuum for the honeycomb case, as is shown in Fig. 9, a plot of the dimensionless pressures at $r/r_1=0.4$ for both plain and honeycomb wall for various gap spacings. A more complete comparison of the two cases is given on Fig. 10 where the vacuum ratio VR^2 is shown as a function of disk Reynolds number for six radii. The honeycomb reduces the vacuum to less than 0.5 of the smooth wall case over the inner 75 percent of the radius. Honeycomb effect is constant with Re at $\bar{r}<0.6$, but decreases with Re near the periphery.

Static Pressure Measurements With Throughflow. Samples of data of the vacuum in the gap ($\Delta\bar{P}$) as measured by stationary wall static pressure taps are shown on Fig. 11 as a function of radial distance $\bar{r}$ for a range of throughflow for two axial gaps and for honeycomb and plain wall. As the

[2] Vacuum ratio, VR, is defined as the vacuum in the gap with honeycomb to that with plain under otherwise similar geometric and operational conditions.

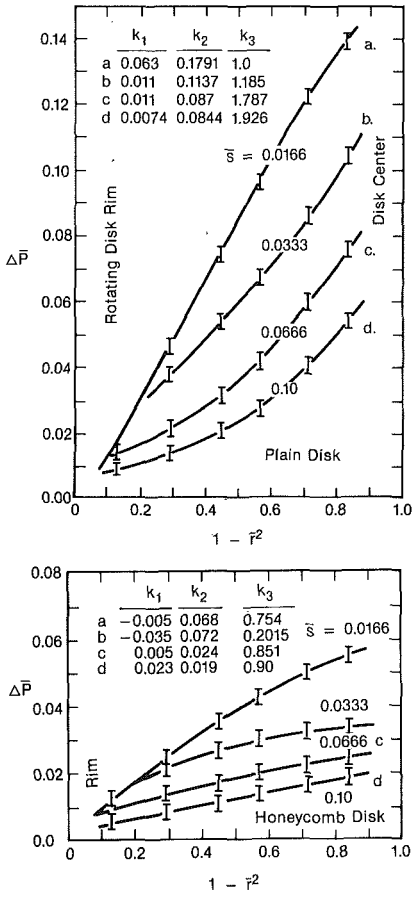

Fig. 6 Dimensionless pressure distribution in the gap, no throughflow

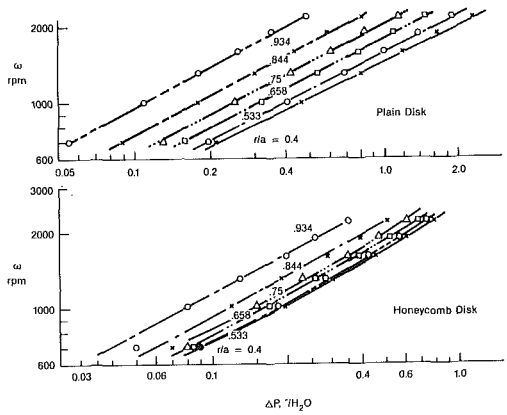

Fig. 7 Pressure distribution in the gap as a function of disk speed

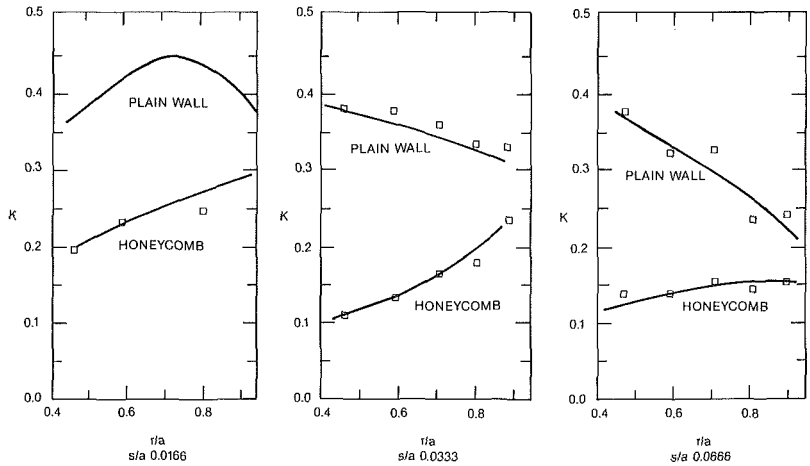

Fig. 8 Effective core rotation in the gap: data points from tangential velocity profile measurements

dimensionless vacuum is dependent on $\bar{r}$, $\bar{S}$, and Q in a nonreducible form (see Appendix), it is not possible to present these three dependencies on single figures as for the zero throughflow case.

The vacuum dependency on throughflow produces an interesting behavior as shown in Fig. 12. As the throughflow is increased at constant rpm, the vacuum $\Delta\bar{P}$ first decreases to a minimum and then increases. This characteristic is attributed to two competing phenomena, i.e., the core rotation which creates gap vacuum proportionate to the square of the rotational velocity, and the radial diffusion of the throughflow which causes vacuum proportionate to the square of the throughflow component of velocity. As shown in Fig. 12, at low throughflow rates, an increase in flow reduces the core rotation and the gap vacuum to a greater extent than the increase in the vacuum due to increased diffusive effect. At high throughflow rates, the core rotation effects are small, and thus, the diffusive effect dominates. The same trends are apparent for either smooth or honeycomb stationary disks, although the magnitude of gap vacuum is much less in the latter case, as previously described.

Critical Flow Measurements. One of the objectives of this program was to determine the critical flow rate which would prevent the inflow from the gap rim or at any specified $\bar{r}$. To determine this, the radial velocity component was first calculated from the probe data to provide a general overview of the radial velocity profiles in the gap. These data are given in Fig. 13 for both plain and honeycomb walls for $\bar{S}=0.0166$, 0.0333, and 0.0666; $Q=0$ to 3.42 at $\bar{r}=0.8875$ and Re $\cong$ 2.24. The uncertainty in these data is high as evidenced by the lack of apparent continuity closure for several of the curves. This is due to the low magnitude of the radial component compared to the total velocity vector as well as the peripheral nonuniformity of the radial profile. A detailed comparison of the corresponding radial velocity profiles for the plain and honeycomb wall indicates that the use of honeycomb:

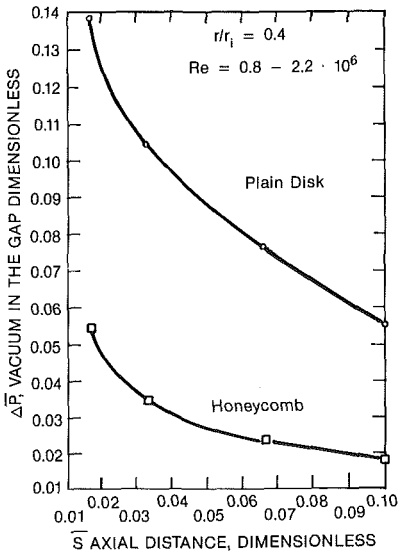

Fig. 9 Pressure in the gap for plain and honeycomb stationary disk

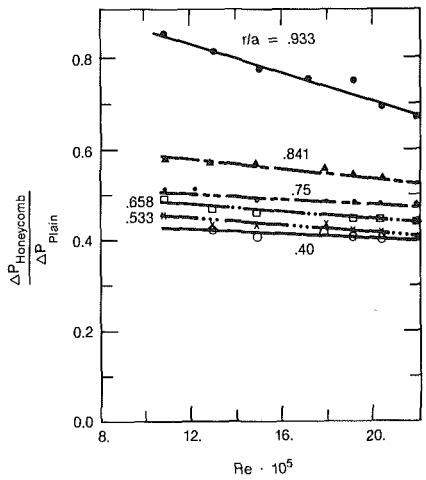

Fig. 10 Ratio of static pressure difference, honeycombed wall

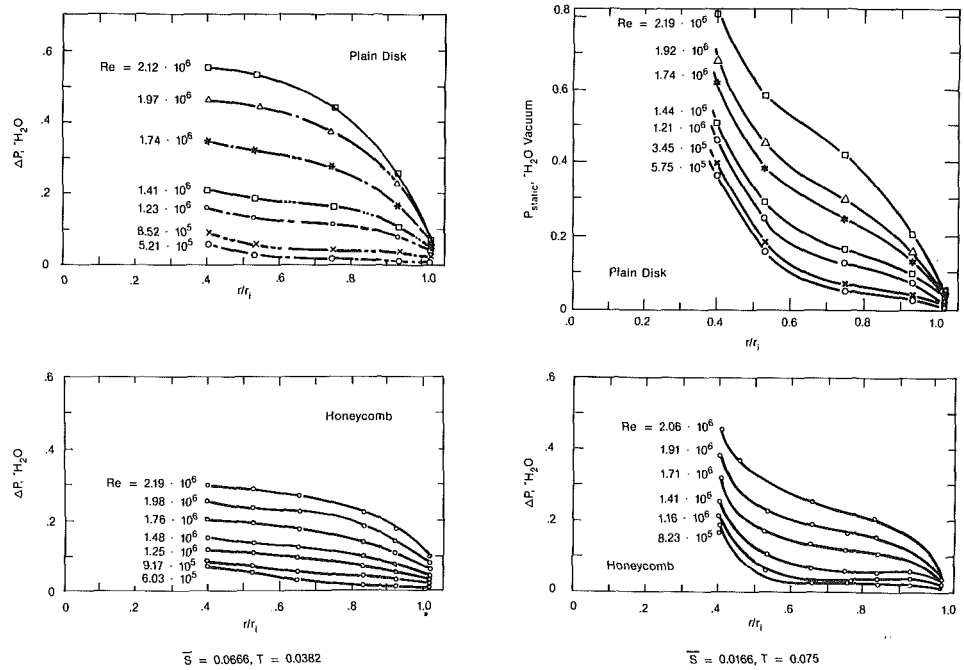

Fig. 11 Examples for static pressure distribution on the stationary disk as a function of dimensionless radius

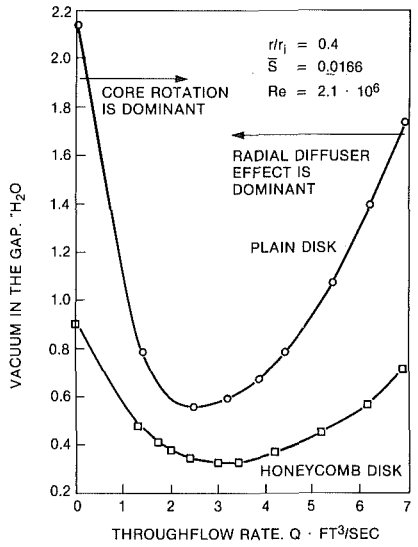

Fig. 12 Pressure variation at a point as a function of throughflow rate for plain and honeycomb stationary disks

1 Moves the location of the zero radial velocity point toward the stationary wall

2 Decreases the radial inflow over the stationary wall

To have more direct evidence about the inhibitive effects of honeycomb on the ingress of air over the stationary wall, a particular test is performed. In this test, the critical flow at a certain radial position ($\bar{r}=0.8875$) is determined by wedge probe measurements of flow angle near the stationary surface. The probe was aligned tangentially as the throughflow rate was increased until the angle tap pressures are nulled. The critical rate for a smooth wall is measured to be 2.46 ft^3/s, while for honeycomb surface it is found to be 1.56 ft^3/s. The use of the honeycomb reduced the ingress of air to about 64 percent of its original value under these conditions.

Disk Torque Measurements

No Throughflow. Disk torque measurements for the plain wall case without throughflow are presented on Fig. 14(*a*) for $\bar{S}=0.0166$, 0.0666, and 0.10. On the same figure, torque correlation curves for free disks (laminar and turbulent flow) are reproduced from (1) and for fully enclosed disks from (2). Important trends are:

1 Disk torque increases and approaches the free disk correlation as $\bar{S}$ increases.

2 The data suggest that the laminar-to-turbulent transition starts about $Re=4.5\times10^5$ and is completed about $Re=1.4\text{–}1.7\times10^6$.

Disk torque measurements for honeycomb walls are presented in Fig. 14(*b*). Although the trends are very similar to the smooth wall case in the fully turbulent regime above $Re=1.6\times10^6$, there are marked differences in the effect of gap spacing $\bar{S}$ at transitional Reynolds numbers.

With Throughflow. The torque data with throughflow are given on Fig. 15 for the two flow rates and wall surface geometry. Comparison of these data with those of Fig. 14 indicate that:

1 Disk torque increases with throughflow rates.

2 After the completion of transition, the torque for a honeycomb surface is larger than that of a plain wall.

3 During the transition region, the disk torque with honeycomb seems to be smaller than that of a plain wall.

Due to the large uncertainty in the torque measurements, the data presented should be treated cautiously.

Conclusions

In this paper, the effect of a honeycomb-shaped stationary wall surface on the flow regime between a rotating disk and a parallel wall is investigated. Static pressure, tangential and radial velocity and torque measurements are compared for plain and honeycomb wall geometries at three throughflow rates and four axial spacings.

The data with plain wall surface indicate that:

1 Radial velocity increases continuously from the wall to the disk. At zero or low throughflows, there is inflow over the stationary wall. The axial distance with inflow increases toward the rim. There is no appreciable extent of the gap with either inflow or outflow.

2 The boundary layer thicknesses for the radial and tangential velocity profiles are different, smaller for the radial and larger for the tangential velocity profiles. This should be considered in constructing analytic models of the flow.

3 An increase in throughflow rate:
- Increases the radial velocity profile almost parallel to itself.
- Decreases the inflow rate and region over the stationary wall and increases the outflow rate and region over the disk.
- Moves the point of zero radial velocity toward the stationary wall.
- Decreases the tangential velocity in the core region.
- Increases the disk torque.
- Can increase or decrease the vacuum in the gap, depending on the flow regime and radial position.

4 An increase in the axial gap:
- Reduces radial velocity.
- Increases the amount and region of radial inflow on the stationary wall.
- Decreases the tangential velocity in the core region.
- Increases the disk torque.
- Decreases the vacuum in the gap.

5 The vacuum in the gap increases toward the axis that can be represented with a relation such as

$$\Delta P=k_1+k_2(1-\bar{r}^2)^{k_3}$$

The values of coefficients k_1, k_2, and k_3 are determined from data.

6 When there is throughflow, two regions of major influence can be envisioned, namely: the disk pumping dominated region near the circumference and the radial diffuser dominated region near the axis. As the amount of throughflow is increased, the region of diffuser domination enlarges toward the circumference, and when the disk rotation increases, the region of disk pumping penetrates further toward the axis. At a certain point of the disk pumping dominated region, the vacuum decreases, goes through a minimum, and then increases, with increasing throughflow rates.

The above physical trends of flow were used as the basic model for the analytic prediction of inflow rates by one of the authors [5].

A comparison of data with the honeycomb-faced stationary wall relative to that of a smooth wall indicates that the use of honeycomb:

1 Reduces the radial inflow on the wall by about 20–40 percent. This reduction effect is more dominant for small $\bar{S}$ values.

2 Moves the point of zero radial velocity toward the stationary wall by about 20–30 percent.

3 Increases the outflow region near the disk and decreases the inflow region near the wall.

4 Reduces the tangential velocity by about 30–40 percent.

5 Reduces the vacuum in the gap about 40–60 percent.

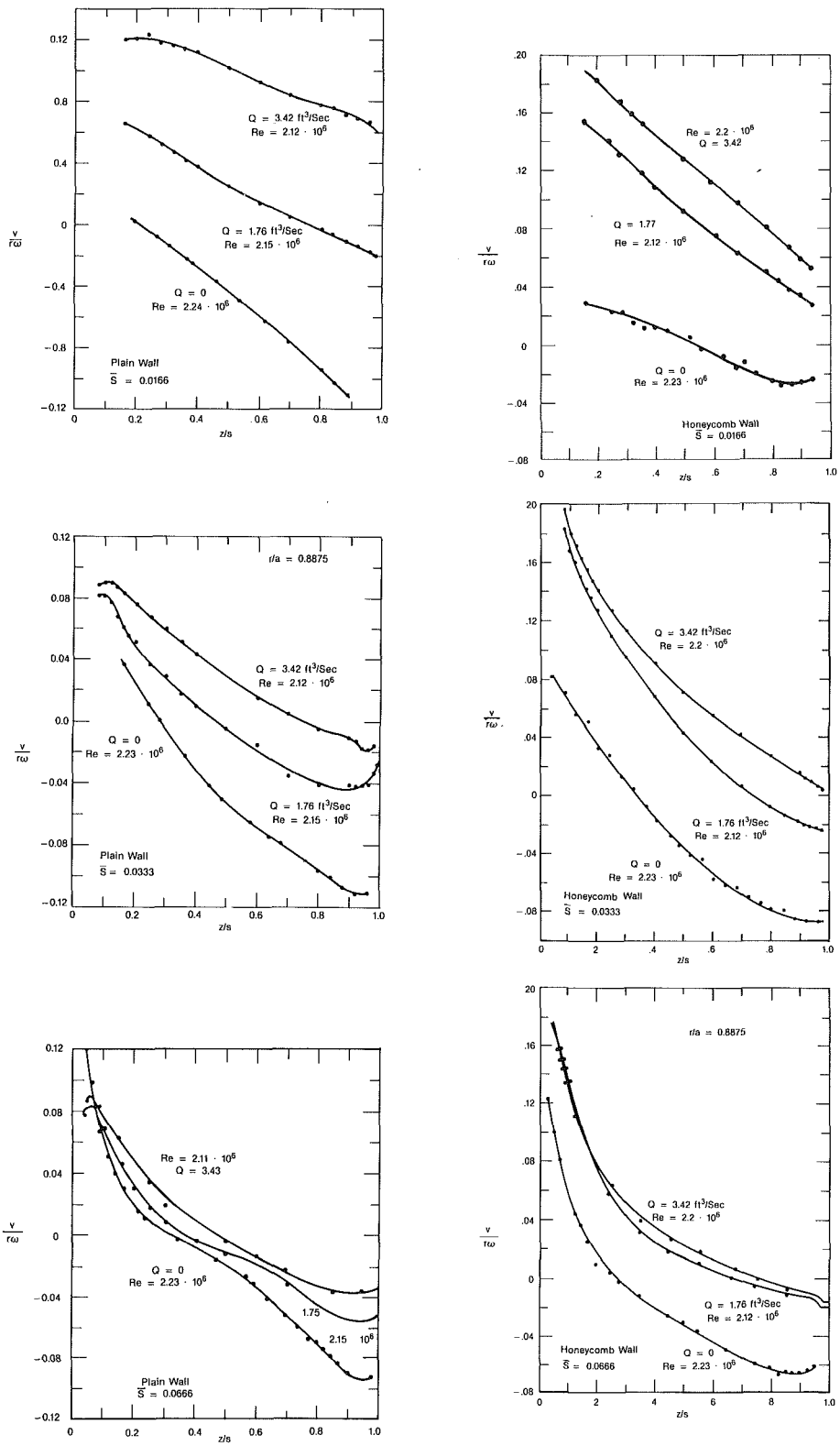

Fig. 13 Radial velocity profiles in the gap, $\bar{r} = 0.8875$

6 Increases the disk torque with throughflow after the transition to turbulent flow is completed.

These experiments clearly indicate that it is effectively possible to modify the flow field by changing the surface geometry of the stationary wall. Honeycomb geometry is an example.

Acknowledgments

The authors express their appreciation to the General Electric Company Corporate Research and Development and Gas Turbine Department for supporting this investigation and allowing data to be published. Also, our thanks to Mrs. Kim Reksc for preparing the manuscript.

References

1 Dorfman, L. A., *Hydrodynamic Resistance and Heat Loss of Rotating Solids*, Oliver and Boyd, London, 1963.

2 Daily, J. W., and Nece, R. E., "Chamber Dimension Effects on Induced Flow and Friction Resistance of Enclosed Rotating Disks," ASME *J. Basic Eng.*, 1960, p. 218.

3 Bayley, F. J., and Owen, J. M., "The Fluid Dynamics of a Shrouded Disk System With a Radial Outflow of Coolant," ASME JOURNAL OF ENGINEERING FOR POWER, Vol. 92, 1970, p. 335.

4 Sokolov, V. S., "Determining the Temperature of the Cooling Air Around the Side Surface of a Rotor Disk With Radial Cooling," *Teploenergetika*, Vol. 21(s), 1974, p. 66 (translation available as UDC 621.165).

5 Uzkan, T., "Effects of Coolant Air Inlet Conditions on Turbulent Flow Between a Turbine Disk and Its Casing," ASME JOURNAL OF ENGINEERING FOR POWER, Vol. 103, 1981, p. 637.

6 Owen, J. M., and Pincombe, J. R., "Velocity Measurements Inside a Rotating Cylindrical Cavity With Radial Outflow of Fluid," *J. of Fluid Mechanics*, Vol. 99, 1980, p. 111.

7 Phadke, U. P., and Owen, J. M., "An Investigation of Ingress for an Air Cooled Shrouded Rotating Disk System With Radial Clearance Seals," ASME JOURNAL OF ENGINEERING FOR POWER, Vol. 105, 1983, p. 178.

8 Owen, J. M., and Phadke, U. P., "An Investigation of Ingress for a Simple Shrouded Rotating Disk System With a Radial Outflow of Coolant," ASME Paper No. 80-GT-49.

9 Watabe, K., "Experiments on the Fluid Friction of a Rotating Disk With Blades," *Bull. JSME*, Vol. 5, No. 17, 1962, p. 49.

10 Watabe, K., *On the Frictional Resistance of Enclosed Rotating Disk of Various Surfaces*, Mem. Fac. Nagoya Univ., 1962, Vol. 14, p. 81.

11 Watabe, K., "Effect of Clearances and Grooves on Fluid Friction of Rotating Disks," *Bull. JSME*, Vol. 8, No. 29, 1955, p. 55.

12 Watabe, K., "On Fluid Friction of Rotational Rough Disk in Rough Vessel," *Bull. JSME*, Vol. 1, No. 1, 1958, p. 69.

13 Watabe, K., "On Fluid Resistance of Enclosed Rotating Rough Disks," *Bull. JSME*, Vol. 8, No. 32, 1965.

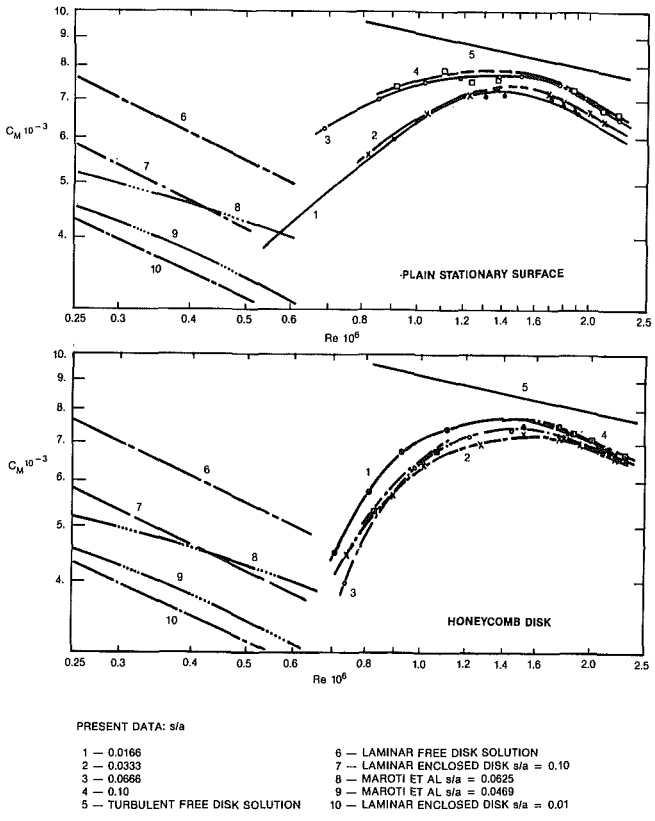

Fig. 14 Disk torque coefficient data

APPENDIX

For first approximation, one may assume that the pressure in the gap is a function of r only and is constant in axial direction. This assumption is expected to be valid for small values of $\bar{S}$. Moreover, in the midsection, one may assume that the radial pressure gradient is mainly influenced by:

1 The centrifugal force due to fluid rotation
2 Radial diffuser effects due to enlargement of flow area

For an elemental control volume in the core, the balance of forces in the radial direction is

$$r\frac{dP}{dr}=\rho u^2-\rho\frac{d}{dr}(rV^2)$$

Using the average radial velocity, V_r, based on volume flow rate and dimensionless throughflow parameter K_ν defined as

$$K_\nu=\frac{2\pi r_1^2 S\cdot\omega}{Q}$$

one can obtain

$$d\bar{P}=K^2\bar{r}d\bar{r}+\frac{1}{K_\nu^2}\frac{d\bar{r}}{\bar{r}^3}$$

Integrating from $\bar{r}$ to $\bar{r}=1.0$ and using mean value theorem for K, within this range one obtains

$$\Delta\bar{P}=\left[\frac{K_m^2}{2}+\frac{1}{2K_\nu^2\bar{r}^2}\right](1-\bar{r}^2)$$

This equation shows that when throughflow is zero, $\Delta\bar{P}$ dependency on $\bar{r}$ can be represented as the $(1-\bar{r}^2)$ term, but with throughflow this is not possible due to the second term.

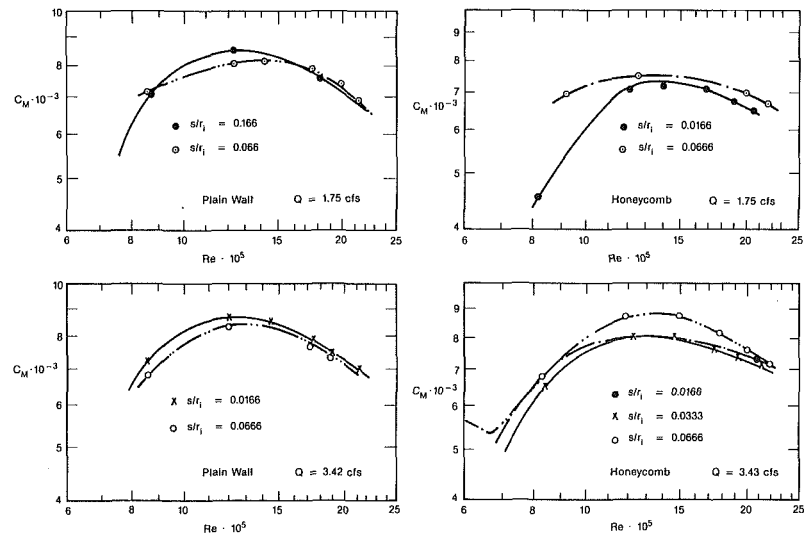

Fig. 15 Disk torque coefficient as a function of Reynolds number with throughflow

Z. W. He
Lecturer.

S. Y. Zhang
Professor.

Department of Aeroengine Design,
Nanjing Aeronautical Institute,
Nanjing, People's Republic of China

Lip Separate Flow Blowing and Analysis of Coherence of Inlet

It is found experimentally that blowing at the lip separation of an inlet obviously reduces the turbulence at the inlet exit, and apparently reduces the intensity of pressure fluctuations caused by the shock-boundary layer interaction downstream of the throat. The coherence between pressure in the interaction region and total pressure at the exit is also reduced. The coherence between the pressure in the lip separation region and total pressure at the exit is 0.32. If, in addition, there is a stronger shock downstream of the throat, the abovementioned coherence is reduced to 0.06.

Introduction

It is noteworthy that the lip flow separation of the supersonic inlet during airplane takeoffs or flying at large angles of attack may seriously reduce the total pressure recovery and increase the flow distortion at the inlet exit [1–4]. In this paper the effects of blowing at the lip separation on the dynamic characteristics of inlet are presented, and some sources of the dynamic distortion are analyzed by means of the coherence theory.

Experimental Model and Instrumentation

The model used in the experimental investigation is an axial symmetric double cone mixed compression inlet of 1/10 scale as shown in Fig. 1. The cone angles of centerbody are 35 and 50 deg. The cowl lip inner and outer angles are 10 and 14 deg, respectively. The centerbody is supported by four equally spaced streamline struts. The inlet cross-sectional area distribution along the axis is plotted in Fig. 2.

There are eight Kulite transducers mounted at positions of x/R_c = 0.19, 0.59. 1.09, 2.49, 2.78, 4.37, 5.9, and 7.85, respectively, and with the central angle of θ = 315 deg circumferentially on the cowl of the inlet model. There is a two-leg rotating pressure rake with three Kulite transducers on one leg and six pitot tubes on the other. Downstream the inlet is connected to suction pumps. The mass flow of the inlet is controlled by a special exit plug downstream of the inlet.

The measuring instruments of the static pressure consist of an SYD-1 transducer and an L-S recording system. A schematic drawing of the dynamic pressure measuring system employed is shown in Fig. 3.

Flow Feature at the Entrance and Lip Separation Blowing

There is a serious nonuniform flow and lip separation at the entrance of the inlet at takeoff with M_e = 0.257, as shown in Fig. 4.

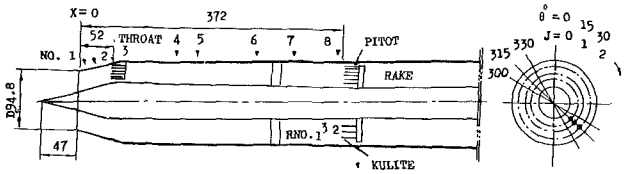

Fig. 1 Inlet model (unit MM)

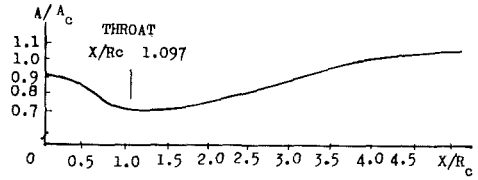

Fig. 2 Inlet cross-sectional area distribution

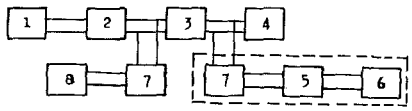

Fig. 3 Block diagram of dynamic pressure measuring system: (1) Kulite transducer; (2) amplifier; (3) magnetic recorder; (4) oscillograph; (5) FFT analyzer; (6) X-Y recorder; (7) band-pass filter; (8) r.m.s. meter

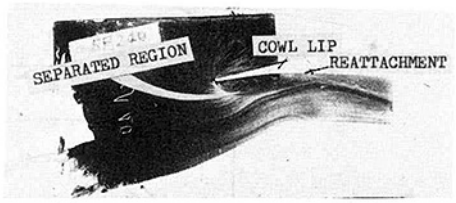

Fig. 4 Flow pattern

To control the lip separation and improve the nonuniform flow at the entrance, a special blowing slot is designed as shown in Fig. 5. The inclination of the slot is so carefully designed that the blowing is at the lip separation region. Experimental results show that the lip flow separation is for

Contributed by the Gas Turbine Division and presented at the 1985 Beijing International Gas Turbine Symposium and Exposition, Beijing, People's Republic of China, September 1–7, 1985. Manuscript received at ASME Headquarters May 31, 1985. Paper No. 85-IGT-68.

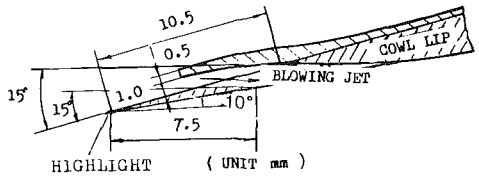

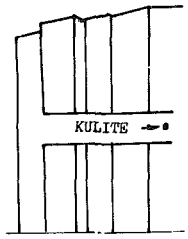

Fig. 5 A special blowing slot

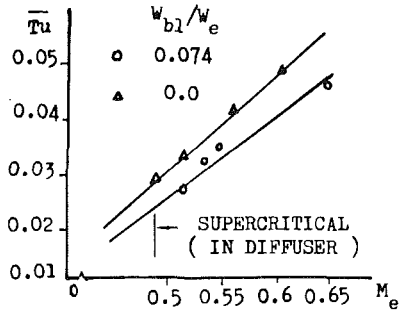

Fig. 6 $\overline{Tu}$-M_e

the most part eliminated and the flow at the entrance becomes apparently uniform after blowing. It is necessary to point out that for the nonblowing case the slot is closed and the inner surface of the cowl is smooth.

Results and Discussion

1 As shown in Fig. 6, $\overline{Tu}$ is reduced by lip blowing, and more obviously if M_e is increased.

2 For subsonic flow in the duct of the inlet, a peak value of $\Delta P_{r.m.s}$ is found close to the reattachment of the lip separation; then the $\Delta P_{r.m.s}$ values decrease rapidly, as shown in Fig. 7 (curves *A* and *B*), with blowing mass flow, $W_{bl}/W_e = 0.05$, at Mach $M_e = 0.241$ and without blowing at $M_e = 0.257$, respectively.

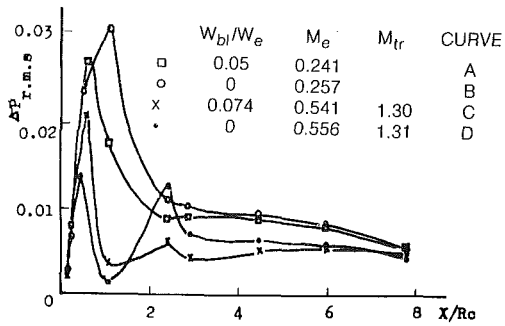

Fig. 7 $\Delta P_{r.m.s.}$-X/R_c

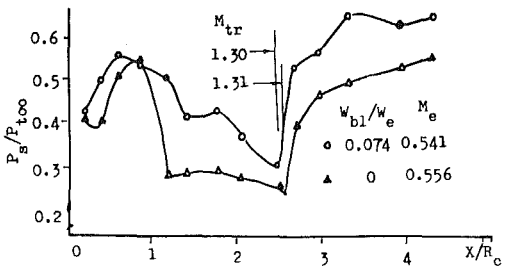

Fig. 8 $P_s/P_{t\infty}$-X/R_c

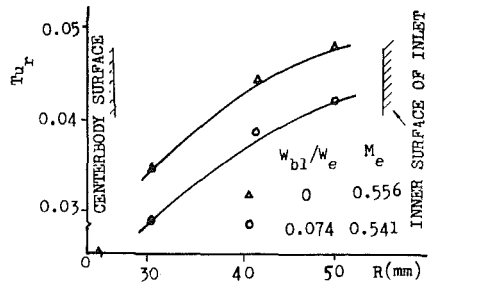

Fig. 9 Tu_r-R

For the case with $M_{tr} = 1.31$ Fig. 8 shows the position of a terminal shock. Figure 7 (curve *D*) shows that, downstream of the throat, there occur not only a peak value of $\Delta P_{r.m.s}$ near the reattachment of the separation, but also a peak value of $\Delta P_{r.m.s}$ near the region of the shock-boundary layer interaction. By blowing at the lip separation with $W_{bl}/W_e = 0.074$ it is found that the first peak value is increased as shown in Fig. 7 (curve *C*). This may be caused by the strong mixing of the flow near the measuring point lying between the lip

Nomenclature

A = area of inlet channel, cm^2
A_c = inlet entrance area, cm^2
D_c = inlet entrance diameter, mm
M_e = average Mach number at inlet exit
M_t = average Mach number at geometry throat of inlet
M_{tr} = Mach number before terminal shock in diffuser
$\bar{P}_{te}$ = average total pressure at inlet exit, kg/cm^2
P_s = surface static pressure of inlet, kg/cm^2
$P_{t\infty}$ = free-stream total pressure, kg/cm^2
$\Delta P_{tr.m.s.r}$ = average root-mean-square value of total pressure fluctuations in any annular area at inlet exit, kg/cm^2
$\Delta P_{tr.m.s.\,60}$ = average root-mean-square value of total pressure fluctuations in any 60 deg sector at inlet exit, kg/cm^2
$\overline{\Delta P}_{tr.m.s}$ = average root-mean-square value of total pressure fluctuations at inlet exit, kg/cm^2
$\Delta P_{r.m.s.}$ = root-mean-square value of static pressure fluctuations, kg/cm^2
q_e = average dynamic pressure at inlet exit, kg/cm^2
R = radius, mm
R_c = $D_c/2$
$\overline{Tu}$ = average turbulence at the inlet exit $= \overline{\Delta P}_{tr.m.s}/\bar{P}_{te}$
Tu_{cj} = turbulence distribution at inlet exit $= \Delta P_{tr.m.s\,60j}/\bar{q}_e$
Tu_r = annular average turbulence at inlet exit = $\Delta P_{tr.m.sr}/\bar{P}_{te}$
W_{bl} = lip blowing mass flow, kg/s
W_e = mass flow of inlet, kg/s
X = axial distance measured from the cowl lip, mm
θ = central angle, deg
ω = frequency, Hz

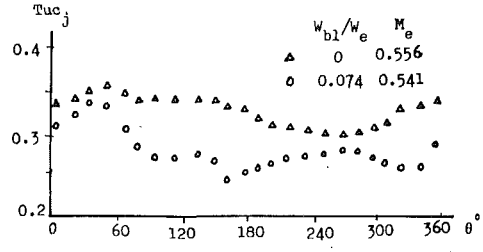

Fig. 10 Tu_{cj}-θ

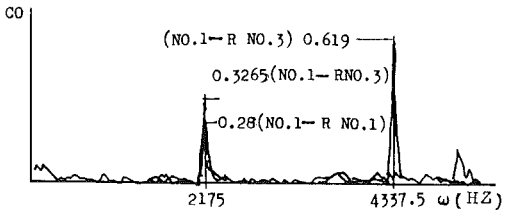

Fig. 11 CO-ω

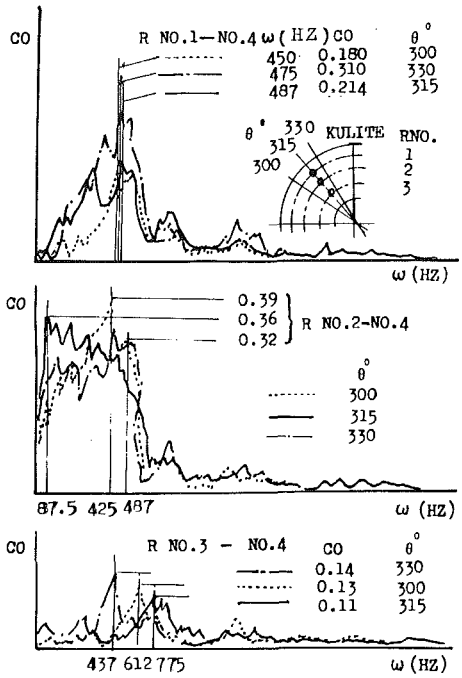

Fig. 12 CO-ω

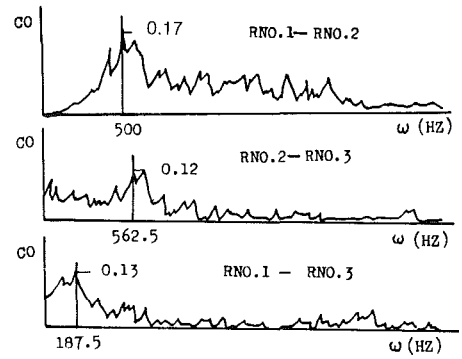

Fig. 13 CO-ω (θ = 300 deg, M_e = 0.556, W_{bl}/W_e = 0)

blowing slots shown in Fig. 5. Moreover, the blowing flow could be underexpanded at the exit of the blowing slot resulting in a zone of supersonic flow followed by expansion waves. These could also affect the first peak of turbulence. The reason for reducing the second peak is that the lip flow separation is essentially eliminated and the flow of the entrance of inlet becomes more uniform by blowing; moreover, as the static pressure behind the terminal shock rises sharply the terminal shock is forced to move toward the throat of the inlet. So the shock-boundary layer interaction is reduced as shown in Fig. 8. The curves shown are at the conditions of M_e = 0.556, M_{tr} = 1.31 (without blowing) and M_e = 0.541, M_{tr} = 1.30 with W_{bl}/W_e = 0.074.

3 The effect of the lip blowing on the turbulence distribution of the inlet is discussed. It is found that the annular average turbulences Tu_r are all reduced at M_e = 0.541 with W_{bl}/W_e = 0.074 if they are compared to the results at M_e = 0.556 without blowing as shown in Fig. 9. Also, their variations are of the same pattern: increasing from the inner to the outer annulus. In Fig. 10 the comparison of the turbulence distribution Tu_{cj} with lip blowing and without is shown. It is indicated that this turbulence is also reduced by blowing at the lip separation.

4 For analysis of the sources of dynamic distortion at the inlet exit the authors have just picked up some typical dynamic response, such as that of the static pressure in the lip flow separation region, the static pressure in the terminal shock boundary layer interaction region, and the total pressure of the rotating rake. With the model scale used, the cutoff frequency of 5 kHz is chosen.

The coherence between the fluctuation of the static pressure in the lip separation region and that of the total pressure at the exit is discussed.

For subsonic flow in the duct, for example, with M_e = 0.257 and M_t = 0.57 the coherences showing the degree of interdependence between the above two pressure fluctuations are presented in Fig. 11. Static pressure probe No. 1 in the lip separation region is correlated with RNo. 1 and RNo. 3 of the total pressure probe of the rake, respectively, at θ = 315 deg. It is shown that the coherences of the fluctuation between the static probe No. 1 and that of the total pressure probe RNo. 1 are 0.3265 and 0.6195 at frequencies of 2175 Hz and 4337 Hz, respectively. It means that the abovementioned pressure fluctuations are obviously interdependent on each other. Of course, the coherence at a frequency of about 2100 Hz is more important by considering the response of the engine to the fluctuation of the pressure. The coherence between the fluctuations of the No. 1 static pressure probe and that of the RNo. 1 total pressure probe is also shown in Fig. 11. By comparing the coherence for RNo. 3 to that of RNo. 1 it is shown that the effect of the lip separation on the total pressure near the centerbody is slightly larger than the effect upon that near the inner wall of the inlet.

For the flow having both lip flow separation and terminal shock, for example, with M_{tr} = 1.31 and M_e = 0.556 in the diffuser, the coherence value is quite different from that of the pure subsonic flow as mentioned above. At the rake position of θ = 315 deg the rake total pressure fluctuations RNo. 1, RNo. 2, and RNo. 3 are correlated, respectively, to those of the three static pressures as at the lip separation point, its downstream, and the reattachment. Experimental results show that the maximum coherence is about 0.04. According to this value it can be concluded that the lip flow separation has only a little effect on the fluctuation of the total pressure at the exit when a strong terminal shock is found downstream of the throat.

The coherence between the fluctuation of static pressure near the terminal shock-boundary layer interaction region and that of the total pressure of the rake is discussed.

At a rake position of θ = 300, 315, and 330 deg, and M_e = 0.556 without blowing, the fluctuation of the No. 4 static pressure probe near the terminal shock-boundary layer interaction region is correlated with that of the three other rake

total pressure probes RNo. 1, RNo. 2 and RNo. 3, respectively. As shown in Fig. 12, the fluctuation of pressure caused by the terminal shock-boundary layer interaction has an obvious effect on that of the total pressures of the rake downstream of the terminal shock within the frequencies up to 487 Hz, especially on that of the RNo. 2 total pressure probe. The maximum coherence is 0.39.

It is noteworthy that the fluctuation of the static pressure of probe No. 4 near the shock-boundary layer interaction region has only a little effect on that of the rake total pressure when the lip separation is blown off by a stronger jet. As an example, the maximum coherence is about 0.06 within the frequency of 5 kHz when $M_e = 0.541$ with $W_{bl}/W_e = 0.074$ and $M_{tr} = 1.30$.

It should be pointed out that when a small-scale inlet model is used to find the dynamic distortion at the exit with a rotating rake in which several Kulite transducers are fixed, it is important to check the mutual effect of the total pressure fluctuations.

The coherence between any two total pressure fluctuations measured by the three total pressure probes RNo. 1, RNo. 2, and RNo. 3 of the rotating rake is presented in Fig. 13. The maximum coherence is about 0.17 within the frequencies of 187–562 Hz at $M_e = 0.556$. It means that they have little effect on each other.

Conclusions

Blowing at the lip separation can obviously reduce the effect of the separation on the turbulence of the inlet exit.

Lip blowing apparently may also reduce the fluctuation of the static pressure near the terminal shock-boundary layer interaction zone, and according to the coherence analysis, it also reduces the effect of the terminal shock-boundary layer interaction on the fluctuation of the exit total pressure.

The coherences between fluctuation of the static pressure of the lip separation zone and that of the total pressure at the exit are 0.326 and 0.69 with the frequencies of 2175 Hz and 4337 Hz, respectively, for subsonic flow in the duct. It is obvious that the coherence of 0.326 with frequency of 2175 Hz is more important. If strong terminal shock is found in the diffuser, the maximum coherence of fluctuations between the static pressure near the reattachment of separation and total pressure at the exit is less than 0.04 within the frequency of 5 kHz.

The coherences between the fluctuations of the static pressure of terminal shock-boundary layer and those of the total pressure at the exit are about 0.3–0.39 corresponding to the frequencies of 475–425 Hz. At the frequency of interest, the value of coherence is much less than 1.0. It means that there may be other factors affecting the turbulence at the exit of the inlet besides fluctuating static pressure of terminal shock-boundary layer.

When a model with smaller scale is used to investigate the dynamic distortion of the inlet exit, a special effort must be made to check the mutual effect between any two total pressure fluctuations.

References

1 Fradenburgh, E. A., "Theoretical Performance Characteristics of Sharp Lip Inlets at Subsonic Speeds," NACA TN 3004, 1953.

2 Lotter, K. W., and Malefakis, J., "Intake Design and Intake/Airframe Integration for a Post-stall Fighter Aircraft Concept," AGARD CP-247.

3 Camthon, J. A., "Design and Preliminary Evaluation of Inlet Concepts Selected for Maneuver Improvement," AIAA Paper No. 76-701.

4 Sherman, D. A., and Motycka, D. L., "Experimental Evaluation of a Hypothesis for Scaling Inlet Turbulence Data," AIAA Paper No. 71-669.

5 Smith, R. H., "Preliminary Flight Investigation on Dynamic Phenomena Within Air Breathing Propulsion Systems of Supersonic Aircraft," AIAA Paper No. 68-593.